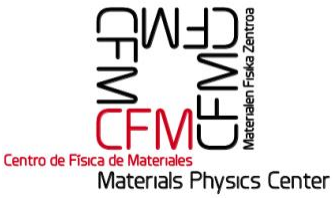

Single-Chain Nanoparticles: Exploring Novel Synthesis Routes, Basic Properties and Potential Applications

PhD Thesis Submitted by

Marina Gonzalez Burgos

Donostia – San Sebastián, November 2017

Single-Chain Nanoparticles: Exploring Novel Synthesis Routes, Basic Properties and Potential Applications

by

Marina Gonzalez Burgos

Thesis Supervisors:

Arantxa Arbe Mendez

José A. Pomposo Alonso

Donostia – San Sebastián, November 2017

Abstract

In the Nanotechnology era, many methods for synthesis of materials with well-defined nanoscale dimensions ($1\,\text{nm} = 10^{-9}\,\text{m}$) have been developed. As a remarkable example, excellent size and shape control has been achieved for the synthesis of hard nanoparticles, such as quantum dots, gold nanoclusters or metal oxide nanoparticles. Similar control to produce soft nanoparticles based on polymers with dimensions below 10 nm has not been possible until just the beginning of the 21st Century. Advances in the synthesis of well-defined functional polymers through living radical polymerization processes, post-functionalization techniques, as well as development of highly-efficient intra-chain coupling reactions have paved the way to reliable production of single-chain polymer nanoparticles.

The field of single-chain nanoparticles strives to create innovative nanostructures while also attempting to mimic biological nanomaterials. Natural macromolecules display primary structures with exact monomer sequence control allowing for the precise folding into three-dimensional shapes containing specific arrangements of functional groups on the surface and exterior. Obtaining synthetic nanostructures with the level of complexity seen in nature presents a significant challenge, with current systems unable to match the precision. Many areas of research including polymers are beginning to bridge the gap between synthetic and natural materials. The manipulation of single polymer chains, specifically intra-molecular folding into well-defined

nanoparticles termed single-chain nanoparticles, or in brief SCNPs, is one particular avenue continually gaining interest. This area of research is simple conceptually, yet has results in many systems with complex behaviors.

In “Single-chain nanoparticles: exploring novel synthesis routes, basic properties and potential applications” we try to made progress in this evolving field by exploring novel synthesis routes towards the development of functional single-chain nanoparticles, and by performing proof-of-concept experiments to show their possible use in potential applications. We also provide a deeper knowledge about the basic properties of these nano-objects, which is of utmost importance to stablish reliable structure-properties relationship.

We start the manuscript with a general introduction about single-chain nanoparticles. First, we describe in brief some concepts about polymers and nanotechnology. Then, we provide a general overview about the current synthesis routes and morphology in solution of single-chain nanoparticles, as well as about the potential applications of these functional nano-objects. We finish chapter 1 with the objectives of this thesis.

After the introduction, we provide useful information about all the samples as well as all the techniques employed in this thesis. In chapter 2 we report on the synthesis of all the single-chain nanoparticles employed, including already known and new synthesis methods. A large set of techniques has allowed extracting information of all the samples investigated, which are all explained in chapter 3.

Abstract

In chapter 4 we explore the basic properties of single-chain nanoparticles in comparison with their precursor counterparts. We focus on the stability, structural and dynamical features in solution. For this purpose, we combine the information provided by different techniques. Conventional techniques such as size exclusion chromatography and dynamic light scattering are employed to unveil the stability of single-chain nanoparticles in solution, while the use of scattering techniques –in particular neutron scattering– is needed in order to unravel the structure and dynamics of these nano-objects in solution. The study of fundamental properties is focused on already known single-chain nanoparticles.

In chapter 5 we try to contribute to the design of nano-objects with improved capabilities. We present three novel synthesis routes for the preparation of functional single-chain nanoparticles and we provide information about their structure as well as their emerging properties, obtained by the combination of a wide range of techniques. Moreover, we try to demonstrate their use in potential applications such as nanomedicine or catalysis by performing proof-of concept experiments or combined with molecular dynamics simulations.

Finally, in chapter 6 we summarize the main results and conclusions obtained in this thesis. The main general conclusion from this thesis is that a strategy combining synthesis, proof-of-concept experiments, simulations and scattering techniques could be an ideal approach for the production of single-chain nanoparticles endowed with useful functions as well as to disentangle the emerging properties of this complex materials.

Resumen

En la era de la Nanotecnología, se han desarrollado muchos métodos para la síntesis de materiales con dimensiones bien definidas en la nanoescala ($1\ \text{nm} = 10^{-9}\ \text{m}$). Un ejemplo notable es el excelente control sobre el tamaño y forma que se ha logrado en la síntesis de nanopartículas duras, tales como puntos cuánticos, nanopartículas de oro o nanopartículas de óxido metálico. Por el contrario, hasta principios del siglo XXI no ha sido posible obtener un control similar para producir nanopartículas blandas basadas en polímeros con dimensiones inferiores a 10 nm. Los avances en la síntesis de polímeros funcionales bien definidos a través de procesos de polimerización viva por radicales, técnicas de post-funcionalización, así como el desarrollo de reacciones de acoplamiento intra-cadena altamente eficientes, han allanado el camino hacia la producción fiable de nanopartículas poliméricas unimoleculares.

El campo de las nanopartículas unimoleculares se esfuerza por crear nanoestructuras innovadoras a la vez que intentan imitar a los nanomateriales biológicos. Las macromoléculas naturales poseen un control exacto sobre la secuencia monomérica presente en sus estructuras primarias, lo que permite el plegado muy preciso en formas tridimensionales que contienen disposiciones específicas de grupos funcionales en la superficie y el exterior. Uno de los desafíos más significativos es la obtención de nanoestructuras sintéticas con el mismo nivel de complejidad que el que se halla en la naturaleza, ya que los sistemas desarrollados hasta el momento no son del todo capaces de igualar

dicha precisión. Muchas áreas de investigación, incluida la ciencia de polímeros, están empezando a cerrar la brecha entre los materiales sintéticos y naturales. La manipulación de cadenas de polímeros individuales, específicamente el plegamiento intra-molecular para dar lugar a nanopartículas bien definidas denominadas “nanopartículas unimoleculares”, es una vía de particular interés que está en continuo crecimiento. Dicha área de investigación es conceptualmente simple, pero posee resultados prometedores en muchos sistemas con comportamiento complejo.

En "Nanopartículas unimoleculares: explorando rutas de síntesis novedosas, propiedades básicas y aplicaciones potenciales" tratamos de avanzar en este campo evolutivo mediante la exploración de nuevas rutas de síntesis para el desarrollo de nanopartículas funcionales unimoleculares y mediante la realización de experimentos de ‘prueba de concepto’ que sirven para demostrar su posible uso en aplicaciones potenciales, tales como nanomedicina. Además, queremos proporcionar un conocimiento más profundo acerca de las propiedades básicas de estos nano-objetos, ya que es de suma importancia a la hora de establecer una relación fiable entre la estructura y sus propiedades.

Empezamos el manuscrito con una introducción general sobre las nanopartículas unimoleculares. Primero, describimos brevemente varios conceptos sobre los polímeros y la nanotecnología. A continuación, proporcionamos un resumen general acerca del estado de arte de las nanopartículas unimoleculares, en particular de las actuales rutas de síntesis y la morfología que normalmente poseen en disolución, así como de sus posibles

usos en aplicaciones potenciales. Finalizamos el capítulo 1 explicando los objetivos de esta tesis.

Después de la introducción, proporcionamos información útil acerca de todas las muestras utilizadas así como de las técnicas empleadas en esta tesis. En el capítulo 2 describimos la síntesis de todas las nanopartículas unimoleculares utilizadas, incluyendo rutas ya conocidas y nuevas rutas de síntesis elaboradas en este trabajo. La información de todas las muestras investigadas se ha obtenido a través del uso de diversas técnicas, bien sean experimentales o de simulación, que se explican en el capítulo 3.

En el capítulo 4 exploramos las propiedades básicas de las nanopartíuclas unimoleculares y las comparamos con las de sus respectivos polímeros precursores. El estudio se centra en investigar su estabilidad, estructura y dinámica en disolución. Para este propósito, combinamos información obtenida a través de distintas técnicas. El uso de técnicas convencionales como son la cromatografía de exclusión por tamaño o la dispersión de luz dinámica son suficientes para revelar la estabilidad de las nanopartículas, mientras que el uso de técnicas de dispersión –en particular dispersión de neutrones– es imprescindible para desenmarañar la estructura y dinámica de estos nano-objetos en disolución. El estudio de propiedades fundamentales se realiza con las nanopartículas que son ya conocidas.

En el capítulo 5 tratamos de contribuir en el diseño de nano-objetos con cualidades mejoradas. En particular, presentamos tres rutas de síntesis novedosas para la obtención de nanopartículas funcionales unimoleculares y

proporcionamos información acerca de su estructura así como de sus nuevas propiedades, mediante la combinación de un amplio rango de técnicas. Además, para demostrar su potencial uso en aplicaciones como la nanomedicina o catálisis, realizamos experimentos de 'prueba de concepto' combinados con simulaciones de dinámica molecular.

Finalmente, en el capítulo 6 se resumen los principales resultados obtenidos y las conclusiones de estas tesis. La conclusión general que destacamos de esta tesis es que un método que combine la síntesis, experimentos de 'prueba de concepto', simulaciones y técnicas de dispersión, podría ser una aproximación ideal para la producción de nanopartículas unimoleculares dotadas con funciones útiles así como para desenmarañar las propiedades emergentes de estos materiales complejos.

Contents

CHAPTER 1

Introduction

1.1. Polymers: General Aspects

The structural units in polymers are macromolecules which are formed by a large number of repeating units linked by covalent bonds. The term polymer includes not only synthetic materials but also natural macromolecules such as proteins or nucleic acids. Their structure-properties relationship has motivated a great effort towards developing new synthetic routes over the last decades, in an attempt to fulfill the increasing demand of the polymer industry.

The repeat unit is called monomer and the number of monomers in a polymer chain determines the degree of polymerization. Polymers, unlike proteins, do not have a fixed number of repeat units per chain as a consequence of the imperfect methods used to prepare them. As different chains have usually different length, the molar mass distribution has to be determined. The most common statistical methods to determine it are the number-average method and the weight average method.[1] The number average molecular weight (M_n) is obtained by dividing the total mass by the number of chains in the ensemble. In other words, it is the arithmetic mean of the mass:

$$M_n = \frac{\sum_i N_i M_i}{\sum_i N_i} \tag{1.1}$$

where M_i is the mass of the chain and N_i the number of chains of mass M_i.

The weight average molecular weight (M_w) is defined as:

$$M_w = \frac{\sum_i N_i {M_i}^2}{\sum_i N_i M_i} \tag{1.2}$$

Always $M_w > M_n$ and the ratio M_w/M_n, called polydispersity index, provides a characterization of the width of the molecular weight distribution. Same polymers with different polydispersity value can exhibit very different properties.

Polymer features are affected not only by the polydispersity index, but also by the steric arrangement of the repeating units along the chain, by the chain conformations (the spatial organization of the chain as zig-zag, helical, folded chain, etc.) and by the chain configuration, also called microstructure. Homopolymers are polymers formed by a single type of monomers, while polymers which contain different monomeric units are called copolymers. There also exist many different architectures in which polymers can be found, like star, branched, linear, etc. All these characteristics contribute to the mechanical and dynamical features of each specific system.

Since the chemical details are not important for the large scale features of a polymer chain, the positions of the monomers (which can be represented as beads) can be described by a position vector r_i ($1 < i < N$, being N the number of i monomers in each chain). Thus, the bond vectors $r_i - r_{i-1} (2 < i < N)$ can be used to define the conformation of a chain. The size of the chain is usually characterized by the end-to-end vector R_e, which is the vector connecting the first and the last bead or the sum of all N bond vectors:

$$R_e = r_N - r_1 \tag{1.3}$$

Another magnitude used for the characterization of the size of a polymer chain is the radius of gyration R_g, which is defined in terms of the sum of the squared distances between the individual beads and the center of mass of the chain R_{cm}:

$$R_g^2 = \frac{\sum_{i=1}^{N} m_i (r_i - R_{cm})^2}{\sum_{i=1}^{N} m_i} \tag{1.4}$$

where m_i is the mass of the bead and R_{cm} is given by:

$$R_{cm} = \frac{\sum_{i=1}^{N} m_i \, r_i}{\sum_{i=1}^{N} m_i} \tag{1.5}$$

If the mass of a monomer m_i is assumed to be constant, Eq. 1.4 can be simplified to:

$$R_g^2 = \frac{1}{N} \sum_{i=1}^{N} (r_i - R_{cm})^2 \tag{1.6}$$

For polymers, the squared end-to-end distance and the squared radius of gyration are usually averaged over the ensemble of allowed conformations giving the mean squared end-to-end distance $\bar{R}_e^2$ and the mean squared radius of gyration $\bar{R}_g^2$.

The dimension of a polymer chain in solution can be also characterized by the hydrodynamic radius R_H, which is defined as the radius of a hypothetical sphere that diffuses through a viscous medium at the same rate as the polymer. In other words, a linear chain with a hydrodynamic radius R_H diffuses with the same diffusion coefficient as the sphere of radius R_H. Once the center of mass diffusion coefficient D_{CM} is measured, the hydrodynamic radius R_H can be obtained by the Stokes-Einstein law:

$$R_H = \frac{k_B T}{6\pi\eta_s D_{CM}} \tag{1.7}$$

where η_s is the viscosity of the solvent and k_B the Boltzmann constant.

1.2. Nanotechnology

Nanotechnology is the science that deals with matter at scales of about a nanometer, i.e., a thousand millionth of a meter ($1\,\text{nm} = 10^{-9}\,\text{m}$). It is commonly defined as the understanding, control, and restructuring of matter on the order of nanometers (i.e., less than 100 nm) to create materials with fundamentally new properties and functions.[2]

Since nanotechnology was introduced by Nobel laureate Richard P. Feynman during his now famous 1959 lecture "*There's Plenty of Room at the Bottom*",[3] there have been many revolutionary developments in physics, chemistry and biology that have demonstrated Feynman's ideas of manipulating matter at an extremely small scale, the level of molecules and atoms, i.e., the nanoscale.[2] The properties of materials change as their size approaches to the nanoscale and as the percentage of the surface in relation to the percentage of the volume of a material becomes significant.

In nature, a diversity of functional nanoentities result from the self-structuring of dynamic individual biomacromolecules at multiscale levels,[4] leading to such advanced materials as DNA or viruses. In this sense, nature may serve as a model for the building-up of small structures. A nanoparticle is the most fundamental component in the fabrication of a nanostructure and is far smaller than the world of everyday objects that are described by Newton's laws of motion, but larger than an atom or a simple molecule that are governed by quantum mechanics.[5] Different types of nanoparticles have been developed depending on their nature; "hard nanoparticles", usually made by inorganic materials and "soft

nanoparticles", made by organic materials. Excellent size and shape control has been achieved for the synthesis of hard nanoparticles, such as quantum dots, gold nanoclusters or metal oxide nanoparticles.

Concerning soft nanoparticles, some very promising examples of controlled chain compaction *via* folding/collapse have been demonstrated in recent years in the synthetic polymer field.[6-13] Moreover, intriguing examples of soft nano-objects constructed though the compaction of linear single chains and endowed with useful enzyme-mimetic functions have been described.[14-16] Even so, there is still a markedly difference from the precise architectural control observed in nature.

Thus, the topology and precise morphology found in natural biomacromolecules continues to be a powerful driving force towards artificial functional soft nano-objects.[17] The development achieved in manipulating and visualizing single atoms at the atomic level, giving rise to the modern bottom-up technology, paves the way to a similar exquisite degree of control at the individual synthetic polymeric chain level for producing functional soft nanoentities, through full development of what is called "single-chain technology".[18-19]

1.1.2. Single-Chain Technology

Synthetic polymer materials are generally seen and studied as a whole. However, a polymer chain can be more than a modest component of a larger assembly. Indeed, if carefully engineered at the molecular level, a single polymer chain can behave as a discrete object with its own characteristics and functions.[18] Macromolecules with controlled molecular architectures and also linear polymer

chains can today be engineered into single-chain polymer devices, i.e., individual molecules with a given function, such as artificial enzymes.

Ultra-small unimolecular soft nano-objects endowed with useful, autonomous and smart functions are the long-term valuable output of single chain technology.[4] Thus, the precision synthesis of precursors with predefined sequences, positionable reactive groups, tailored interactions and useful functions is needed in single-chain technology. Within the past few years, different soft nano-objects have been constructed *via* chain compaction by means of single-chain technology. Some of these nano-objects are illustrated in figure 1.1.

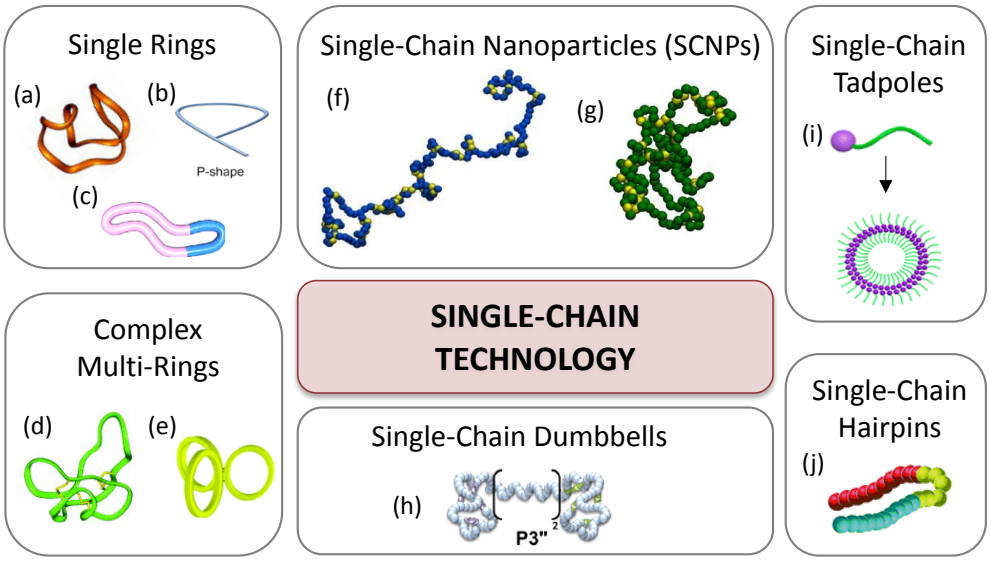

Figure 1.1: Illustration of soft nano-objects obtained by means of single-chain technology *via* chain compaction. Examples of dynamic (stimuli responsive) (a), letter-shaped (b) and compositionally unsymmetrical (c) single rings; complex multi-rings based on connected rings (d) and from pre-formed rings (e); sparse (f) and globular (g) single-chain nanoparticles; single-chain dumbbells (h), tadpoles (self-assembly in micelles) (i) and hairpins (j).

Within the wide variety of different soft nano-objects, single rings are found to be of huge interest, especially dynamic (stimuli-responsive),[20-25] letter-shaped[26-27] and compositionally unsymmetrical single rings.[28-31] A diversity of complex, high-precision multi-ring systems has recently been prepared by means of single-chain technology *via* covalent and supramolecular interactions.[32-37]

By means of single-chain technology, individual polymer chains of different natures, compositions and molar masses have been folded/collapsed to single-chain nanoparticles (SCNPs)[6-9, 11-13, 38-39] and tadpoles (monotailed SCNPs).[40-45] Single-chain dumbbells[46] and hairpins[47-48] have also been constructed *via* single-chain technology (figure 1.1).

In this thesis, the soft nano-objects studied are single-chain nanoparticles (SCNPs). These nanoentieties, while simple in concept, exhibit behaviors far more complex than initially anticipated and they offer a wide range of possibilities to be used in potential applications.

1.3. Single-Chain Nanoparticles (SCNPs)

Single-chain nanoparticles (SCNPs) are ultra-small soft nano-objects synthesized by means of intra-molecular folding/collapse of individual polymer chains (figure 1.2). One of the main characteristics of SCNPs is their ultra-small size (<20 nm) and consequently their inherent large surface-to-volume ratio.

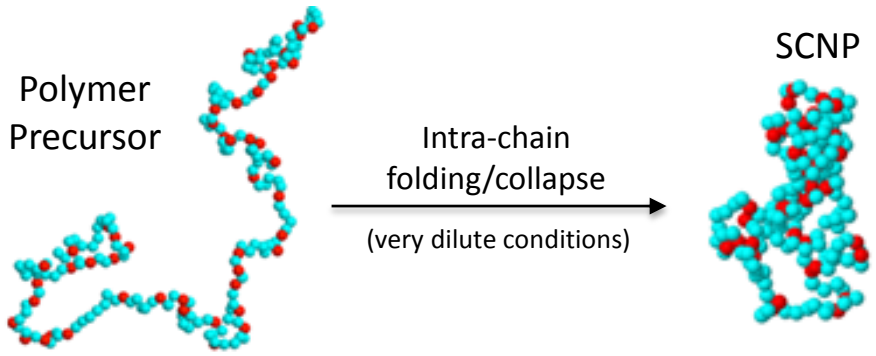

Figure 1.2: Schematic illustration of a linear polymer precursor and a single-chain nanoparticle (SCNP) obtained through intra-chain folding/collapse of individual polymer chains at very dilute conditions.

The concept of SCNPs constructed *via* intra-molecular cross-linking of individual linear polymer chains was introduced 16 years ago.[49] Research in SCNPs is currently at the boundary between polymer science, nanotechnology and biology. The folding of individual polymer chains to functional SCNPs is reminiscent of protein folding to its functional, native state although current SCNPs lack the perfection in sequence, uniformity in size and precise morphology found in these natural biomacromolecules.[50]

1.3.1. SCNPs Construction

The molecular weight of the SCNP precursor polymer and its functionalization degree are essential parameters to control SCNP size, in addition to the nature of the interactions employed to perform the folding/collapse as well as the solvent quality (good solvent, selective solvent).[51-52]

As illustrated in figure 1.3, three main different techniques are involved in the synthesis of single-chain nanoparticles.[8]

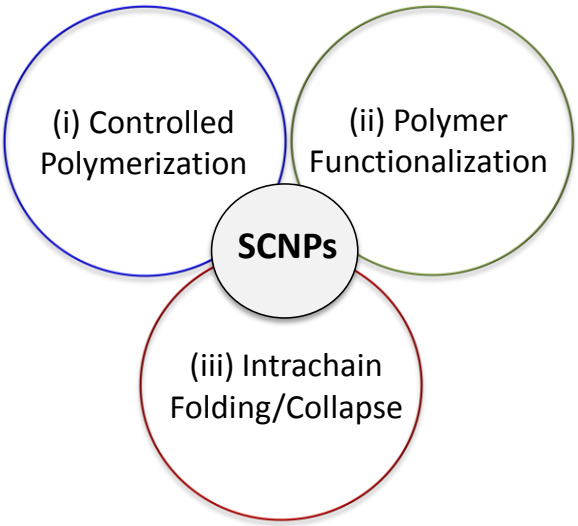

Figure 1.3: Different techniques involved in the construction of single-chain nanoparticles. (i) Controlled polymerization, (ii) polymer functionalization, and (iii) intra-chain folding/collapse of individual polymer chains.

The first technique is *controlled polymerization*, allowing the development of well-defined single-chain polymeric precursors of controlled molar mass and narrow size distribution.

Polymer functionalization is the second technique involved, which consists of decorating the polymeric linear chains with appropriate functional groups for the corresponding folding/collapse process. In some cases, the use of this second technique can be avoided through the preparation of well-defined polymer precursors containing both inert and reactive functional groups randomly distributed along the individual chains.

The third fundamental technique is the *intra-chain folding/collapse* process for the efficient transformation of the precursor coils to folded unimolecular nanoparticles. The strategies typically used to achieve intra-chain folding/collapse can be classified according to the type of chemistry used, as it is shown in figure 1.4.

i. Intra-chain homocoupling: Identical functional groups, that are present in the linear polymer chain, react between them in a pairwise manner [blue beads in figure 1.4(a)].

ii. Intra-chain heterocoupling: Reaction between two (or more) complementary functional groups often randomly distributed along the same polymer chain [blue and green beads in figure 1.4(b)].

iii. Cross-linker induced collapse: An external multifunctional cross-linker is employed to promote SCNP formation [green beads represent the cross-linking agent in figure 1.4(c)].

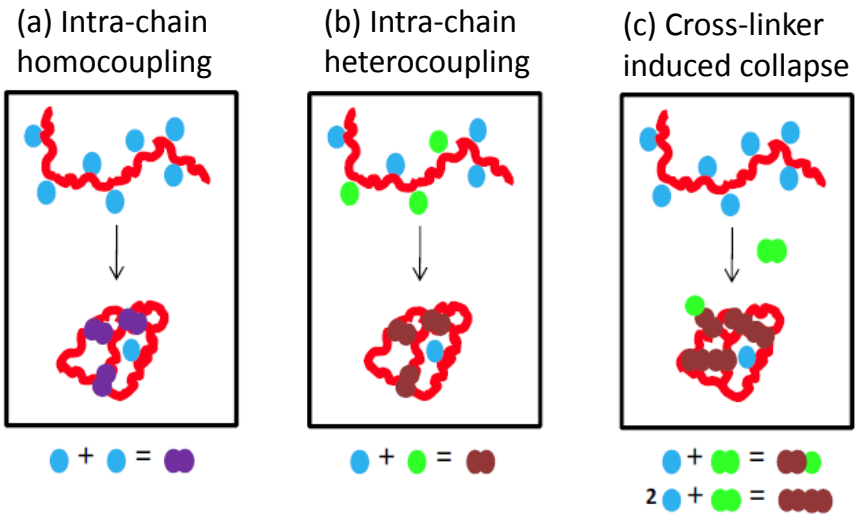

Figure 1.4: Illustration of different techniques employed for the construction of SCNPs according to the type of chemistry used: (a) intra-chain homocoupling, (b) intra-chain heterocoupling, and (c) cross-linker induced collapse.

Another way to classify the compaction of SCNPs is through the nature of the interactions employed to perform the folding/collapse of individual polymer chains; they can be permanent covalent bonds or dynamic (reversible) interactions (e.g., hydrogen bonding, metal complexation, dynamic covalent bonds).[4]

From the point of view of applications, the nature and degree of the intra-chain cross-linking of SCNPs is of great concern. On one hand, irreversible or permanent single-chain polymer nanoparticles involve strong intra-chain covalent bonds, which endow them with increased stability against thermal degradation at high temperatures. On the other hand, reversible single-chain polymer nanoparticles are based on the use of relatively weak supramolecular interactions and/or dynamic covalent bonds and they can be disassembled back

to individual polymer chains by means of one (or several) appropriate stimulus (stimuli).

A significant effort has been recently performed to predict the size reduction upon folding/collapse of a precursor polymer chain *via* dynamic interactions[52] or covalent bonds[51] as a function of precursor molar mass (*M*) and amount of functional groups (*x*). In fact, covalent-bonded SCNPs in solution with similar nature, and identical values of *M* and *x* than responsive SCNPs do display, on average, a higher level of chain compaction. Moreover, in both good and selective solvents SCNPs constructed from exactly the same precursor polymer *via* non-covalent interactions are expected to show a larger size than SCNPs prepared through covalent bonds.[53]

1.3.2. Morphology of SCNPs in Solution

Concerning the morphology of SCNPs in solution, two limiting conformations (sparse and globular) can be obtained depending on the synthesis conditions followed, and the nature of the precursor polymer employed and/or external cross-linker used.

A. Sparse single-chain nanoparticles

In general, single-chain nanoparticles formation in good solvent results in sparse, non-globular morphologies in solution even by employing highly-efficient intra-chain cross-linking techniques (e.g., "click" chemistry) or supramolecular interactions.[54]

The ultimate reason behind this open, non-compact morphology, as revealed by molecular dynamics (MD) simulations, is the intrinsically self-avoiding character of the polymer precursors in good solvent, which severely restricts the reactions between cross-linkers separated by long contour distances (creating long-range loops). Consequently, most of the cross-linking events taking place during SCNP formation are actually inefficient for global compaction, since they involve cross-linkers separated by short contour distances.[55]

It is noteworthy that the global conformations exhibited by SCNPs in dilute solutions, synthesized in good solvent conditions, are very similar to those displayed by certain biomacromolecules, in particular by intrinsically disordered proteins (IDPs).[56] IDPs are ubiquitous in nature and responsible of functions of utmost relevance in biological systems. Another common feature with IDPs is that SCNPs are intrinsically polydisperse both in size and topology, even if they are produced by the same chemical route.[54-55, 57-58]

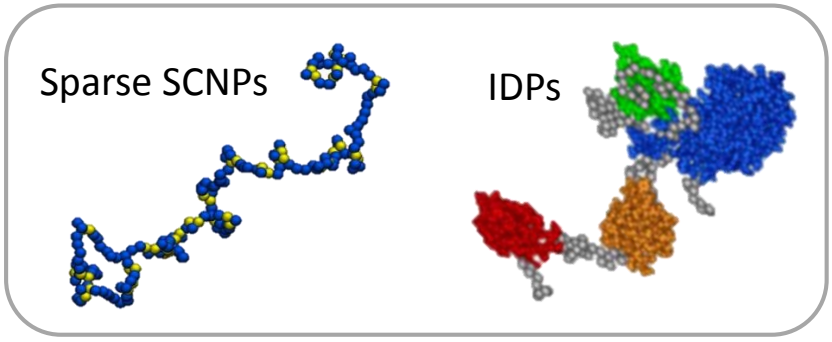

Figure 1.5: Illustration of the sparse morphology adopted by single-chain nanoparticles (SCNPs) resembling that typical of intrinsically disordered proteins (IDPS).

Figure 1.5 illustrates the similar conformations found in sparse SCNPs and IDPs, showing locally compact portions connected by flexible segments.[59] This finding is especially important because the potential applications of single-chain nanoparticles depend on their precise morphology in solution. Consequently, the control of the distinct compacted subdomains created inside the SCNPs (i.e., pseudo-tertiary structure) is of significant interest.[4]

B. Globular single-chain nanoparticles

When the folding/collapse process is carried out by more complex synthesis routes a global core-shell morphology is usually obtained. This morphology is very similar to that displayed by native proteins like enzymes, showing a single locally compact portion, as illustrated in figure 1.6.

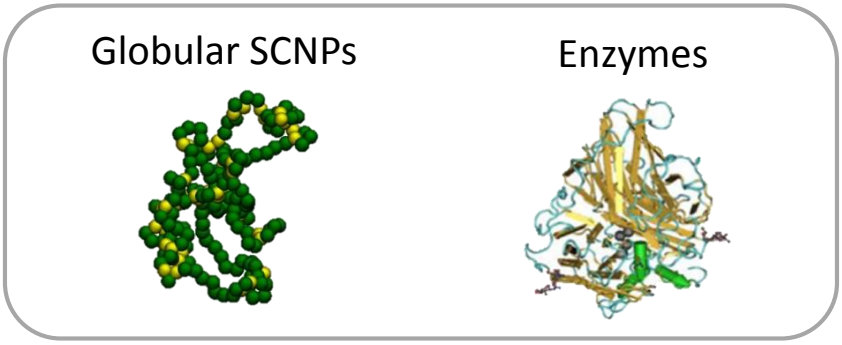

Figure 1.6: Illustration of globular morphology adopted by single-chain nanoparticles as often found in enzymes.

Among the complex synthesis routes employed to obtain globular SCNPs, an efficient synthesis of permanent SCNPs with an almost globular morphology was developed based on the combination of thiol-yne coupling reaction and relatively long cross-linkers.[60] The microscopic origin of this substantial

difference with standard SCNPs was elucidated by MD-simulations. It showed that intra-chain bonding mediated by relatively long cross-linkers, combined with the use of bifunctional groups in the SCNP precursor largely increases the probability of forming long-range loops, which are efficient for global chain compaction.[60]

Other approaches to obtain SCNPs displaying nearly globular morphology have been recently reported based on self-assembly of neutral[61-63] or charged[64] amphiphilic random copolymers.

The above results indicate that single chain technology allows, by proper selection of the synthesis route, the construction of SCNPs with a morphology resembling that of intrinsically disordered proteins (conventional synthesis methods in good solvent) or that showed by native, globular proteins (special synthesis methods).[4] The potential applications of SCNPs broaden significantly by taking inspiration from the functions of both ordered and disordered proteins.[17]

1.4. Applications of Single-Chain Nanoparticles

Because this field is still in its infancy, only a limited number of proof-of-concept investigations have been carried out to endow single-chain nanoparticles with useful functions. In spite of this limitation, certain preliminary results illustrate the possibilities offered by these unimolecular nanoentities for a variety of potential applications.

In general, the main advantages of folded/collapsed single chains over their linear counterparts are (i) the presence of locally compact, but accessible, sites/cavities/zones, (ii) the possibility to bound, temporally or permanently, active species, such as drugs or catalyst onto these local pockets, and (iii) their reduced size and hydrodynamic volume. Properties (i) and (ii) are useful for nanomedicine, catalysis and sensing applications, whereas (iii) is especially relevant for applications where a reduction in viscosity is required.[4]

1.4.1. Nanomedicine

One of the most promising fields of application of nanoparticles in general, and single-chain polymer nanoparticles in particular, is the design of engineered nano-systems to address diseases and to monitor and to protect human health. Nanomedicine can be defined as the use of nanoparticles for diagnosis, monitoring of physical and pathologic processes, for therapy and for control of biological systems.[65] Nanoparticles, when compared to typical small molecules, show a size large enough to avoid rapid clearance through the kidney, but small enough to be retained in the body based on a range of physiological changes,

morphological and biochemical differences that occur in different tissues in the presence of a variety of diseases and disorders.

Nanoparticles can be used to encapsulate toxic, insoluble anti-cancer drug molecules and can be functionalized with peptides or antibodies to accumulate in tumors by targeting specific biomarkers overexpressed in cancer cells. In this sense, an important feature of these nanoparticles should be to display low toxicity and high biodegradability. Several cytotoxicity studies have been carried out to demonstrate the non-toxic character of a variety of single-chain polymer nanoparticles.[66-68] Even if more systematic studies are certainly required, these cytotoxicity studies paves the way to the use of SCNPs as biocompatible drug delivery systems.[69]

A. Controlled drug delivery systems

The analogies found in the morphology and inspired by the behavior of carrier proteins, the drug-delivery properties of sparse single-chain nanoparticles have been recently studied, in particular of "Michael" single-chain polymer nanoparticles.[59, 70] They were tested as novel transient-binding disordered nanocarriers, from which the controlled delivery in water of both dermal protective (folic acid, i.e., vitamin B_9) and anticancer (hinokitiol) cargos was carried out (figure 1.7).[70]

Another several proof-of-concept experiments have been performed involving single-chain polymer nanoparticles as controlled drug delivery nanocarriers of: chiral amino acid derivates,[71] peptides,[72] vitamins[59] and small molecule drugs.[70, 73-74]

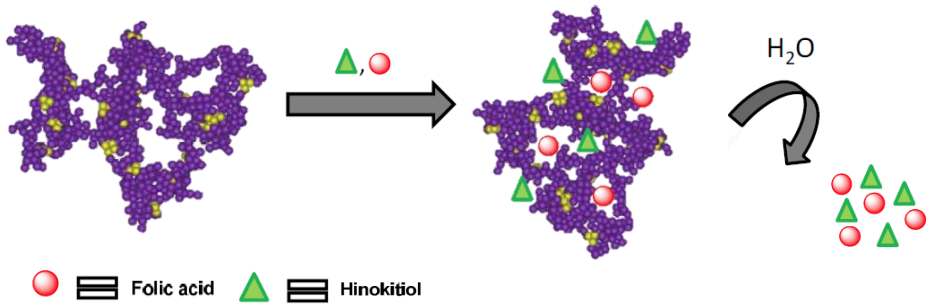

Figure 1.7: Simultaneous delivery of both dermal protective (folic acid, i.e., vitamin B_9) and anticancer (hinokitiol) cargos from single-chain "Michael" nanocarriers mimicking intrinsically disordered proteins (IDPs).

B. Image contrast agents

Single-chain polymer nanoparticles have been evaluated as: image contrast agents for magnetic resonance imaging (MRI),[75-76] and gamma emitters for single photon emission computerized tomography (SPECT)[68]. In addition, several synthetic routes have been followed to construct fluorescent single-chain polymer nanoparticles with potential applications in materials science and nanomedicine. Some routes rely on the entrapment of fluorescent probes by the nanoparticles, while others are based in the conjugation of the probes to the nanoparticles via covalent bonds.

Efficient entrapment of fluorescent probes (fluorescein, pyrene, quantum dots) has been reported for polynorbornene,[67] polyhydroxyethyl methacrylate[74] and polyacrylic acid[77] single-chain polymer nanoparticles, respectively. On the contrary, fluorescent nanoparticles based on conjugation to single-chain nanoparticle precursors of a variety of fluorophores (polyfluorene, bipyridine, pyrene, anthracene, carbazole) have been prepared by using precursors based on polyacrylic acid,[76] polynorbornene[78] and polystyrene.[79-82]

1.4.2. Catalysis

Single-chain polymer nanoparticles offer many possibilities for the development of catalytic systems, including enzyme-mimic nano-objects [13, 17, 50]: (i) a large surface-to-volume ratio which facilitates the diffusion of reagents and products to catalytic sites; (ii) two limiting morphologies, sparse and globular, with multiple small "local pockets" or a single pocket of larger size, respectively; (iii) availability of reversible (responsive) and irreversible (permanent) single-chain nanoparticles based on intra-molecular dynamic interactions or covalent bonds, respectively.

Main proof-of-concept applications of SCNPs in catalysis include their use as nanoreactors for the synthesis of chemical compounds, polymers and nanomaterials.

A. SCNPs as nanoreactors for the synthesis of chemical compounds

Incorporation of insoluble catalysts into single-chain polymer nanoparticles has revealed as a useful way to perform efficient chemical synthesis in water, i.e., enzyme-like organic chemistry. Many different chemical compounds have been synthesized using SCNPs as bioinspired nanoreactors. In fact, the possibility to tune the size of the SCNPs, as well as type of intra-molecular cross-linking chemistry used and solvent characteristics offer many possibilities for endowing SCNPs with enzyme-mimetic activity in both organic and aqueous media. Table 1.1 summarizes reactions catalyzed by different single-chain polymer nanoparticles.

Table 1.1: Reactions catalyzed by different single-chin polymer nanoparticles

Reaction	Solvent	T (°C)	t (h)	Conv. (%)	TOF (h^{-1})
Hydrogenation of ketones [14]	H_2O	40	50	98	20
Aldol reaction [15]	H_2O	25	24	99	8
Reduction of α-diketones [16]	CH_2Cl_2	RT	0.1	96	5580
Alkyne dimerization [83]	-	60	8	>98	25
Reduction of secondary amines [84]	THF	RT	16	>99	0.6
Allylation of benzophenone [84]	THF	35	24	97	8
Biphenyl formation [84]	THF	80	16	>99	0.2
CuAAC [85]	PBS	RT	0.2	>99	13
Mono-depropargylation reaction [85]	PBS	RT	5	>99	0.2
Bis-depropargylation reaction [85]	PBS	RT	25	>99	0.04
Sonogashira coupling [86]	Et_2N	RT	24	45	21
Oxidation of secondary alcohols [87]	H_2O	RT	0.07	>99	600
CuAAC [88]	H_2O	50	24	>99	16667

TOF (turnover frequency) = Amount of products (mol)/[Amount of catalyst active sites (mol) x time (h)]. RT = Room temperature. THF = Tetrahydrofuran. CuAAC = Cu(I)-catalyzed azide-alkyne cycloaddition. PBS = Phosphate buffer (0.01 M). Et_2N = Diethylamine.

All these examples illustrate the huge possibilities that SCNPs offer, as efficient nanoscale catalysts, for the synthesis of a variety of chemical compounds even inside bacteria and mammalian cells.[88]

B. SCNPs as nanoreactors for the synthesis of polymers

SCNPs have been used as bioinspired nanoreactors for the synthesis of several polymers *via* ring-opening polymerization[16] as well as controlled/living radical polymerization.[63, 89]

Natural polymerase enzymes use templates (*m*RNA, DNA) to synthesize perfectly defined (in length and sequence) biomacromolecules.[69] Polymerase-like activity towards tetrahydrofuran (THF) *via* ring-opening polymerization was found for organocatalytic SCNPs containing entrapped $B(C_6F_5)_3$ molecules.[16] The term "polymerase-like" was employed to distinguish the ability of these SCNPs to polymerize THF in the presence of small amount of glycidyl phenyl ether (GPE) which played the role of co-catalyst, from the exquisite activity of natural polymerase enzymes [figure 1.8(a)].

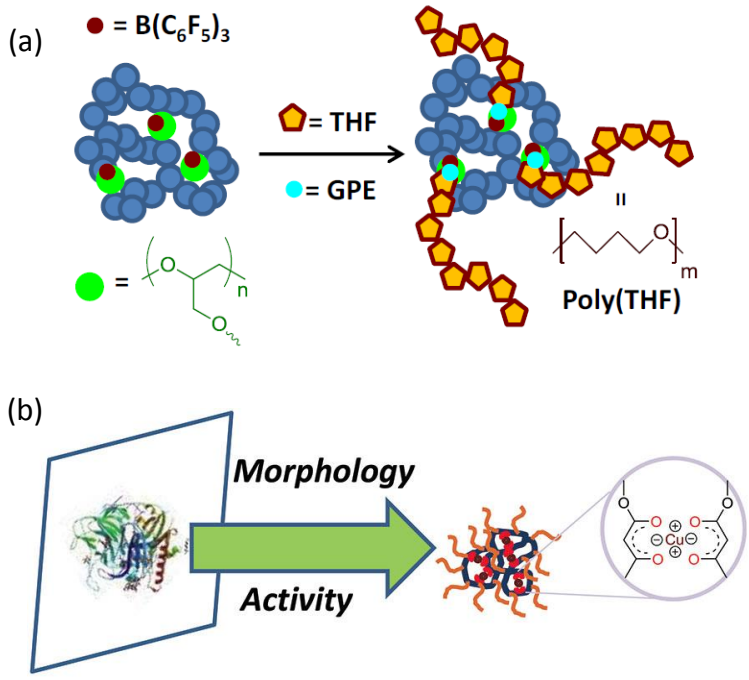

Figure 1.8: Schematic illustration of the use of SCNPs as bioinspired nanoreactors for the synthesis of polymers through: (a) ring-opening polymerization, and (b) controlled/living radical polymerization (see text for details).

Metalloenzymes have the ability to catalyze the controlled radical polymerization of water-soluble vinyl-type monomers.[90-93] This polymerase activity displayed by metalloenzymes was taken as inspiration to prepare copper-containing globular SCNPs mimicking their globular morphology and living radical polymerization activity [figure 1.8(b)].[63]

C. SCNPs as nanoreactors for the synthesis of nanomaterials

A diversity of nanomaterials have been synthesized involving single-chain nanoparticles as highly-efficient nanoreactors (figure 1.9). SCNPs have been employed for the synthesis of gold nanoparticles,[94] quantum dots[77] and carbon nanodots.[95] The promising results obtained prompt to the evaluation of single-chain nanoparticles as nanoreactors for the efficient synthesis of other nanomaterials.

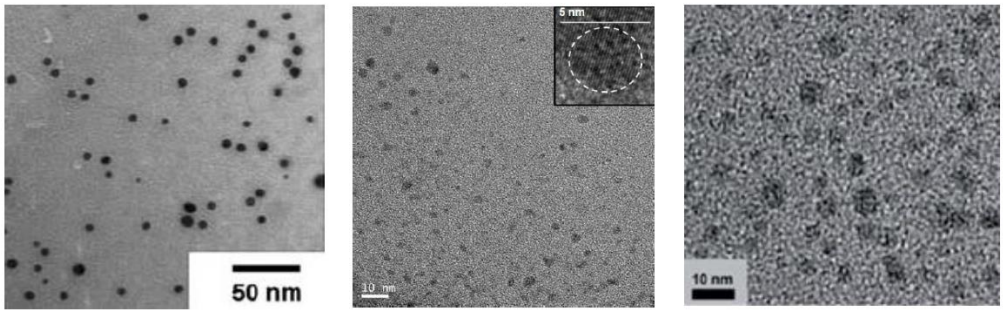

(a) (b) (c)

Figure 1.9: Examples of nanomaterials synthesized by using SCNPs as individual nanoreactors: (a) gold nanoparticles (Au-NPs), (b) cadmium sulfide quantum dots (CdS-QDs) and (c) carbon nanodots (C-NDs).

1.4.3. Sensing

Single-chain polymer nanoparticles offer interesting possibilities for the development of sensors and biosensors. Fluorescent polynorbornene-based SCNPs were evaluated as compartmentalized sensors of metal ions. These SCNPs were found to be efficient sensors for metal ions, such as Cu(II), due to the strong quenching of nanoparticle fluorescence upon metal binding.[78]

Endowing single-chain nanoparticles with biosensing activity (i.e., the capability for detection of biological macromolecules) is a promising field of research. In a recent work,[96] pyridine-functionalized single-chain nanoparticles were used as biosensors. A simple, fast, highly sensitive and robust colorimetric detection of zein protein based on the formation of gold nanoparticles in the presence of these SCNPs was reported (figure 1.10).

Figure 1.10: Photographs of the sensing system based on pyridine-gold-zein interactions involving pyridine-functionalized single-chain nanoparticles in the presences of decreasing concentrations of zein.

1.4.4. Other Uses

Several other uses of single-chain polymer nanoparticles haven been investigated. Initially, SCNPs were evaluated as porogens for microelectronic applications.[49, 97]

The use of SCNPs as functional nanoparticles for bioscience of amine-containing SCNPs,[67, 98] amino acid-decorated nanoparticles,[81, 99] porphyrin-containing SCNPs[85] or SCNPs prepared from a single-chain coumarin-containing precursors[100] has been proposed.

Neutral single-chain nanoparticles have been widely investigated as rheology-improving agents for melts of thermoplastics,[101] elastomeric polymers,[102] and nanocomposites.[103-104] Moreover, charged SCNPs have been employed in coating formulations.[64, 105-107]

The effect of SCNPs on the dynamics of all-polymer nanocomposites is currently the subject of intense interest.[108-110] SCNPs are also promising materials for promoting miscibility in immiscible polymer blends, as revealed by several theoretical[111-115] and experimental results.[116-117]

In addition, SCNPs have also been employed as reversible hydrogels,[118] supramolecular films[119-121] and surfactants.[122]

1.5. Aim and Outline of this Thesis

The aim of this thesis is to explore novel synthesis routes towards single-chain nanoparticles endowed with useful functions for their use in potential applications, as well as to provide a deeper knowledge about the basic properties of these nano-objects. Unravelling the stability, structure and dynamics of functional single-chain nanoparticles is of utmost importance to establish reliable structure-properties relationship.

In this thesis we report on three different synthesis routes for the preparation of single-chain nanoparticles with unique and novel properties to be used in potential fields. We provide detailed information about the structure of these novel SCNPs by using a wide range of powerful characterization techniques, and in some cases combined with molecular dynamics (MD) simulations. Moreover, we present proof-of-concept experiments on these functional SCNPs to demonstrate their possible use in some applications, like catalysis and nanomedicine (drug delivery and fluorescent probes).

Furthermore, we present a study on the stability, structural and dynamical features of single-chain nanoparticles in solution, in order to provide a deep insight into the basic properties of these functional nano-objects. For this purpose, we exploit scattering techniques –in particular neutron scattering–, which are specially well suited to realize a significant advance in this novel field, and combine these experiments with MD-simulations This study on fundamental properties is focused on already known single-chain nanoparticles, i.e., 'standard SCNPS'. Motivated by their analogy with intrinsically disordered proteins, we

have also investigated the impact of crowding –an inherent situation in cells– on the conformation of these SCNPs.

The thesis is organized as follows. In Chapter 2 the synthesis of all the single-chain nanoparticles employed in this work is presented. All the experimental techniques as well as the details of the measurements and the conditions used for the characterization of the samples are described in Chapter 3. The basic properties of SCNPs in comparison with their precursor counterparts are presented in Chapter 4. Chapter 5 reports on the new synthesis routes developed in this thesis, including the complete characterization as well as proof-of-concept experiments of these novel single-chain nanoparticles. Finally, the conclusions of this thesis are summarized in Chapter 6.

1.6. References

[1] A. Ravve, *Principles of Polymer Chemistry*, Springer, New York, **2012**.

[2] F. Sanchez, K. Sobolev, *Construction and Building Materials* **2010**, *24*, 2060-2071.

[3] R. P. Feynman, *There's Plenty of Room at the Bottom (reprint from speech given at annual meeting of the American Physical Society), Vol. 23*, Engineering and Science, **1960**.

[4] M. Gonzalez-Burgos, A. Latorre-Sanchez, J. A. Pomposo, *Chemical Society Reviews* **2015**, *44*, 6122-6142.

[5] J. Estelrich, M. Quesada-Pérez, J. Forcada, J. Callejas-Fernández, in *Soft Nanoparticles for Biomedical Applications*, The Royal Society of Chemistry, **2014**, pp. 1-18.

[6] M. K. Aiertza, I. Odriozola, G. Cabanero, H. J. Grande, I. Loinaz, *Cell Mol Life Sci* **2012**, *69*, 337-346.

[7] O. Altintas, C. Barner-Kowollik, *Macromol Rapid Commun* **2012**, *33*, 958-971.

[8] A. Sanchez-Sanchez, I. Pérez-Baena, J. Pomposo, *Molecules* **2013**, *18*, 3339.

[9] A. Sanchez-Sanchez, J. A. Pomposo, *Particle & Particle Systems Characterization* **2014**, *31*, 11-23.

[10] J. A. Pomposo, (Eds.: D. Bradburn, T. Bittinger), Nova Science Publishers, Incorporated, **2013**.

[11] L. Li, K. Raghupathi, C. Song, P. Prasad, S. Thayumanavan, *Chem Commun (Camb)* **2014**, *50*, 13417-13432.

[12] C. K. Lyon, A. Prasher, A. M. Hanlon, B. T. Tuten, C. A. Tooley, P. G. Frank, E. B. Berda, *Polym. Chem.* **2015**, *6*, 181-197.

[13] M. Huo, N. Wang, T. Fang, M. Sun, Y. Wei, J. Yuan, *Polymer* **2015**, *66*, A11-A21.

[14] T. Terashima, T. Mes, T. F. De Greef, M. A. Gillissen, P. Besenius, A. R. Palmans, E. W. Meijer, *J Am Chem Soc* **2011**, *133*, 4742-4745.

[15] E. Huerta, P. J. Stals, E. W. Meijer, A. R. Palmans, *Angew Chem Int Ed Engl* **2013**, *52*, 2906-2910.

[16] I. Perez-Baena, F. Barroso-Bujans, U. Gasser, A. Arbe, A. J. Moreno, J. Colmenero, J. A. Pomposo, *ACS Macro Letters* **2013**, *2*, 775-779.

[17] J. A. Pomposo, *Polymer International* **2014**, *63*, 589-592.

[18] M. Ouchi, N. Badi, J. F. Lutz, M. Sawamoto, *Nat Chem* **2011**, *3*, 917-924.

[19] J. F. Lutz, M. Ouchi, D. R. Liu, M. Sawamoto, *Science* **2013**, *341*, 1238149.

[20] Y. Inoue, P. Kuad, Y. Okumura, Y. Takashima, H. Yamaguchi, A. Harada, *J Am Chem Soc* **2007**, *129*, 6396-6397.

[21] J. Willenbacher, B. V. Schmidt, D. Schulze-Suenninghausen, O. Altintas, B. Luy, G. Delaittre, C. Barner-Kowollik, *Chem Commun (Camb)* **2014**, *50*, 7056-7059.

[22] J. Willenbacher, O. Altintas, P. W. Roesky, C. Barner-Kowollik, *Macromol Rapid Commun* **2014**, *35*, 45-51.

[23] O. Altintas, P. Gerstel, N. Dingenouts, C. Barner-Kowollik, *Chem Commun (Camb)* **2010**, *46*, 6291-6293.

[24] D. Danilov, C. Barner-Kowollik, W. Wenzel, *Chem Commun (Camb)* **2015**, *51*, 6002-6005.

[25] O. Altintas, T. Rudolph, C. Barner-Kowollik, *Journal of Polymer Science Part A: Polymer Chemistry* **2011**, *49*, 2566-2576.

[26] B. V. Schmidt, N. Fechler, J. Falkenhagen, J. F. Lutz, *Nat Chem* **2011**, *3*, 234-238.

[27] M. Zamfir, P. Theato, J.-F. Lutz, *Polym. Chem.* **2012**, *3*, 1796-1802.

[28] Z. Ge, Y. Zhou, J. Xu, H. Liu, D. Chen, S. Liu, *J Am Chem Soc* **2009**, *131*, 1628-1629.

[29] S. Honda, T. Yamamoto, Y. Tezuka, *J Am Chem Soc* **2010**, *132*, 10251-10253.

[30] J. E. Poelma, K. Ono, D. Miyajima, T. Aida, K. Satoh, C. J. Hawker, *ACS Nano* **2012**, *6*, 10845-10854.

[31] B. Zhang, H. Zhang, Y. Li, J. N. Hoskins, S. M. Grayson, *ACS Macro Letters* **2013**, *2*, 845-848.

[32] M. Schappacher, A. Deffieux, *Science* **2008**, *319*, 1512-1515.

[33] D. E. Lonsdale, M. J. Monteiro, *Chem Commun (Camb)* **2010**, *46*, 7945-7947.

[34] H. Oike, H. Imaizumi, T. Mouri, Y. Yoshioka, A. Uchibori, Y. Tezuka, *Journal of the American Chemical Society* **2000**, *122*, 9592-9599.

[35] Y. Tezuka, A. Tsuchitani, Y. Yoshioka, H. Oike, *Macromolecules* **2003**, *36*, 65-70.

[36] N. Sugai, H. Heguri, K. Ohta, Q. Meng, T. Yamamoto, Y. Tezuka, *J Am Chem Soc* **2010**, *132*, 14790-14802.

[37] O. Altintas, E. Lejeune, P. Gerstel, C. Barner-Kowollik, *Polym. Chem.* **2012**, *3*, 640-651.

[38] J. A. Pomposo, in *Micelles: Structural biochemistry, formation and functions & usage* (Eds.: D. Bradburn, T. Bittinger), Nova Science Publishers, New York, **2013**.

[39] M. Artar, E. Huerta, E. W. Meijer, A. R. A. Palmans, in *Sequence-Controlled Polymers: Synthesis, Self-Assembly, and Properties, Vol. 1170* (Eds.: J.-F. Lutz, T. Y. Meyer, M. Ouchi, M. Sawamoto), ACS Symp. Series, American Chemical Society, Washington, DC, **2014**, pp. 313-325.

[40] Y. Kim, J. Pyun, J. M. Frechet, C. J. Hawker, C. W. Frank, *Langmuir* **2005**, *21*, 10444-10458.

[41] E. Harth, B. V. Horn, V. Y. Lee, D. S. Germack, C. P. Gonzales, R. D. Miller, C. J. Hawker, *Journal of the American Chemical Society* **2002**, *124*, 8653-8660.

[42] L. Cheng, G. Hou, J. Miao, D. Chen, M. Jiang, L. Zhu, *Macromolecules* **2008**, *41*, 8159-8166.

[43] J. Wen, L. Yuan, Y. Yang, L. Liu, H. Zhao, *ACS Macro Letters* **2013**, *2*, 100-106.

[44] J. Wen, J. Zhang, Y. Zhang, Y. Yang, H. Zhao, *Polymer Chemistry* **2014**, *5*, 4032.

[45] W. Li, C.-H. Kuo, I. Kanyo, S. Thanneeru, J. He, *Macromolecules* **2014**, *47*, 5932-5941.

[46] R. K. Roy, J. F. Lutz, *J Am Chem Soc* **2014**, *136*, 12888-12891.

[47] J. Romulus, M. Weck, *Macromol Rapid Commun* **2013**, *34*, 1518-1523.

[48] J. Lu, N. Ten Brummelhuis, M. Weck, *Chem Commun (Camb)* **2014**, *50*, 6225-6227.

[49] D. Mecerreyes, V. Lee, C. J. Hawker, J. L. Hedrick, A. Wursch, W. Volksen, T. Magbitang, E. Huang, R. D. Miller, *Advanced Materials* **2001**, *13*, 204-208.

[50] A. Latorre-Sánchez, J. A. Pomposo, *Polymer International* **2016**, *65*, 855-860.

[51] J. De-La-Cuesta, E. González, A. J. Moreno, A. Arbe, J. Colmenero, J. A. Pomposo, *Macromolecules* **2017**, *50*, 6323-6331.

[52] J. A. Pomposo, J. Rubio-Cervilla, A. J. Moreno, F. Lo Verso, P. Bacova, A. Arbe, J. Colmenero, *Macromolecules* **2017**, *50*, 1732-1739.

[53] M. A. J. Gillissen, T. Terashima, E. W. Meijer, A. R. A. Palmans, I. K. Voets, *Macromolecules* **2013**, *46*, 4120-4125.

[54] J. A. Pomposo, I. Perez-Baena, F. Lo Verso, A. J. Moreno, A. Arbe, J. Colmenero, *ACS Macro Letters* **2014**, *3*, 767-772.

[55] A. J. Moreno, F. Lo Verso, A. Sanchez-Sanchez, A. Arbe, J. Colmenero, J. A. Pomposo, *Macromolecules* **2013**, *46*, 9748-9759.

[56] A. M. Stadler, L. Stingaciu, A. Radulescu, O. Holderer, M. Monkenbusch, R. Biehl, D. Richter, *J Am Chem Soc* **2014**, *136*, 6987-6994.

[57] F. Lo Verso, J. A. Pomposo, J. Colmenero, A. J. Moreno, *Soft Matter* **2015**, *11*, 1369-1375.

[58] F. Lo Verso, J. A. Pomposo, J. Colmenero, A. J. Moreno, *Soft Matter* **2014**, *10*, 4813-4821.

[59] A. Sanchez-Sanchez, S. Akbari, A. Etxeberria, A. Arbe, U. Gasser, A. J. Moreno, J. Colmenero, J. A. Pomposo, *ACS Macro Letters* **2013**, *2*, 491-495.

[60] I. Perez-Baena, I. Asenjo-Sanz, A. Arbe, A. J. Moreno, F. Lo Verso, J. Colmenero, J. A. Pomposo, *Macromolecules* **2014**, *47*, 8270-8280.

[61] T. Terashima, T. Sugita, K. Fukae, M. Sawamoto, *Macromolecules* **2014**, *47*, 589-600.

[62] T. Akagi, P. Piyapakorn, M. Akashi, *Langmuir* **2012**, *28*, 5249-5256.

[63] A. Sanchez-Sanchez, A. Arbe, J. Kohlbrecher, J. Colmenero, J. A. Pomposo, *Macromolecular Rapid Communications* **2015**, *36*, 1592-1597.

[64] M. Chen, C. J. Riddles, M. R. Van De Mark, *Langmuir* **2013**, *29*, 14034-14043.

[65] A. K. Mishra, *Nanomedicine for Drug Delivery and Therapeutics*, Wiley, New Jersey & Scrivener Publishing, Massachusetts, **2013**.

[66] E. H. H. Wong, S. J. Lam, E. Nam, G. G. Qiao, *ACS Macro Letters* **2014**, *3*, 524-528.

[67] Y. Bai, H. Xing, G. A. Vincil, J. Lee, E. J. Henderson, Y. Lu, N. G. Lemcoff, S. C. Zimmerman, *Chem. Sci.* **2014**, *5*, 2862-2868.

[68] A. B. Benito, M. K. Aiertza, M. Marradi, L. Gil-Iceta, T. Shekhter Zahavi, B. Szczupak, M. Jimenez-Gonzalez, T. Reese, E. Scanziani, L. Passoni, M. Matteoli, M. De Maglie, A. Orenstein, M. Oron-Herman, G. Kostenich, L. Buzhansky, E. Gazit, H. J. Grande, V. Gomez-Vallejo, J. Llop, I. Loinaz, *Biomacromolecules* **2016**, *17*, 3213-3221.

[69] J. Rubio-Cervilla, E. González, J. A. Pomposo, in *Single-Chain Polymer Nanoparticles: Synthesis, Characterization, and Applications* (Ed.: J. A. Pomposo), **2017**.

[70] A. Sanchez-Sanchez, S. Akbari, A. J. Moreno, F. L. Verso, A. Arbe, J. Colmenero, J. A. Pomposo, *Macromol Rapid Commun* **2013**, *34*, 1681-1686.

[71] G. Njikang, G. Liu, L. Hong, *Langmuir* **2011**, *27*, 7176-7184.

[72] S. K. Hamilton, E. Harth, *ACS Nano* **2009**, *3*, 402-410.

[73] C.-C. Cheng, D.-J. Lee, Z.-S. Liao, J.-J. Huang, *Polym. Chem.* **2016**, *7*, 6164-6169.

[74] C. Song, L. Li, L. Dai, S. Thayumanavan, *Polym. Chem.* **2015**, *6*, 4828-4834.

[75] I. Perez-Baena, I. Loinaz, D. Padro, I. García, H. J. Grande, I. Odriozola, *Journal of Materials Chemistry* **2010**, *20*, 6916.

[76] C. T. Adkins, J. N. Dobish, S. Brown, E. Harth, *ACS Macro Lett* **2013**, *2*, 710-714.

[77] G. Qian, B. Zhu, Y. Wang, S. Deng, A. Hu, *Macromol Rapid Commun* **2012**, *33*, 1393-1398.

[78] M. A. J. Gillissen, I. K. Voets, E. W. Meijer, A. R. A. Palmans, *Polymer Chemistry* **2012**, *3*, 3166.

[79] C. K. Lyon, E. O. Hill, E. B. Berda, *Macromolecular Chemistry and Physics* **2016**, *217*, 501-508.

[80] C. T. Adkins, H. Muchalski, E. Harth, *Macromolecules* **2009**, *42*, 5786-5792.

[81] G. Li, F. Tao, L. Wang, Y. Li, R. Bai, *Polymer* **2014**, *55*, 3696-3702.

[82] P. Wang, H. Pu, J. Ge, M. Jin, H. Pan, Z. Chang, D. Wan, *Materials Letters* **2014**, *132*, 102-105.

[83] A. Sanchez-Sanchez, A. Arbe, J. Colmenero, J. A. Pomposo, *ACS Macro Letters* **2014**, *3*, 439-443.

[84] S. Mavila, I. Rozenberg, N. G. Lemcoff, *Chem. Sci.* **2014**, *5*, 4196-4203.

[85] Y. Liu, T. Pauloehrl, S. I. Presolski, L. Albertazzi, A. R. Palmans, E. W. Meijer, *J Am Chem Soc* **2015**, *137*, 13096-13105.

[86] J. Willenbacher, O. Altintas, V. Trouillet, N. Knöfel, M. J. Monteiro, P. W. Roesky, C. Barner-Kowollik, *Polym. Chem.* **2015**, *6*, 4358-4365.

[87] M. Artar, E. R. J. Souren, T. Terashima, E. W. Meijer, A. R. A. Palmans, *ACS Macro Letters* **2015**, *4*, 1099-1103.

[88] Y. Bai, X. Feng, H. Xing, Y. Xu, B. K. Kim, N. Baig, T. Zhou, A. A. Gewirth, Y. Lu, E. Oldfield, S. C. Zimmerman, *J Am Chem Soc* **2016**, *138*, 11077-11080.

[89] Y. Azuma, T. Terashima, M. Sawamoto, *ACS Macro Letters* **2017**, *6*, 830-835.

[90] Y. H. Ng, F. di Lena, C. L. Chai, *Chem Commun (Camb)* **2011**, *47*, 6464-6466.

[91] Y.-H. Ng, F. di Lena, C. L. L. Chai, *Polym. Chem.* **2011**, *2*, 589-594.

[92] S. J. Sigg, F. Seidi, K. Renggli, T. B. Silva, G. Kali, N. Bruns, *Macromol Rapid Commun* **2011**, *32*, 1710-1715.

[93] T. B. Silva, M. Spulber, M. K. Kocik, F. Seidi, H. Charan, M. Rother, S. J. Sigg, K. Renggli, G. Kali, N. Bruns, *Biomacromolecules* **2013**, *14*, 2703-2712.

[94] J. He, L. Tremblay, S. Lacelle, Y. Zhao, *Soft Matter* **2011**, *7*, 2380.

[95] B. Zhu, S. Sun, Y. Wang, S. Deng, G. Qian, M. Wang, A. Hu, *J. Mater. Chem. C* **2013**, *1*, 580-586.

[96] A. Latorre-Sanchez, J. A. Pomposo, *Chemical Communications* **2015**, *51*, 15736-15738.

[97] B. Zhu, J. Ma, Z. Li, J. Hou, X. Cheng, G. Qian, P. Liu, A. Hu, *Journal of Materials Chemistry* **2011**, *21*, 2679.

[98] J. Jiang, S. Thayumanavan, *Macromolecules* **2005**, *38*, 5886-5891.

[99] A. R. de Luzuriaga, N. Ormategui, H. J. Grande, I. Odriozola, J. A. Pomposo, I. Loinaz, *Macromolecular Rapid Communications* **2008**, *29*, 1156-1160.

[100] W. Fan, X. Tong, Q. Yan, S. Fu, Y. Zhao, *Chem Commun (Camb)* **2014**, *50*, 13492-13494.

[101] M. E. Mackay, T. T. Dao, A. Tuteja, D. L. Ho, B. van Horn, H. C. Kim, C. J. Hawker, *Nat Mater* **2003**, *2*, 762-766.

[102] L. Oria, R. Aguado, J. A. Pomposo, J. Colmenero, *Adv Mater* **2010**, *22*, 3038-3041.

[103] M. E. Mackay, A. Tuteja, P. M. Duxbury, C. J. Hawker, B. Van Horn, Z. Guan, G. Chen, R. S. Krishnan, *Science* **2006**, *311*, 1740-1743.

[104] A. Tuteja, P. M. Duxbury, M. E. Mackay, *Macromolecules* **2007**, *40*, 9427-9434.

[105] J. K. Mistry, M. R. Van De Mark, *Journal of Coatings Technology and Research* **2013**, *10*, 453-463.

[106] M. Chen, C. Riddles, M. Van De Mark, *Colloid and Polymer Science* **2013**, *291*, 2893-2901.

[107] A. M. Natu, M. R. Van De Mark, *Progress in Organic Coatings* **2015**, *81*, 35-46.

[108] D. Bhowmik, J. A. Pomposo, F. Juranyi, V. García Sakai, M. Zamponi, A. Arbe, J. Colmenero, *Macromolecules* **2014**, *47*, 3005-3016.

[109] D. Bhowmik, J. A. Pomposo, F. Juranyi, V. García-Sakai, M. Zamponi, Y. Su, A. Arbe, J. Colmenero, *Macromolecules* **2014**, *47*, 304-315.

[110] A. Arbe, J. A. Pomposo, I. Asenjo-Sanz, D. Bhowmik, O. Ivanova, J. Kohlbrecher, J. Colmenero, *Macromolecules* **2016**, *49*, 2354-2364.

[111] J. A. Pomposo, A. Ruiz de Luzuriaga, A. Etxeberria, J. Rodríguez, *Phys. Chem. Chem. Phys.* **2008**, *10*, 650-651.

[112] A. R. de Luzuriaga, A. Etxeberria, J. Rodríguez, J. A. Pomposo, *Polymers for Advanced Technologies* **2008**, *19*, 756-761.

[113] A. Ruiz de Luzuriaga, H. Grande, J. A. Pomposo, *Journal of Nano Research* **2008**, *2*, 105-114.

[114] S. Montes, H. Grande, A. Etxeberria, J. A. Pomposo, *Journal of Nano Research* **2009**, *6*, 123-132.

[115] A. Ruiz de Luzuriaga, H. J. Grande, J. A. Pomposo, *J Chem Phys* **2009**, *130*, 084905.

[116] J. A. Pomposo, A. R. de Luzuriaga, I. Garcia, A. Etxeberria, J. Colmenero, *Macromol Rapid Commun* **2011**, *32*, 573-578.

[117] S. Y. Kim, K. S. Schweizer, C. F. Zukoski, *Phys Rev Lett* **2011**, *107*, 225504.

[118] D. E. Whitaker, C. S. Mahon, D. A. Fulton, *Angew Chem Int Ed Engl* **2013**, *52*, 956-959.

[119] E. J. Foster, E. B. Berda, E. W. Meijer, *J Am Chem Soc* **2009**, *131*, 6964-6966.

[120] E. B. Berda, E. J. Foster, E. W. Meijer, *Macromolecules* **2010**, *43*, 1430-1437.

[121] J. A. Kaitz, C. M. Possanza, Y. Song, C. E. Diesendruck, A. J. H. Spiering, E. W. Meijer, J. S. Moore, *Polym. Chem.* **2014**, *5*, 3788-3794.

[122] Y. Zhang, H. Zhao, *Polymer* **2015**, *64*, 277-284.

CHAPTER 2

Standard and New Synthesis Routes of SCNPs

2.1. Introduction

Precisely defined linear polymers folded into functional nanostructures, capable of completing complex tasks, are omnipresent in nature.[1] In this sense, an obvious research goal becomes apparent: exploiting our understanding of biomolecules to mimic this behavior in the laboratory using recent advances in controlled polymerization chemistry, polymer functionalization and cross-linking, as well as the well-known theories of modern polymer physics.

In order to fabricate soft nanomaterials that more closely mimic folded biomolecules in structure and activity, the new paradigm in polymer synthesis involves the manipulation of single polymer chains to construct ultra-small functional unimolecular nano-objects,[2-3] *i.e.,* single-chain nanoparticles (SCNPs). SCNPs are individual polymer chains that have been intra-molecularly cross-linked, usually at very high dilution. Recent reviews provide detailed information about the different techniques involved in SCNP construction:[1, 4-12] (i) controlled polymerization for the synthesis of SCNP precursor, (ii) polymer functionalization, if necessary, and (iii) intra-chain folding/collapse *via* covalent, non-covalent (supramolecular) or dynamic-covalent bonding interactions (see figure 2.1).

A vast majority of the cross-linking strategies developed for single-chain collapse is made by covalent chemistry. Among them, radical coupling,[13-14] Diels-Alder reaction,[15] Bergmann cyclation,[16-19] Glaser-Hay coupling,[20] nitrene cross-linking,[21-23] Michael addition,[24-26] etc., are frequently used. Covalent cross-linking delivers irreversible nanoparticles that remain stable and unaffected by

external stimuli, thus SCNPs synthesized by covalent interactions lose their dynamic nature.

On the contrary, the synthesis of SCNPs *via* supramolecular (non-covalent) interactions and dynamic covalent-bonds offers the possibility to develop structurally dynamic or reversible materials, which can adapt their constitution, and hence properties, to external stimuli (such as pH, temperature, oxidizing or reducing agents, etc.).[27] Different non-covalent bonding-based strategies (benzamide dimerization,[28] Cu complexation,[26, 29] amphiphilic random copolymer self-assembly,[30] etc.), as well as successful approaches based on dynamic covalent bonds (hydrazine bonds,[31-32] disulfide bridges,[33] anthracene dimerization,[34] enamine bonds,[35] etc.) have been developed over recent years.

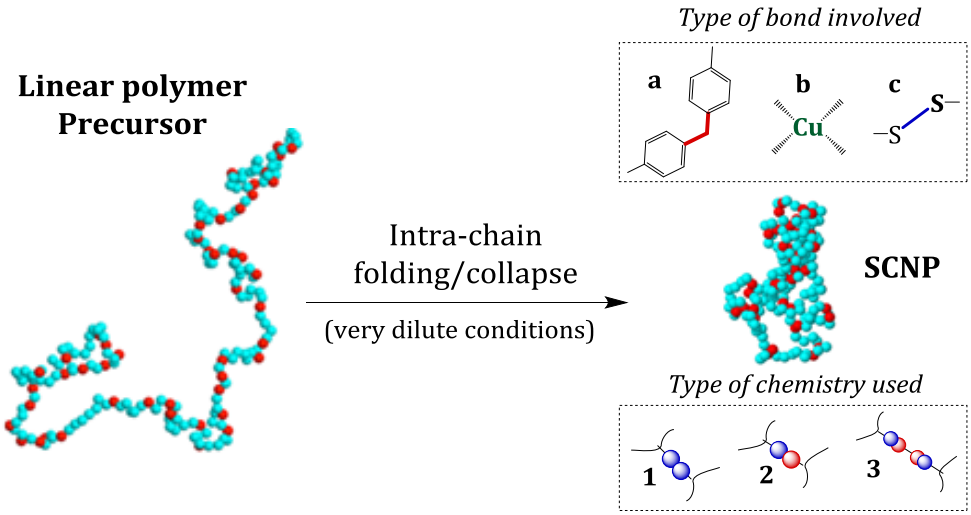

Figure 2.1: Schematic illustration of a linear polymer precursor and a single-chain nanoparticle (SCNP) obtained through intra-chain folding/collapse, *via* covalent bond (a), supramolecular interaction (b) and dynamic-covalent bond (c). The type of chemistry used is also involved on SCNP construction; intra-chain homocoupling (1), intra-chain heterocoupling (2) and cross-linker induced collapse (3).

The strategies typically used to achieve intra-chain collapse can also be classified according to the type of chemistry used (see figure 2.1): intra-chain homocoupling, where pendant functional groups can react with each other to generate a bond, intra-chain heterocoupling, where two complementary functionalities are attached to the polymer chain to promote its intra-molecular cross-linking, and the cross-linker induced collapse, which uses a cross-linking molecule to bind functional groups in the polymer.[5] Importantly, the method chosen for polymer collapse will also in turn affect the overall structure and potential properties of the single-chain nanoparticle formed.[36]

This chapter reports on the synthesis of all the single-chain nanoparticles (SCNPs) employed in this thesis. In the first part, already known synthetic methods toward single-chain nanoparticles (standard SCNPs) are explained, while in the second part new synthesis routes developed in this thesis are described.

Within the standard synthesis routes, three types of SCNPs starting from the same linear precursor are produced, by means of three different synthesis methods: covalent bonding (denoted as Mi-SCNPs in scheme 2.1), non-covalent interactions (denoted as Cu-SCNPs in scheme 2.1) and dynamic covalent-bonding (denoted as e-SCNPs in scheme 2.1). The goal is to explore the basic properties of these SCNPs using scattering techniques, as will be shown in chapter 4.

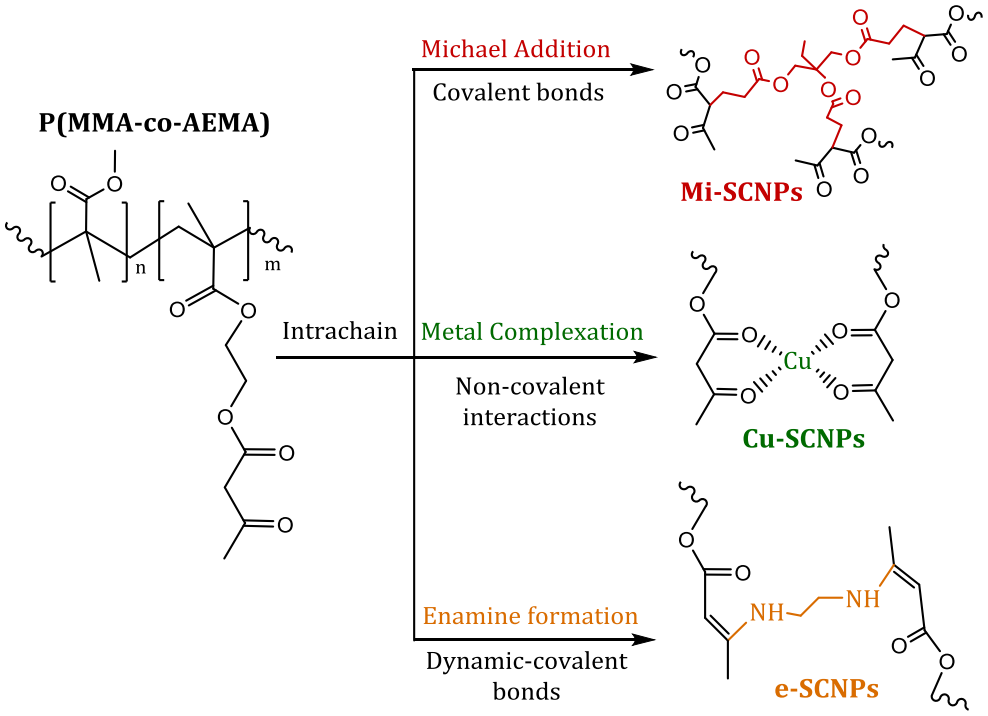

Scheme 2.1: Standard synthesis routes of SCNPs employed in this work by starting from the same linear copolymer precursor, involving MMA and AEMA repeating units. MMA = Methyl methacrylate. AEMA = (2-acetoacetoxy)ethyl methacrylate.

Copper complexation is also involved in another synthesis route applied to amphiphilic precursors with the aim to obtain more compact SCNPs (results will be shown in chapter 5). Subsequently, new synthesis routes developed in this thesis are described. On the one hand, microwave-assisted synthesis is employed to obtain polystyrene (PS) based functional single-chain nanoparticles, with the unexpected presence of aldehyde groups along the SCNPs. On the other hand, the synthesis of water-soluble poly(vinyl pyrrolidone) single-chain nanoparticles *via* Fenton reaction is reported for the first time. The results obtained for these novel SCNPs will be discussed in chapter 5.

2.2. Standard Synthesis Routes of SCNPs

2.2.1. Materials

Methyl methacrylate (**MMA**, 99%), (2-acetoacetoxy)ethyl methacrylate (**AEMA**, 95%), oligo(ethylene glycol) methyl ether methacrylate (**OEGMA**, M_n ~ 300 g/mol), 2,2-azobis(2-methylpropionitrile) (AIBN, ≥98%), trimethylolpropane triacrylate (TMT, technical grade), potassium hydroxide (ACS reagent, ≥85%), copper (II) acetate ($Cu(OAc)_2$, 98%), ethylenediamine (99.5%), ethyl acetate (anhydrous, 99.8 %), 1,4-dioxane (anhydrous, 99.8%), hexane (anhydrous, 95%), diethyl ether (ACS reagent, anhydrous, >99.0%) and deuterated chloroform ($CDCl_3$, 99.96 atom % D, containing 0.03 % (v/v) tetramethylsilane, TMS) were purchased from Aldrich and used, unless specified, as received. 2-Cyanoprop-2-yl-dithiobenzoate (CPDB, ≥97%) and 4-Cyanopentanoic acid dithiobenzoate (CPADB) were purchased from Strem Chemicals. Methanol (MeOH, synthesis grade), tetrahydrofuran (THF, HPLC grade) and hydrochloric acid (37%, extra pure) were purchased from Scharlab. Deionized water obtained from a Thermo Scientific apparatus was employed in this work. **MMA**, **AEMA** and **OEGMA** were purified by passing through basic alumina before use.

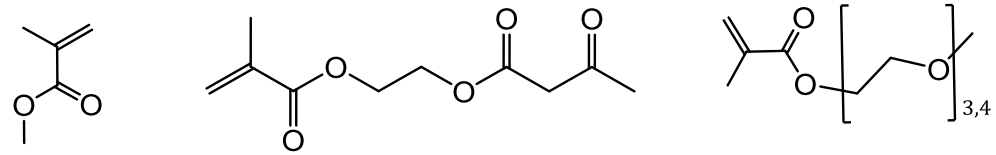

Scheme 2.2: Structure of the monomers used for the polymer precursor synthesis.

2.2.2. Polymer Precursors

A. Synthesis of poly(MMA-co-AEMA) copolymers

In a typical procedure, MMA (1 ml, 9.4 mmol), AEMA (0.6 ml, 3.1 mmol), CPDB (6.9 mg, $3.1x10^{-2}$ mmol) and AIBN (1.3 mg, $7.8x10^{-2}$ mmol) were dissolved in ethyl acetate (1.6 ml). The reaction mixture was degassed by passing argon for 15 min. The copolymerization reaction was carried out at 65 °C for 18 h. The resulting precursor was isolated by precipitation in methanol and further drying under vacuum. (P1: Yield = 59%, M_w (SEC) = 52.5 kg/mol, M_w/M_n = 1.03, composition (^{1}H NMR) = 28 % AEMA). Varying the amount of initiator and CTA, copolymers P1-P4 were obtained with different molecular weights (from ~50 kg/mol to ~270 kg/mol) and relatively narrow polydispersity. The main characteristics of these copolymers are summarized in table 2.1.

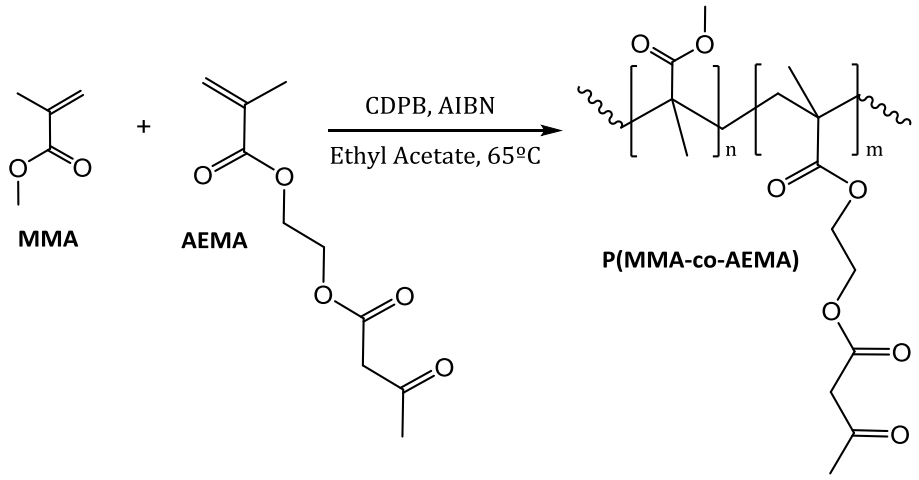

Scheme 2.3: Synthesis of poly(MMA-co-AEMA) copolymer precursor via RAFT polymerization (see text for details).

B. Synthesis of poly(OEGMA-co-AEMA) copolymers

In a standard procedure, OEGMA (1.1 ml, 4 mmol), AEMA (0.6 ml, 3.2 mmol), CPADB (15.2 mg, 5.3×10^{-2} mmol) and AIBN (1.8 mg, 1.0×10^{-2} mmol) were dissolved in 1,4-dioxane (3 ml). The reaction mixture was degassed by passing argon for 15 min. The copolymerization reaction was carried out at 70 ℃ for 24 h. The resulting pink oil (P4) was isolated by precipitation in hexane (Yield: 76%). After that, the copolymer was redissolved in a minimal amount of THF and added to a large excess of hexane (twice), the residual solvent was concentrated and further drying was performed at r.t. under vacuum. Copolymers O1-O4 were obtained as pink oils with 11-40 mol% of AEMA content, as determined by ^{1}H NMR spectroscopy following reported procedures[37]. The main characteristics of these copolymers are summarized in table 2.1.

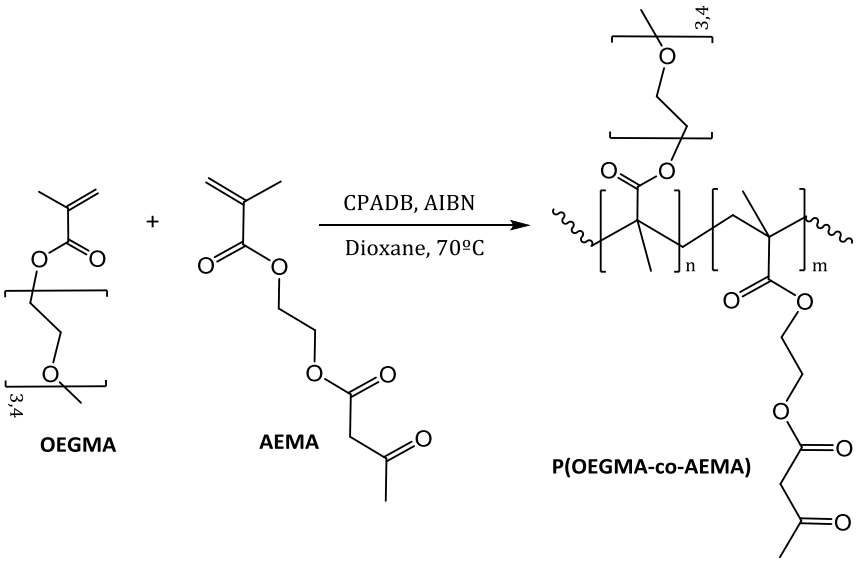

Scheme 2.4: Synthesis of poly(OEGMA-co-AEMA) copolymer precursor via RAFT polymerization (see text for details).

Table 2. 1: Characteristics of P(MMA-co-AEMA) and P(OEGMA-co-AEMA) copolymer precursors.

Code	Copolymer	M_w (kg/mol)[a]	M_w/M_n[a]	AEMA (mol %)[b]
P1	MMA-AEMA	52.5	1.03	28
P2	MMA-AEMA	123.5	1.11	30
P3	MMA-AEMA	209.1	1.37	27
P4	MMA-AEMA	272.1	1.40	30
O1	OEGMA-AEMA	110.1	1.04	11
O2	OEGMA-AEMA	90.4	1.10	20
O3	OEGMA-AEMA	175.0	1.08	35
O4	OEGMA-AEMA	208.0	1.05	40

[a)]As determined by SEC with triple detection (DRI, MALLS and VI detector) in THF at 30 °C; [b)]AEMA content in the copolymer as determined by ^{1}H NMR spectroscopy.

2.2.3. Single-Chain Michael Nanoparticles (Mi-SCNPs)

This synthesis method relies on multidirectional self-assembly of individual polymeric chains at r.t. driven by Michael addition reactions involving external multifunctional acrylate-based cross-linkers. For more details about the chemistry involved in the synthesis see Ref. [24]

A. Synthesis of single-chain Michael nanoparticles

In a typical reaction, P(MMA-co-AEMA) copolymer precursor (P1**,** 150 mg, 0.31 mmol), multifunctional cross-linker (TMT, 28.2 mg, 0.10 mmol) and catalyst (KOH, 8.9 mg, 0.16 mmol) were dissolved in THF (150 ml) at room temperature. The progressive folding/collapse process was followed through simultaneous SEC measurements. After reaction completion (3 days), a few drops of hydrochloric acid were added to deactivate the catalyst, the mixture was

concentrated and the single-chain "Michael" nanoparticles (Mi-SCNPs) were isolated by precipitation in diethyl ether and further drying under vacuum. (Mi-SCNP1: Yield = 65%, M_w (SEC) = 55.1 kg/mol, M_w/M_n = 1.02).

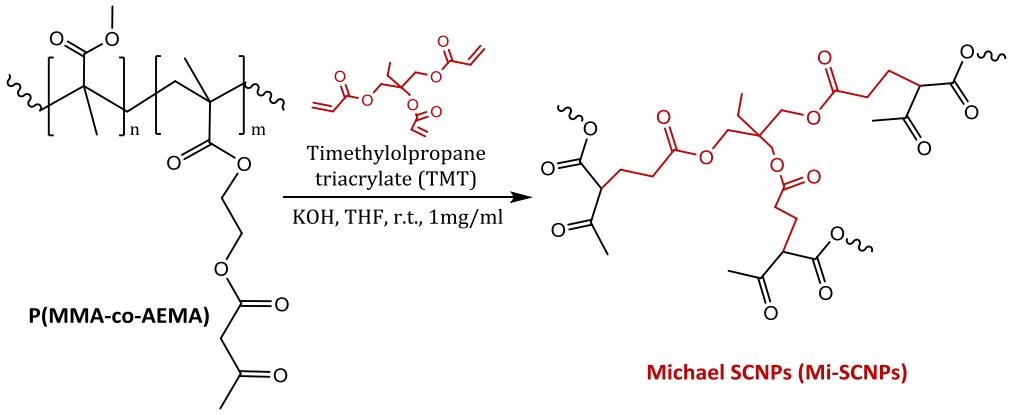

Scheme 2.5: Single-chain Michael nanoparticle formation with multifunctional cross-linker (see text for details).

2.2.4. Metallo-Folded Single-Chain Nanoparticles (Cu-SCNPs)

Metallo-folded SCNPs were obtained *via* intra-chain Cu(II) complexation of AEMA units by exploiting the β-ketoester functional groups in the copolymer precursors as ligands. On the one hand, poly(MMA-co-AEMA) linear precursor was used to obtain Cu-SCNPs[29], resulting only soluble in organic solvents. On the other hand, water soluble OEGMA-CuSCNPs were obtained by starting from amphiphilic poly(OEGMA-co-AEMA) precursors.[37] Although two different copolymer precursors were employed, the folding/collapse mechanism involved in the metallo-folded SCNPs was the same, due to the presence of AEMA monomer in both copolymers.

A. Synthesis of metallo-folded poly(MMA)-based SCNPs

In a typical procedure, P(MMA-co-AEMA) copolymer precursor (P1, 150 mg, 0.31 mmol) was dissolved in THF (150 ml) at room temperature. Then, a solution of $Cu(OAc)_2$ (14.3 mg, 0,078 mmol) in THF was progressively added, and the mixture was maintained under stirring for 24h. Finally, the mixture was concentrated and the metallo-folded single-chain nanoparticles (Cu-SCNPs) were isolated by precipitation in diethyl ether and further drying under vacuum. (Cu-SCNP1: Yield = 77%; M_w (SEC) = 55.9 kg/mol, M_w/M_n = 1.02).

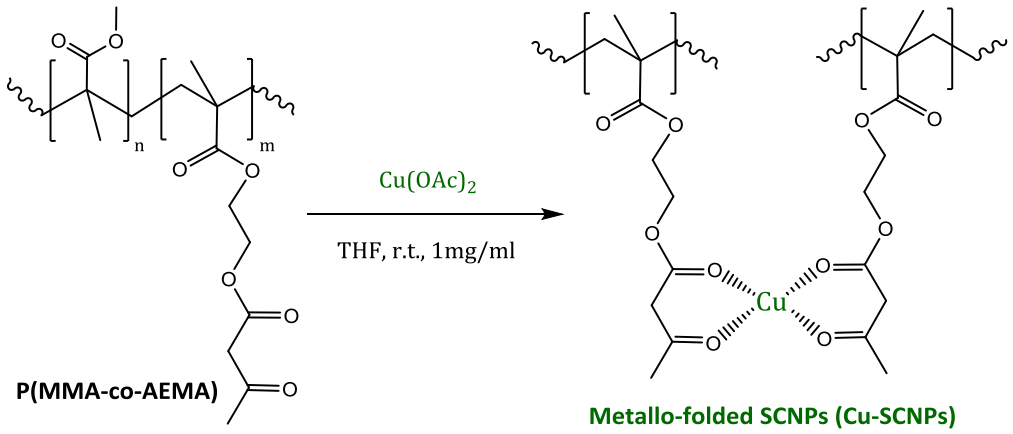

Scheme 2.6: Synthesis of poly(MMA)-based metallo-folded single-chain nanoparticles, via intra-chain Cu(II) complexation of AEMA units

B. Synthesis of metallo-folded poly(OEGMA)-based SCNPs

Starting from the amphiphilic copolymer poly(OEGMA-co-AEMA), two different synthesis procedures involving selective and nonselective solvents, that we call "protocols" were used. The protocol I was carried out in THF (which is a good solvent for both, OEGMA and AEMA), while the protocol II was carried out in water (good solvent for OEGMA, bad solvent for AEMA).

a) Synthesis of OEGMA-CuSCNPs by Protocol I:

Typically, poly(OEGMA-co-AEMA) copolymer precursor (O4, 100 mg, 0.126 mmol) was dissolved in THF (90 ml) at room temperature. Then, a solution of $Cu(OAc)_2$ (16 mg, 0.081 mmol Cu) in 10 ml of THF was added, and the mixture was maintained under stirring for 24 h. After reaction completion, the system was concentrated and precipitated in MeOH (twice) to purify the copper-containing SCNPs from potential traces of $Cu(OAc)_2$, which is highly soluble in MeOH. No traces of $Cu(OAc)_2$ in the samples were detected by ^1H NMR and FTIR spectroscopy. Finally, the resulting OEGMA-CuSCNPs-I were dried in a vacuum oven at r.t. under vacuum (O4-CuSCNPs-I: Yield = 61%, M_w (SEC) = 206.5 kg/mol, M_w/M_n = 1.05).

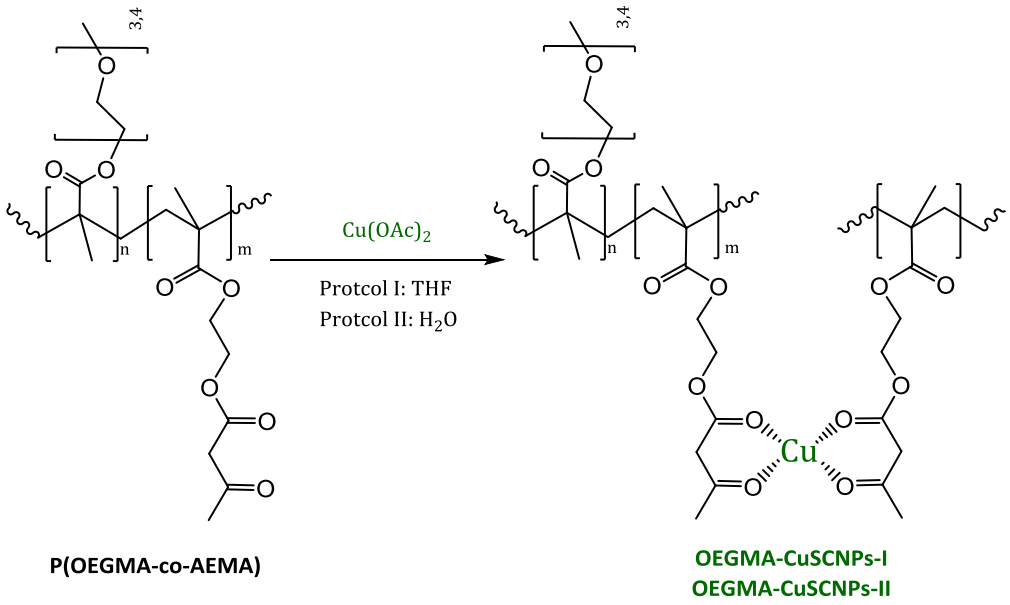

Scheme 2.7: Synthesis of poly(OEGMA)-based metallo-folded single-chain nanoparticles, *via* protocol I and protocol II (see text for details).

b) Synthesis of OEGMA-CuSCNPs by Protocol II:

In a typical reaction, poly(OEGMA-co-AEMA) copolymer precursor (O1, 100 mg, 0.126 mmol) was dissolved in deionized water (90 ml) at room temperature. Then, a solution of $Cu(OAc)_2$ (16 mg, 0.081 mmol Cu) in 10 ml of deionized water was added, and the mixture was maintained under stirring for 24 h. After reaction completion, the system was freeze-dried, redissolved in THF and precipitated in MeOH (twice). No traces of $Cu(OAc)_2$ in the samples were detected by ^1H NMR and FTIR spectroscopy. Finally, the resulting OEGMA-CuSCNPs-II were dried in a vacuum oven at r.t. (O1-CuSCNPs-II: Yield = 55%, M_w (SEC) = 94.2 kg/mol, M_w/M_n = 1.12).

2.2.5. Reversible Single-Chain Nanoparticles (e-SCNPS)

In this route the folding/collapse process is achieved by using dynamic covalent enamine bonds. β-ketoester functional groups that are present in poly(MMA-co-AEMA) precursor, undergo an exchange process with ethylenediamine, leading to reversible SCNPs formation.[35] Disassembly of the e-SCNPs is possible at low pH values.

A. Synthesis of reversible single-chain nanoparticles

In a typical procedure, P(MMA-co-AEMA) copolymer precursor (P3, 25 mg, 0.191 mmol) and cross-linker (ethylenediamine, 1.7 µl, 0.026 mmol) were dissolved in 25 ml of THF at room temperature. The progressive folding-collapse process was followed by simultaneous SEC and SAXS measurements. After reaction completion (24 h), the obtained reversible single-chain nanoparticles

(e-SCNPS) were characterized with different techniques without further purification (e-SCNP3: M_w (SEC) = 207.2 kg/mol, M_w/M_n = 1.33).

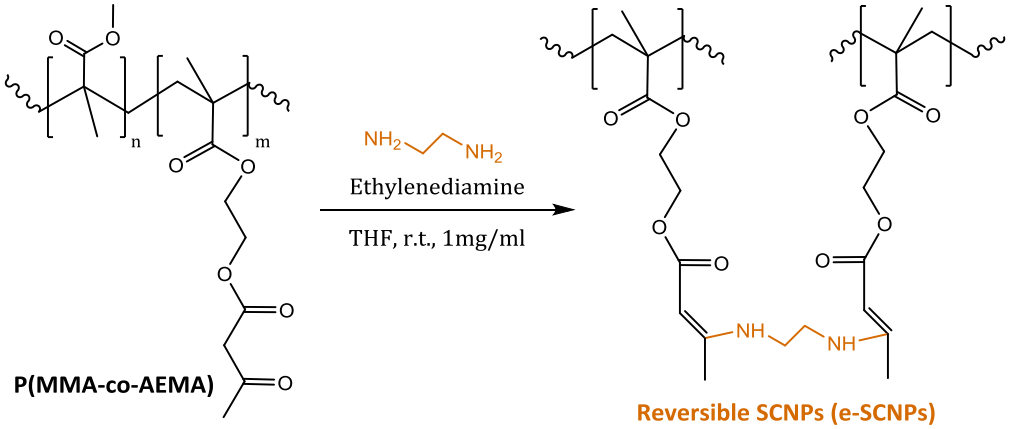

Scheme 2.8: Synthesis of reversible single-chain nanoparticles, *via* enamine formation (see text for details).

2.3. New Synthesis Routes of SCNPs

2.3.1. Polystyrene-based Single-Chain Nanoparticles

A. Materials

Styrene (**St**, ≥ 99%), 4-(chloromethyl) styrene (**CMS**, ≥ 90%), sodium azide (NaN_3, ≥ 99%), dansylhydrazine (98%), 4,4'-Azobis(4-cyanovaleric acid) (ACVA, ≥ 98%), N-N-Dimethylformamide (DMF, ≥ 99.9%), N-methyl-2-pyrrolidone (NMP, ≥ 99%), benzaldehyde (BA, purified by redistillation, ≥99.5%), chloroform ($CHCl_3$, ≥ 99.8%) and deuterated chloroform ($CDCl_3$, 99.96 atom % D, containing 0.03 % (v/v) tetramethylsilane, TMS) were purchased from Aldrich and used, unless specified, as received. Methanol (MeOH, synthesis grade) and tetrahydrofuran (THF, HPLC grade) were purchased from Scharlab. Benzyl azide (BAz, 94%) was purchased from Alpha Aesar. Deionized water obtained from a Thermo Scientific apparatus (Barnstead TII Pure Water System) was employed in this work. **St** and **CMS** were purified by passing through basic alumina.

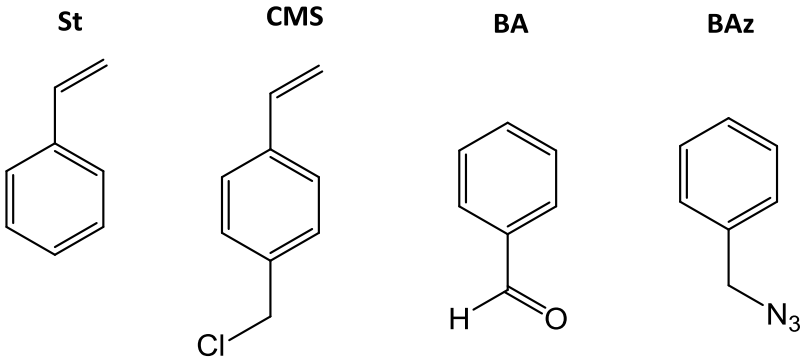

Scheme 2.9: Structures of some compounds used in the current study; styrene (St), chloromethyl styrene (CMS), benzaldehyde (BA) and benzyl azide (BAz).

B. Synthesis of reference P0 (neat polystyrene)

The synthesis of neat polystyrene (P0) was carried out by using St (2 ml, 17.4 mmol) as monomer and ACVA (1.7 mg, $6.1x10^{-3}$ mmol) as initiator. The reaction mixture was degassed by passing argon for 15 min and then stirred for 3 h at 80 °C. The resulting homopolymer (P0) was isolated by precipitation in methanol and further drying at r.t. under vacuum (Yield: 10 %, M_w (SEC) = 283 kg/mol, M_w/M_n = 1.2).

C. Synthesis of poly(styrene-co-chloromethyl styrene) precursors

In a typical procedure, the copolymerization of St (2 ml, 17.4 mmol) and CMS (0.434 ml, 3.1 mmol) was carried out using ACVA (1.7 mg, $6.1x10^{-3}$ mmol) as initiator. The reaction mixture was degassed by passing argon for 15 min and then stirred for 3 h at 80 °C. After that, the copolymer was redissolved in a minimal amount of THF and added to a large excess of methanol. The resulting precursor (C21) was isolated by filtration and further dried at r.t. under vacuum (C21: Yield: 30 %, M_w (SEC) = 235 kg/mol, M_w/M_n = 1.3). Copolymers C9, C16, C21 and C30 were obtained as yellow powders with 9-30 mol% of CMS content, as determined by ^{1}H NMR spectroscopy following reported procedures.[38]

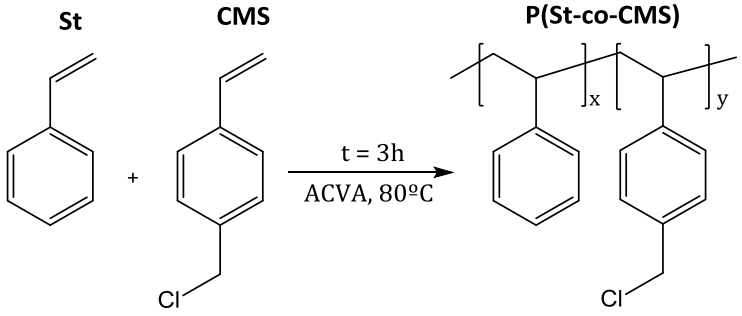

Scheme 2.10: Synthesis of poly(styrene-co-chloromethyl styrene) copolymers (y=9-30 mol%).

D. Synthesis of poly(styrene-co-azidomethyl styrene) precursors

In a typical reaction, poly(styrene-co-chloromethyl styrene) (C21, 350 mg, 0.64 mmol CMS) was dissolved in DMF (14 ml) at room temperature. Then, NaN_3 (2eq., 83.2 mg, 1.3 mmol,) was added and the mixture was maintained under stirring for 24 h. After reaction completion, the system was concentrated and precipitated in a mixture of $MeOH/H_2O$ (1:1). Finally, the resulting precursor (P21) was dried in a vacuum oven at room temperature (P21: Yield: 90 %, M_w (SEC) = 242 kg/mol, M_w/M_n = 1.3). Precursors P9, P16, P21 and P30 were obtained as powders with 9 - 30% mol of AMS content.

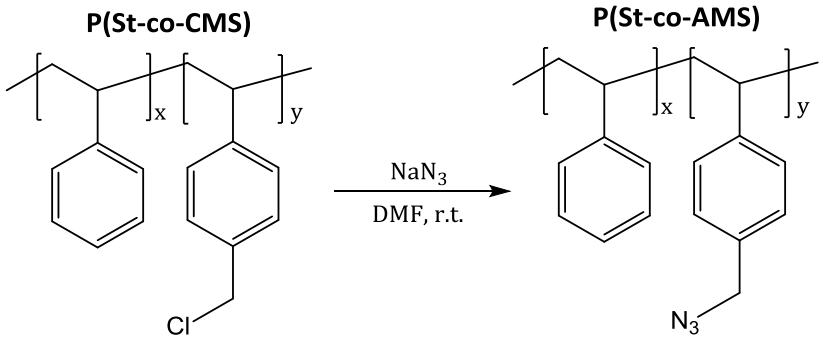

Scheme 2.11: Synthesis of poly(styrene-co-azidomethyl styrene) copolymer precursors.

The complete transformation of chloromethyl to azidomethyl moieties was confirmed by ^1H NMR spectroscopy, showing s shift of the band placed at 4.5 ppm corresponding to methylene protons from $–CH_2$-Cl groups to 4.2 ppm upon formation of the new $–CH_2$-N_3 moieties (figure 2.2). The lack of any residual signal at 4.5 ppm confirmed the quantitative replacement of –Cl atoms by $–N_3$ groups, when excess of NaN_3 was used. Figure 2.3 shows the complete ^1H NMR spectra of the resulting copolymer precursors, P(St-co-AMS), and neat polystyrene, as reference, synthesized in this work.

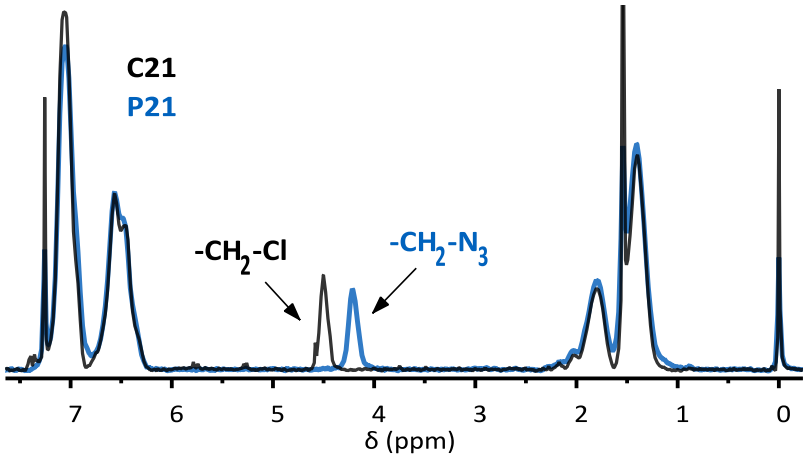

Figure 2.2: ^{1}H NMR spectra in $CDCl_3$ of poly(St-co-CMS) (C21) and poly(St-co-AMS) (P21).

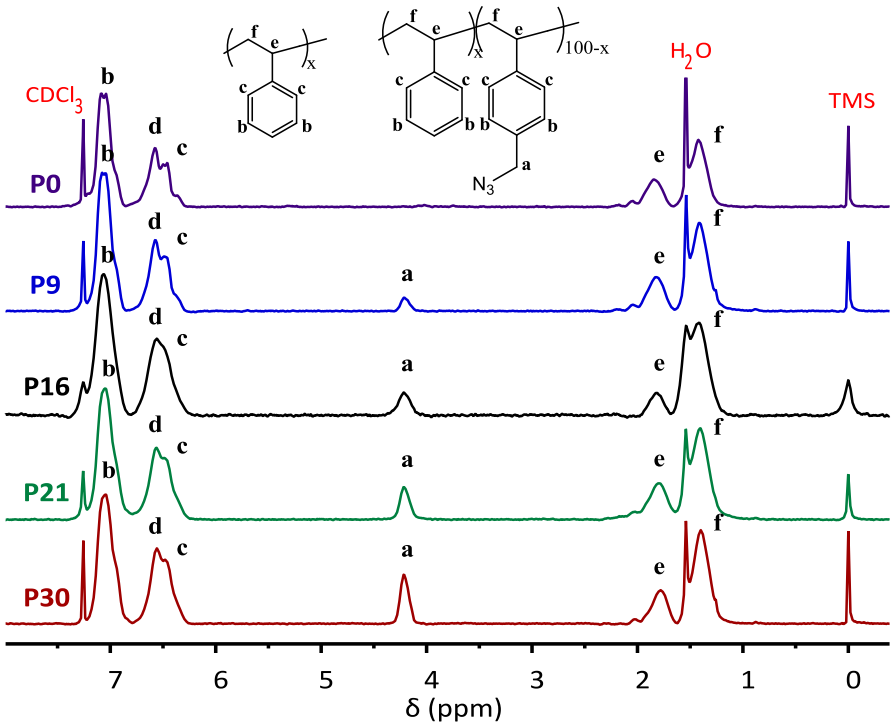

Figure 2.3: ^{1}H NMR spectra in $CDCl_3$ of neat polystyrene (P0) and poly(styrene-co-azidomethyl styrene) precursors (P9, P16, P21 and P30).

E. Synthesis of intra-chain cross-linked polystyrene single-chain nanoparticles

In a typical reaction, P(St-co-AMS) copolymer precursor (P21, 50 mg, 0.432 mmol) was dissolved in DMF or NMP (50 ml) at room temperature. Then, the mixture was heated to 200 °C under microwave irradiation (300 W, 150 psi) and maintained there for 30 min. Then, the system was cooled down to room temperature and concentrated in a vacuum line using Schlenk flasks. The resulting polystyrene single-chain nanoparticles (PS-SCNPs) were isolated by precipitation in a mixture of MeOH/H_2O (1:1) and dried in a vacuum oven at 40 °C under vacuum (PS-SCNP21: Yield: 57%, M_w (SEC) = 242 kg/mol, M_w/M_n = 1.3).

F. Control experiments with network cross-linked materials

In a typical procedure, the precursor (P21, 5 mg, 0.0432 mmol) was dissolved in $CHCl_3$ (5 ml) at room temperature. Then, the mixture was deposited over a gold-coated electrode of 20 mm and dried at 80 °C under vacuum for 48 h in order to remove any residual solvent. The formed film was covered with a gold-coated electrode of 15 mm, heated in the DS instrument to 200 °C and maintained there for 3 h. The resulting network cross-linked material (B21) was found to be insoluble in any solvent.

G. Control experiments with benzyl azide

The same experimental procedure followed for single-chain nanoparticles synthesis was carried out with benzyl azide (BAz), but using a solution of 500 mg of benzyl azide in 50 ml of DMF. After reaction, a portion of the crude mixture was concentrated and directly measured by ^{1}H NMR. Another portion of

the crude mixture was precipitated in water, centrifuged, isolated and redissolved in deuterated chloroform for ^{1}H NMR analysis.

H. Functionalization of PS-SCNP30 with dansylhydrazine (fluorescent probe)

For functionalization of nanoparticle PS-SCNP30 with dansylhydrazine, 10 mg of benzaldehyde-decorated polystyrene single-chain nanoparticles and 4.4 mg of dansylhydrazine were dissolved in 1 ml of chloroform and maintained under agitation for 20 h. After reaction, the mixture was precipitated in a large excess of methanol to remove any amount of unreacted dansylhydrazine and to recover the functionalized nanoparticles, which were dried in a vacuum oven at r.t. under vacuum. Then, 2 mg of the resulting functionalized nanoparticles were dissolved in 1 ml of THF. The resulting solution was placed under UV light (wavelength: 365 nm) and showed intense fluorescence.

2.3.2. Poly(Vinyl Pyrrolidone) Single-Chain Nanoparticles

A. Materials

Poly(vinyl pyrrolidone) (**PVP**, homopolymers of molecular weight 55 kg/mol and 360 kg/mol), hydrogen peroxide solution (H_2O_2, 30 wt.% in H_2O, ACS reagent), iron (II) chloride ($FeCl_2$, 98%), sodium phosphate dibasic (Na_2HPO_4, BioXtra, ≥99%), cis-Diammineplatinum(II) dichloride (cisplatin), acetic acid (ACS reagent, ≥99.8%), chloroform ($CHCl_3$, ≥ 99.8%), and dialysis tubing cellulose membrane (avg. flat width 76 mm, typical molecular weight cut-off = 14,000) were purchased from Aldrich and used, unless specified, as received. Sodium chloride (NaCl, puriss, for HPLC) was purchased from Fluka. Deionized water obtained from a Thermo Scientific apparatus (Barnstead TII Pure Water System) was employed in this work.

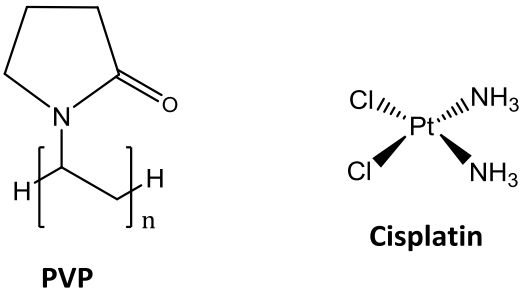

Scheme 2.12: Structures of some compounds used in the current study.

B. Synthesis of poly(vinyl pyrrolidone) SCNPs via Fenton reaction

In a typical procedure, PVP single-chain nanoparticles were produced by mixing two solutions (see figure 2.4): solution A containing PVP dissolved in water (50 mg, 100ml, 0.5 mg/ml) and H_2O_2 (113 µl, 10 mM), and solution B, containing PVP dissolved in water (same concentration and amount as solution A) and $FeCl_2$

(63.4 mg, 5 mM), at room temperature. After reaction completion (24 h), the mixture was dialyzed for 24 h in order to remove traces of unreacted $FeCl_2$. Finally, the system was freeze-dried and PVP single-chain nanoparticles *via* Fenton reaction (PVP-SCNPS) were obtained as white powders. The concentration of H_2O_2 was set as 10 mM or 100 mM and that of $FeCl_2$ as 5 mM or 10 mM, such that the ratio $[H_2O_2]/[Fe^{2+}]$ was 1, 2 and 10. Moreover, to evaluate the pH influence, PVP solutions were adjusted at pHs 3.5 (acetic acid, 0.1 M) and 7.5 (sodium phosphate, 0.1 M).

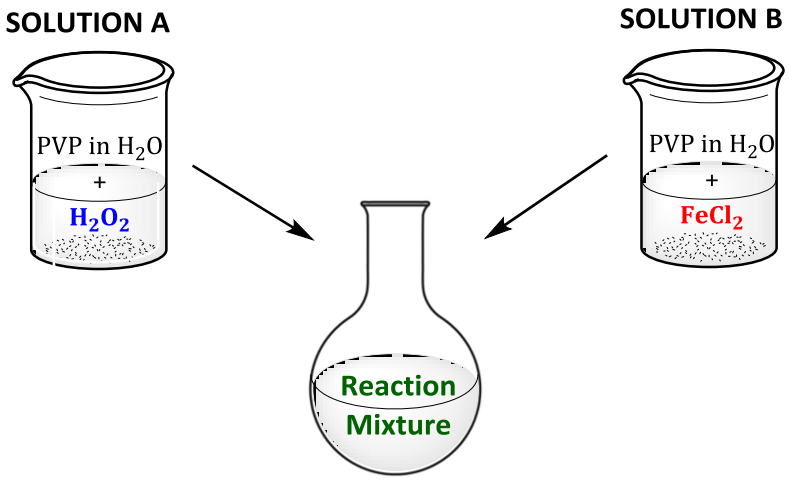

Figure 2.4: Schematic representation of the synthesis of PVP-SCNPs *via* fenton reaction.

C. Cisplatin loaded PVP nanocarriers

Single-chain PVP nanocarriers, PVP-SCNPs, were loaded with cisplatin (CP) to study its potential use for drug delivery. First, a solution of cisplatin (CP) in water (5 µg/ml, containing 0.9% of NaCl) was prepared. Then, 1.5 mg of single-chain PVP nanocarriers were dissolved in 5 ml of the solution containing CP and

the mixture was incubated for 24 h in the dark at room temperature. In order to purify the CP loaded PVP nanocarries, an extraction with 5 ml of $CHCl_3$ was carried out (this process was repeated twice); the chloroform was evaporated using a continuous argon air stream and the CP loaded PVP nanocarriers were transferred to a flask containing 5 ml of water.

The delivery of cisplatin from the single-chain PVP nanocarriers was determined by UV-Vis spectroscopy measurements at 265 nm. To quantify the *in vitro* release of CP from PVP nanocarriers, a dialysis method was used and samples were collected during next 96 h. After each time interval, that is, 1 h, 2 h, 24 h, 48 h and 96 h, the absorbance of each sample was recorded at 265 nm and the released CP from PVP nanocarriers was calculated by using the following equation:

$$\text{CP Release (\%)} = \frac{\Delta(CP_t - CP_{t=0})}{\Delta(CP_{t=96h} - CP_{t=0})} \tag{2.1}$$

where CP_t is the absorbance measured (265 nm) at time t, $CP_{t=0}$ is the absorbance measured at the beginning of the experiment, and $CP_{t=96h}$ is the last absorbance measured.

2.4. References

[1] C. K. Lyon, A. Prasher, A. M. Hanlon, B. T. Tuten, C. A. Tooley, P. G. Frank, E. B. Berda, *Polym. Chem.* **2015**, *6*, 181-197.

[2] M. Ouchi, N. Badi, J. F. Lutz, M. Sawamoto, *Nat Chem* **2011**, *3*, 917-924.

[3] J. F. Lutz, M. Ouchi, D. R. Liu, M. Sawamoto, *Science* **2013**, *341*, 1238149.

[4] M. Gonzalez-Burgos, A. Latorre-Sanchez, J. A. Pomposo, *Chem Soc Rev* **2015**, *44*, 6122-6142.

[5] M. K. Aiertza, I. Odriozola, G. Cabanero, H. J. Grande, I. Loinaz, *Cell Mol Life Sci* **2012**, *69*, 337-346.

[6] O. Altintas, C. Barner-Kowollik, *Macromol Rapid Commun* **2012**, *33*, 958-971.

[7] A. Sanchez-Sanchez, I. Pérez-Baena, J. Pomposo, *Molecules* **2013**, *18*, 3339.

[8] A. Sanchez-Sanchez, J. A. Pomposo, *Particle & Particle Systems Characterization* **2014**, *31*, 11-23.

[9] D. Bradburn, T. Bittinger, *Micelles: Structural Biochemistry, Formation and Functions and Usage*, Nova Science Publishers, Incorporated, **2013**.

[10] L. Li, K. Raghupathi, C. Song, P. Prasad, S. Thayumanavan, *Chem Commun (Camb)* **2014**, *50*, 13417-13432.

[11] M. Huo, N. Wang, T. Fang, M. Sun, Y. Wei, J. Yuan, *Polymer* **2015**, *66*, A11-A21.

[12] M. Artar, E. Huerta, E. W. Meijer, A. R. A. Palmans, **2014**, *1170*, 313-325.

[13] K.-s. Park, D.-y. Kim, S.-k. Choi, D. H. Suh, *Japanese Journal of Applied Physics* **2003**, *42*, 3877-3880.

[14] J. Jiang, S. Thayumanavan, *Macromolecules* **2005**, *38*, 5886-5891.

[15] E. Harth, B. V. Horn, V. Y. Lee, D. S. Germack, C. P. Gonzales, R. D. Miller, C. J. Hawker, *Journal of the American Chemical Society* **2002**, *124*, 8653-8660.

[16] B. Zhu, J. Ma, Z. Li, J. Hou, X. Cheng, G. Qian, P. Liu, A. Hu, *Journal of Materials Chemistry* **2011**, *21*, 2679.

[17] B. Zhu, G. Qian, Y. Xiao, S. Deng, M. Wang, A. Hu, *Journal of Polymer Science Part A: Polymer Chemistry* **2011**, *49*, 5330-5338.

[18] G. Qian, B. Zhu, Y. Wang, S. Deng, A. Hu, *Macromol Rapid Commun* **2012**, *33*, 1393-1398.

[19] B. Zhu, S. Sun, Y. Wang, S. Deng, G. Qian, M. Wang, A. Hu, *J. Mater. Chem. C* **2013**, *1*, 580-586.

[20] A. Sanchez-Sanchez, I. Asenjo-Sanz, L. Buruaga, J. A. Pomposo, *Macromol Rapid Commun* **2012**, *33*, 1262-1267.

[21] X. Jiang, H. Pu, P. Wang, *Polymer* **2011**, *52*, 3597-3602.

[22] G. Li, F. Tao, L. Wang, Y. Li, R. Bai, *Polymer* **2014**, *55*, 3696-3702.

[23] M. González-Burgos, A. Alegría, A. Arbe, J. Colmenero, J. A. Pomposo, *Polym. Chem.* **2016**, *7*, 6570-6574.

[24] A. Sanchez-Sanchez, S. Akbari, A. Etxeberria, A. Arbe, U. Gasser, A. J. Moreno, J. Colmenero, J. A. Pomposo, *ACS Macro Letters* **2013**, *2*, 491-495.

[25] A. Sanchez-Sanchez, S. Akbari, A. J. Moreno, F. L. Verso, A. Arbe, J. Colmenero, J. A. Pomposo, *Macromolecular Rapid Communications* **2013**, *34*, 1681-1686.

[26] A. J. Moreno, F. Lo Verso, A. Sanchez-Sanchez, A. Arbe, J. Colmenero, J. A. Pomposo, *Macromolecules* **2013**, *46*, 9748-9759.

[27] R. J. Wojtecki, M. A. Meador, S. J. Rowan, *Nat Mater* **2011**, *10*, 14-27.

[28] M. Seo, B. J. Beck, J. M. J. Paulusse, C. J. Hawker, S. Y. Kim, *Macromolecules* **2008**, *41*, 6413-6418.

[29] A. Sanchez-Sanchez, A. Arbe, J. Colmenero, J. A. Pomposo, *ACS Macro Letters* **2014**, *3*, 439-443.

[30] T. Terashima, T. Sugita, K. Fukae, M. Sawamoto, *Macromolecules* **2014**, *47*, 589-600.

[31] B. S. Murray, D. A. Fulton, *Macromolecules* **2011**, *44*, 7242-7252.

[32] D. E. Whitaker, C. S. Mahon, D. A. Fulton, *Angew Chem Int Ed Engl* **2013**, *52*, 956-959.

[33] B. T. Tuten, D. Chao, C. K. Lyon, E. B. Berda, *Polymer Chemistry* **2012**, *3*, 3068.

[34] P. G. Frank, B. T. Tuten, A. Prasher, D. Chao, E. B. Berda, *Macromol Rapid Commun* **2014**, *35*, 249-253.

[35] A. Sanchez-Sanchez, D. A. Fulton, J. A. Pomposo, *Chemical Communications* **2014**, *50*, 1871-1874.

[36] S. Mavila, O. Eivgi, I. Berkovich, N. G. Lemcoff, *Chem Rev* **2016**, *116*, 878-961.

[37] A. Sanchez-Sanchez, A. Arbe, J. Kohlbrecher, J. Colmenero, J. A. Pomposo, *Macromolecular Rapid Communications* **2015**, *36*, 1592-1597.

[38] K.-W. Huang, S.-W. Kuo, *Macromolecular Chemistry and Physics* **2012**, *213*, 1509-1519.

CHAPTER 3

Techniques Employed

3.1. Introduction

Characterization techniques have played a fundamental role in the development of this thesis. A large set of techniques has allowed extracting information concerning properties of all the samples investigated in this work. In this chapter, a brief description about the experimental techniques and the conditions used for the characterization of the samples is provided. Special emphasis is made on scattering techniques with a brief background about the magnitudes measured followed by a description about the instrumentation employed in this thesis. Finally, the details about molecular dynamics simulations used in this work are described.

3.2. Scattering Techniques

3.2.1. Introduction

Scattering techniques are specially well suited to realize a significant advance in the understanding of the structural and dynamical properties of SCNPs. Scattering experiments provide spatial resolution through the wavevector dependence of the measured magnitudes. Using different probes (mainly photons and neutrons) and experimental configurations, static and dynamic properties can be explored at molecular level. Particularly useful for the investigation of complex soft materials –like those containing SCNPs– is the application of neutron scattering (NS). Among other advantages of NS like high penetrability, two are of crucial importance: the simultaneous accessibility of the proper length and time scales together with the possibility of changing the scattering contrast at will.

3.2.2. Magnitudes measured by Neutron, X-Ray and Dynamic Light Scattering

Scattering experiments consist of bombarding a given sample with a beam of particles and obtain information about the structure and/or dynamics of the sample constituents by analyzing the particles scattered out into a solid angle $d\Omega$ (see figure 3.1).[1-4] The particles used as probes can be of different nature, being photons and neutrons the most commonly employed ones. The incident particles are characterized by their wavevector $\vec{k}$ which modulus is determined by the wavelength λ, $k = \left|\vec{k}\right| = 2\pi/\lambda$. During a scattering event, the interaction with the sample involves a momentum transfer $\hbar\vec{Q}$ leading to a change from the

incident $\vec{k}$ to the final $\vec{k'}$ wavevector of the probe. Their difference $\vec{Q} = \vec{k'} - \vec{k}$ is called scattering vector. Scattering experiments provide spatial resolution through the Q-dependence of the measured magnitudes (usually we investigate isotropic systems and the relevant magnitude is just the modulus of the scattering vector $Q = |\vec{Q}|$). The spatial scale probed ζ is inversely proportional to the Q-value, $\zeta \sim 2\pi/Q$. This means, tuning the Q-value we can explore different spatial scales, ranging from atomic resolution ($\zeta \sim 1$Å with Q of a few $Å^{-1}$) to experiments matching macromolecular dimensions ($\zeta \sim$ hundreds of nanometers with $Q \sim 10^{-3} Å^{-1}$).

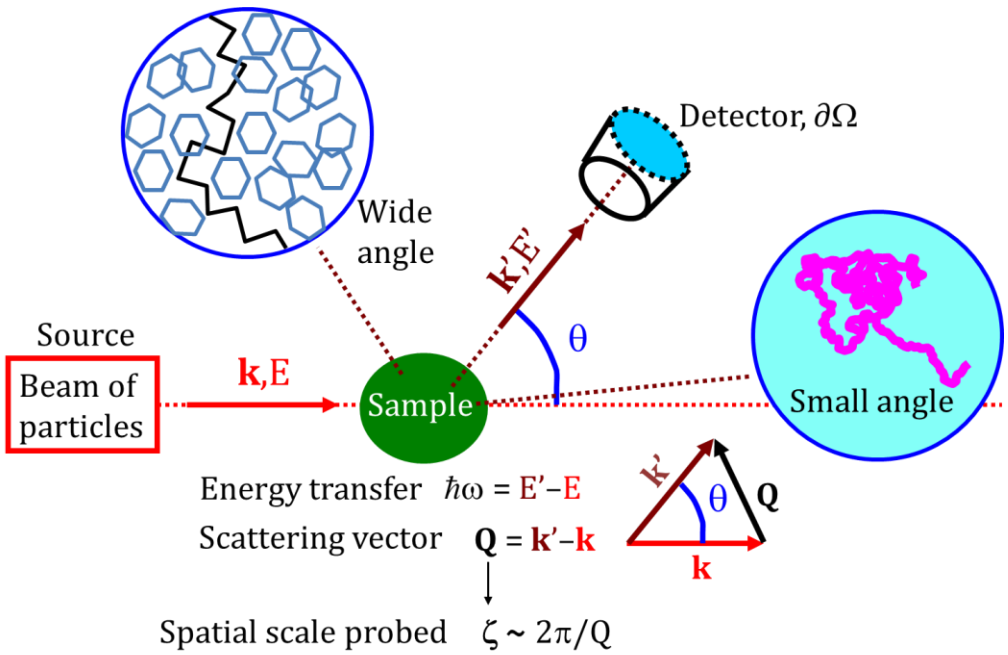

Figure 3.1: Schematic representation of a scattering experiment.

The Q-value investigated in an experimental configuration is determined as $Q = 2\pi \sin(\theta/2)/\lambda$, being θ the scattering angle (see figure 3.1)[1)]. Thus, we can change the explored Q-value by varying the wavelength of the probe and/or the scattering angle. To study big entities, small angle conditions and long wavelengths are appropriate, while wide-angle experiments with particles characterized by $\lambda \sim 1$Å favor the resolution of atomic details. For instance, the use of dynamic light scattering (DLS) is widely spread to get quick information about the dimensions of particles in solution. However, finer structural details on the macromolecular conformations cannot be resolved by photons in the visible spectrum. Thanks to the range of their typical wavelengths, X-Ray (XR) and neutrons constitute ideal probes to decipher the structural features at intra- and inter-molecular length scales (atomic/monomeric level) by wide angle experiments. They are also adequate to determine the macromolecular conformation from the analysis of the intensity scattered at small angles.

If the magnitude measured in the experiment is just the number of the scattered particles into a solid angle comprised between Ω and $\Omega + \mathrm{d}\Omega$ relative to the number of incident particles –the so-called differential scattering cross section $d\sigma/d\Omega$– we deal with a diffraction experiment giving information about structural features of the sample. In more complex –so-called 'quasielastic'– experiments, also the energy E' of the scattered particles is analyzed. Changes with respect to that of the incident particles, E, reflect an energy transfer to the sample, $\hbar\omega = E' - E$. From this kind of measurements, information about the dynamics of the sample can also be extracted. In order to resolve dynamical processes in condensed matter, probes with energies comparable to the typical

[1)] This formula is valid in elastic conditions or for small values of the energy transfer.

excitations (meV) have to be used. This is not the case of XR[2)], but cold and thermal neutrons have kinetic energies in this range. Therefore, even the slow relaxational motions in soft condensed matter can be detected by a velocity change of the neutron. Quasielastic neutron scattering (QENS) experiments exploit this capability, providing a unique tool for the investigation of the molecular dynamics at the proper length/time scales.

First, the more general and complex formulation of the magnitudes involved in a QENS experiment will be presented; taking this as basis, the information accessible by other kinds of scattering experiments will be introduced.

In QENS experiments, the double differential scattering cross section $d^2\sigma/(d\Omega d\hbar\omega)$ is the measured quantity. This is defined as the number of neutrons scattered into a solid angle comprised between Ω and $\Omega + \mathrm{d}\Omega$, which have experienced a change in energy between $\hbar\omega$ and $\hbar\omega + d\hbar\omega$, relative to the number of incident particles. On the one hand, this magnitude depends on the interaction between the atoms in the sample and the probe particles –quantified by the so-called scattering length. The scattering length b_α can be positive, negative or complex. Since neutrons interact with the nucleus, for this probe b_α depends on the isotope considered (α: H, D, C, O, …) and the relative orientation of the neutron-nuclear spin pairs. Table 3.1 shows the mean values of b_α for the isotopes commonly present in soft materials.

[2)] In some synchrotrons the XR-photon correlation spectroscopy technique is available. By means of this technique it is possible to address dynamical processes at large scattering vectors and long times; however, the radiation damage produced by the intense coherent XR beam employed is usually very important in soft materials.

Table 3.1: Values of the average neutron scattering lengths $\bar{b}_\alpha$, their squares $\bar{b}_\alpha^2$ and their deviations $\overline{\Delta b_\alpha^2}$ for different isotopes α

Isotope α	$\bar{b}_\alpha/fm$	$\bar{b}_\alpha^2/fm^2$	$\overline{\Delta b_\alpha^2}/fm^2$
^{1}H	-3.7406	13.992	638.78
^{2}H (D)	6.6710	44.502	16.322
^{12}C	6.6511	44.237	0
^{16}O	5.8030	33.675	0

On the other hand, the double differential scattering cross section is determined by the (time dependent) distribution of scattering centers in the sample. It can be expressed as (see, e. g.,[2]):

$$\frac{\partial^2\sigma}{\partial\Omega\,\partial\hbar\omega} \propto \sum_{\alpha,\beta} \bar{b}_\alpha \bar{b}_\beta S_{coh}^{\alpha\beta}(\vec{Q},\omega) + \sum_{\alpha} \overline{\Delta b_\alpha^2} S_{inc}^{\alpha}(\vec{Q},\omega). \tag{3.1}$$

There, the indexes α and β run over all the possible kinds of isotopes in the sample (α: H, D, C, O, …). In $\partial^2\sigma/\partial\Omega\,\partial\hbar\omega$ we can identify a coherent ('coh') and an incoherent ('inc') contribution. The latter arises from the random distribution of the deviations of the scattering lengths from their mean value, $\overline{\Delta b_\alpha^2} = \overline{b_\alpha^2} - \bar{b}_\alpha^2$. The features ($\vec{Q}$ and ω-dependencies) of both contributions are determined by the corresponding scattering functions [$S_{coh}^{\alpha\beta}(\vec{Q},\omega)$ involving nuclei of kinds α and β, and $S_{inc}^{\alpha}(\vec{Q},\omega)$ involving nuclei of kind α]. The interpretation of these functions is straightforward in terms of the *correlation functions* defined in the van Hove (1954) formalism. These are related, *via* Fourier transformation, with the intermediate scattering functions [$S_{coh}^{\alpha\beta}(\vec{Q},t)$ and $S_{inc}^{\alpha}(\vec{Q},t)$] and the van Hove correlation functions [$G^{\alpha\beta}(\vec{r},t)$ and its self-part $G_{self}^{\alpha}(\vec{r},t)$]:

$$S_{coh(inc)}^{\alpha\beta(\alpha)}(\vec{Q},t) = \hbar \int S_{coh(inc)}^{\alpha\beta(\alpha)}(\vec{Q},\omega)e^{i\omega t}d\omega \tag{3.2}$$

$$G_{self}^{\alpha\beta(\alpha)}(\vec{r},t) = \frac{1}{(2\pi)^3}\int S_{coh(inc)}^{\alpha\beta(\alpha)}(\vec{Q},t)e^{-i\vec{Q}\vec{r}}d\vec{Q} \tag{3.3}$$

In the classical limit, $G^{\alpha\beta}(\vec{r},t)$ can be written as:

$$G^{\alpha\beta}(\vec{r},t) = \langle\frac{1}{N}\sum_{i\alpha,j\beta}^{N_\alpha,N_\beta}\delta\{\vec{r} - [\vec{r}_{i\alpha}(t) - \vec{r}_{j\beta}(0)]\}\rangle \tag{3.4}$$

Here $\vec{r}_{i\alpha}(t)$ $[\vec{r}_{j\beta}(0)]$ is the position of the vector i^{th} atom of kind α [j^{th} atom of kind β] at time = t [time = 0] and the sum runs over all the different atoms of kinds α and β [$N_\alpha(N_\beta)$: total number of atoms of kind $\alpha(\beta)$; $N = \sum_\alpha N_\alpha$]. Thus, $G^{\alpha\beta}(\vec{r},t)d\vec{r}$ is the probability that, given a particle of kind β at the origin at time $t = 0$, any particle of kind α is in the volume $d\vec{r}$ at position $\vec{r}$ at time t. It can easily be seen that in the static case $G^{\alpha\beta}(\vec{r},t=0) = \delta_{\alpha\beta}(\vec{r}) + g^{\alpha\beta}(\vec{r})$, where $g^{\alpha\beta}(\vec{r})$ is the static pair distribution function. Note that in diffraction experiments, scattered particles are counted irrespectively of their energy. This is equivalent to perform an integral over the ω-variable, i. e., it corresponds to the static $t = 0$ limit. Thus, the accessed magnitude in a diffraction experiment is the sum of the partial structure factors weighed by the corresponding scattering lengths products. On the other hand, the self-part of the van Hove correlation function $G_{self}^{\alpha}(\vec{r},t)$ is obtained by restricting the correlations considered in Eq. 3.4 to those relating the positions of a single particle of kind α at different times:

$$G_{self}^{\alpha}(\vec{r},t) = \langle \frac{1}{N} \sum_{i\alpha}^{N_\alpha} \delta\{\vec{r} - [\vec{r}_{i\alpha}(t) - \vec{r}_{i\alpha}(0)]\}\rangle \tag{3.5}$$

$G_{self}^{\alpha}(\vec{r},t)$ is the Fourier transform of $S_{inc}^{\alpha}(\vec{Q},t)$ in space: incoherent scattering relates to single-particle motions. Equation 3.1 can thus finally be written as:

$$\begin{aligned}\frac{\partial^2\sigma}{\partial\Omega\,\partial\hbar\omega} \propto \sum_{\alpha,\beta} \bar{b}_\alpha \bar{b}_\beta \int e^{i\omega t} \langle \sum_{i\alpha,i\beta} e^{-i\vec{Q}[\vec{r}_{i\alpha}(t) - \vec{r}_{j\beta}(0)]}\rangle\, dt + \\ + \sum_{\alpha} \overline{\Delta b_\alpha^2} \int e^{i\omega t} \langle \sum_{i\alpha} e^{-i\vec{Q}[\vec{r}_{i\alpha}(t) - \vec{r}_{i\alpha}(0)]}\rangle\, dt\end{aligned} \tag{3.6}$$

Equation 3.1 (equivalently, 3.6) shows that the weights of the coherent and incoherent contributions to the scattered intensity are determined by the scattering lengths of the isotopes involved. From table 3.1 it is clear that:

- Due to the large value of $\overline{\Delta b_H^2}$, in hydrogen-containing systems the signal is dominated by the incoherent scattering from hydrogens, revealing their self-motions.
- Substituting H by D this incoherent contribution is drastically reduced and differently weighted coherent contributions are obtained.
- The intensity scattered by fully deuterated samples is mainly coherent and, since $\bar{b}_D \approx \bar{b}_C$, all pair correlations are almost equally weighted.
- There is a very large difference in the average scattering length values of H and D ($\bar{b}_D = 6.67\ fm$ vs $\bar{b}_H = -3.74\ fm$). As it will be shown next, this provides a unique tool for investigating soft materials by NS: deuterium

labeling. It results in a marked difference in scattering power (contrast) between molecules synthesized from normal (protonated) and deuterated units. Thus, deuterium labeling techniques can be exploited to 'stain' molecules and make them 'visible' not only in dilute solutions, but also in crowded environments, such as concentrated solutions of overlapping chains and even in the condensed state.

Many polymer problems depend on the structure and dynamics at mesoscopic scales. Considering only scattering at small Q-values, the detailed atomic arrangements within e. g. a monomer or a solvent molecule may be neglected and a coarse-grained description in terms of the scattering length density (SLD) is adequate. The scattering length densities ρ_M and ρ_S of such scattering units ('monomer' and 'solvent') are defined as

$$\rho_M = \frac{1}{v_M}\sum_j \bar{b}_j^M \; ; \; \rho_S = \frac{1}{v_S}\sum_j \bar{b}_j^S \tag{3.7}$$

where the summation includes the coherent scattering length of all atoms within a monomer or a solvent molecule; v_M and v_S are the respective molecular volumes. The scattering contrast in scattering experiments arises from the different scattering length densities of the molecules. The coherent cross section of a system of uniform SLD is zero. However, fluctuations may be introduced by means of isotopic substitution, thus giving rise to a finite scattering cross section. The contrast scattering length density is defined as:

$$\Delta\rho = (\rho_M - \rho_S) \tag{3.8}$$

This contrast can be highly enhanced for NS if one of the two scattering units ('monomer' or 'solvent') is deuterated and the other is protonated. Note that the same applies if we consider as 'solvent' molecules other monomers from different chains in a melt.

For non-interacting, incompressible polymer systems the dynamic structure factors of Eq. 3.1 may be significantly simplified for small-angle scattering conditions. The sums, which in the previous formulation (see Eq. 3.6) have to be carried out over all atoms in the sample, can be restricted to only one average macromolecule yielding the so-called single chain dynamic structure factor. This function shall be denoted as $S_{chain}(Q,t)$ [$S_{chain}(Q,\omega)$ in the frequency domain]. Under these assumptions, the normalized macroscopic coherent cross section (scattering per volume unit) can be expressed as:

$$\frac{d\sum}{d\sigma d\omega} = \phi\Delta\rho^2 V^2 S_{chain}(Q,\omega) \tag{3.9}$$

with ϕ the volume fraction of the labeled polymer and V the volume of the macromolecule. In a diffraction experiment at small angles (SANS) experiment, the static counterpart of Eq. 3.9 is accessed. Thus, with these conditions, SANS on diluted solutions of labeled macromolecules reveals the macromolecular form factor $S_{chain}(Q,t=0) = S_{chain}(Q)$ [note that the form factor is also usually denoted as $P(Q)$] which contains information about the static intra-molecular correlations. It is noteworthy that, as the coherent term represents the interference of scattered waves at different nuclei, in concentrated solutions of labeled macromolecular 'objects' the interference of scattering from different 'objects' is also reflected in the recorded intensity through the structure factor of

their centers of mass $S_{CM}(Q)$. For a monodisperse collection of spherically symmetric particles (a possible simplified model for e. g. a SCNPs solution), the coherent scattering cross section can then be written as:

$$\left(\frac{d\sum(Q)}{d\Omega}\right)_{coh} = \phi\Delta\rho^2V^2P(Q)S_{CM}(Q) \tag{3.10}$$

where $P(Q)$ is the form factor of the particles.

Furthermore, contrast variation methods can be used to remove a component of the scattered intensity by matching its scattering power with that of the medium in which it is dispersed and thus removing the fluctuations in SLD which give rise to the scattering. The procedure consists of adjusting the average SLD of molecules (summed over protonated and deuterated species) until it matches the SLD of the other component (see, e. g.,[5-9]).

As above mentioned, quasielastic experiments are not possible with XRs due to high values of their typical energies ($\approx keV$ for $\lambda \approx 1$Å). Conversely, XRs interact primarily with the electrons and therefore the strength of interaction of XRs with an atom depends on the number of electrons it contains. Thus, the equivalent to the above introduced scattering length b_α for neutron-nucleus interaction is the product of the XR scattering length b_e of a single electron with the atomic scattering factor $f(Q)$ of the atom concerned. The atomic scattering factor increases linearly with atomic number and decreases with increasing Q. This is because the range of atomic electron clouds is comparable to the XR wavelength, and as a result rays scattered from different parts of the atom

experience a phase difference that increases with increasing scattering angle. The intensity recorded in a wide-angle XR scattering (WAXS) experiment thus reveals, in analogy to the neutron scattering diffraction experiments, the sum of the partial structure factors involving pairs of atoms weighed by the corresponding XR-atomic form factor products (that now are Q-dependent). Small-angle XR scattering (SAXS) experiments on the other hand are also sensitive to inhomogeneities in the scattering power; this time the contrast is due to differences in the electronic density. Isotopic labeling is thus not useful with SAXS techniques. However, choosing the proper solvents, macromolecular solutions might be susceptible to be investigated by this technique, provided that enough contrast is achieved between solute and solvent molecules.

Dynamic light scattering (DLS) experiments are very useful to determine macromolecular sizes. This technique probes the relaxation of concentration fluctuations on mesoscopic time and length scales (the typical wavelengths are in the hundreds of nanometers range). The contrast is provided by the refractive index increment $\delta n/\delta c$. In a homodyne experiment, the measured intensity autocorrelation function is given by

$$\frac{\langle I(Q,O)I(Q,t)\rangle}{\langle I\rangle^2} = 1 + f_c\left[\frac{S(Q,t)}{S(Q,0)}\right]^2 \tag{3.11}$$

with f_c an experimental factor and $S(Q,t)$ the Fourier transform of the density correlation function of the scattering medium:

$$S(Q,t) = \frac{\int_V [\rho(0,0)\rho(\vec{r},t)]e^{i\vec{Q}\vec{r}}d^3\vec{r}}{\langle\rho\rangle} \quad (3.12)$$

Here $\rho(\vec{r},t)$ is the local density at position $\vec{r}$ at time t in the sample. The scattering vector Q for light scattering is given by $Q = 4\pi n_d \sin(\theta/2)/\lambda_0$, with λ_0 the wavelength in vacuum and n_d the refractive index.

3.2.3. Sources and Instrumentation

Neutron scattering experiments are realized in large facilities including a neutron source (either a nuclear reactor –providing a continuous flux– or a spallation –pulsed– source) and dedicated instrumentation. Visiting http://neutronsources.org/ information about the available and future neutron facilities worldwide can be found.

XR instruments may be either laboratory instruments based on an irradiated anode source, or located at synchrotron facilities. DLS experiments are very spread since laboratory instruments are commercially available at usually affordable prices.

In this thesis, small angle (SANS and SAXS) techniques were applied to decipher structural details of SCNPs in solution, while neutron spin echo (NSE) experiments were performed to investigate their dynamical features. Complementary DLS measurements were also performed. This technique was in fact also used routinely to determine the size (hydrodynamic radius) of the linear precursors and the single-chain nanoparticles obtained through the different synthesis routes.

A. Small-Angle Instrumentation

A typical (basic) design of a small-angle diffractometer is shown in figure 3.2. The position of the detector can usually be shifted back and forth such that different sample-detector distances can be chosen, changing thereby the Q-range explored with a given value of the incident wavelength.

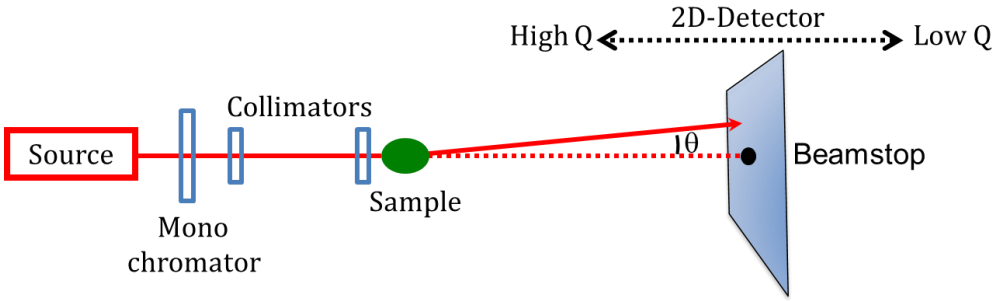

Figure 3.2: Illustration of small angle scattering

In this thesis, small-angle neutron scattering (SANS) experiments where performed on the instrument KWS-2[10] at the Forschungs-Neutronenquelle Heinz Maier-Leibnitz in Garching.[11] KWS-2[12] represents a classical pinhole SANS instrument where, combining the pinhole mode using different neutron wavelengths and detection distances with the focusing mode using MgF_2 lenses, a wide Q-range between 1 x 10^{-4} and 0.5 $Å^{-1}$ can be explored.

The instrument is dedicated to high intensity/wide-Q investigation of mesoscopic structures and structural changes due to rapid kinetic processes in soft condensed matter, chemistry, and biology.[13]

The high neutron flux, comparable with that of the world leading SANS instruments, which is supplied by the neutron delivery system (cold source, selector, guides)[14-15], and the possibility to use large sample area using focussing lenses, enable high intensity and time-resolved studies.

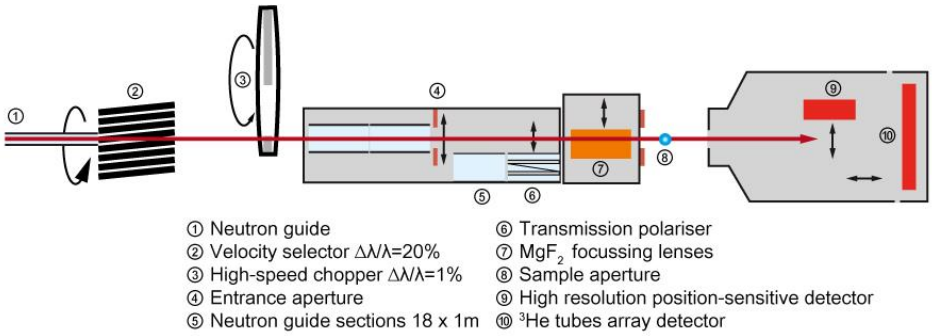

Figure 3.3: Illustration of the KWS-2 small angle neutron scattering difractometer

In the SANS experiments performed in this thesis a Q-range between 0.003 and 0.35 Å^{-1} was covered, with $\lambda = 5.27$ Å^{-1} and using three sample-detector distances (SSD): 1.15, 5.76 and 19.76 m. The solutions were filled in 2mm thick Hellma Quarz cells.

Small-angle X-ray (SAXS) experiments on the assembly of reversible SCNPs were conducted on the Rigaku 3-pinhole PSAXS-L equipment at the Centro de Física de Materiales in San Sebastian. The MicroMax-002+ X-Ray Generator System consists of a microfocus sealed tube source module and an integrated X-Ray generator unit, which produces $Cu - K_\alpha$ transition photons of wavelength $\lambda =$ 1.54 Å. Flight path and sample chamber are under vacuum. The scattered X-Rays are detected on a two-dimensional multiwire X-Ray Detector (Gabriel

design, 2D-200X). This gas-filled proportional type detector offers a 200 mm diameter active area with c.a. 200 mm resolution. SCNPs solutions in THF or DMF were filling capillaries of 2 mm thickness, with a SSD of 2 m. The Q-range covered was $0.01 \leq Q \leq 0.2$ Å^{-1}.

All small angle scattering (SAS) experiments were carried out in transmission geometry and at room temperature. After usual calibration of intensities by comparison with standard scatterers and background corrections, the 2D-results were azimuthally integrated, providing finally the scattered intensity as function of wavevector.

B. Neutron Spin Echo

Neutron Spin Echo (NSE) is a neutron spectroscopic technique sensitive to QENS signal. The fundamentals of NSE consist of coding for each neutron individually the energy transfer in the scattering process into its spin rotation.[16] Applying precession magnetic fields before and after the scattering event, the polarization of the neutron depends only on the velocity difference of each neutron individually, irrespective of its initial velocity. This technique is unique since it delivers the information directly in the time domain, allowing for a deconvolution of the experimental results from resolution effects by simple division. The time is proportional to $J\ x\ \lambda^3$, where J is the field integral. For a given wavelength, the Fourier time range is limited to short times (typically 2 ps) by spin depolarization due to vanishing guide field and to long times by the maximum achievable field integral. Also, the measuring procedure strongly suppresses incoherent contributions. Actually, the magnitude measured in a NSE experiment is a normalized function:[16]

$$\tilde{S}_{NSE}(Q,t) = \frac{I_{coh}\tilde{S}_{coh}(Q,t) - \frac{1}{3}I_{inc}\tilde{S}_{inc}(Q,t)}{I_{coh} - \frac{1}{3}I_{inc}} \tag{3.13}$$

where $\tilde{S}_{coh}(Q,t)$ and $\tilde{S}_{inc}(Q,t)$ are the normalized intermediate pair and self correlation functions (they are normalized to their value at $t = 0$). I_{coh} and I_{inc} denote the total ('static') coherent and incoherent intensities. The suppression of the incoherent signal can be advantageous for many soft matter questions, where the dynamic structure factor or the single chain dynamic structure factor are on the focus.[16] For details of experimental setup involved in this kind of instruments, the reader might be directed to Ref.[5, 16]

In this thesis, neutron spin echo (NSE) experiments were performed at 300 K by the J-NSE instrument[17] at the Forschungs-Neutronenquelle Heinz Maier-Leibnitz in Garching. Using two wavelengths (8 and 12 Å), Fourier times in the range $0.1 \leq t \leq 140\,ns$ were covered for Q-values in the range: $0.03 \leq Q \leq 0.2$ Å^{-1}.

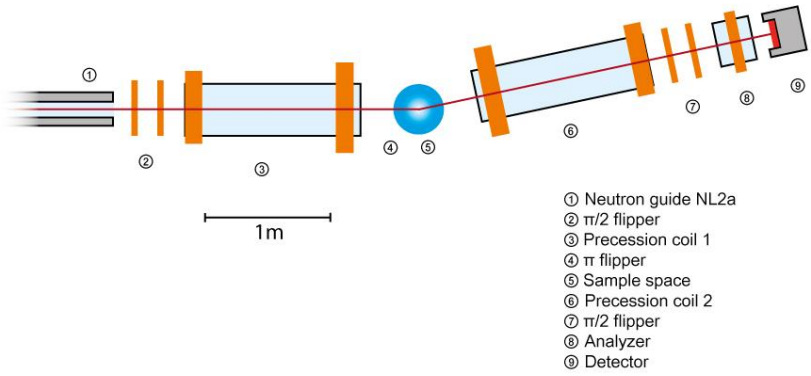

Figure 3.4: Illustration of the J-NSE neutron spin echo spectrometer

Samples (solutions of either the protonated precursors or the protonated SCNPs in deuterated solvent) were placed in Hellma cuvettes of 4 mm thickness. In the explored Q-range, the scattered intensity is completely dominated by the coherent contribution of the macromolecular dynamic structure factor.

C. Dynamic Light Scattering

Dynamic light scattering (DLS) experiments were performed on a Malvern Zetasizer Nano ZS apparatus at 298 K. In this thesis, solutions of polymer precursors and SCNPs in different solvents (dDMF, THF and H_2O) were investigated. At the experimental conditions employed ($\theta = 173º, \lambda_0 = 633\ nm$), the Q-value explored was $0.00284\ Å^{-1}$ for dDMF $[n_d(dDMF) = 1.431]$, $Q = 0.00208\ Å^{-1}$ for THF $[n_d(THF) = 1.409]$ and $Q = 0.00264\ Å^{-1}$ for water $[n_d(H_2O) = 1.330]$.

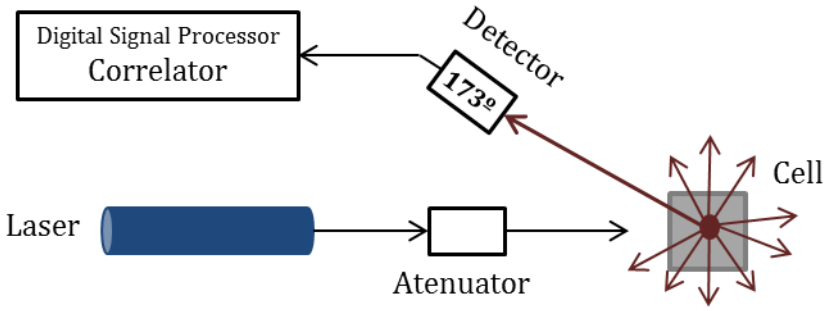

Figure 3.5: Illustration of Zetasizer Nano ZS apparatus operation

3.3. Other Experimental Techniques

3.3.1. Size Exclusion Chromatography (SEC)

Size exclusion chromatography has become an essential tool in polymer science. It is a standard technique for determining molar mass averages and molar mass distributions of polymers. The principle of SEC is the separation of molecules based strictly on their hydrodynamic radius (R_H) or volume (V_H), rather than their molecular weight. Due to limited accessibility of the pore volume within the particles of the column packing, polymer molecules are separated according to their hydrodynamic volumes, with a faster elution corresponding to the larger molecules and the last elution corresponding to the smaller ones, due to these smaller molecules can enter into the pores.[18] Figure 3.6 illustrates the mechanism of SEC separation.

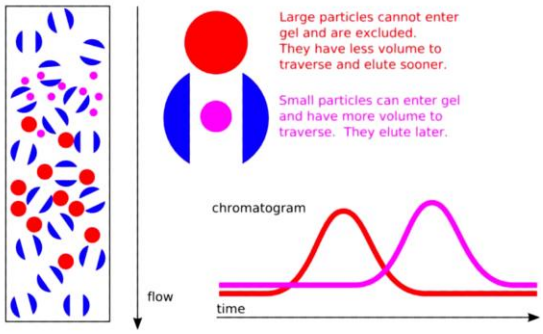

Figure 3.6: Schematic illustration of the principle of SEC.

In a SEC process, the mobile phase (solvent), known as liquid carrier, is continuously flowing through the system. When the sample elutes from the column, it passes through a series of detectors and the output is often analyzed

by a SEC software package on the computer. In this thesis, SEC with triple detection was used to determine the molecular weight and polydispersity index of polymer precursors and the corresponding SCNPs and to follow the evolution of the intra-chain collapse process. Depending on the nature of the polymer, the measurements were performed in different SEC devices.

For water-soluble polymers, SEC measurements were performed at 30 ℃ on a triple-detection Agilent PL-GPC 50 system -with Agilent light scattering, refractive index and viscosimetry detectors- equipped with PL aquagel-OH Guard (8μm) and PL aquagel-OH MIXED-H (8μm) columns. Data analysis was performed with the Agilent GPC/SEC software. Deionized water (filtered to 0.2μm) was used as eluent at a flow rate of 1 ml/min.

For other polymers, SEC measurements were performed at 30 ℃ on an Agilent 1200 system equipped with PLgel 5μm Guard and PLgel 5μm MIXED-C columns, a differential refractive index (DRI) detector (Optilab Rex, Wyatt), a multi-angle laser light scattering (MALLS) detector (MiniDawn Treos, Wyatt) and a viscosimetric (VI) detector (ViscoStar-II, Wyatt). THF was used as eluent at a flow rate of 1 ml/min. Data analysis was performed with ASTRA Software (version 6.1) from Wyatt.

3.3.2. Nuclear Magnetic Resonance (NMR) Spectroscopy

Nuclear magnetic resonance (NMR) spectroscopy is one of the most powerful and widely used techniques in chemical research for investigating structures and dynamics of molecules. The method is based on spectral lines of different atomic nuclei that are excited when a strong magnetic field and a radiofrequency

transmitter are applied.[19] The nuclei of some atoms have an overall spin with a number of possible orientations with equal energy levels. When placed in a magnetic field, NMR active nuclei (such as ^{1}H or ^{13}C) exhibit energy splitting, therefore, the energy difference between the possible orientations appears. Absorption of electromagnetic radiation from the radiofrequency source by the atoms/molecules placed in external magnetic field induces energy transfer from the lower energy (preferred spin orientation) to higher energy orientation. When the spin returns to its preferred orientation (basic level), energy at the same frequency level is released, which when measured and processed yields an NMR spectrum for the nucleus concerned.[20]

^{1}H-NMR spectra together with ^{13}C-NMR spectra were used to characterize the structure of the polymer precursors as well as to identify changes in the structure upon SCNPs formation. Moreover, ^{1}H-NMR spectra was used to calculate the composition of the copolymers and to obtain the cross-linking degree of SCNPs. ^{1}H-NMR and ^{13}C-NMR spectra were recorded at room temperature on Bruker spectrometers operating at 500.13 MHz for hydrogen nuclei and 125.06 MHz for carbon nuclei, using $CDCl_3$ as solvent in all cases.

3.3.3. Fourier Transform Infrared Spectroscopy (FTIR)

Fourier transform infrared spectroscopy (FTIR) is a very important technique to qualitatively identify organic materials and to determine the molecular structure. A FITR spectrometer simultaneously collects high spectral resolution data over a wide spectral range. This technique is based on the absorption of the electromagnetic radiation by the molecules at specific frequencies (resonant

frequencies) that are characteristic of their structure. Thus, the frequency of the vibrations can be associated with a particular bond type.[21]

FTIR was employed as a complementary technique to NMR, analyzing the disappearance (and appearance) of specific bonds after the intra-chain folding/collapse process on SCNPs formation and the formation of network cross-linked materials. FTIR spectra were recorded at room temperature on a JASCO 3600 FTIR spectrometer. Attenuated total reflection spectra were obtained by using 50 scans with 4 cm^{-1} resolution.

3.3.4. Thermogravimetric Analysis (TGA)

Thermogravimetric analysis (TGA) is an analytical technique used to determine the material's thermal stability and the fraction of volatile components by monitoring the weight change that occurs as a specimen is heated.[22] In these experiments, the sample weight is recorded as a function of the temperature in air or in an inert atmosphere, such as helium or argon.

In this thesis, TGA measurements were used to observe the decomposition temperature of the azide groups present in polymer precursors, as well as to compare the thermal stability of SCNPs with their parent precursors. These measurements were performed in a Q500-TA Instruments apparatus at a heating rate of 10 °C/min under nitrogen atmosphere from room temperature to 700 °C.

3.3.5. Differential Scanning Calorimetry (DSC)

The differential scanning calorimetry (DSC) is a technique that measures the difference in the amount of heat required to increase the temperature of a sample and an inert reference as a function of the temperature.[23] The heat flow difference is related to the temperature changes of the sample, which might indicate both physical phase transitions and/or chemical reactions. The temperature of both the sample and the reference are increased at a constant rate. The basic principle underlying this technique is that when the sample undergoes a physical transformation such as phase transitions, more or less heat will need to flow to it than the reference to maintain both at the same temperature.[24]

Through this technique, the glass transition temperatures of the polymer precursors and SCNPs were obtained. Measurements were carried out on ~ 5 mg specimens using a Q2000 TA Instruments in standard mode. A helium flow rate of 25 ml/min was used throughout. Measurements were performed by placing the samples in sealed aluminum pans, heating to 130 °C (SCNPs to 150 °C) at 10 °C/min, then cooling to 0 °C at 10 °C/min, and heating back to 130 °C (SCNPs to 150 °C) at 10 °C/min.

3.3.6. Broadband Dielectric Spectroscopy (BDS)

Dielectric spectroscopy is a technique mainly used to study the relaxation processes caused by the rotational fluctuations of molecular dipoles. The study of the interaction of electromagnetic waves with matter in the frequency regime between 10^{-6} and 10^{12} Hz is the core of broadband dielectric spectroscopy (BDS).

The basis of dielectric relaxation spectroscopy as a tool to investigate molecular dynamics is the 'Fluctuation-Dissipation Theorem', which states that the response of a system in thermodynamic equilibrium to a small applied disturbance (linear regime) is the same as its response to a spontaneous fluctuation.[25-26]

When materials containing permanent dipoles (with spontaneous fluctuation and randomly oriented due to thermal fluctuations) are placed in an alternating (sinusoidal) external electric field, the latter distorts the arrangement of molecular dipoles which tend to be preferentially oriented in the direction of the field.[25] The dipolar orientation depends on the frequency of the applied field, and it is related to the dielectric permittivity (ε). This parameter characterizes the dielectric properties of materials containing polar molecules, and it can be interpreted as a measure (on neglecting atomic and electronic polarization) of the number of molecules oriented by an external electric field of unit strength. Dielectric permittivity is usually written as function of the frequency in the complex form:[25]

$$\varepsilon^*(\omega) = \varepsilon'(\omega) - i\varepsilon''(\omega) \tag{3.14}$$

where ε^* is the complex dielectric permittivity, and ε' and ε'' the real and the imaginary parts, respectively, being $\omega = 2\pi f$.

In this thesis, a broadband dielectric spectrometer, Novocontrol Alpha, was used to measure the complex dielectric function covering a frequency range of f = 10^{-1} – 10^{6} Hz. The sample capacitor preparation for this setup consisted in an upper

gold-coated electrode of 15 mm placed on a prepared film of the sample over a 20 mm gold-coated electrode. A separation of 100 μm between both electrodes was maintained by using a Teflon spacer of small area. The sample cell was set in a cryostat, and its temperature was controlled via nitrogen gas jet stream coupled with the Novocontrol Quatro controller.

The isothermal dielectric experiments of SCNPs were performed while cooling the sample from 147 °C to -143 °C in steps of 10 °C. The data reproducibility was checked during subsequent heating from -143 °C to 147 °C. The maximum temperature for the precursor was set at 127 °C to avoid degradation. The films were prepared by solvent casting and dried at 120 °C under dynamic vacuum for 48 h, in order to remove any trace of moisture and / or solvent residues.

3.3.7. Ultraviolet-Visible (UV-Vis) Spectroscopy

Ultraviolet-visible (UV-Vis) spectroscopy refers to absorption spectroscopy or reflectance spectroscopy in the ultraviolet-visible spectral region. This means it uses light in the visible and adjacent (near-UV and near-infrared [NIR]) ranges. The absorption or reflectance in the visible range directly affects the perceived color of the chemicals involved. In this region of the electromagnetic spectrum, atoms and molecules undergo electronic transitions.[27]

UV-Vis spectroscopy is routinely used in analytical chemistry for the quantitative determination of different analytes, such as transition metal ions, highly conjugated organic compounds, and biological macromolecules. It measures the intensity of light passing through a sample (I) and compares it to the intensity of light before it passes through the sample (I_0). The ratio (I/I_0) is called the

transmittance (*T*) and is usually expressed as a percentage. The absorbance (*A*) is based on the transmittance: $A = -\log(T)$.

In this thesis, UV-Vis spectroscopy was employed to follow the release of the drug cisplatin from SCNPs. The measurements were carried out at 25 °C in an Agilent 8453A apparatus with a Peltier thermostatic cell holder, T-controller 89090A.

3.3.8. Microwave-Assisted Synthesis

Microwave synthesis creates new possibilities in performing chemical reactions. Because microwaves can transfer energy directly to the reactive species, so-called "molecular heating", they can promote transformations that are currently not possible using conventional heat.[28] A microwave is a form of electromagnetic energy that falls at the lower frequency end of the electromagnetic spectrum, and is defined in the 300 to about 300000 MHz frequency range. Within this region of electromagnetic energy, only molecular rotation is affected, not molecular structure.[28-29]

Microwave energy consists of an electric field and a magnetic field, though only the electric field transfers energy to heat a substance.[29] Microwave heating, as shown in figure 3.7(a), is a process where the microwaves couple directly with the molecules that are present in the reaction mixture, leading to a rapid rise in temperature. Because the process is not dependent upon the thermal conductivity of the vessel materials, the result is an instantaneous localized superheating of anything that will react to either dipole rotation or ionic

conduction, the two fundamentals mechanism for transferring energy from microwaves to the substance being heated.[28]

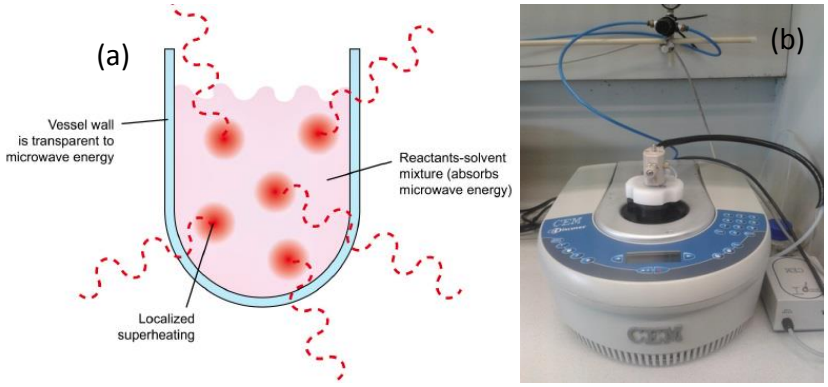

Figure 3.7: Schematic illustration of sample heating by microwaves (a) and microwave set-up employed in this work (b).

In this thesis, microwave-assisted synthesis was employed to obtain single-chain nanoparticles *via* intra-chain folding/collapse of azide containing copolymer precursors. All the reactions were performed in a CEM Discover LabMate™ apparatus, equipped with an 80 ml Sealed Vessel Accessory, which has a working volume ranging from 15 ml to 50 ml [figure 3.7(b)]. The reactions were carried out in N-N-Dimethylformamide (DMF) or N-methyl-2-pyrrolidone (NMP) at 200 °C for 30 min (300 W, 150 psi).

3.3.9. Ultrasound Irradiation

Ultrasonic degradation is claimed to be a non-random process, with cleavage taking place roughly at the center of the molecule and with degrading rate faster with larger molecule.[30] The chemical effects of ultrasound do not come from a direct interaction of the ultrasonic sound wave with the molecules in the

solution. The simplest explanation for this is that sound waves propagating through a liquid at ultrasonic frequencies do so with a wavelength that is significantly longer than that of the bond length between atoms in the molecule. Therefore, the sound wave cannot affect that vibrational energy of the bond, and can therefore not directly increase the internal energy of a molecule.[31] Instead, sonochemistry arises from acoustic cavitation: the formation, growth, and implosive collapse of bubbles in a liquid.[32]

Ultrasound irradiation experiments were performed by using VC505 VibraCell ultrasonic processor, equipped with a 1/2'' tapered microtip. The sonicator is capable of delivering 500 watts at a frequency of 20 kHz and the amplitude can be varied between 10% and 40%. The SCNPs solution in water was contained in a 30 ml flask submerged in an ice bath, in order to avoid an increase in the temperature due to the ultrasound irradiation. The irradiation was carried out at 30% of amplitude with an irradiation pulse of 10 seconds ON / 5 second OFF, until the ON irradiation time was 45 min. During the process, 2 ml of reaction mixture were withdrawn at certain irradiation times for further analysis by SEC and DLS. The same procedure was followed for precursors.

3.4. Molecular Dynamics Simulations

Understanding the behavior of complex systems such as the single-chain nanoparticles (SCNPs) is sometimes difficult through direct analysis of the experimental data and intuition. Fortunately, the advances in computing allow using theoretical models that provide further insight. In particular, molecular dynamics (MD) simulations are well suited to obtain valuable information about these complex systems.

MD-simulations were carried out to obtain information about the internal structure of metallo-folded SCNPs described in chapter 5. A simple bead-spring model[33] with implicit solvent was used for the precursor. This consisted of a linear backbone of 400 beads, with an attached side group per backbone bead. Reactive and unreactive side groups contained one and three beads respectively. The number of reactive groups was 100 (i.e., 25 %) and they were randomly distributed along the chain contour. Qualitatively, a bead represents a segment containing about 5 'big' atoms (C,O,N...) and their bonded hydrogens, with a bead diameter $\sigma \sim$5-10 Å.[33] Therefore the selected lengths for the reactive and unreactive side groups are qualitatively consistent with the lengths of the AEMA and OEGMA groups, respectively. The selected length of the backbone in the simulated bead-spring model is also qualitatively consistent with the molecular weights of the experimental samples.

The standard FENE potential[33] was used to model bonding between connected beads,

$$V_{FENE}(r) = -15\varepsilon R_0^2 \ln[1 - (r/R_0\sigma)^2], \tag{3.15}$$

with $R_0 = 1.5$. The non-bonded interactions between any two beads were modeled by the following potential:[34]

$$V_{nb}(r)\begin{cases} V_{rep} = 4\varepsilon[(\sigma/r)^{12} - (\sigma/r)^6 + 1/4] - \epsilon\sigma & r \le 2^{1/6}\sigma \\ V_{att} = (\phi\epsilon/2)[\cos(\alpha(r/\sigma)^2 + \beta) - 1] & 2^{1/6}\sigma < r \le 1.5\sigma \\ 0 & r > 1.5\sigma \end{cases} \tag{3.16}$$

By using $\alpha = \pi\left(2.25 - 2^{1/3}\right)^{-1}$ and $\beta = 2\pi - 2.25\alpha$ the potential and forces are continuous at every distance r. We used reduced units $\varepsilon = \sigma = 1$ for the energy and length scales. The term V_{rep} is a purely repulsive interaction representing excluded volume interactions. The combined contribution of V_{FENE} and V_{rep} guarantees uncrossability of the bonds.[33] The term V_{att} is an attractive tail that can be tuned by changing the depth ϕ.[34]

For simulating good solvent conditions (THF-like, protocol I) we only considered the exclude volume interactions and switched off the attractive tail ($\phi = 0$) for all beads. To simulate selective solvent conditions (water-like, protocol II), we assigned solvophobic character to the beads of both the backbone and the reactive side groups (denoted as A-beads) and kept the solvophilic character for the unreactive side groups (denoted as B-beads). For this purpose we switched on the attractive tail for the A-A interactions ($\phi = 2$) and kept pure excluded volume ($\phi = 0$) for the A-B and B-B interactions. The used amphiphilic structure mimics that of the poly(OEGMA-co-AEMA) copolymers, which consist of an

hydrophobic PMMA-backbone, hydrophobic reactive AEMA groups and hydrophilic unreactive OEGMA groups.

All simulations were performed under Langevin dynamics[35] at temperature $T = 1$. The precursors were first equilibrated in good (protocol I) or selective solvent (protocol II). In both protocols the irreversible cross-linking of the reactive groups was performed following the procedure described in e.g., Ref.[35], with a single bonding event allowed for each reactive group. The SCNPs obtained by both protocols were re-equilibrated in good solvent ($\phi = 0$ for all beads) and finally acquisition runs were carried out for computing observables of interest. Several hundreds of independent SCNPs were simulated for statistical averages.

3.5. References

[1] T. Springer, in *Springer Tracts in Modern Physics, Volume 64*, Springer Berlin Heidelberg, Berlin, Heidelberg, **1972**, pp. 1-100.

[2] S. W. Lovesey, *Theory of Neutron Scattering from Condensed Matter*, Clarendon Press, Oxford, **1984**.

[3] M. Bée, *Quasielastic Neutron Scattering*, Adam Hilger, Bristol, **1988**.

[4] G. L. Squires, *Introduction to the Theory of Thermal Neutron Scattering*, Dover Publication Inc., New York, **1996**.

[5] J. S. Higgins, H. C. Benoit, *Polymers and Neutron Scattering*, Oxford University Press, Oxford, **1997**.

[6] R. J. Roe, *Methods of X-Ray and Neutron Scattering in Polymer Science*, Oxford University Press, New York, **2000**.

[7] G. D. Wignall, Y. B. Melnichenko, *Reports on Progress in Physics* **2005**, *68*, 1761-1810.

[8] B. Gabrys, *Applications of Neutron Scattering to Soft Condensed Matter*, Gordon and Breach Science Publishers, Amsterdam, **2000**.

[9] P. Lindner, T. Zemb, *Neutrons, X-rays and Light: Scattering Methods Applied to Soft Condensed Matter*, North-Holland Delta Series, Elsevier, **2002**.

[10] A. Radulescu, N. K. Szekely, M.-S. Appavou, *Journal of large-scale research facilities JLSRF* **2015**, *1*.

[11] http://www.mlz-garching.de/englisch.

[12] A. Radulescu, V. Pipich, H. Frielinghaus, M. S. Appavou, *Journal of Physics: Conference Series* **2012**, *351*, 012026.

[13] A. Radulescu, N. K. Szekely, M. S. Appavou, V. Pipich, T. Kohnke, V. Ossovyi, S. Staringer, G. J. Schneider, M. Amann, B. Zhang-Haagen, G. Brandl, M. Drochner, R. Engels, R. Hanslik, G. Kemmerling, *J Vis Exp* **2016**.

[14] A. Radulescu, A. Ioffe, *Nuclear Instruments and Methods in Physics Research Section A: Accelerators, Spectrometers, Detectors and Associated Equipment* **2008**, *586*, 55-58.

[15] A. Radulescu, V. Pipich, A. Ioffe, *Nuclear Instruments and Methods in Physics Research Section A: Accelerators, Spectrometers, Detectors and Associated Equipment* **2012**, *689*, 1-6.

[16] F. Mezei, *Neutron Spin Echo, Lectures Notes in Physics, Vol. 28*, Springer-Verlag Heidelberg, **1980**.

[17] O. Holderer, O. Ivanova, *Journal of large-scale research facilities JLSRF* **2015**, *1*.

[18] B. Trathnigg, *Size-Exclusion Chromatography of Polymers. Encyclopedia of Analytical Chemistry*, John Wiley & Sons, Ltd, **2006**.

[19] H. Günther, *NMR Spectroscopy: Basic Principles, Concepts and Applications in Chemistry*, John Wiley & Sons, **2013**.

[20] R. Tomovska, A. Agirre, A. Veloso, J. R. Leiza, *Characterization Techniques for Polymeric Materials in Reference Module in Chemistry, Molecular Sciences and Chemical Engineering*, Elsevier, **2014**.

[21] P. R. Griffiths, J. A. de Haset, *Fourier Transform Infrared Spectrometry*, John Wiley & Sons, Inc., Hoboken, New Jersey, **2007**.

[22] S. Vyazovkin, *Characterization of Materials. Thermogravimetric Analysis*, John Wiley and Sons, Inc., **2012**.

[23] P. Gill, T. T. Moghadam, B. Ranjbar, *Journal of Biomolecular Techniques : JBT* **2010**, *21*, 167-193.

[24] G. W. H. Höhne, W. F. Hemminger, H. J. Flammersheim, *Differential Scanning Calorimetry*, Springer-Verlag Berlin Heidelberg, **2003**.

[25] F. Kremer, A. Schönhals, *Broadband Dielectric Spectroscopy*, Springer-Verlag, Berlin, **2003**.

[26] R. Kubo, *Reports on Progress in Physics* **1966**, *29*, 255-284.

[27] D. A. Skoog, F. J. Holler, S. R. Crouch, *Principles of Instrumental Analysis*, Thomson Brooks/Cole, **2007**.

[28] B. L. Hayes, *Microwave Synthesis: Chemistry at the Speed of Light*, CEM Publishing, **2002**.

[29] H. M. Kingston, L. B. Jassie, *Introduction to Microwave Sample Preparation: Theory and Practice*, American Chemical Society, **1988**.

[30] K. S. Suslick, G. J. Price, *Annual Review of Materials Science* **1999**, *29*, 295-326.

[31] K. S. Suslick, *Science* **1990**, *247*, 1439-1445.

[32] K. S. Suslick, *The Chemical Effects of Ultrasound, Vol. 260*, Scientific American, a division of Nature America, Inc., **1989**.

[33] K. Kremer, G. S. Grest, *The Journal of Chemical Physics* **1990**, *92*, 5057-5086.

[34] T. Soddemann, B. Dünweg, K. Kremer, *The European Physical Journal E* **2001**, *6*, 409-419.

[35] A. J. Moreno, F. Lo Verso, A. Sanchez-Sanchez, A. Arbe, J. Colmenero, J. A. Pomposo, *Macromolecules* **2013**, *46*, 9748-9759.

CHAPTER 4

Exploring Basic Properties of SCNPs

4.1. Introduction

The compaction of individual polymer chains to single-chain nanoparticles (SCNPs) is a subject that has attracted significant interest in recent years.[1] Research in SCNPs is currently at the boundary between polymer science, nanotechnology and biology. In this sense, the folding/collapse of single chains to SCNPs is reminiscent of protein folding to its functional, native state although it is still very far from the extreme precision found in these natural biomacromolecules. Recently, the potential prospects of SCNPs have been expanded significantly by taking inspiration from the different morphologies displayed by native, globular proteins (e.g., enzymes) and intrinsically disordered proteins (IDPs).[2-4]

The folding of isolated non-natural chains can be a reversible or irreversible process induced by supramolecular (i.e., non-covalent and dynamic covalent) interactions or covalent bonds, respectively.[5-7] Recently, successful proof-of-concept experiments have been carried out with SCNPs in drug delivery, sensing and catalysis applications. From a technological point of view, characterizing the stability of SCNPs is an issue of extreme importance for determining their final application range. Also, unraveling the actual structure and dynamics of SCNPS in solution and, hence, to establish reliable structure-properties relationships is obviously at the basis of a rational design of SCNPs with tailor-made properties.

In this context, scattering techniques are especially well suited to realize a significant advance in this novel field. Scattering experiments provide spatial resolution through the wavevector dependence of the measured magnitudes.

Using different probes (mainly photons and neutrons) and experimental configurations, static and dynamic properties can be explored at molecular level. Particularly useful for the investigation of complex soft materials –like those containing SCNPs– is the application of neutron scattering (NS). Among other advantages of NS like high penetrability, two are of crucial importance: the simultaneous accessibility of the proper length and time scales together with the possibility of changing the scattering contrast at will.

In this chapter we explore basic properties of SCNPs in comparison with those in the precursor counterparts. We focus on the stability, structural and dynamical features in solution. First, a study about the stability of SCNPs against degradation induced by ultrasound irradiation is presented. Such investigation is based on the determination of the overall sizes of the macromolecules upon irradiation, and therefore a combination of conventional techniques as they are SEC and DLS has been employed. Then, we exploit small-angle techniques to deal with structural aspects of these SCNPs. In this way, not only the chain dimensions but also their internal organization is susceptible of being investigated. Finally, we face the dynamics of SCNPs in dilute solution. For this task, we combine the information provided by DLS on the diffusion coefficient of the chain center of mass with the unique insight facilitated by the neutron scattering technique on the internal motions of the macromolecules. Thus, with these investigations we intend to demonstrate the potential of scattering techniques –in particular of NS– to unravel structural and dynamical properties of SCNPs in solution (which is extensible to other soft matter systems).

4.2. Stability of SCNPs

4.2.1. Introduction

SCNPs constructed by means of intra-molecular covalent bonds have permanent intra-chain cross-links that affect to a large extent the final compaction degree achieved and often endow them with increased stability against thermal degradation at high temperatures.[8] Potential applications of these SCNPs include their use as additives for conventional thermoplastic materials to produce so-called all-polymer nanocomposites,[9] and the development of stabilized supported catalysts.[10] In addition to thermal stability, several potential applications of covalent-bonded SCNPs in nanomedicine do depend critically on their mechanical stability (e.g., artificial synoidal fluids for joint lubrication).

In fact, mechanical force has been demonstrated to promote several chemical reactions, with sonication experiments illustrating the degradation of a variety of natural macromolecules (cellulose, polypeptides, polysaccharides, proteins, DNA) and synthetic polymers *via* force-induced bond rupture.[11] When ultrasound is used to apply force to dilute polymer solutions, polymer chain scission is observed as a consequence of solvodynamic shear caused by cavitation: the nucleation, growth and collapse of bubbles in solution. It is generally accepted that the solvodynamic shear elongates the polymer backbone leading to scission that generally occurs near the midpoint of the polymer chain, where solvodynamic forces are the greatest.[12] Consequently, a progressive reduction in the molecular weight (and polymer size) and a certain decrease in

chain length polydispersity are often observed during sonication experiments of dilute polymer solutions.[11]

The few data reported until now about the mechanical stability of SCNPs under ultrasound irradiation[13] led us to carry out sonication experiments for water-soluble covalent-bonded SCNPs and their corresponding precursor polymer under exactly the same conditions. This study demonstrate the superior stability against degradation induced by ultrasound irradiation of covalent-bonded SCNPs when compared to their parent precursor polymer in water, as determined by a combination of size exclusion chromatography (SEC) and dynamic light scattering (DLS) measurements.

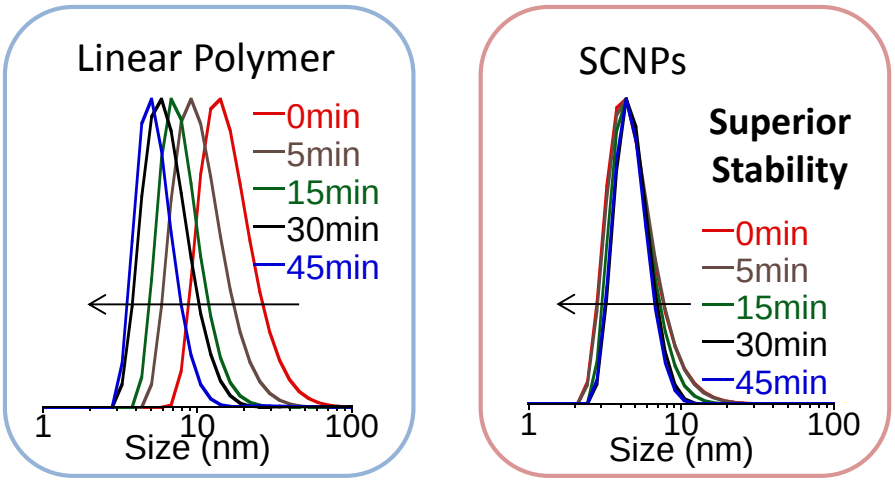

Scheme 4.1: Illustration of the superior stability against degradation induced by ultrasound irradiation of SCNPs when compared to their parent precursor polymer, as demonstrated by DLS measurements.

4.2.2. Ultrasound Irradiation Experiments

As water-soluble single-chain nanoparticles, we selected poly(vinyl pyrrolidone) (PVP) SCNPs (denoted as N1) and their corresponding precursor PVP (P1) of high molecular weight (360 kg/mol). The synthesis of both SCNPs and precursor are described in 'Standard and New Synthesis Routes' in chapter 2.

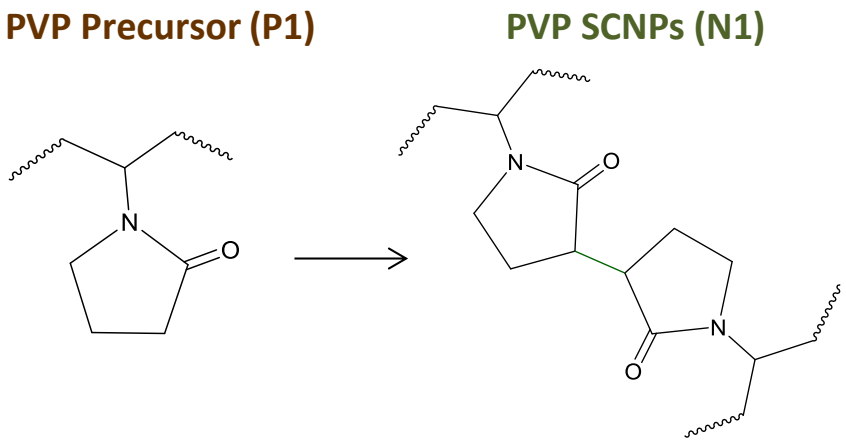

Scheme 4.2: Illustration of the chemical structures of water-soluble PVP SCNPs (N1) and their corresponding PVP homopolymer precursor (P1).

As a control experiment, we initially subjected the precursor polymer P1 to ultrasound irradiation (details about the ultrasound irradiation experiments are described in 'Techniques Employed' in chapter 3) in water and monitored the evolution of the SEC traces upon ultrasound irradiation as a function of time (see figure 4.1). In SEC experiments, macromolecules are separated according to their respective hydrodynamic size and consequently molecular weight, where bigger macromolecules show shorter SEC retention time than smaller ones.[14]

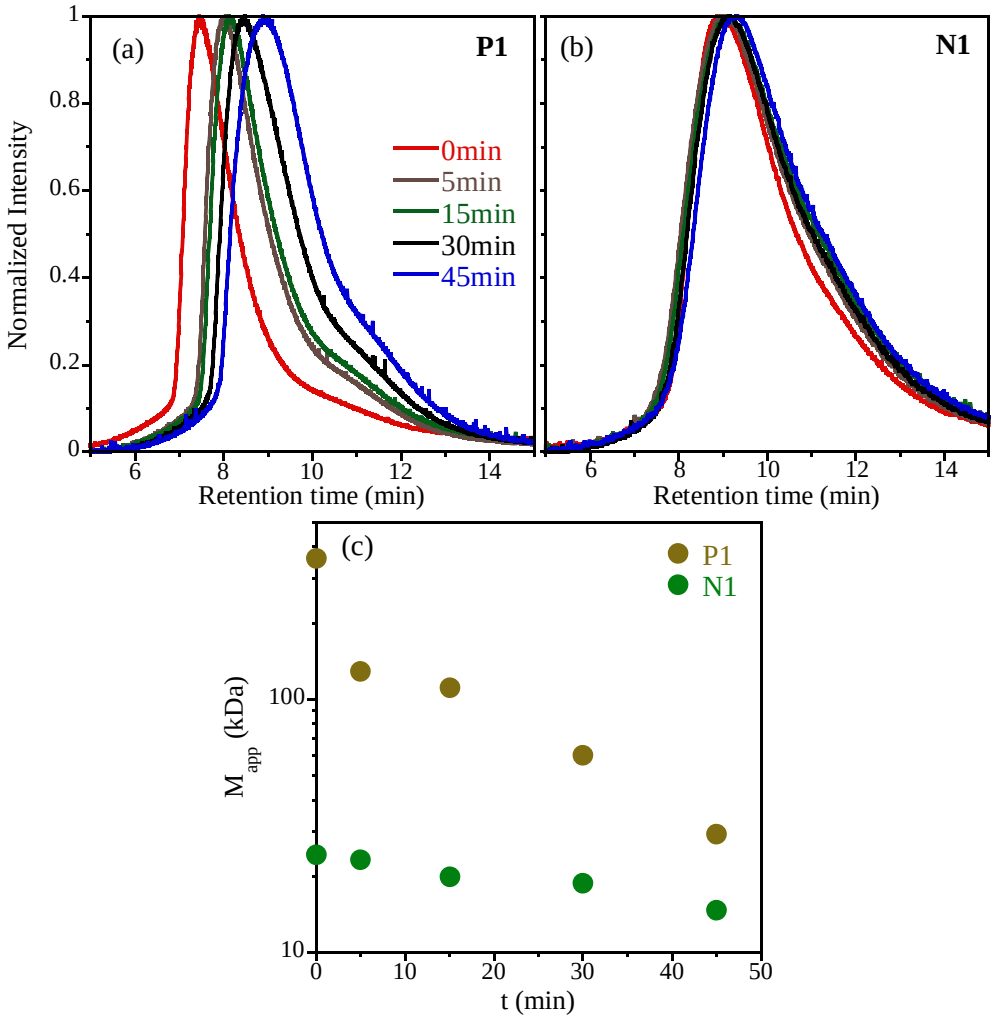

Figure 4.1: Evolution of the SEC traces of P1 (a) and N1 (b) with ultrasound irradiation time and effect of sonication time on the molecular weight at the peak maximum (M_{app}) of P1 and N1 (c). The data corresponds to SEC measurements performed in water.

As illustrated in figure 4.1(a) the SEC trace of P1 is found to shift progressively towards longer retention times (lower molecular weight/smaller size) upon increasing sonication time. This fact can be attributed to degradation by chain

scission which reduces progressively the length of the PVP chains. The results are in good agreement with prior sonication experiments involving PVP.[15] However, the SEC trace of N1 [figure 4.1(b)] showed only a very minor shift even after 45 min of sonication, pointing to an excellent stability against degradation induced by ultrasound irradiation of the single-chain nanoparticles when compared to the linear precursor polymer. The effect of sonication time on the molecular weight at the peak maximum (M_{app}) for P1 and N1 is displayed in figure 4.1(c).

The above SEC results were corroborated by DLS measurements in which the average hydrodynamic size ($\bar{R}_H$) of the SCNPs and the parent polymer precursor, as well as their complete size distributions were determined as a function of ultrasound irradiation time (see figure 4.2). A progressive reduction in the value of $\bar{R}_H$ as a function of sonication time was observed for water-soluble precursor polymer P1 [figure 4.2(a)], whereas water-soluble N1 showed no significant change even after 45 min of ultrasound irradiation time [figure 4.2(b)] in good agreement with the SEC results.

In fact, after 45 min of solvodynamic stress the average size of P1 reduces from 17.2 to 5.6 nm, while the average size of N1 only from 5.2 to 4.8 nm, which is within the experimental error of the DLS technique. Taken together, the SEC and DLS results illustrate the superior mechanical stability of single-chain nanoparticles against chain scission by ultrasound irradiation.

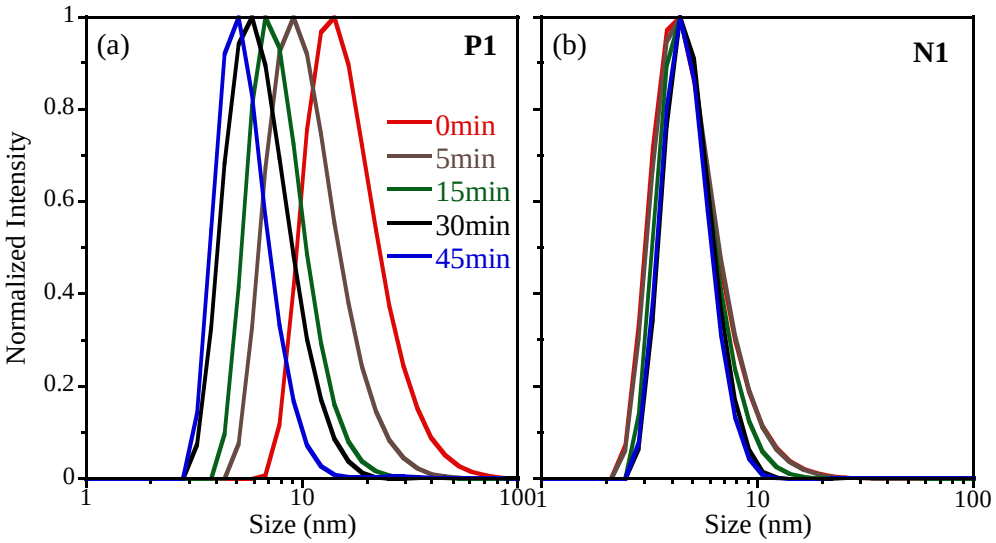

Figure 4.2: Evolution of the distribution of hydrodynamic size of P1 (a) and N1 (b) with ultrasound irradiation time as determined by DLS experiments.

Concerning the mechanism of improved mechanical stability of SCNPs when compared to linear polymers, it is generally accepted that because chain scission is a nonrandom process (with cleavage near the chain center), it is not a thermal process.[16] Figure 4.3 shows a comparison of the thermal stability of P1 and N1 as recorded by thermogravimetic analysis (TGA) measurements. P1 and N1 (which are highly hygroscopic materials) displayed approximately the same thermal stability up to 200 °C, but N1 showed a reduced thermal stability above this temperature. Consequently, the improved mechanical stability of N1 to P1 seems to be unrelated to a thermally activated process.

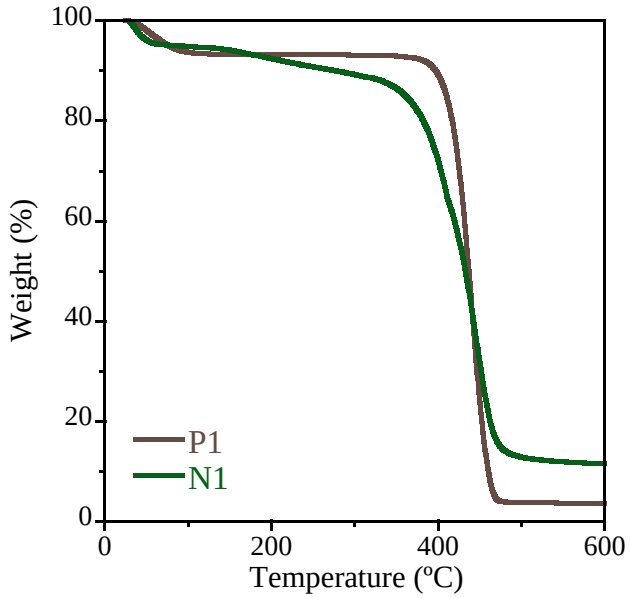

Figure 4.3: Comparison of thermal stability of P1 and N1 as recorded by TGA measurements. They display approximately the same behavior up to 200 °C.

Instead of the accepted chain scission mechanism operative in linear polymers[11-12] [see scheme 4.3(a)], for SCNPs we suggest here a different mechanism involving local loop scission events that accounts for their superior stability against degradation by ultrasound irradiation [scheme 4.3(b)]. Hence, instead of a reduction in molecular weight/polymer size upon force-induced bond rupture as observed for linear polymers, the successive loop scission events taking place in SCNPs under ultrasound irradiation will affect only at a smaller local scale without giving to global chain cleavage.

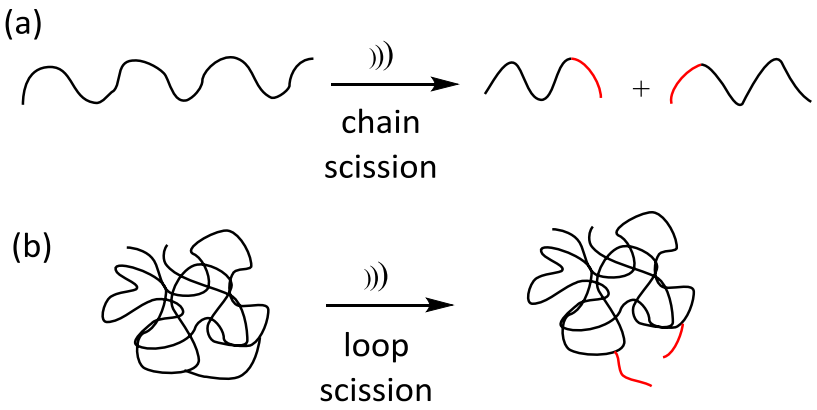

Scheme 4.3: Cartoon-representation of sonication chain scission mechanism operative in linear polymers (a), and proposed mechanism to support the superior stability of single-chain polymer nanoparticles against degradation by ultrasound irradiation, involving loop scission events (b). In both cases, the fragments involved in force-induced bond rupture are shown in red color.

In particular, the loop scission mechanism explains:

i. The nearly constant molecular weight of the single-chain nanoparticles even at large sonication times [figures 4.1(c)] since force-induced bond rupture produces fragments that remain bonded to the SCNP.

ii. The nearly constant hydrodynamic size of the single-chain nanoparticles even at high ultrasound irradiation times [figures 4.2(b)] since no significant change in global size is expected upon a few local loop scission events (by the contrary, midpoint chain fragmentation reduces significantly the hydrodynamic size due to acute shortening of the chain).

iii. That no thermally activated processes need to be invoked to support the excellent stability against degradation induced by ultrasound irradiation of SCNPs when compared to their parent linear precursor polymers.

Obviously, the loop scission rate will depend on the specific chemical composition of the SCNPs since, at the end, scission involves force-induced bond rupture that depends on the strength of the bond.[17]

4.2.3. Conclusion

In summary, we report here the excellent stability against degradation induced by ultrasound irradiation of covalent-bonded SCNPs when compared to their parent linear precursor polymer, as determined by a combination of SEC and DLS measurements in water. Instead of the accepted chain scission mechanism operative in linear polymers, we suggest a different mechanism for SCNPs under sonication involving local loop scission events that accounts for the observed experimental behavior. The increased stability of SCNPs against solvodynamic shear offers new opportunities for the development of a new generation of mechanically stable ultra-fine soft nanomaterials. Further works including computational studies would be of utmost help to support the suggested loop scission mechanism and to know the effect of molecular weight, cross-linking degree, type of cross-linking chemistry, etc. on SCNP stability under sonication.

4.3. Structure of SCNPs

4.3.1. Introduction

Up to date, most of the studies determining size reduction and compaction effects by 'standard' synthesis routes have been performed by SEC and/or DLS. An extensive and thorough compilation of size data obtained through both techniques for a large number of SCNPs synthesized by different 'standard' routes pointed to a relatively poor compaction leading to conformations close to that of a random coil in good solvent conditions.[18] Thus, SEC and DLS experiments suggested that the compaction of SCNPs is much less pronounced than the initially aimed and expected complete collapse of the macromolecules into globular nanoparticles. However, a complete characterization of the macromolecular statistics requires application of scattering techniques able to resolve the full form factor including the internal structure of the nanoparticles.

Here, a careful and systematic study by SAS on structural properties in dilute solution of SCNPs is presented. In a first step, we have carried out a kinetic SAXS study on the macromolecular conformation of SCNPs during the internal cross-linking synthesis procedure. Thereafter, we have determined the chain dimensions and conformation (full form factor) of SCNPs obtained through two different synthesis routes and investigated the effects of crowding in the macromolecular structure. Prior to the description of these studies, some general considerations about the information provided by scattering techniques on the macromolecular conformation are presented.

4.3.2. The Form Factor of Macromolecules

The size and conformation of a macromolecule in dilute solution can be experimentally determined by small-angle XR and/or neutron scattering measurements on samples where contrast between solvent and solute is provided. Using deuterated solvents and protonated macromolecules enhances the intensity scattered by SANS, while it obviously has no effect on SAXS experiments. In general, we can distinguish three different Q-regimes where we obtain different kind of information about the macromolecule:

i. At low $Q \lesssim 1/\bar{R}_g$ one does not 'see' the details of the shape and the structure of the macromolecules but only their dimensions. In this regime – the so-called Guinier domain– one measures the average radius of gyration, $\bar{R}_g$. The Q-dependence of the intensity is directly determined by $I\left(Q << 1/\bar{R}_g\right) \propto \exp\left[-\bar{R}_g^2 Q^2/3\right]$.

ii. If we increase the Q further one 'sees' only a part of a macromolecule; the scattering does not depend on molecular weight and polydispersity and one obtains information about the statistics of the chain. This regime extends between $1/\bar{R}_g < Q < 1/\ell_K$ (i.e., spatial scales larger than the Kuhn segment ℓ_K).

iii. In the region $1/\ell_K < Q$, the local rigidity of the macromolecule is the determining factor; if the monomer is thin enough, the chain behaves like a rigid rod. This regime extends up to Q-values where Q^{-1} is of the order of the chemical bond.

When $Q^{-1} \sim chemical\ bond$, the local structure of the chain begins to play a role. One is no more in the small angle regime and the experiments are sensitive to both, solvent and solute atomic pair correlations.

Of particular interest is region (ii), also called intermediate or fractal regime. It can be shown[19-20] that there, the form factor of the macromolecule –and thereby the scattered intensity– varies as $\sim Q^{-1/\nu}$, where ν is the so-called scaling exponent. This exponent determines the dependence of the macromolecular size on the number of chain segments, $\bar{R}_g \sim N^{\nu}$, i.e., it reflects the chain compaction. The form factor of chains characterized by a scaling exponent ν, where $\langle \left(\vec{R}_j - \vec{R}_i\right)^2 \rangle = \ell^2 |j-i|^{2\nu}$, can be described by generalized Gaussian coil functions[21]

$$P(Q) = \frac{1}{\nu U^{\frac{1}{2\nu}}} \gamma\left(\frac{1}{2\nu}, U\right) - \frac{1}{\nu U^{\frac{1}{\nu}}} \gamma\left(\frac{1}{\nu}, U\right) \tag{4.1}$$

with $U = (2\nu+1)(2\nu+2)Q^2\bar{R}_g^2/6$ and $\gamma(a,x) = \int_0^x t^{a-1}\, exp(-t)\, dt$. For a given ν-exponent:[22]

$$\bar{R}_e = \sqrt{(2\nu+1)(2\nu+2)}\bar{R}_g \tag{4.2}$$

In the case of linear polymers in dilute solution with a good solvent, the conformation is a self-avoiding path. The value of the scaling exponent is then the Flory exponent, $\nu_F \approx 0.59$.[20] In the case of a Gaussian chain –like a linear macromolecule in bulk or in θ-solvent– the value of the scaling exponent is $\nu \approx 0.5$.

4.3.3. Kinetics of Intra-chain Bond Formation

The standard synthesis of reversible single-chain nanoparticles, e-SCNPs, (see chapter 2 for details about the synthesis procedure) was followed by SAXS, measuring the form factor of the macromolecule (M_w = 207 kg/mol) during the reaction with diamines. First, we considered the typical reaction conditions, i.e., at a concentration of 1 mg/ml. Prior to the addition of the cross-linking agent, SAXS measurements on the solution of the linear precursor macromolecules revealed the expected Flory-value for the scaling exponent $\nu = \nu_F = 0.59$ and an average radius of gyration of 14.5 nm. These are the reference values shown at the origin in figure 4.4 (reaction time $t_R = 0$). Diamines were then added to the solution, and patterns were collected with measuring times of 1 h.

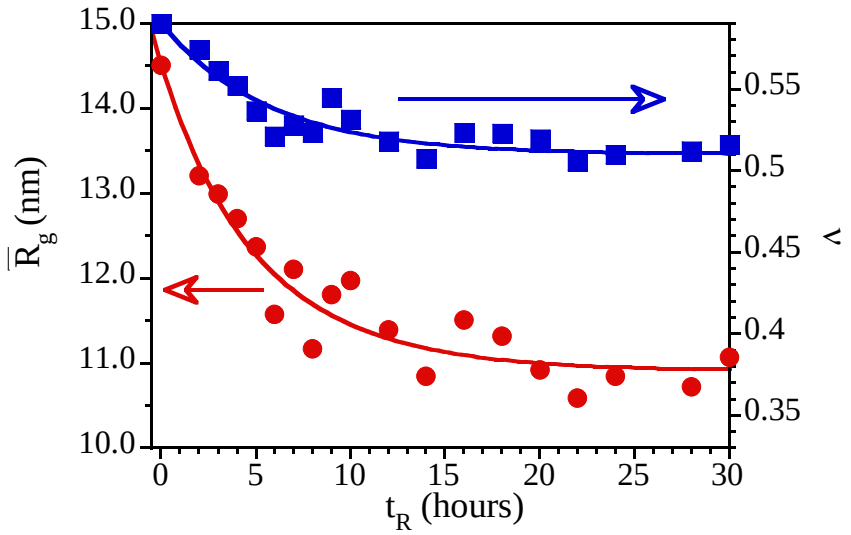

Figure 4.4: Time evolution of the radius of gyration (circles) and scaling exponent ν (squares) of the macromolecules while bond formation through the reaction with diamine molecules. The ν-scale on the right covers the range between the globular state (1/3) and the Flory exponent value (0.59). Solid lines are fits of Eq. (4.3) to ν-results and of Eq. (4.4) to $\bar{R}_g$-results.

The results were described by Eq. (4.1) delivering the fitting parameters ν and $\bar{R}_g$ shown in figure 4.4. The observed decrease of both the scaling exponent and the radius of gyration with increasing t_R reveals the gradual compaction of the macromolecules induced by the reaction with the diamines. The main changes occur during the first 15 h approximately. The reaction time dependence of the ν-exponent can be fitted by an exponential dependence:

$$\nu(t_R) = (\nu_F - \nu_\infty)exp[-(t_R/\tau_R)] + \nu_\infty \tag{4.3}$$

That describes its decay from the Flory value at $t_R = 0$ to a plateau-value ν_∞. This value turns out to be ~0.51. We note how far is this value from that corresponding to the globular case (1/3, lower limit of the ν-scale in figure 4.4). The characteristic time of the reaction τ_R is 5.67 h. The evolution of the average radius of gyration can be well described by assuming a chain with a constant statistical segment length b and a varying scaling exponent $\nu(t_R)$:[22]

$$\bar{R}_g(t_R) = \frac{b}{\sqrt{[2\nu(t_R)+1][2\nu(t_R)+2]}}\, N^{\nu(t_R)} \tag{4.4}$$

where $\nu(t_R)$ is parametrized as in Eq. (4.3) with the above given values of the parameters involved. The fit of the experimental $\bar{R}_g$ data corresponds to a chain consisting of 52 segments of length $b = 3.27\, nm$ (and mass $m_b = M_w/52 \approx 4020\, g/mol$). This value is larger than the length of the Kuhn segment in poly(methyl methacrylate) (PMMA)[20] (1.7 nm).

As can be seen in figure 4.4, this kind of description works very well for reaction times of about 1 day. If the reaction goes on, a further decrease of the exponent value is observed (figure 4.5). This is accompanied by an increase of the $Q \to 0$ value of the measured intensity (figure 4.5, left scale).

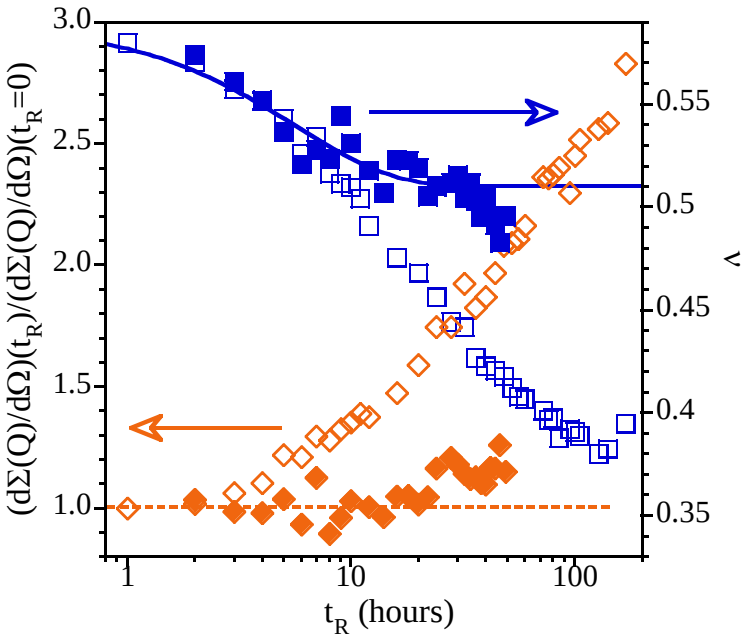

Figure 4.5: Evolution with reaction time t_R of the asymptotic $Q \to 0$ intensity normalized to its value at $t_R \approx 0$ (diamonds) and scaling exponent ν (squares) of the macromolecules while bond formation through the reaction with diamine molecules. Filled symbols: reaction at 1 mg/ml; empty symbols: reaction at 4 mg/ml. Solid line is the fit of Eq. (4.3) to ν-results at 1 mg/ml for $t_R \lesssim 30h$ (see figure 4.4).

This behavior indicates the appearance of some fraction of aggregates in the solution. The moderate increase of the intensity means that this fraction cannot be very important, but reveals that the solution ceases to exclusively contain individual single-chain nanoparticles. After about 20 h, the fraction of remaining unreacted diamines that bind to monomers of different macromolecules

(through occasional collisions driven by Brownian motion in the solvent) starts to be significant. The contribution to the scattered intensity of dimers, trimers, etc. that emerge leads to an apparent decrease of the scaling exponent.

This effect becomes more pronounced and starts at much earlier times if the precursor concentration is increased, as can be seen from the results obtained on the sample at 4 mg/ml (empty symbols in figure 4.5). In this case, already after about 6 h the presence of aggregates starts to become evident. Thus, from these experiments we can infer that in order to obtain unimolecular SCNPs the synthesis has to be carried out at very dilute concentrations and stopped after some time of reaction, that in the case of these e-SCNPs is of about 1 day. Otherwise, unwanted reactions leading to inter-molecular cross-links may take place in the solution.

4.3.4. Form Factor of Standard SCNPs in dilute solution

A comparative structural characterization of two different types of standard SCNPs and linear precursor as reference in solution was carried out. The samples explored in this study were single-chain Michael nanoparticles (Mi-SCNPs, covalent bonds), metallo-folded single-chain nanoparticles (Cu-SCNPs, non-covalent interactions) and poly(MMA-co-AEMA) –their random copolymer precursor– as reference. For details about the synthesis procedure see chapter 2 ('Standard Synthesis Routes'). Two different molecular weights ($M_w^{High} =$ 272.1 kg/mol and $M_w^{Low} = 52.5$ kg/mol) and solutions at concentrations of 2, 4, 8 and 25 mg/ml were explored. In all cases deuterated N,N-dimethyl formamide (dDMF) was used as solvent to achieve a high contrast for neutron scattering.

Table 4.1: Parameters characterizing the molecular weight and form factor of the precursors and SCNPs in dilute solution at a concentration of 2 mg/ml

Sample	M_w (kg/mol)	M_w/M_n	$\bar{R}_g$ (nm)	ν	c* (mg/ml)
Precursor	272.1	1.40	16.5	0.59	13
Mi-SCNPs			9.3	0.45	70
Cu-SCNPs			13.4	0.55	24
Precursor	52.2	1.03	7.3	0.59	28
Mi-SCNPs			5.9	0.52	53
Cu-SCNPs			5.8	0.54	56

Figure 4.6 shows the differential cross sections measured on solutions of Mi-SCNPs and Cu-SCNPs in comparison with the solution of the linear polymer precursor. The considered concentration is very low (4 mg/ml), well below the overlap concentration ($c^* = M_w/\left(2\bar{R}_g\right)^3 N_A$, see table 4.1). In this way, there are no position-position correlations and the structure factor of the center of mass $S_{CM}(Q)$, describing the interference of scattering from different particles [Eq. (3.10) in chapter 3], can be considered as 1 to a good approximation. Thus, the Q-dependence of the measured curves is entirely determined by the form factor of the dissolved particles $P(Q)$:

$$\left(\frac{d\sum(Q)}{d\Omega}\right)_{coh} \approx \phi\Delta\rho^2 V^2 P(Q) \tag{4.5}$$

A simple inspection of the curves in figure 4.6 reveals a change in the shape of the macromolecule: the slope in the intermediate (fractal) regime is clearly increased from the precursor case to the Cu-SCNPs and even more to the Mi-SCNPs. As above mentioned, in this Q-regime the form factor scales as

$\sim Q^{-1/\nu}$.[19-20] From the slopes, values of $\nu \approx 0.6$, 0.55 and 0.45 are deduced for linear precursors, Cu-SCNPs and Mi-SCNPs, respectively. As expected, the scaling exponent obtained for the precursors is $\nu_F \approx 0.59$ (corresponding to a self-avoiding path). The lower values of ν observed for the SCNPs reflect compaction of the chains and conformations close to random walks.

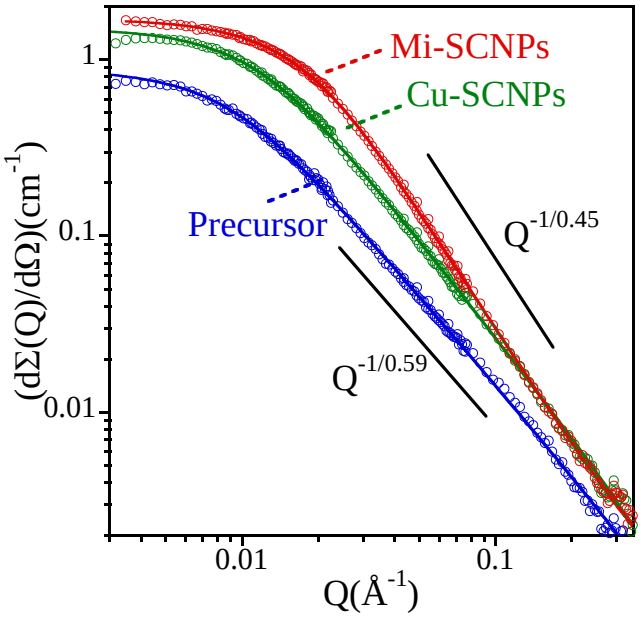

Figure 4.6: Measured intensity by SANS at 4 mg/ml of linear precursor chains (blue) and the SCNPs obtained from it by Michael addition (red) and Cu-complexation (green); fit by Eq. (4.5) with generalized Gaussian coil form factors [Eq. (4.1)] (lines).

This can be well appreciated in the Kratky representation shown in figure 4.7. In this kind of plot, where the scattered intensity is multiplied by Q^2, the closeness or deviations from a Debye-like function ($\nu = 0.5$) are evidenced. At intermediate Q-values, the Debye function shows a plateau in the Kratky representation (dashed line in figure 4.7); a positive slope there indicates thus a

swollen behavior with respect to the random coil, and the presence of a maximum points to a more compact conformation. The limiting case of the equilibrium globule is shown in figure 4.7 as the dotted line. As can be seen in this figure, though the SCNPs obtained by Michael addition indeed present a maximum in this kind of plot, it is not as pronounced as that expected for a globular object.

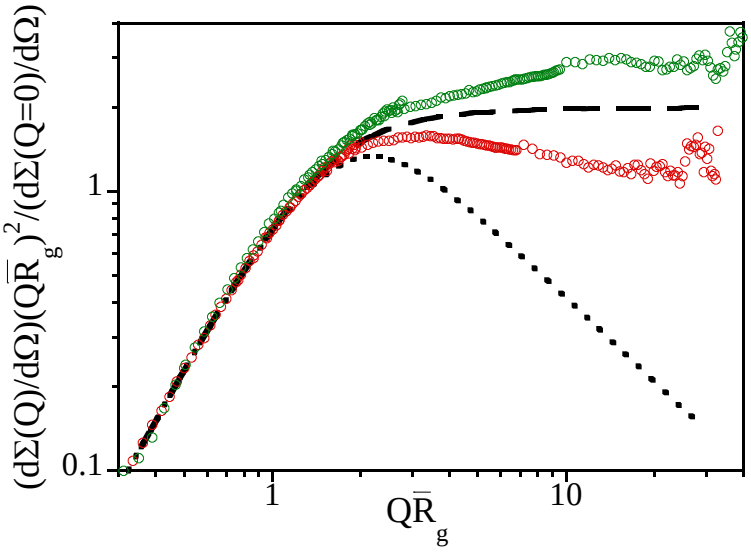

Figure 4.7: Krakty representation of the Mi-SCNPs (red) and Cu-SCNPs (green) data obtained by SANS, compared with the cases of a random coil ($\nu = 0.5$, dashed line) and a compact globule ($\nu = 1/3$, dotted line).

Figure 4.6 shows that the experimental form factors of the macromolecules can be well described over the whole Q-range investigated by means of generalized Gaussian coil functions[21] expressed by Eq. (4.1). These descriptions allow to obtain accurate values of the scaling exponent and the average radius of gyration $\bar{R}_g$ of the macromolecules (namely, 16.5 nm for precursor, 13.4 nm for Cu-SCPs

and 9.3 nm for Mi-SCNPs). Thus, accompanying the reduction of the scaling exponent, a decrease of the macromolecular size is observed in the SCNPs, and these effects are more pronounced for the Mi-SCNPs than for the Cu-SCNPs. The compaction is more efficient by the former synthesis route.

As shown previously, the form factors of Mi-SCNPs, Cu-SCNPs and e-SCNPs in the intermediate regime exhibit scaling exponents of 0.45, 0.55 and 0.51 respectively, very far from the scaling exponent expected for globular nano-objects ($\nu = 0.33$). This means that SCNPs behavior is closer to that of a linear chain in a θ-solvent ($\nu = 0.5$). Notably, SCNPs involving permanent bonds (i.e., Mi-SCNPs) show smaller scaling exponents –more compaction– than SCNPs in which reversible interactions are present (i.e., Cu-SCNPs and e-SCNPs).

As it has been previously commented, in Ref.[18] size data from the literature obtained by SEC and/or DLS for a large number of SCNPs in solution, covering from covalent to non-covalent bonded SCNPs synthesized in good solvents (30 different systems, 11 different cross-linking chemistries) have been analyzed and provided a comparison with the corresponding data for compact or partially swollen globules of the same nature and molar mass. This comparison illustrated that, in general, current synthesis techniques do not yield compact globular SCNPs. Remarkably, the analysis revealed that SCNPs produced in the usual good solvent conditions of synthesis adopt open, sparse morphologies characterized by scaling exponents $\nu \approx 0.5$ instead of globular conformations. These conclusions are now corroborated by this structural study directly addressing the chain conformation at a molecular level.

Molecular dynamics simulations have elucidated the underlying physical mechanism for such sparse morphologies.[23] The synthesis of the SCNPs is generally carried out in good solvents, where the linear precursors universally adopt self-avoiding conformations.[24] Hence, such conformations mostly favor bonding of reactive groups that are separated by short contour distances, whereas long-range loops –which are the important ones to lead to global compaction– are highly unfrequent. Thus, this mechanism promotes local globulation along the chain, but is not efficient for global, large-scale chain compaction. Interestingly enough, we note the similarity of the average value of the scaling exponent with those reported for intrinsically disordered proteins ($\nu \approx 0.5$).[25] The structural similarity emphasizing the analogies between SCNPs and IDPs in dilute conditions can be invoked to consider SCNPs as model systems to mimic bio-macromolecules in different environments and situations.

Up to this point, only the results on the lowest concentration measured have been discussed. Now, we turn to the SANS experiments performed on Cu-SCNPs and Mi-SCNPs at different concentrations. The explored range was restricted to values below the overlap concentration c^* (see table 4.1). Fits of Eq. (4.5) together with Eq. (4.1) to the SANS results delivered concentration-dependent values of the scaling exponent and average radius of gyration, as can be seen in figure 4.8. An apparent contraction of the SCNPs upon increasing concentration could thus be deduced from such an analysis, at least at first sight.

We know, however, that with increasing concentration the interactions between the centers of mass of different particles may start to be non-negligible and the arising structure factor, $S_{CM}(Q)$, contributes to the measured intensity.

Disentangling the form factor and structure factor is not an easy task but we made an attempt by SANS combined with MD-simulations. This is explained in the following section.

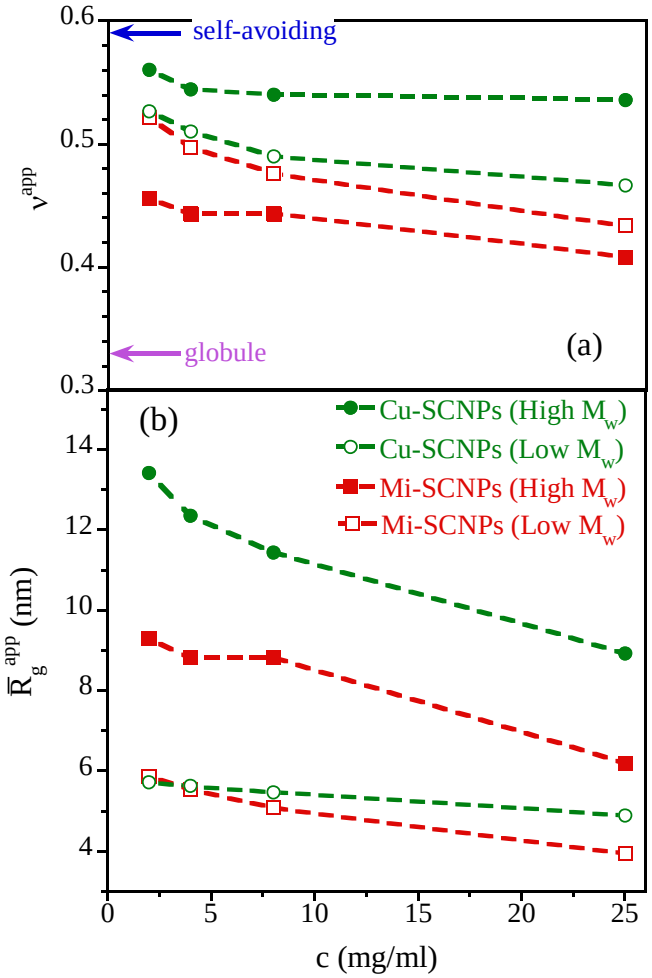

Figure 4.8: Apparent scaling exponent (a) and apparent average radius of gyration (b) as function of the concentration for the SCNPs in solution investigated by SANS; Cu-SCNPs (green circles) and Mi-SCNPs (red squares). Filled symbols are high M_w samples and empty symbols low M_w samples.

4.3.5. Crowding the Solutions of SCNPs

Though the conformational properties of SCNPs at high dilution have been actively investigated over recent years, their eventual modification in concentrated solutions is an essentially unexplored problem. Still, there are indications from other fields of research –in particular from the problem of crowding in cellular environments– that suggest that the properties of SCNPs in concentrated solutions can significantly differ from those at high dilution.

Inspired by the former analogies with biomolecules, we aimed to investigate the conformational properties of SCNPs in concentrated solutions as model systems of crowded environments. In this section, we exploit neutron scattering selectivity achieved by isotopic (deuterium) labelling and present a SANS investigation on the conformational properties of SCNPs in increasingly crowded environments. This SANS investigation was conducted in an independent experiment on a new set of precursors and SCNPs. Crowding was induced by two means, namely by adding either linear polymeric chains or SCNPs, which however, turned out to be more complicated revealing the presence of aggregates. A systematic complementary study by dynamic light scattering (DLS) has been carried out to determine under which conditions aggregation of SCNPS takes place and its reversibility. The generalizability of the experimental findings is addressed by parallel MD-simulations.

A. SANS on Michael-SCNPs in dilute conditions

We investigated SCNPs obtained through Michael addition (Mi-SCNPs) starting from linear precursors (Prec) consisting of random copolymers of MMA and AEMA, namely P($MMA_{0.71}$-$AEMA_{0.29}$). Details about the synthesis are described in

'Standard Synthesis Routes' in chapter 2. Three different molecular weights for precursors were investigated. The molecular weights and polydispersities determined by SEC are displayed in table 4.2.

Table 4.2: Chain characteristics and overlap concentrations of precursors and SCNPs obtained through Michael addition as determined by SANS on solutions in dDMF at 5 mg/ml. The results on the linear PMMA crowders are also shown.

Sample	M_w (kg/mol)	M_w/M_n	$\bar{R}_g$ (nm)	ν	c* (mg/ml)
Hi_Prec	271.8	1.42	13.5	0.59	23 (14[α])
Hi_Mi-SCNPs			9.78	0.49	60
Me_Prec	123.5	1.11	9.97	0.59	26
Me_Mi-SCNPs			7.21	0.46	68
Lo_Prec	52.1	1.19	5.91	0.59	52
Lo_Mi-SCNPs			4.81	0.47	97
Me_dPMMA	99.1	1.09	10.20	0.59	19
Lo_dPMMA	9.6	1.11	3.07	0.59	69

[α]Value obtained imposing the $\bar{R}_g \propto N^{0.59}$ law shown in figure 4.9.

A first set of experiments was performed in dilute conditions (5 mg/ml) on precursors, SCNPs as well as on the linear deuterated PMMA chains that were used to induce crowding in the solutions (see table 4.2). In the later case, the solvent was protonated DMF to enhance the contrast for neutrons. The values obtained for $\bar{R}_g$ and ν are compiled in table 4.2. We also considered linear protonated PMMA chains of different molecular weights in deuterated DMF to increase the range of molecular weights explored. Figure 4.9 shows the macromolecular average size as function of the main-chain length, represented by the number of main-chain bonds N.

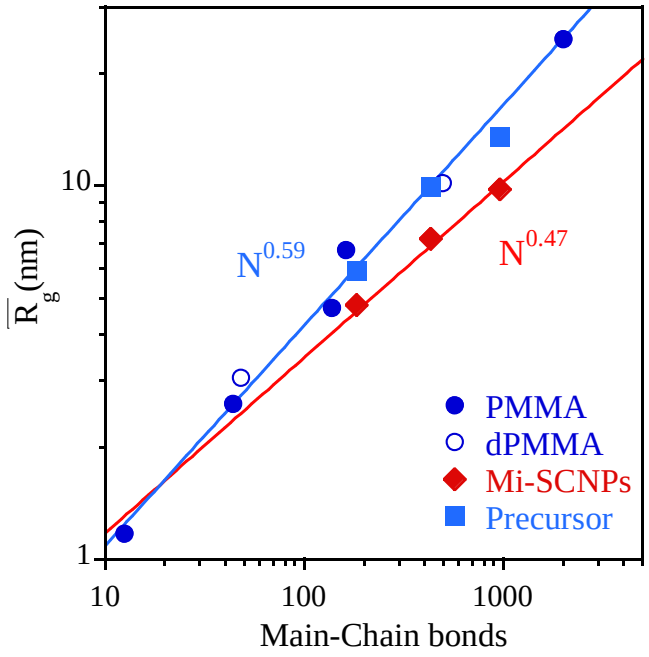

Figure 4.9: Average radius of gyration obtained from the SANS experiments in high dilution as function of the number of main-chain bonds for protonated PMMA (full circles), deuterated PMMA (empty circles), copolymer precursor (squares) and Mi-SCNPs (diamonds). The protonated polymers were dissolved in deuterated DMF and the deuterated PMMA chains in protonated DMF. The lines are fits to power laws with fixed scaling exponents (0.59 for the linear chains and 0.47 for the SCNPs).

Within the uncertainties, we can see that the results on the linear macromolecules collapse on the top of the expected law $\bar{R}_g \propto N^{\nu_F}$. This implies that the length of the statistical segment for all these polymers is the same, independently of the presence of side groups. On the other hand, as in the previously investigated Mi-SCNPs presented in the preceding section, a certain collapse –characterized by $\nu \approx 0.47$, see table 4.2– is achieved through the Michael addition method for the different macromolecular sizes investigated (see table 4.2 and figure 4.9). As can be seen in figure 4.9, for the single-chain

nanoparticles the N-dependence of the size can be well described by $\bar{R}_g \propto N^{\nu=0.47}$, i.e., the macromolecular dimensions scale with an average value of the scaling exponents obtained for the different molecular weights explored.

B. SANS on Michael-SCNPs in crowding conditions

1. Crowding with linear polymers

The effect of crowding the environment on the structure of SCNPs was first investigated by using linear polymeric chains (deuterated PMMA) as crowders. In a first set of SANS experiments, low-molecular weight chains ($M_w \approx$ 10 kg/mol) were added to dDMF-solutions of the three kinds of Michael SCNPs. The concentration of SCNPs, c_{SCNP}, was always kept fixed to c_{SCNP} = 5 mg/ml of the total solution. This value is well below the overlap concentration of the SCNPs in the three cases (c^*_{SCNP} =60, 68 and 97 mg/ml for Hi_Mi-SCNPs, Me_Mi-SCNPs and Lo_Mi-SCNPs respectively, see table 4.2). The concentration of the crowder (c_{crow}) was varied between 0 and 395 mg/ml, such that the total polymer concentration c in the solution increased from 5 mg/ml up to 400 mg/ml.

Given the low contrast between the crowders and the solvent (both deuterated), and the high contrast between the protonated SCNPs and the rest of the solution, the scattered intensity is overwhelmingly dominated by the contribution of the SCNPs against the surrounding medium. Moreover, as $c_{SCNP} << c^*_{SCNP}$, inter-molecular correlations are expected to be negligible [$S_{CM}(Q) \approx 0$] and thus the results directly reveal the SCNPs form factor in the differently crowded solutions. For the intermediate molecular weight SCNPs investigated, figure 4.10 shows the SANS results for several concentrations.

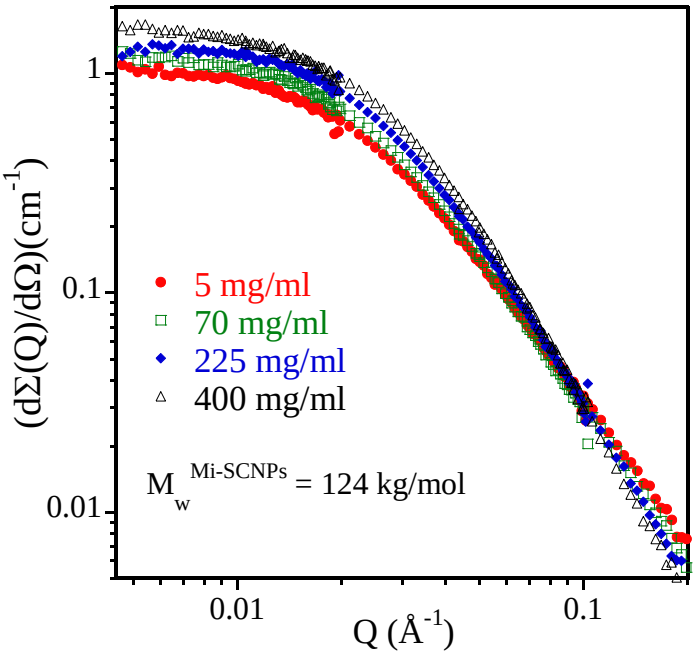

Figure 4.10: Form factor of Mi-SCNPs of M_w = 124 kg/mol (Me_Mi-SCNPs) obtained by SANS on solutions in dDMF with increasing low-molecular weight linear dPMMA concentration (0, 65, 220 and 395 mg/ml); the Mi-SCNPs concentration is always 5 mg/ml.

From the simple inspection of the curves, a decrease of the dimensions and of the scaling exponent of the SCNPs with increasing concentration can be directly deduced. The description of the results in terms of generalized Gaussian functions (Eq. 4.1) delivered the values of $\bar{R}_g$ and ν represented in figure 4.11(b) as a function of the total polymer concentration in the solutions.

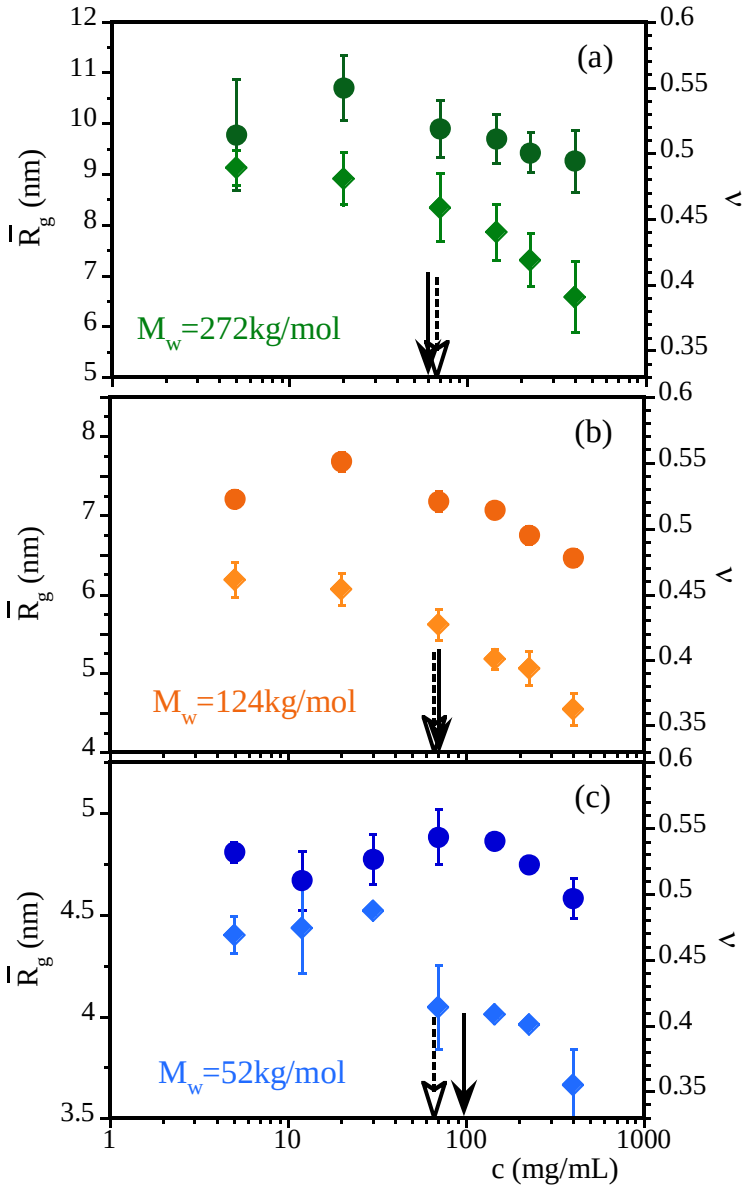

Figure 4.11: Average radius of gyration (circles) and scaling exponent (diamonds) of the Mi-SCNPs of M_w=272 kg/mol (a), M_w=124 kg/mol (b) and M_w=52 kg/mol (c) as function of the total concentration. Vertical arrows show the location of the overlap concentration of the crowders (dashed) and of the Mi-SCNPs (solid).

As can be seen, above a given concentration range, both parameters decrease with increasingly crowded environment. The chain size reveals a clear shrink and the scaling exponent shows an increasingly compaction upon crowding above such concentration range. For high concentrations, values of ν close to the globular limit ($\nu_g = 1/3$) are reached. The experiments on the solutions with the same crowder and SCNPs of different sizes reveal a qualitatively similar behavior, as can be seen in figures 4.11(a) and (c).

Two concentrations might be invoked to be key ingredients in this situation: the overlap concentration of the SCNPs (c^*_{SCNP}) and that of the crowders (c^*_{crow}). From the $\bar{R}_g$-values obtained from the SANS experiments in dilute conditions, these values were calculated (see table 4.2). They are represented by the arrows in figure 4.11. They both are in the range where the crossover from unperturbed to collapsed dimensions takes place, within the experimental uncertainties. Since for the chosen molecular weight of the crowder the differences between the values of its c^* and those of the SCNPs are not very large, it is not possible to univocally discern which one of the overlap concentrations plays the most important role in inducing the collapse of the SCNPs. It seems however that the crossover takes place in a concentration range that shifts toward larger values with decreasing molecular weight of the SCNPs, pointing to c^*_{SCNP} as the most plausible candidate for being the key magnitude.

To check this hypothesis we investigated the effects induced by much longer crowding chains –thereby with a much smaller overlap concentration $c^*_{crow} << c^*_{SCNP}$. This was realized for the case of the Me_Mi-SCNPs, namely using dPMMA with $M_w \approx 100$ kg/mol. As can be seen in table 4.2, for these chains c^*_{crow} = 19

mg/ml, more than three-fold lower than c^*_{SCNP}. Figure 4.12 shows the concentration dependence of the scaling exponent ν of the SCNPs in the such crowded solutions. The compaction degree of the SCNPs is insensitive to increase the concentration across c^*_{crow}. The crossover to collapsed conformation clearly starts at much higher concentrations, in a similar range than for the solutions with the low-molecular weight linear PMMA chains, coinciding, within the uncertainties, with c^*_{SCNP}.

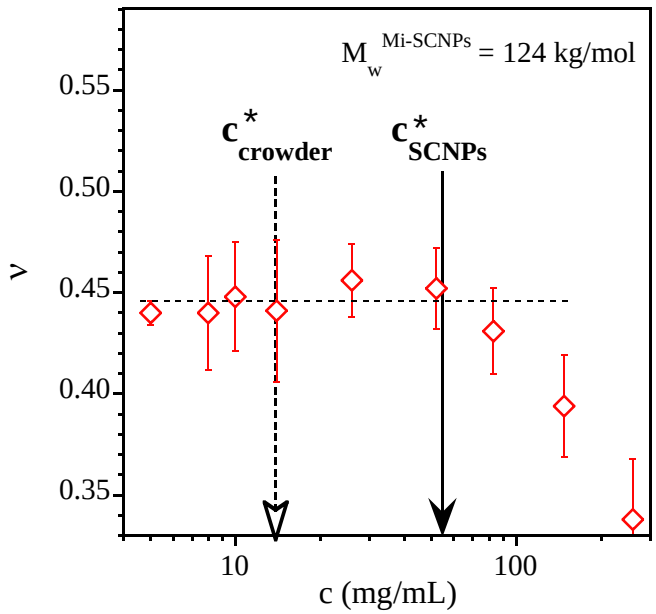

Figure 4.12: Scaling exponent of the Mi-SCNPs of M_w = 124 kg/mol in solutions with dPMMA of M_w = 100 kg/mol as function of the total concentration.

The construction of master curves for the size and scaling parameter (figure 4.13) against the reduced variable c/c^*_{SCNP} nicely supports this result. For building the master curve of the chain dimensions [figure 4.13(a)], we have normalized the average radius of gyration of the SCNPs to the value obtained for

the solutions without crowders (table 4.2). Since the value of ν at high dilution was very similar for the three molecular weights investigated, this variable was not renormalized in figure 4.13(b). The obtained masters demonstrate that c^*_{SCNP} is the relevant magnitude determining the onset of collapse of the SCNPs.

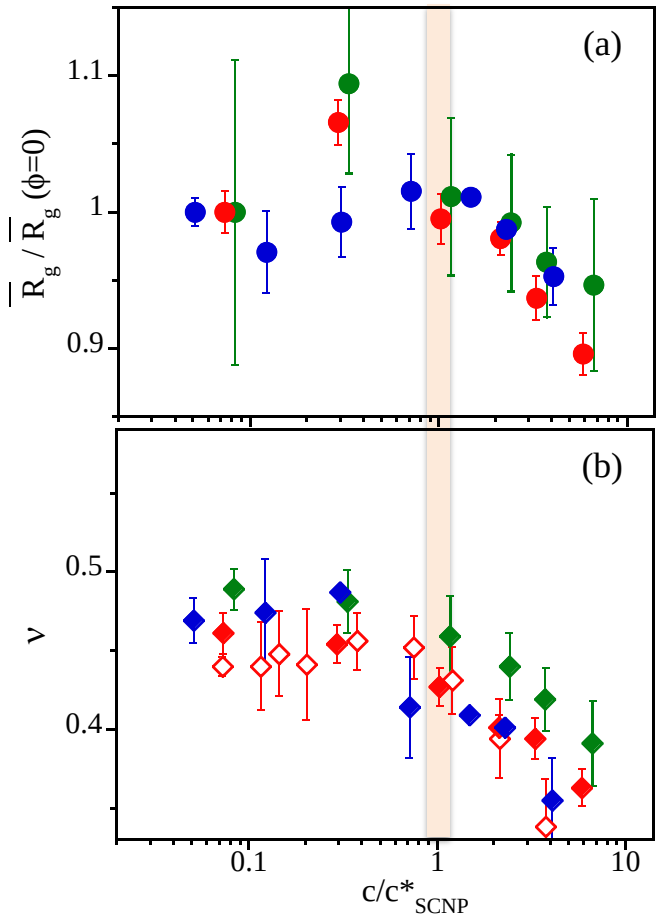

Figure 4.13: Average radius of gyration normalized to its value at the lowest concentration investigated (a) and scaling exponent (b) of the Mi-SCNPs as function of the ratio between the total concentration and the overlap concentration of the SCNPs. Symbols as in figures 4.11 and 4.12. The determination of the chain size in the case of the big crowders was subjected to large uncertainties and the corresponding results have been omitted.

2. Crowding with SCNPs

Similar experiments were intended with SCNPs as crowders, as previously investigated by MD-simulations in a recent work.[26] Realizing these experiments presented however several difficulties. When solutions with high concentrations of protonated macromolecules in deuterated solvent are investigated by SANS, the scattered intensity reveals not only the form factor of the individual nano-objects but also the structure factor, which cannot be approximated by unity anymore. To prevent this interference term, only few protonated macromolecules might be labelled in a deuterated sea –as in the situation investigated with dPMMA linear chains as crowders. However, since the functionalized AEMA groups and cross-linking agents could not be obtained in their deuterated forms, the 'deuterated' SCNPs (dMi-SCNPs) contained a non-negligible fraction of hydrogenated stuff.

Therefore we performed the experiments dissolving a fixed amount of protonated Mi-SCNPs (5 mg/ml) in solutions of dMi-SCNPs and mixtures of dDMF and DMF such that the dDMF/DMF ratio matched the dMi-SCNPs scattering. To find the matching conditions we first measured the scattering from solutions of dMi-SCNPs in different dDMF/DMF ratios. The coherently scattered intensity was minimal for a solution with a composition of 70% dDMF/30% DMF for the solvent. With this solvent ratio fixed, crowding was induced by increasing the concentration in dMi-SCNPs. The molecular weight considered in this kind of experiments was 272 kg/mol.

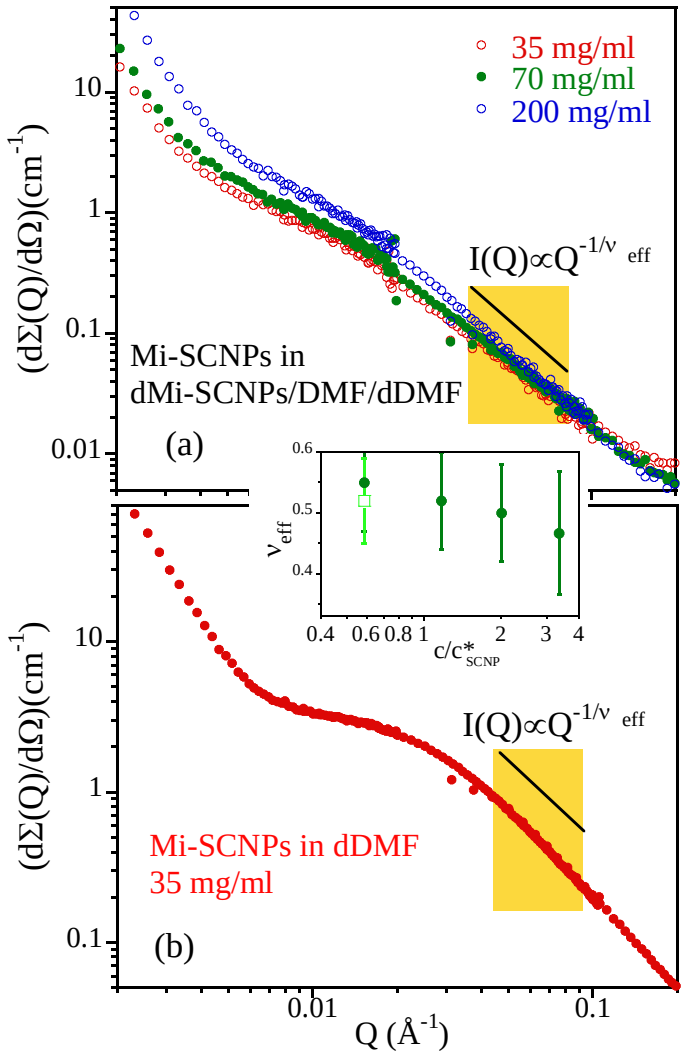

Figure 4.14: SANS results on solutions of hydrogenated and deuterated Mi-SCNPs in mixtures of dDMF/DMF for different polymer concentrations (see the text) (a) and on a solution of hydrogenated Mi-SCNPs in dDMF at 35 mg/ml (b). The inset shows the concentration dependence of the scaling exponent obtained from the slopes in the fractal regime (indicated by shadowed areas) from the solutions in (a) (solid circles) and in (b) (empty squares).

After background corrections, the results are shown in figure 4.14(a) for some of the concentrations investigated. They are supposed to be dominated by the contrast between the protonated SCNPs and the surrounding medium, revealing the form factor of the protonated macromolecules. Superimposed to the expected result for the form factor, for all compositions there is a strong additional small-angle contribution which prevents any reliable fit of Eq. (4.1) to the experimental data to accurately determine the $\bar{R}_g$ and ν-values. The low-Q feature observed is indicative for the presence of extremely large objects in the solutions.

To discard the hypothesis that the small angle contribution could be an artifact of the kind of isotopic mixtures used, we also measured a solution of 35 mg/ml (about half the overlap concentration) of Mi-SCNPs in dDMF. Figure 4.14(b) shows that the data obtained are also clearly affected by a strong increase of the intensity at small angles. Thus, there seems to be a strong tendency of SCNPs to aggregate in concentrated solutions.

From the slope of the curves in the fractal regime at intermediate Q-values we defined what we called an effective scaling exponent ν_{eff}. The inset in figure 4.14 displays the such obtained values. This parameter somehow should reflect the scaling exponent of the single-chain nanoparticles, but could be severely affected by (i) uncertainties in the subtraction of the high incoherent background; (ii) the low-Q contribution from the aggregates and, in the case of the measurements of the Mi-SCNPs in dDMF at 35 mg/ml, by the structure factor.

C. DLS on solutions crowded with SCNPs

Given the evidences for the presence of aggregates in the solutions with high SCNPs concentrations, a systematic investigation was performed by DLS to determine under which conditions the SCNPs aggregate and whether the complexes formed are again soluble upon dilution. This study was carried out on solutions of Mi-SCNPs of M_w = 124 kg/mol (c^*_{SCNP} =68 mg/ml) and Cu-SCNPs of M_w = 272 kg/mol (c^*_{SCNP} = 37 mg/ml).

First, solutions of different concentrations (5, 10, 20 and 30 mg/ml) were prepared. DLS revealed unimolecular features for $c \leq 20$ mg/ml and contributions from large objects for 30 mg/ml for the Mi-SCNPs [figures 4.15(a) and (b)]; in the case of Cu-SCNPs, isolated macromolecules were found for $c \leq 10$ mg/ml, while aggregates were present already for 20 mg/ml [figures 4.15(c) and (d)]. Thus, SCNPs seem to aggregate for concentrations above $c^*_{SCNP}/3$ approximately.

In order to check whether the aggregates are soluble again, we started from solutions at 200 mg/ml. These were progressively diluted again, up to 5 mg/ml in different steps. We found that Cu-SCNPs solutions form gel-like structures in the concentration range $200 \geq c \geq 50$ mg/ml [figure 4.16(a)]; at lower concentrations ($c \sim 30$ mg/ml) the system behaves as a viscous liquid and becomes liquid-like for $c \leq 30$ mg/ml, as can be seen in figure 4.16(b).

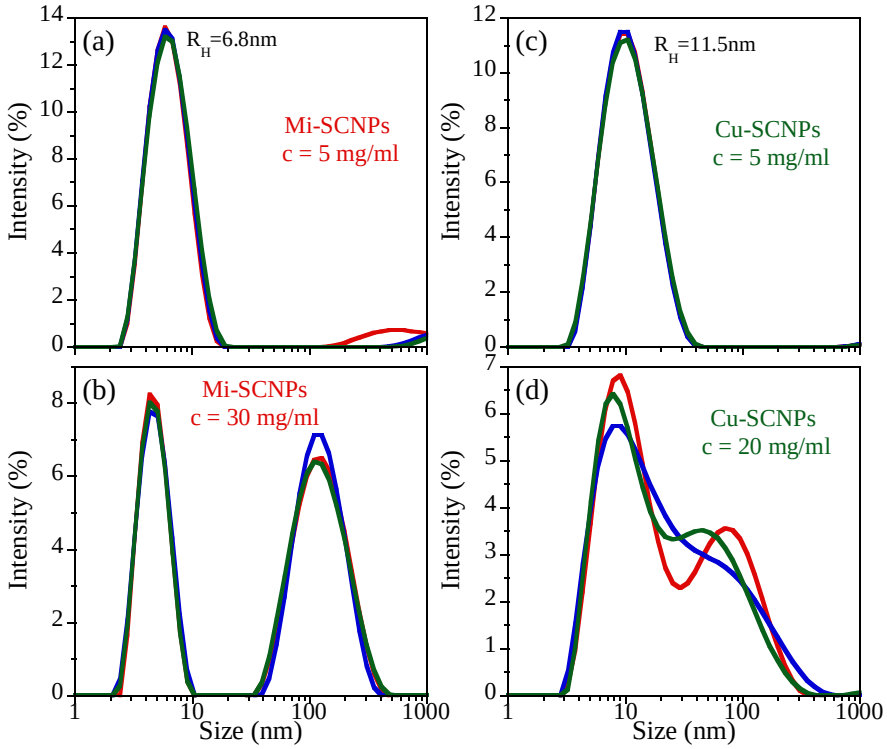

Figure 4.15: DLS results on solutions at 5 mg/ml of Mi-SCNPs (a) and Cu-SCNPs (c) showing unimolecular features; aggregates at 30 mg/ml for Mi-SCNPs (b) and at 20 mg/ml for Cu-SCNPs (d). Different curves correspond to different measurements performed on the same sample.

However, as it is shown in figure 4.16(c), only after several (~8) days unimolecular entities are obtained. Recovering solutions of isolated macromolecules turns to be impossible for Mi-SCNPs systems. In this case, the aggregates cannot be dissolved, even under high dilution conditions (5 mg/ml), as can be seen in figure 4.16(d) and waiting for very long times [figure 4.16(e)].

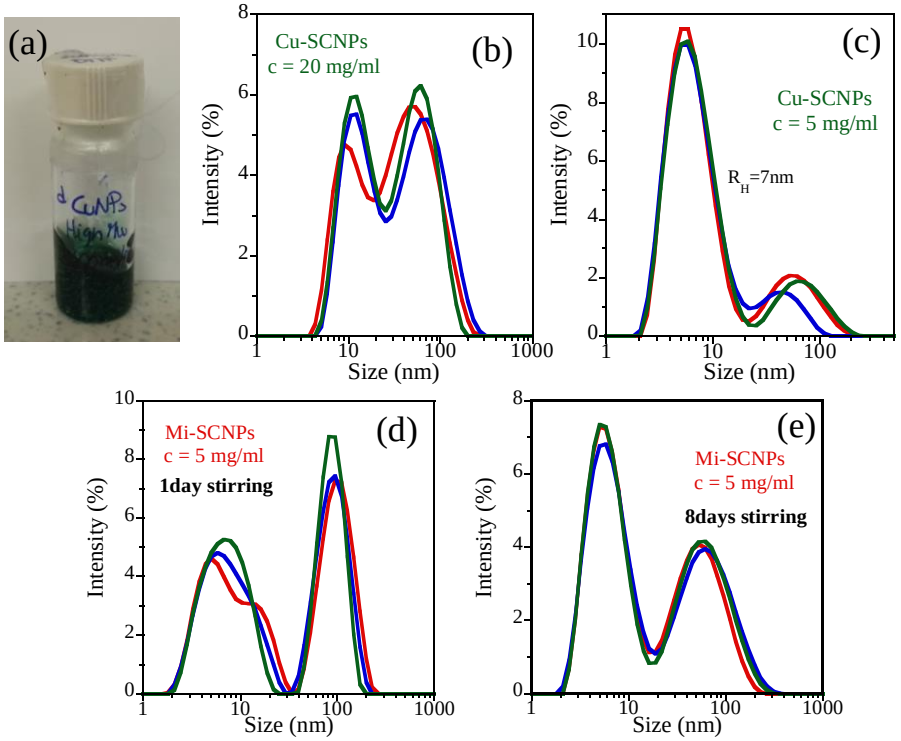

Figure 4.16: (a) Illustration of Cu-SCNPs solution at 200 mg/ml showing a gel structure. DLS results on liquid Cu-SCNPs at 20 mg/ml (b) and recovery of unimolecular entities of Cu-SCNPs at 5 mg/ml (c). DLS results on Mi-SCNPs at 5 mg/ml displaying the presence of aggregates after 1 day (d) and 8 days stirring (e). Different curves correspond to different measurements performed on the same sample.

We also diluted the starting 200 mg/ml solutions to 5 mg/ml in one single shot. The systems with Cu-SCNPs recovered the unimolecular character after one week, as can be seen in figure 4.17(a); however, for Mi-SCNPs solutions waiting did not help: even after two weeks the aggregates persisted [figure 4.17(b)].

We note that similar experiments carried out on low-M_w Mi-SCNPs solutions gave the same results as those obtained for the M_w = 124 kg/mol Mi-SCNPs above described.

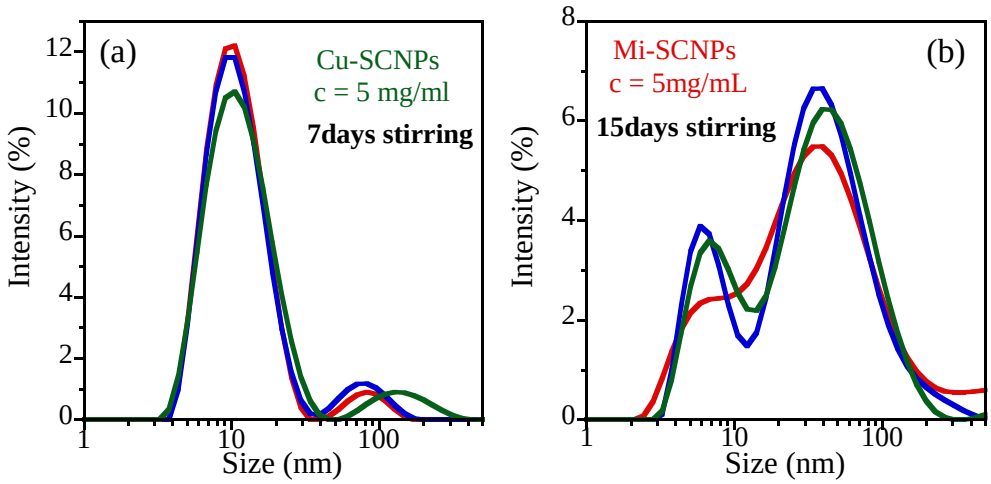

Figure 4.17: DLS results on solutions diluted to 5 mg/ml in one single shot. (a) Cu-SCNPs after 7 days stirring and (b) Mi-SCNPs after 15 days stirring. Different curves correspond to different measurements performed on the same sample.

SANS and DLS experiments have demonstrated the formation of supramolecular aggregates for concentrated solutions of SCNPs, namely for concentrations above approx. $c^*_{SCNP}/3$. This aggregation phenomenon is absent in the solutions crowded with linear PMMA chains, where the concentrations of SCNPs remains low. Thus, SCNPs tend to react with similar entities above a concentration threshold. The mechanism presumably consists of inter-molecular reactions mediated by functionalized AEMA groups of different SCNPs that do not participate in the intra-molecular cross-link network generated during the SCNPs synthesis. In concentrated conditions, the probability of close spatial proximity between such unreacted groups increases and interactions might occur. We note that the creation of a single inter-molecular bond leads already to the apparition of a dimer.

The reversibility of the aggregation process is determined by the kind of reaction involved in the cross-linking synthesis route. Cu-complexation is a reversible mechanism leading thus to aggregates of transitory character. On the contrary, the covalent nature of the cross-links induced in the synthesis by Michael addition leads obviously to also permanent bonds between the functionalized groups of different macromolecules, and consequently to irreversibility of the aggregation process.

For our experimental investigation on the role of crowding on the morphology of SCNPs, this aggregation phenomenon has posed strong difficulties, preventing reliable conclusions from the SANS experiments. We note for example that the effective values of the scaling exponent deduced from the slope of the SANS curves in the intermediate Q-range (denoted as ν_{eff}) are much higher than those obtained from the crowding with linear (and inert) dPMMA crowders. Though they present the same tendency to decrease with increasing concentration above c^*_{SCNP}, we must conclude that they cannot be considered as trustworthy.

D. Molecular Dynamics (MD) Simulations

A simple bead-spring model of the SCNPs in good solvent conditions was simulated. A total of 40 SCNPs were generated by irreversible intra-molecular cross-linking of linear chains (precursors) with the same number of monomers (N=200) and functional reactive groups (40%). Linear chains with different size (10, 50 and 800 monomers denoted as LIN10, LIN50 and LIN800, respectively) as well as the 200-monomers SCNPs themselves (NP) were used as crowders. Figure 4.18 shows the average radius of gyration and the scaling exponent of the

simulated SCNPs as function of the total monomer concentration of the solution, c.

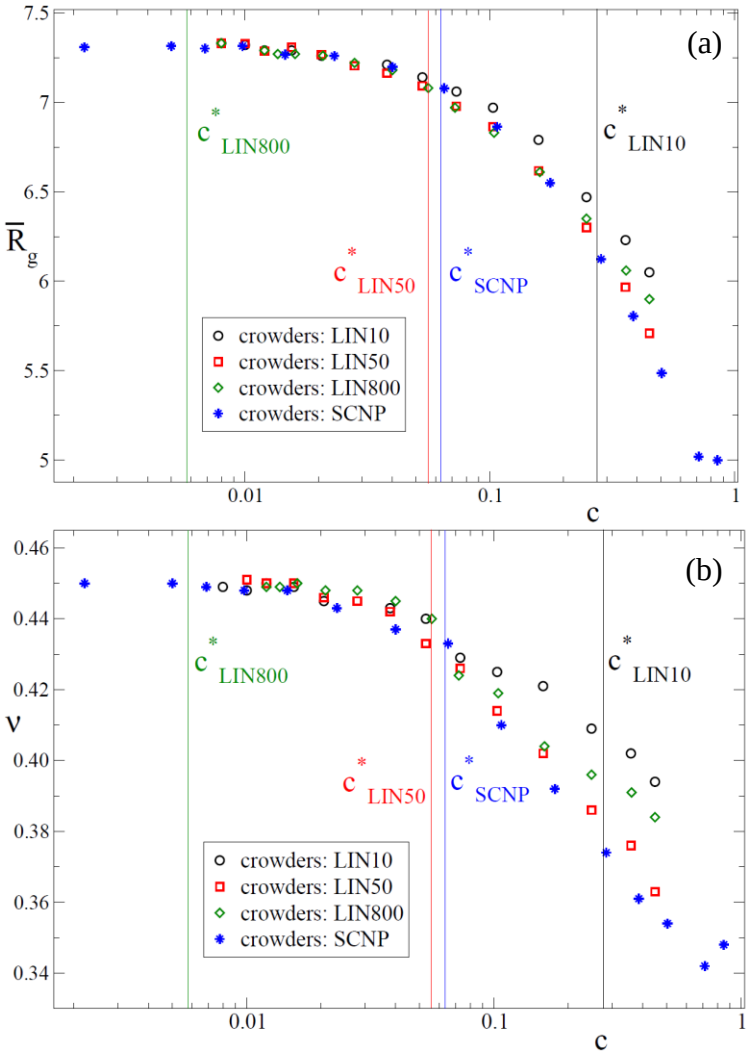

Figure 4.18: Average radius of gyration (a) and scaling exponent (b) of the simulated SCNPs when linear precursor chains and SCNPs are used as crowding element, as function of the total monomer concentration of the solution. The vertical lines mark the location of the overlap concentration, c^*, of the crowders.

As can be seen in the figure, both the radius of gyration and the scaling exponent remain unperturbed until the total concentration of monomers is above the overlap concentration of the SCNPs (c^*_{SCNP}), independently of the size of the crowder used. This result supports that the key magnitude determining the crossover from an almost unperturbed chain conformations in dilute solutions toward a continuous collapse of the macromolecule with increasing crowding is the overlap concentration of the SCNPs, c^*_{SCNP}.

For large crowders, the value of c^* is very small: the chains 'see' each other at low concentrations, when the number of segments per solution volume unit is still very small. Only when the concentration of macromolecular segments around a SCNP –in its immediate neighboring region– is high enough, this SCNP starts feeling topological interactions with other entities, as when it is surrounded by similar SCNP at its own overlap concentration.

An interesting observation from the simulations is that increasing the size of the linear crowders at fixed high monomer concentration initially leads to a stronger collapse of the SCNPs, but when the crowders become too large (several times the SCNP size) this trend is reversed. The microscopic mechanism for such a non-monotonicity of the SCNP collapse behavior is not clear, but it might be mainly related with the spatial arrangement of the crowder monomers within the cloud of the SCNP. By increasing the crowder size, the number of such possible arrangements decreases due to connectivity constraints. This leads to the depletion of the SCNPs –which need to form more compact configurations from the uncrossable long segments of the crowders. When the latter become much longer than the SCNP size, there is a relative swelling of the SCNPs with

respect to the solutions with shorter crowders. A plausible explanation for such a relative swelling might be that when linear crowders are too long the only way to pervade the volume occupied by the SCNP is through some threading events.

The simulations suggest that with small linear crowders the effect on the SCNP conformation at high concentrations is less important. This could be due to the higher adaptability of the smaller chains to the interstices between the SCNPs. Therefore, the constraints imposed by these short chains would be less pronounced than those exerted by longer linear chains or, even more, by equivalent SCNPs, which are internally more rigid than the linear counterparts.

4.3.6. Structure Factor

Based on the previous results, the decrease of ν and $\bar{R}_g$ shown by solutions of SCNPs with increasing concentrations in the range below $\sim c^*_{SCNP}/3$ (like that displayed in figure 4.8) has to be an apparent effect. This effect would be due to the fact that, if the concentration is increased, the interactions between the macromolecules start to be non-negligible and the structure factor of the centers of mass $S_{CM}(Q)$ deviates from unity. Under the hypothesis of unperturbed form factor and assuming the validity of Eq. (3.10) (in chapter 3) for our solutions, the structure factor of the centers of mass at a given concentration c, $S_{CM}(Q)$, can be calculated as follows:

$$S_{CM}(Q,c) \approx \frac{c_0}{c} \frac{\left(\frac{d\sum(Q,c)}{d\Omega}\right)_{coh}}{\left(\frac{d\sum(Q,c_0)}{d\Omega}\right)_{coh}} \tag{4.6}$$

This equation involves the cross sections measured for such concentration c and that measured at a reference low concentration c_0 –for which $S_{CM}(Q, c_0) = 1$. We have applied Eq. (4.6) to obtain the structure factor of the centers of mass at the highest concentration investigated (c=25 mg/ml), considering the lowest concentration (2 mg/ml) as reference c_0. The results are shown in figure 4.19. The structure factor of the centers of mass of the high-molecular weight SCNPs shows appreciable deviations from unity, especially in the low-Q regime. The main feature is a very broad peak, which indicates broadly distributed inter-particle distances.

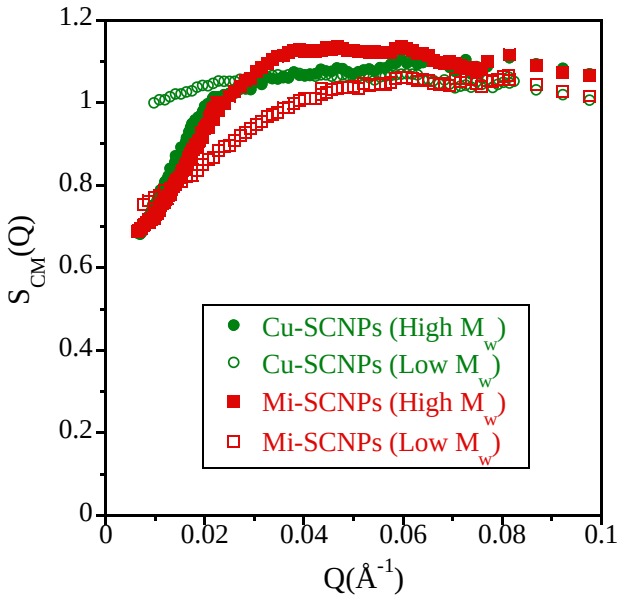

Figure 4.19: Static structure factor of the centers of mass deduced from the SANS measurements at 25 mg/ml: Cu-SCNPs (green circles) and Mi-SCNPs (red squares). Filled symbols are high M_w samples and empty symbols low M_w samples. Data obtained at 2 mg/ml have been used as reference.

The results obtained on the low-molecular weight samples are also included in figure 4.19. Cu-SCNPs show a much weaker interaction between the SCNPs than the low molecular weight Mi-SCNPs and the high molecular weight data at the same concentration.

4.3.7. Conclusion

The application of SANS and SAXS has proved the compaction of the macromolecules upon the creation of internal cross-links. In particular, we have been able to follow the changes in the chain conformation and dimension during bond formation. Despite the patent compaction, the SCNPs obtained by different routes exhibit a far from globular topology in good solvent. The origin of the sparse conformation observed for SCNPs through conventional synthesis routes were rationalized by MD-simulations. Interestingly enough, we note the similarity of the average value of the scaling exponent with those reported for intrinsically disordered proteins (IDPs). The analogies found between SCNPs and IDPs motivated the use of SCNPs as model systems to study crowding effects. We note that crowding is inherently present in the cellular environment.

Experimental crowding of SCNPs with increasing concentration of the same species leads to unavoidable aggregation of the nano-objects for concentrations higher than about c*/3. This phenomenon is attributable to the apparition of inter-molecular cross-links between unreacted functionalized monomers. Depending on the reversible or irreversible character of the bonds involved in the internal cross-linking route followed for the SCNPs creation, the resulting agglomerates can be dissolved again or not.

For this reason, conclusive experimental observations about the impact of crowding on the SCNPs' conformation can only be extracted from the investigation realized on solutions where the macromolecular concentration was increased by adding linear non-reactive chains. Complementary MD-simulations were also considered. The main result from such a joint study involving experiments and MD-simulations is the univocal determination of the overlap concentration of the SCNPs as the key magnitude determining the onset of the crossover from unperturbed morphology at lower concentrations to an increasingly collapsed state at higher concentrations. This has been demonstrated by experiments on solutions with SCNPs of different sizes crowded with linear macromolecules of both, smaller and larger dimensions than the SCNPs. These results have been nicely corroborated by extensive MD-simulations on mixtures of SCNPs and linear chains, covering a large range of relative sizes. In addition, free from unwanted inter-molecular cross-linking reactions, MD-simulations have extended this investigation to the case where the environment of the SCNPs is crowded also with similar entities.

Having established the insensitivity of SCNPs' conformation to crowding in the concentration range $c \leq c^*_{SCNP}/3$ approximately, we have calculated the static structure factor arising from centers of mass correlations from SANS measurements. This information is very important in order to perform a proper analysis of the dynamic data, as it will be shown in the last section of this chapter.

4.4. Dynamics of SCNPs

4.4.1. Introduction

Though DLS is routinely applied in the home laboratories to characterize the center of mass diffusion of SCNPs, the internal dynamics of these macromolecules in dilute solution has not been addressed up to now. Here, we present for the first time a study on the chain dynamics of these nano-objects by means of scattering techniques. To have a complete picture and be in position of a quantitative analysis of the results, three kinds of scattering techniques are combined: (i) SANS, to properly characterize the size and conformation of the macromolecules, (ii) DLS, to get the center of mass diffusion coefficient ($Q \rightarrow 0$ limit) and (iii) NSE, addressing the dynamics at local length scale strongly affected by the internal degrees of freedom.

In a first step, we perform both, a phenomenological and a Zimm model-like analysis on the chain dynamics of linear polymer precursor (low molecular weight, 52 kg/mol) in solution. These results are used as reference to compare to NSE data of Mi-SCNPs and Cu-SCNPs in solution (same M_w as the linear precursor). The chain dynamic structure factor of both SCNPs is also described by the Zimm model and its modifications. Moreover, we perform an 'academic exercise' on chain dynamics of high molecular weight (272 kg/mol) Mi-SCNPs considering two limiting scenarios for Zimm analysis. The form factor and the structure factor of all these samples have been properly determined by SANS, as previously described in section 4.3 of this chapter. Prior to the description of the dynamical studies, some theoretical approaches concerning the chain dynamics of polymers are provided.

4.4.2. Chain Dynamics: Theoretical approaches

At large length scales, coarse-grained theoretical models are adequate to describe single chain properties including dynamics. In the bulk, the Rouse model is the standard theoretical approach while its extension by considering hydrodynamic interactions –the so-called Zimm model– can be applied to polymer solutions.

The Rouse model[27] describes the melt chain dynamics considering the conformational entropy as the only source for restoring forces which stabilizes excursions from equilibrium. The contribution of the surrounding chains is introduced as a stochastic background creating also a friction –characterized by the friction coefficient ξ– on each segment.[24, 27] The N beads connected by bonds of length ℓ of the coarse-grained Gaussian chain are connected by entropic springs. The main variable is the Rouse rate W, determined by the balance between the entropic forces and the friction $W = 3k_BT/(\ell^2\xi)$ (k_B: Boltzmann constant). The resulting Langevin equation can be solved by transforming to the normal ('Rouse') coordinates

$$\vec{X}_p(t) = \frac{1}{N}\sum_{i=1}^{N} \vec{R}_i(t) \cos\left[\frac{p\pi}{N}\left(i - \frac{1}{2}\right)\right] \tag{4.7}$$

where $\vec{R}_i(t)$ is the position vector of the i^{th} bead along the chain and p is the mode number p ($p = 0, \dots, N-1$). The zeroth mode gives the position of the center of mass of the chain and the others are associated with internal motions with a 'wavelength' of the order of N/p. The mode correlators decay

exponentially according to a spectrum of relaxation modes with characteristic times τ_p given by:

$$\tau_p = \frac{\xi \bar{R}_e^2}{3\pi^2 k_B T p^2} = \frac{N^2}{W\pi^2 p^2} \tag{4.8}$$

The Rouse dynamic structure factor is expressed as:

$$\frac{S_{chain}(Q,t)}{P(Q)} = \frac{1}{N} exp(-Q^2 D_{CM} t) \sum_{n,m}^{N} exp\left(-\frac{1}{6} Q^2 B(n,m,t)\right) \tag{4.9}$$

in terms of the translational diffusion coefficient $D_{CM} = W\ell^4/(3N\ell^2)$ and the correlators $B(n,m,t)$:

$$B(n,m,t) = |n-m|\ell^2 + \\ + \frac{4\bar{R}_e^2}{\pi^2} \sum_{p=1}^{N-1} \frac{1}{p^2} \cos\left(\frac{\pi p n}{N}\right) \cos\left(\frac{\pi p m}{N}\right) \left[1 - exp\left(-\frac{t}{\tau_p}\right)\right] \tag{4.10}$$

The validity of the Rouse model has been checked by neutron scattering (in particular, by NSE[28-29] experiments) on a variety of polymers. It provides a very good description of the experimental data, within the range of application. However, at local length scales (high Q-values), the Rouse model fails; there, its simplifying assumptions cease to be valid and the microscopic details come into play. Ingredients like chain stiffness, rotational potentials, local relaxations across the rotational barriers leading to an internal viscosity emerge at short length scales.[27-28, 30] On the other hand, the model also fails for long chains at

long times. The uncrossability of macromolecules leads to topological constrains ('entanglements') that restrict laterally the chain motions. Such 'self-confinement' effect –responsible in fact for the singular viscoelastic character of polymers– is captured by the 'tube' concept invoked in the reptation model:[31] for long times, chain fluctuations take place within a fictitious tube of diameter d_{tube} parallel to the chain profile. NSE experiments on labeled entangled polymeric samples have provided the microscopic evidence for the existence of such confinement effects.[28] They manifest themselves in more moderate decays of the chain structure factor than the Rouse functions, leading to long-time plateaus in $S_{chain}(Q,t)$ from which d_{tube}-values can be extracted.

The Zimm model[32] is the standard theoretical framework to describe the chain dynamics of flexible polymers in dilute solution.[24, 28] It is the counterpart of the Rouse model, where the chain beads are also affected by hydrodynamic interactions. In this case, the mode correlators are given by

$$\tau_p^Z = \frac{\eta \bar{R}_e^3}{\sqrt{3\pi} k_B T} p^{-3\nu} \tag{4.11}$$

where η is the viscosity of the solvent. Note that this expression considers the general case of a generic scaling exponent ν ($\nu = \nu_F$ in good solvent). The Zimm dynamic structure factor is still expressed by Eq. (4.9), now in terms of the correlators $B(n,m,t) = B^Z(n,m,t)$:

$$B^Z(n,m,t) = |n-m|^{2\nu}\ell^2 + \\ + \frac{4\bar{R}_e^2}{\pi^2}\sum_{p=1}^{N-1}\frac{1}{p^{2\nu+1}}\cos\left(\frac{\pi pn}{N}\right)\cos\left(\frac{\pi pm}{N}\right)\left[1-exp\left(-\frac{t}{\tau_p^Z}\right)\right] \quad (4.12)$$

Regarding the center of mass diffusion, for a linear polymer chain in good solvent ($\nu = \nu_F$) the Zimm model predicts $D_{CM}^Z = 0.203k_BT/(\eta\bar{R}_e)$.[32] As in the case of the melt, deviations from Zimm-like dynamics are found at local length scales in e.g. polyisobutylene[33] and, more markedly, for rigid polymers like polynorbornenes.[34] In fact, only for extremely flexible polymers like poly(dimethyl siloxane)[33] or polyisoprene[34] the bare Zimm model seems to work properly up to high Q-values. To a large extent, the deviations can be attributed to dynamical stiffness.[30, 33-35] The internal friction originated from diverse sources –e. g. internal barriers, side-chain interactions, hindered dihedral rotations, or even hydrogen bonding– was implemented in the so-called Rouse/Zimm model with internal friction (RIF/ZIF) by Khatri and McLeish.[36] This ingredient is represented by a relaxation time τ_i which is added to the time of each mode in Eq. (4.8) or (4.11), respectively. The resulting characteristic time for the p^{th}-mode in the polymeric solution thus becomes $\tau_p^{ZIF} = \tau_p^Z + \tau_i$.

4.4.3. Chain Dynamics of Linear Precursor in Solution

A. Phenomenological approach

In order to obtain good signals by the NSE technique, the concentration investigated was 25 mg/ml. Figure 4.20(a) shows the DLS results of the precursor (M_w = 52 kg/mol) in solution, at the concentration measured by NSE. A single exponential function –assuming thereby a single diffusion coefficient–

accounts rather well for the functional form of the decay (see lines describing the data). Applying inverse Laplace transformation (e.g. the CONTIN program) (see, e.g.[37]) it is possible to extract an underlying distribution of diffusion coefficients $g[\log(D_{CM})]$, assuming:

$$\frac{S(Q,t)}{S(Q,0)} = \int g[\log(D_{CM})]\exp[-D_{CM}Q^2t]d[\log(D_{CM})] \tag{4.13}$$

For linear polymers, the origin of this distribution is the polydispersity in mass. Figure 4.20(b) shows the such deduced distribution. It is very narrow, in agreement with SEC results (see table 4.1) and the DLS data are well approximated by a single exponential. The average value of the diffusion coefficient for the linear polymer precursor is $D_{DLS} = 5.77\ \text{Å}^2/ns$.

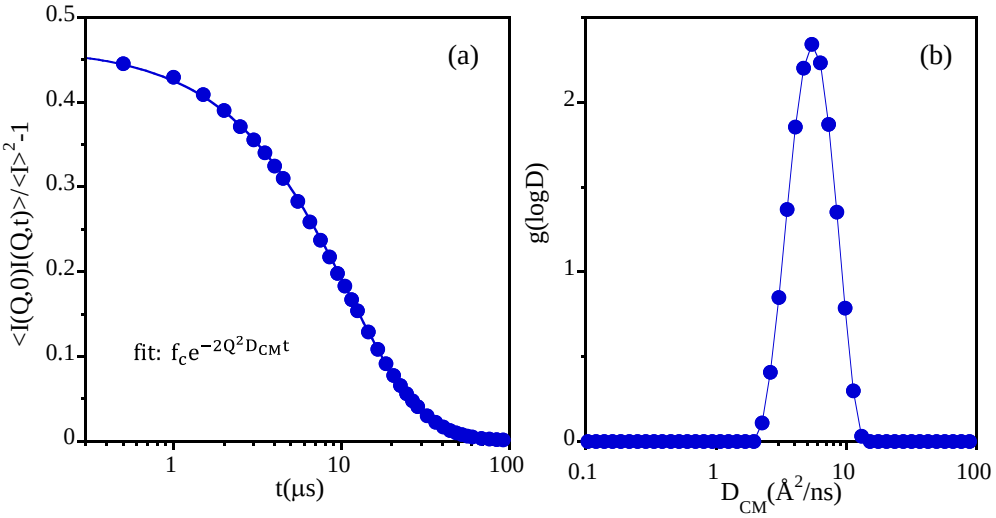

Figure 4.20: (a) DLS results on solutions of a PMMA-AEMA precursor. Line is the fit of single exponential function. (b) Distribution function of diffusion coefficients deduced from a CONTIN analysis of the experimental data; the line is just connecting points.

Now we turn to the more local length scales explored by the NSE experiments. The Q-range investigated by this technique ($0.03 \leq Q \leq 0.20\text{Å}^{-1}$) corresponds to the regime $1/\bar{R}_g \approx 0.02\text{Å}^{-1} < Q$. The NSE results on the linear precursor are presented in figure 4.21(a), where they are described, as a first rough approximation, by single exponential functions:

$$\frac{S_{chain}(Q,t)}{P(Q)} = \exp\left[-D_{eff}(Q)Q^2 t\right] \tag{4.14}$$

This simple parametrization allows for a first quantification of the dynamics of the sample through the effective diffusion coefficient parameter $D_{eff}(Q)$ and provides a rough idea about the nature of the contributions at the different length scales explored. As can be appreciated, exponential functions do not accurately reproduce the functional form of the single chain dynamic structure factors, which show a more stretched behavior, but could be considered as a rough first approximation to the problem. The parameter $D_{eff}(Q)$ deduced from the fits is represented as function of momentum transfer in figure 4.21(b) and compared with the center of mass diffusion coefficient determined from the DLS experiments, D_{DLS}. $D_{eff}(Q)$ clearly shows Q-dependent values larger than those determined by DLS. This enhanced mobility can be attributed to the contributions of internal modes (superimposed to the translational motion), that become apparent when exploring the proper length scales by NSE.

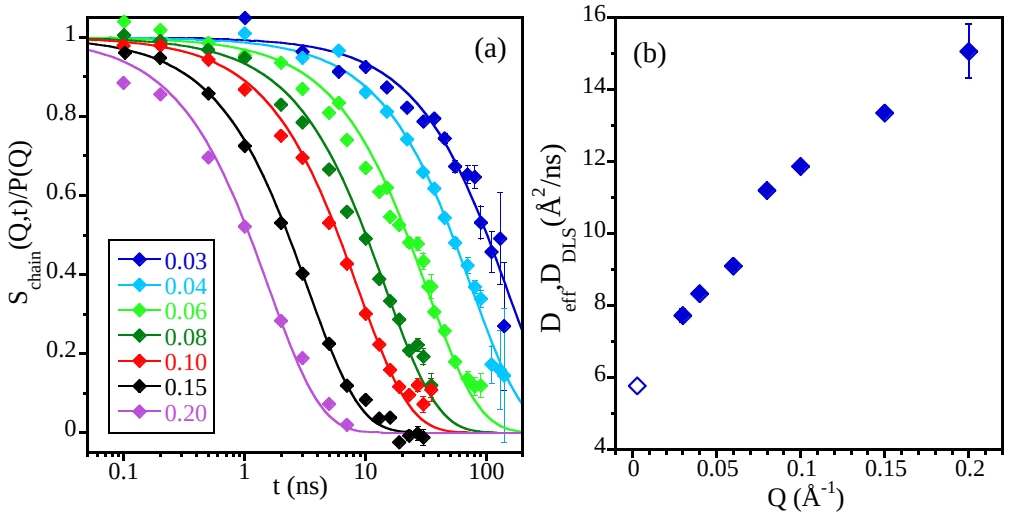

Figure 4.21: (a) NSE-results on precursor solutions at the different Q-values indicated in $Å^{-1}$. Lines are fits of single exponentials to the experimental data. (b) Wave-vector dependence of the effective diffusion coefficient D_{eff} deduced from the fits to the NSE-results. Empty symbol correspond to the value obtained for the diffusion coefficient from DLS measurements D_{DLS} at the same concentration (25 mg/ml).

B. Analysis in terms of the Zimm model

The NSE results on linear macromolecules were analyzed in terms of the Zimm model. Fixing the experimentally determined value for D_{CM} from the DLS study, the dynamic structure factor predicted by the Zimm model [Eqs. (4.9) with (4.12) and (4.11)] was calculated for a linear chain of $N = 370$ beads mapping the 'effective' monomers in the precursor [since this is a copolymer, we defined an 'effective' monomer as a ($MMA_{0.63}AEMA_{0.37}$) unit]. The value of $\bar{R}_e = 19.2\ nm$ was deduced from Eq. (4.2) by using the SANS information ($\bar{R}_g = 7.3$ nm and $\nu = 59$). The resulting theoretical curves are shown in figure 4.22. They describe well the experimental data for the two lowest Q-values investigated, but for $Q \gtrsim 0.06 Å^{-1}$ the model predicts a much more pronounced decay of the dynamic

structure factor. Obviously, approaching local length scales the dynamics strongly deviates from pure Zimm behavior.

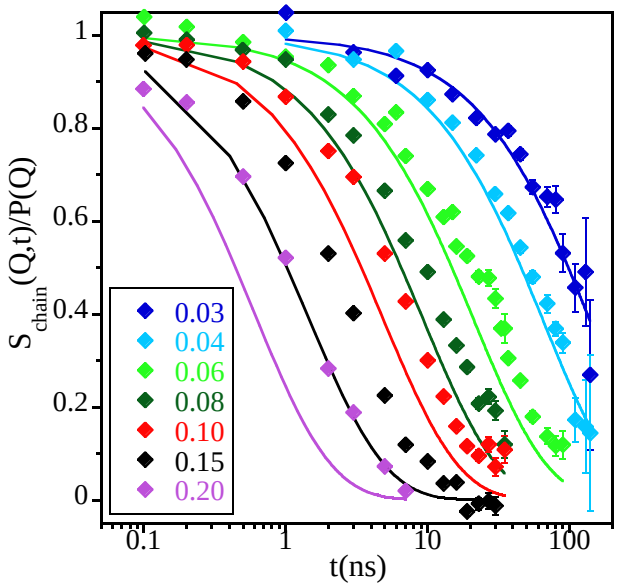

Figure 4.22: Fits of the Zimm model to the NSE results on the precursor solution at the different Q-values indicated in $Å^{-1}$.

The above introduced ZIF model (Eqs. (4.9) and (4.12) with $\tau_p = \tau^{ZIF} = \tau_p^Z + \tau_i$) successfully describes the precursor data [figure 4.23(a)] by choosing $\tau_i = 47\,ns$. The internal friction ingredient may also easily be introduced by restricting the modes contributing to the chain relaxation, i.e., considering in Eq. (4.12) modes up to a given maximum mode number p_{max}. This mode cutoff could be interpreted in terms of virtually rigid subcoils with all internal modes suppressed.[34] A good description (very similar to that obtained by the ZIF model) for the precursor is found by applying $p_{max} = 4$ [figure 4.23(b)]. This maximum mode number allows the estimation of the size of the virtually stiff

chain sections; their average end-to-end radius would be given by $\bar{r}_e^{stiff} = \bar{R}_e p_{max}^{-\nu}$,[34] i.e., $\bar{r}_e^{stiff} = 8.5$ nm. As we have previously seen, the statistical segment of the precursor has the same length as pure PMMA. For PMMA, the Kuhn length is 1.7 nm.[20] The dynamic rigidity thus extends over much larger length scales than the static stiffness of the chain.

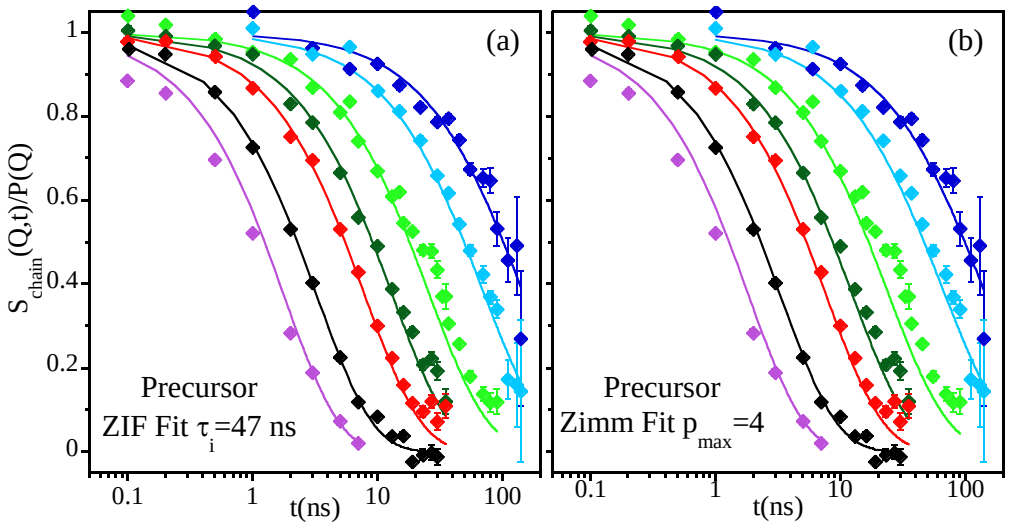

Figure 4.23: Fits of the different models to the NSE results on the precursor solutions at the different Q-values denoted in Fig. 4.22. (a) Zimm model with internal friction and (b) Zimm model restricted to the modes corresponding to the longest wavelengths, up to p_{max}.

The Zimm characteristic times used in the three approaches are represented in figure 4.24 as function of the wavelength of the mode, N/p. In the ZIF model, the drastic effect imposed by the mode cutoff p_{max} (equivalent to freeze the modes with $p > p_{max}$, i.e., $\tau^Z_{p>p_{max}} \equiv \infty$) enters in a smoother way. It is represented by a transition from solvent-friction dominated relaxation (high N/p-values) to

relaxation where internal friction dominates. This crossover occurs when $\tau_p^Z \approx \tau_i$.

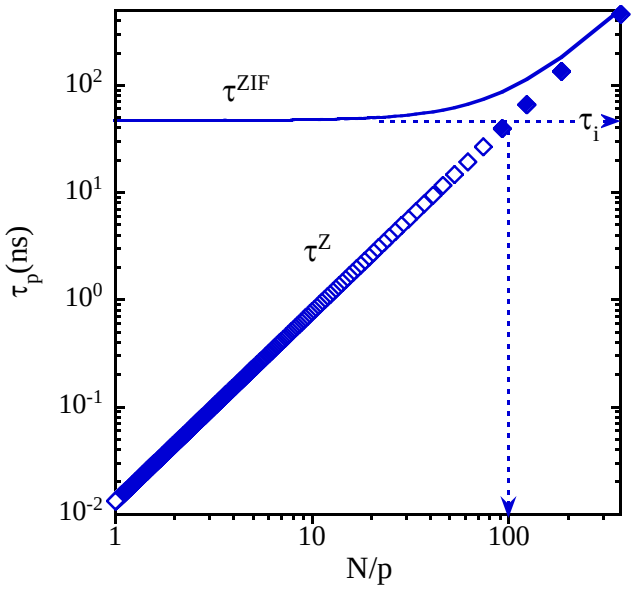

Figure 4.24: Characteristic times of the Zimm modes as function of the scaling variable N/p deduced for the precursor in solution. Only modes with mode-number below or equal to 4 highlighted as filled symbols would substantially contribute. Solid lines represent the characteristic times for the ZIF model. Dotted arrows mark the value of τ_i and the location of the crossover from solvent- to internal friction dominated relaxation for the precursor.

From this analysis, we can conclude that the dynamics of the linear precursor macromolecules in solution exhibits severe deviations from the pure Zimm-like behavior. These deviations could be attributed to internal friction effects that are not surprising, given the chemical nature of the backbone. Poly(methyl methacrylate) is already a rather rigid polymer; copolymerizing MMA monomers with AEMA units leads to a macromolecule with longer side groups scattered

along the chain, that are expected to hinder even more the conformational transitions of the polymer.

4.4.4. Chain Dynamics of SCNPs in solution

A. Phenomenological approach

Low molecular weight Mi-SCNPs and Cu-SCNPs in solution (same molecular weight as the previously presented precursor, M_w = 52 kg/mol) were measured by NSE at the same concentration as the linear precursor (25 mg/ml). The NSE experimental results of both single-chain nanoparticles are presented together in figure 4.25(a), where they are described by single exponential functions. As can be seen, the dynamic structure factor of Michael single-chain nanoparticles (Mi-SCNPs) decay at characteristic times systematically longer than those of copper single-chain nanoparticles (Cu-SCNPS).

The obtained effective diffusion coefficients, $D_{eff}(Q)$, from the fits are represented as function of momentum transfer in figure 4.25(b) and compared to the linear precursor. The center of mass diffusion coefficient determined from the DLS experiments, D_{DLS}, is also included for all the samples. Their values are rather similar. Contrarily, the $D_{eff}(Q)$-values deduced from NSE are systematically smaller in the case of the Cu-SCNPs than in the linear precursors, and even shorter in the case of Mi-SCNPs, indicating the slowing down of the dynamics upon internal cross-link of the macromolecules in the Q-range covered by the NSE experiments. Moreover, the difference seems to be amplified with increasing wave-vector. Thus, the impact of cross-linking in the dynamical features is clearly revealed by NSE. It becomes enhanced when exploring local

length scales, where the internal degrees of freedom of the macromolecule play a relevant role.

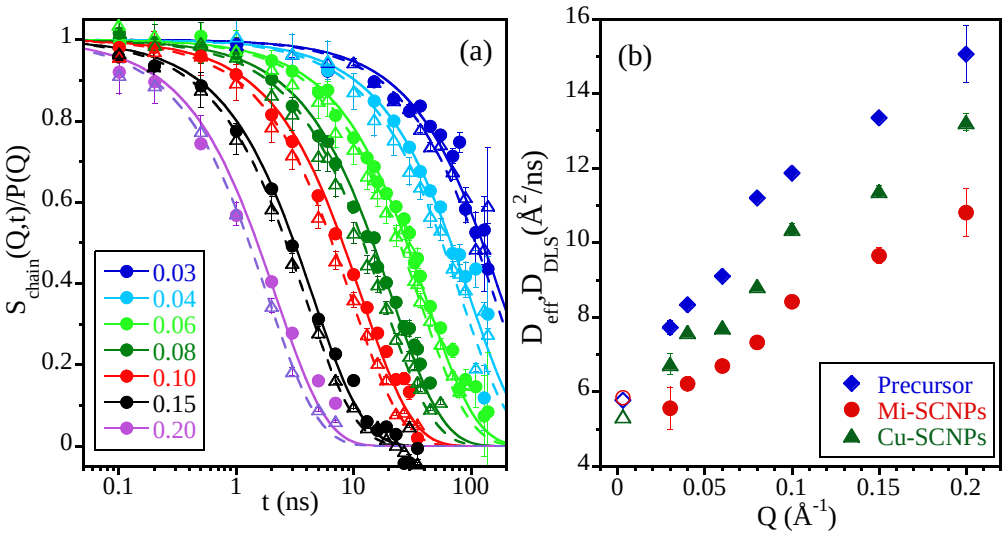

Figure 4.25: (a) NSE-results on Mi-SCNPs (filled circles) and Cu-SCNPs (empty triangles) solutions at the different Q-values indicated in $Å^{-1}$. Lines are fits of single exponentials to the experimental data. (b) Wave-vector dependence of the effective diffusion coefficient D_{eff} deduced from the fits to the NSE-results; precursor (blue diamonds), Mi-SCNPs (red circles) and Cu-SCNPs (green triangles). Empty symbols correspond to the values obtained for the diffusion coefficient from DLS measurements D_{DLS} at the same concentration (25 mg/ml).

It is clear that the dynamic structure factor of macromolecules in the NSE window has two contributions: one from the translational diffusion and another one from the relaxation of the internal modes. Moreover, in general, the translational diffusion coefficient of particles in solution depends on Q and concentration. It can be written as

$$D_{CM}(Q,c) = \frac{D_0 H(Q,c)}{S_{CM}(Q,c)} \tag{4.15}$$

where D_0 is the self-diffusion coefficient at infinite dilution and $H(Q,c)$ is the hydrodynamic factor. The hydrodynamic factor is not easy to obtain and some approximations have to be made. We assume that is Q-independent: $H(Q,c) \approx H(c)$ –a hypothesis which is usually justified.[25, 38] Then, for a given concentration the product $D_0 H(Q,c) = D_0 H(c)$ is a constant. Taking into account Eq. (4.15), under this condition the product $D_{CM}(Q,c)S_{CM}(Q,c)$ is the same independently of the Q-value considered, and, if we are able to determine it for a given Q, it will be known for other Q-values. In particular we can consider the case $Q \to 0$. This is the situation in the DLS experiments. From the DLS experiments we have obtained $D_{DLS}(c) = D_{CM}(Q \approx 0, c)$ for the concentration investigated in the NSE experiments. On the other hand, from the SANS measurements we have determined the structure factor of the centers of mass $S_{CM}(Q,c)$ also at this concentration (figure 4.19). Thus, the diffusion coefficient at any other Q-value can be written as:

$$D_{CM}(Q,c) = \frac{D_{DLS}(c)}{\frac{S_{CM}(Q,c)}{S_{CM}(Q \approx 0, c)}} \tag{4.16}$$

The obtained results are displayed in figure 4.26(a). The weak minimum at $Q \approx 0.05$ Å^{-1} mirrors the broad maximum of the structure factor of the centers of mass. This kind of deGennes-like renormalization reflects the slowing down of the collective diffusion at length scales corresponding to equilibrium inter-particle distances and thus where the correlations between particles are most pronounced.

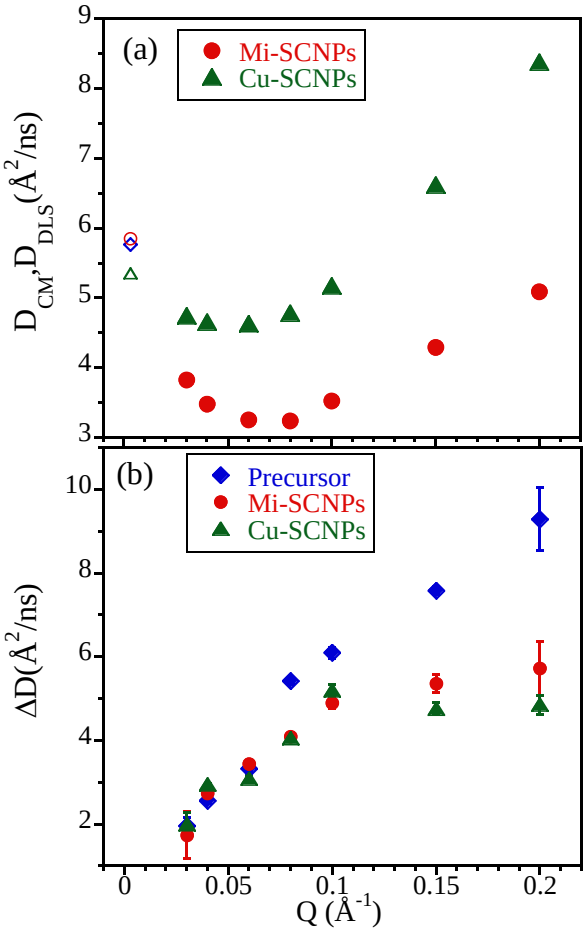

Figure 4.26: (a) Wave-vector dependence of the diffusion coefficient of the center of mass deduced for the Mi-SCNPs (red circles) and Cu-SCNPs (green triangles) from DLS (empty symbols) and SANS measurements as $D_{CM}(Q) = D_{DLS}S_{CM}(Q \to 0)/S_{CM}(Q)$. In (b) the difference between D_{eff} and the translational diffusion coefficients is represented for the precursor (blue diamonds), Mi-SCNPs (red circles) and Cu-SCNPs (green triangles).

The difference between the effective diffusion coefficients and the translational diffusion coefficients $\Delta D = D_{eff} - D_{CM}$ is represented in figure 4.26(b). This quantity represents to a first approach the importance of the internal degrees of freedom in the decay of the dynamic structure factor. The internal dynamics of

both SCNPs seems thus to be strongly suppressed with respect to that of the precursor for Q-values higher than 0.08 Å^{-1} and, in particular, above 0.1 Å^{-1}.

B. Analysis in terms of the Zimm model

In principle, the Zimm model and its modified versions are not directly applicable to a SCNP with topology different from that of a linear chain. However, we can still try to describe the dynamic structure factor of the Mi-SCNPs and Cu- SCNPs in the following way:

i. For the translational contribution, we use the center of mass diffusion coefficient D_{CM} above determined from the SANS and DLS experiments [Eq. (4.16), figure 4.26(a)]. We recall that its Q-dependence accounts for inter-macromolecular interactions.
ii. For the internal motions, we map the macromolecule to an effective linear chain with the same scaling exponent ($\nu = 0.52$ and $\nu = 0.54$) and dimension ($\bar{R}_g = 5.9$ nm, $\bar{R}_e = 14.7$ nm and $\bar{R}_g = 5.8$ nm, $\bar{R}_e = 14.7$ nm) as deduced from SANS for the Mi-SCNPs and Cu-SCNPs, respectively. Coarse-grained MD-simulations justify such a mapping of the large-scale dynamics of the topologically complex SCNPs to the Zimm dynamics of an effective linear chain.[39]

With these two assumptions, the Zimm scenario has been applied to the NSE results on the SCNPs solutions. The resulting curves considering the simplest version of the Zimm model are shown in figure 4.27(a) and figure 4.27(d). As in the case of the linear precursor, the description is reasonable for low Q-values but definitely fails by approaching local length scales.

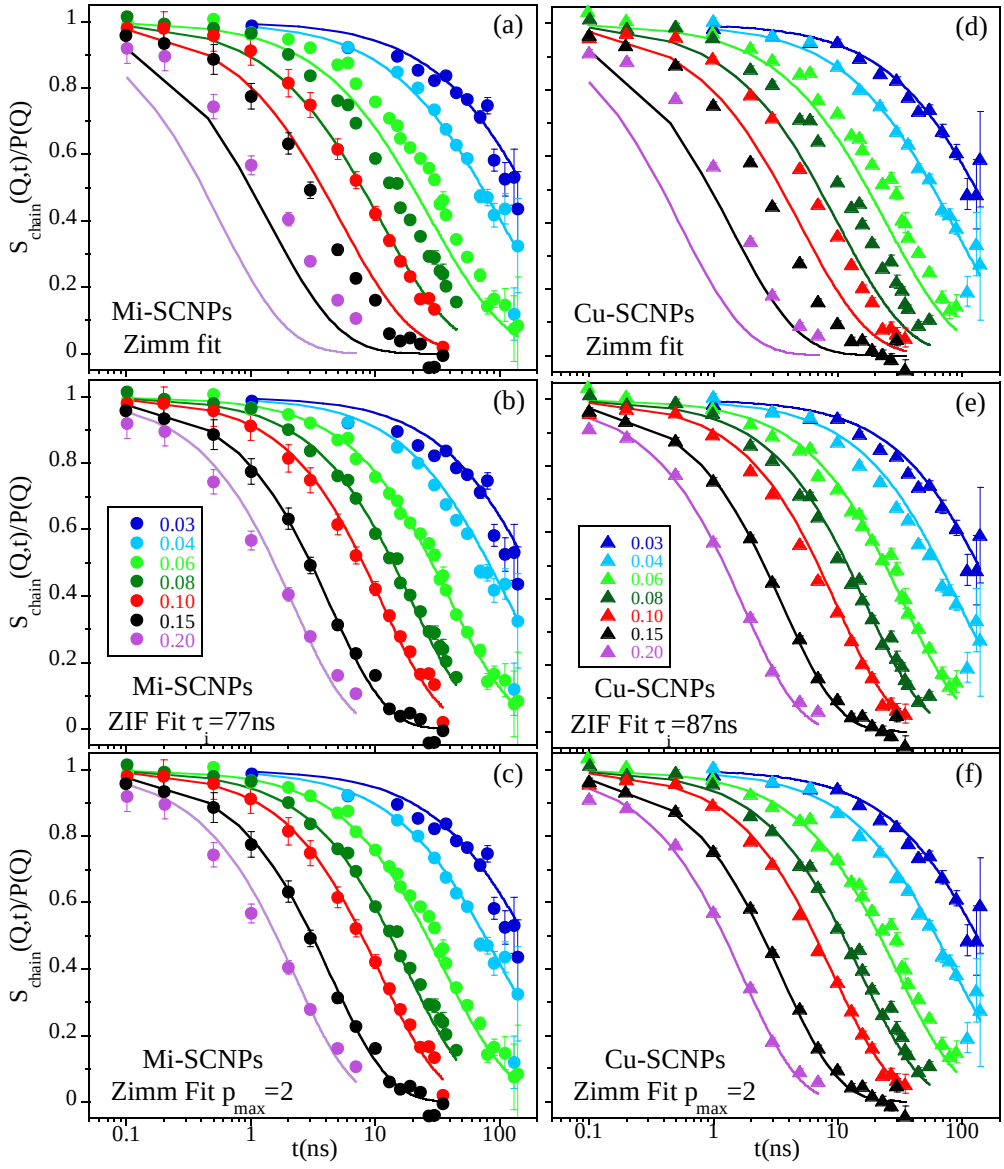

Figure 4.27: Fits of different models to the NSE results on the Mi-SCNPs (left panels) and Cu-SCNPs (right panels) solutions at the different Q-values denoted in $Å^{-1}$. (a) and (d): full Zimm model; (b) and (e): Zimm model with internal friction; (c) and (f): Zimm model restricted to the modes corresponding to the longest wavelength, up to p_{max}.

As can be seen in figure 4.28, the characteristic times for both SCNPs follow a weaker mode-number dependence (due to the smaller value of the scaling exponent) and are shorter in the long wavelength N/p region (due to the smaller dimensions) than those of the precursor. The first Zimm mode $p = 1$ corresponds to the rotational relaxation time. For the Cu-SCNPs it amounts to 206 ns (204 ns for Mi-SCNPs), while in the linear precursor this time is 461 ns.

We have also used the two modified versions of the Zimm model trying to improve the description of the dynamic structure factor of the SCNPs. If the ZIF model is applied a reasonable overall description of the data is achieved with $\tau_i = 77$ns for Mi-SCNPs [see figure 4.27(b)] and $\tau_i = 87$ns for Cu-SCNPs [see figure 4.27(e)]. These times are about twofold that obtained for the linear precursor. The p-dependent characteristic times are displayed in figure 4.28. The presence of internal cross-links shifts the crossover from internal-friction dominated relaxation to solvent-friction driven dynamics toward larger wavelengths for both SCNPs.

Finally, considering a cutoff for the mode summation, we obtain a satisfactory agreement with $p_{max} = 2$ for Mi-SCNPs and Cu-SCNPs [see figure 4.27(c) and figure 4.27(f); the used characteristic times are represented as filled symbols in figure 4.28]. Thus, the internal dynamics of the internally cross-linked macromolecules is extremely hindered. Here, the virtually rigid subcoils would span over about $\bar{r}_e^{Stiff} \approx 10$ nm –a large fraction of the macromolecules, taking into account their typical size $\bar{R}_e = 14.7$ nm. We note that the reflected rigidity is more marked than in the precursor, as it is shown in the schematic illustration included in figure 4.28.

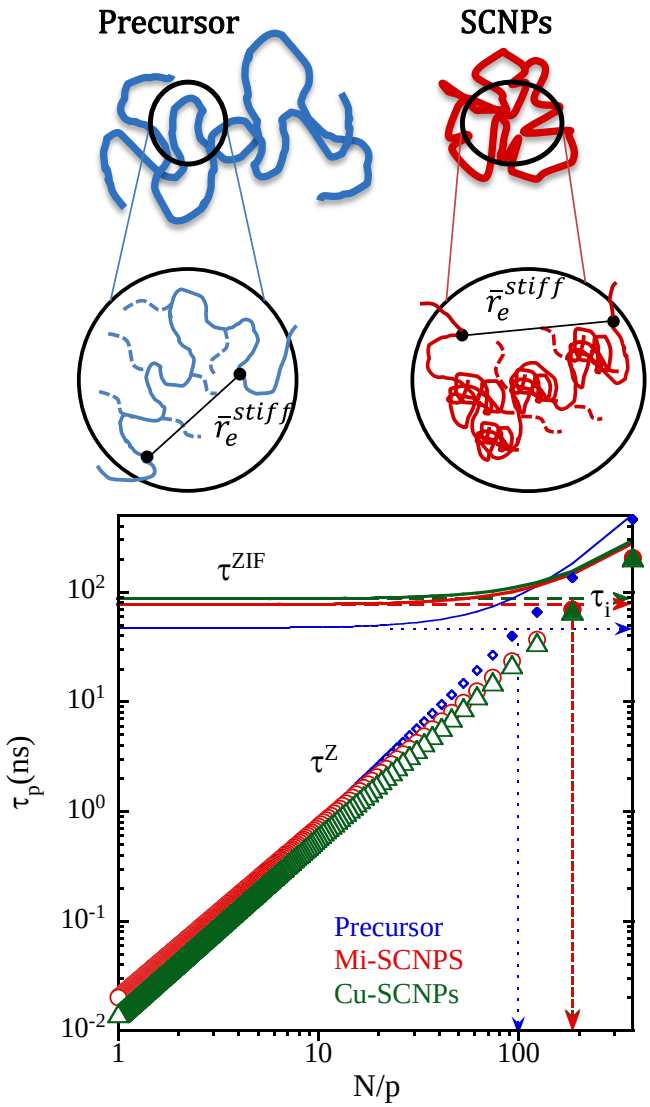

Figure 4.28: Schematic illustration of the virtually rigid subcoils that are present in precursor (blue) and SCNPs (red). Characteristic times of the Zimm modes as function of the scaling variable N/p deduced for the Mi-SCNPs (red circles) and Cu-SCNPs (green triangles) in solution. Precursor data (blue diamonds) is also included as reference. Only-modes with mode-number below or equal to 2 (Mi-SCNPs and Cu-SCNPs) and 4 (precursor) highlighted as filled symbols would substantially contribute. Lines represent the characteristic times for the ZIF model for the Mi-SCNPs (red), Cu-SCNPs (green) and precursor (blue). Dotted arrows mark the value of τ_i and the location of the crossover from solvent- to internal-friction dominated relaxation.

In summary, from this comparative analysis of the dynamics of both single-chain nanoparticles (Mi-SCNPs and Cu-SCNPs) and precursors in terms of similar theoretical approximations we can deduce a clear impact of the internal cross-linking on the chain dynamics. This is roughly the same independently of the particular internal cross-linking mechanism employed for the nanoparticle formation. The differences observed in the NSE spectra seem to arise from the distinct Q-dependence of the diffusion coefficient, i.e., from the interactions between different SCNPs reflected in the structure factor.

We now compare the dynamical features, revealed by NSE for our Mi-SCNPs and Cu-SCNPs, with those reported from the same kind of experiments for IDPs, in particular for the myelin basic protein (MBP) in D_2O.[25] In that work, a ZIF analysis was also carried out. Systematic deviations with respect to this model were found. In addition, a value of the characteristic time for internal friction was obtained, which was larger than that of the first mode of the pure Zimm model. From this finding, the breakdown of the Zimm model in that IDP was concluded. The slowing down of MBP motions with respect to a Gaussian polymer behavior was attributed to the fact that the protein is not completely unfolded, but retains a compact core and a folded secondary structure content of 44%.

As it has been mentioned above, the closeness of the ν-exponents in both kinds of macromolecules, IDPs and SCNPs, points to a similar degree of compaction. Recently, the analogies between their topological disorder and the common presence of locally compact, weakly deformable regions (domains) connected by flexible disordered chain segments have been discussed.[26] It could be expected

that the existence of such internal compartmentation would in both cases lead to a high internal friction. We note that the reported value of the characteristic time for internal friction in MBP ($\tau_i = 82$ ns) is nearly identical to that obtained here for the Mi-SCNPs ($\tau_i = 77$ ns) and for the Cu-SCNP ($\tau_i = 87$ ns), supporting this hypothesis.

On the other hand, due to the much smaller size of MBP ($\bar{R}_g \approx 3.4$ nm), even if the solvent viscosity in the protein solution is more than twofold higher than in our systems, the longest Zimm characteristic times in MBP are much shorter. In particular, the rotational time corresponding to the first mode is $\tau_{p=1} = 74$ ns for MBP and 204 ns for the Mi-SCNPs (206 ns for Cu-SCNPs). Thus, while for the small IDPs the overwhelming contribution of the internal friction prevents the application of the Zimm model or its more sophisticated versions, some of the later –like the ZIF– might still be plausible simplified scenarios for describing the dynamics of SCNPs in solution, as far as the dimensions of the nanoparticles are large enough.

4.4.5. An 'Academic Exercise': Exploring the Limiting Scenarios for Zimm Analysis

In the structural study of SCNPs above described, the experiments performed under crowding conditions revealed that the form factor remains constant at dilute conditions, i.e., below the overlap concentration. In the light of these results, we have applied the Zimm model and its modified versions to SCNPs in solution by considering that the form factor is not changing with the

concentration, and that the structure factor is not constant, which makes the diffusion coefficient Q-dependent, as described by Eq. (4.16).

However, without a detailed structural investigation on the crowding effects, it is not possible to unambiguously discern between that situation or an alternative scenario considering that the SCNPs changed their shape and size upon increasing concentration leading, to the observed reduction of the characteristic form factor parameters (figure 4.8) without appreciable interactions among them (uncorrelated center of mass positions). Though this extreme case now can be discarded, it is constructive to show the differences obtained when the two limiting cases are considered. This study gives an idea of the robustness of the application of the Zimm-based models and the sensitivity of the values of the different parameters involved on the assumptions made in the analysis procedure.

With this idea in mind, in this part of the chapter we apply the whole Zimm model by considering these two limiting scenarios: (i) the same conditions as with the already analyzed SCNPs, i.e., the structure factor is Q-dependent and the form factor is the one obtained at high dilution, namely $P(Q)_0$; (ii) the structure factor is constant, $S_{CM}(Q) = 1$, so the diffusion coefficient is independent of Q. Thus, taking into account Eq. (4.16), the diffusion coefficient is the one determined by DLS, $D_{CM}(Q, c) = D_{DLS}(c)$. In this case, the form factor is the one measured at the same concentration that the NSE experiments were performed, $P(Q)_c$.

Both scenarios are applied to NSE measurements on high M_w (272 kg/mol) Mi-SCNPs at 25 mg/ml. For this sample, the value of $D_{DLS}(c)$ was 3.38Å2/ns. The results of the SANS experiments can be found in figure 4.8. We first realize about the quite different pictures of the system invoked in both cases: in the first scenario, nano-objects of R_g^0 = 9.3nm (R_e^0 = 22nm) with a scaling exponent ν_0 = 0.46 interacting through the static structure factor shown in figure 4.19 are considered. This structure factor corresponds to broadly distributed inter-particle distances with an average value of about 15 nm. In the second scenario, the nanoparticles are sensitively compacted ($\nu_c \sim 0.41$) and smaller (R_g^c = 6.2 nm); their positions would not show an appreciable correlation pattern, i.e., they would be as a 'gas' of SCNPs. We now apply the different models based on Zimm dynamics to both cases.

In the first scenario, Eq. (4.16) was applied to obtain the Q-dependent values for the diffusion coefficient, $D_{CM}(Q, c)$. The resulting curves considering the simplest version of the Zimm model are shown in figure 4.29(a), and, not surprisingly, the model fails. If the ZIF model is applied a good description of the data is achieved with $\tau_i = 120$ ns [figure 4.29(b)] and finally, considering the 'mode-cutoff' model, we obtain a satisfactory agreement with $p_{max} = 4$ [figure 4.29(c)]. In this case, the size of the virtually stiff chain sections is $\bar{r}_e^{stiff} = 11.6$ nm, which covers half the size of the average end-to-end distance of the SCNPs.

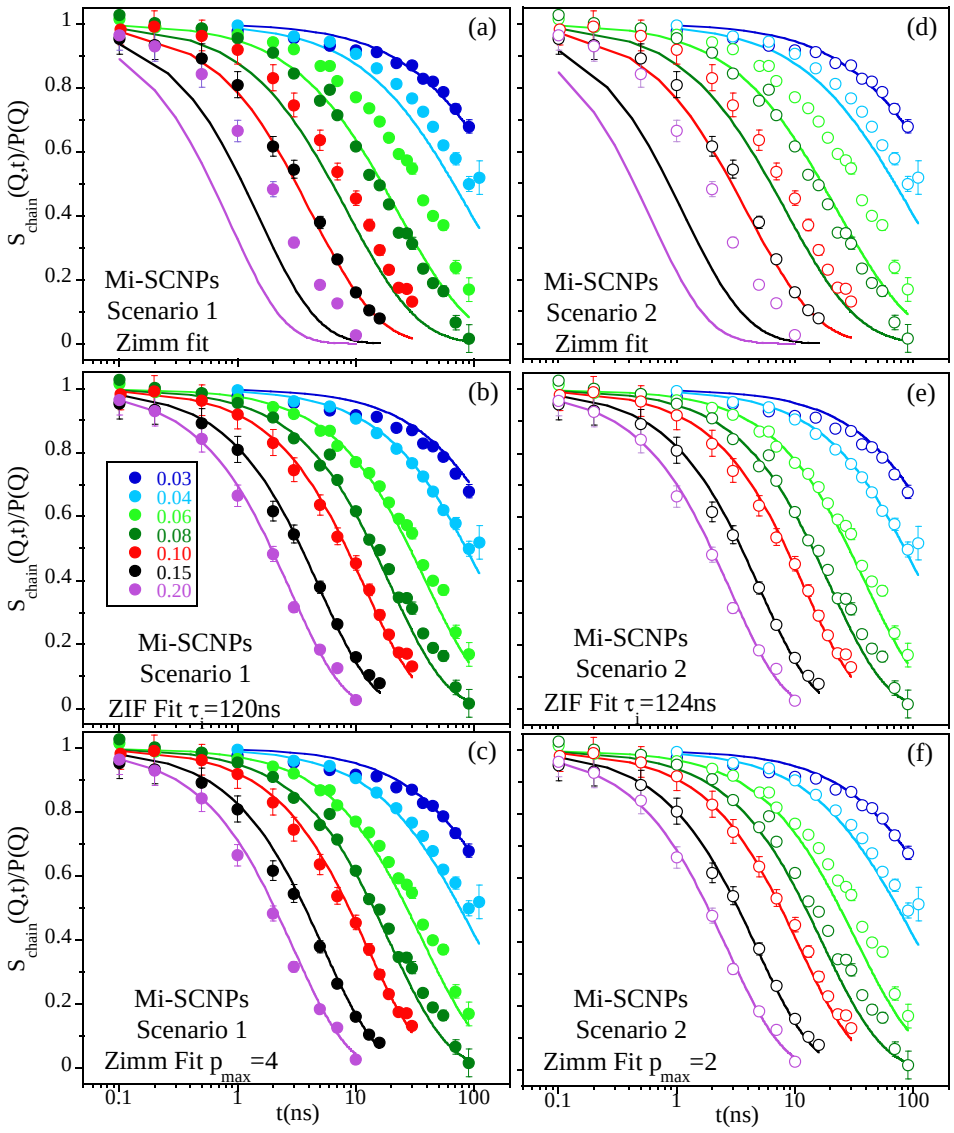

Figure 4.29: Fits of different models to the NSE results on the high M_w Mi-SCNPs solutions at the different Q-values denoted in $Å^{-1}$. Results obtained for 1st scenario (left panels) and 2nd scenario (right panels). (a) and (d): full Zimm model; (b) and (e): Zimm model with internal friction; (c) and (f): Zimm model restricted to the modes corresponding to the longest wavelength, up to p_{max}.

For the second scenario the Zimm model was applied fixing for all Q-values the experimentally determined value for D_{CM} (D_{DLS}). As expected, the simplest version of the model fails [figure 4.29(d)]. The ZIF model in figure 4.29(e) successfully describes the Mi-SCNPs data by choosing $\tau_i = 124$ ns. Moreover, cutting the modes to a maximum number of 2, $p_{max} = 2$, a reasonable description of the data is also obtained [figure 4.29(f)]. Here, the virtually rigid subcoils would span over about $\bar{r}_e^{stiff} = 10.6$ nm, a large fraction of the macromolecule, even larger than in the first scenario, taking into account that in this case the typical size is $R_e^c = 14.1$ nm.

The Zimm characteristic times used in the three approaches are represented in figure 4.30 as function of the wavelength of the mode, N/p, for both scenarios. The characteristic times for the second scenario follow a weaker mode-number dependence (due to the smaller value of the scaling exponent) and are shorter in the long wavelength N/p region (due to the smaller dimensions) than those for the first scenario. Interestingly, we found that the internal friction, τ_i, and the size of the virtually rigid subocoils, $\bar{r}_e^{stiff}$, is nearly the same in both cases. However, the modes that would substantially contribute to the chain relaxation are different, due to the fact that the dimensions of the macromolecule considered in the 2nd scenario are smaller.

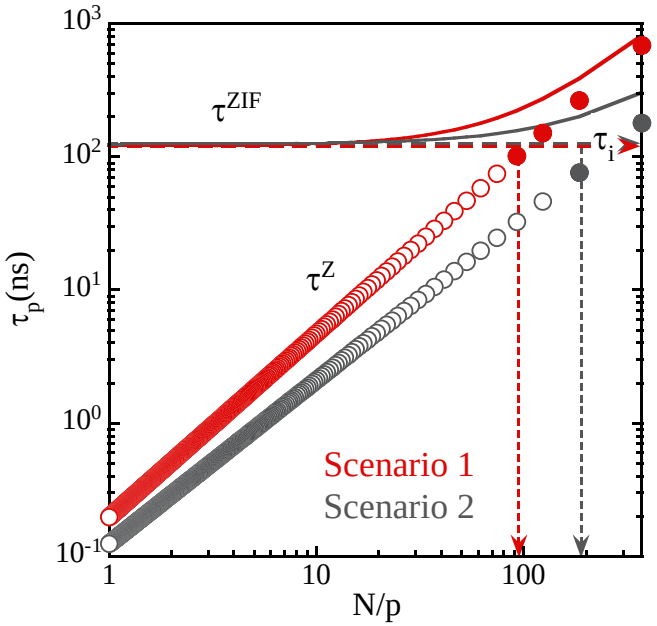

Figure 4.30: Characteristic time of the Zimm modes as function of the scaling variable N/p deduced for the Mi-SCNPs in solution: 1st scenario (red) and 2nd scenario (gray). Only modes with mode-number below or equal to 4 (1st scenario) and 2 (2nd scenario) highlighted as filled symbols would substantially contribute. Lines represent the characteristic times for the ZIF model for both scenarios. Dotted arrows mark the value of τ_i and the location of the crossover from solvent- to internal-friction dominated relaxation.

A comparative summary of the results and the interpretation of the modes that are involved in each scenario are illustrated in figure 4.31. From this comparative analysis we can conclude that the deduced internal friction and the dynamic rigidity of the macromolecule are very much the same for both scenarios, i.e., independent of the assumptions made for the structure factor and form factor. Contrarily, the modes that contribute to the chain relaxation is very different in both scenarios. As it is illustrated in figure 4.31, the rotation of the whole macromolecule (represented by mode p = 1) would be much faster in the smaller entities representing scenario 2. Also, more long-wavelength internal

modes would contribute to the overall dynamics in scenario 1. In fact, only one internal mode in addition to the overall rotation would be active in the second scenario; this mode is also characterized by a much shorter time than the counterpart in scenario 1 (see figure 4.30). However, the absolute value of the size of the virtually frozen segments in both cases would be rather similar. Finally, we note that the zeroth mode gives the position of the center of mass of the chain. Applying the theoretical approximation for the diffusion coefficient, $D_{CM}^{Z} = 0.203 k_B T/(\eta \bar{R}_e)$, we obtain a rather close value to the one measured by DLS (3.38 Å^2/ns) in the 1st scenario ($D_{CM}^{Z} = 4.5$ Å^2/ns), while that deduced from the second scenario (7.3 Å^2/ns) is by far overestimated and unrealistic.

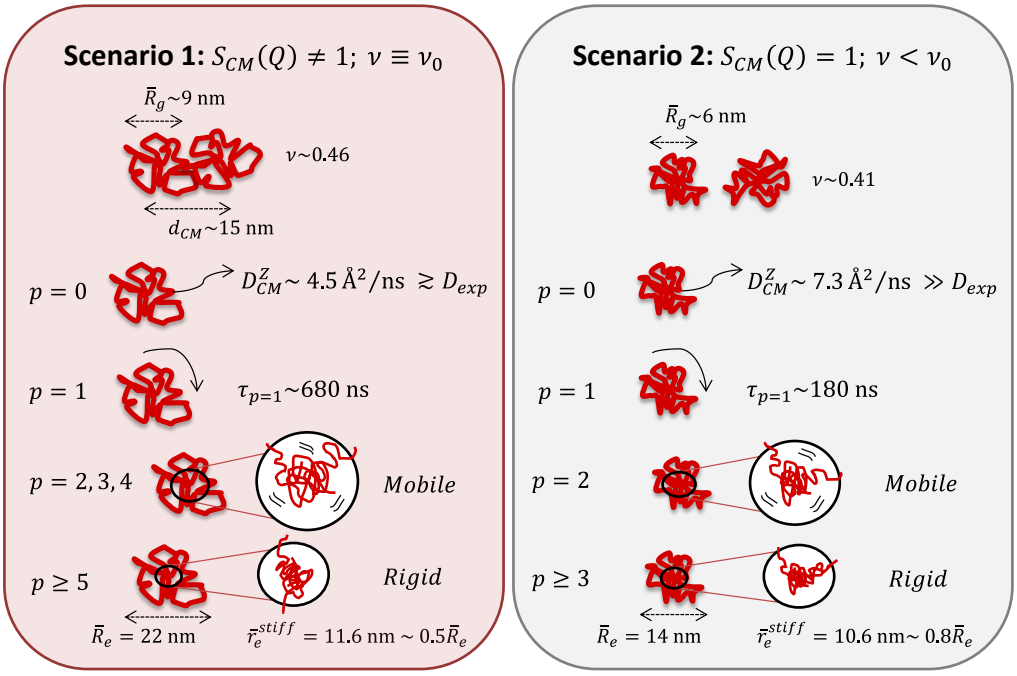

Figure 4.31: Schematic illustration of the modes involved in the chain relaxation and its interpretation for the 1st scenario (left) and the 2nd scenario (right).

Thus, taking into account this result together with the structural investigation above described, we think that the more realistic situation is the 1st scenario, i.e., the form factor remains unperturbed at dilute conditions (below the overlap concentration), and the structure factor is not constant, so that inter-particle interactions have to be considered.

4.4.6. Conclusion

We have presented the first experimental investigation on the dynamic structure factor of SCNPs in solution. The comparison of the results on both type of SCNPs, Cu-SCNPs and Mi-SCNPs, and their precursor reveals a clear impact of the internal cross-links on the dynamics. This is reflected in an important slowing down on the internal modes revealed by the microscopic insight provided by neutron spin echo (NSE).

The data have been analyzed in terms of theoretical approximations based on the Zimm model. Internal friction is a major ingredient in the dynamics, even for the linear precursor chains. This can be attributed to the rigidity of the PMMA-AEMA backbone, enhanced by the presence of AEMA monomers. The internal friction clearly increases in the SCNPs. It is noteworthy the similarity with the dynamical behavior reported for solutions of the myelin basic protein (MBP) in D_2O. Thus, the behavior of SCNPs and intrinsically disordered proteins (IDPs) is similar not only regarding the macromolecular static properties but also the dynamical features, as determined by scattering techniques.

A comparative study applying the Zimm model to high molecular weight Mi-SCNPs data reveals that the internal friction deduced is roughly independent of

the assumptions made about the impact of crowding on chain conformation and static structure factor. However, as previously concluded in the structural study, the more realistic picture to describe the chain dynamics is obtained by assuming that the form factor remains unperturbed below the overlap concentration and the diffusion coefficient is affected by a deGennes-like narrowing reflecting the inter-particle interactions.

4.5. References

[1] J. A. Pomposo, *Single-Chain Polymer Nanoparticles: Synthesis, Characterization, and Applications*, Wiley-VCH, Weinheim, **2017**.

[2] J. A. Pomposo, *Polymer International* **2014**, *63*, 589-592.

[3] M. Huo, N. Wang, T. Fang, M. Sun, Y. Wei, J. Yuan, *Polymer* **2015**, *66*, A11-A21.

[4] A. Latorre-Sánchez, J. A. Pomposo, *Polymer International* **2016**, *65*, 855-860.

[5] O. Altintas, C. Barner-Kowollik, *Macromol Rapid Commun* **2015**.

[6] M. Gonzalez-Burgos, A. Latorre-Sanchez, J. A. Pomposo, *Chemical Society Reviews* **2015**, *44*, 6122-6142.

[7] C. K. Lyon, A. Prasher, A. M. Hanlon, B. T. Tuten, C. A. Tooley, P. G. Frank, E. B. Berda, *Polym. Chem.* **2015**, *6*, 181-197.

[8] J. De-La-Cuesta, E. González, A. J. Moreno, A. Arbe, J. Colmenero, J. A. Pomposo, *Macromolecules* **2017**, *50*, 6323-6331.

[9] M. E. Mackay, T. T. Dao, A. Tuteja, D. L. Ho, B. van Horn, H. C. Kim, C. J. Hawker, *Nat Mater* **2003**, *2*, 762-766.

[10] N. D. Knofel, H. Rothfuss, J. Willenbacher, C. Barner-Kowollik, P. W. Roesky, *Angew Chem Int Ed Engl* **2017**, *56*, 4950-4954.

[11] M. M. Caruso, D. A. Davis, Q. Shen, S. A. Odom, N. R. Sottos, S. R. White, J. S. Moore, *Chem Rev* **2009**, *109*, 5755-5798.

[12] K. S. Suslick, G. J. Price, *Annual Review of Materials Science* **1999**, *29*, 295-326.

[13] A. Levy, F. Wang, A. Lang, O. Galant, C. E. Diesendruck, *Angew Chem Int Ed Engl* **2017**, *56*, 6431-6434.

[14] S. Podzimek, *Light Scattering, Size Exclusion Chromatography and Asymmetric Flow Field Flow Fractionation*, John Wiley & Sons, Inc., Hoboken, NJ, **2011**.

[15] S. Koda, *Polymer* **1994**, *35*, 30-33.

[16] B. M. E. Van der hoff, C. E. Gall, *Journal of Macromolecular Science: Part A - Chemistry* **1997**, *11*, 1739-1758.

[17] M. V. Encina, E. Lissi, M. Sarasúa, L. Gargallo, D. Radic, *Journal of Polymer Science: Polymer Letters Edition* **1980**, *18*, 757-760.

[18] J. A. Pomposo, I. Perez-Baena, F. Lo Verso, A. J. Moreno, A. Arbe, J. Colmenero, *ACS Macro Letters* **2014**, *3*, 767-772.

[19] J. S. Higgins, H. C. Benoit, *Polymers and Neutron Scattering*, Oxford University Press, Oxford, **1997**.

[20] M. Rubinstein, R. H. Colby, *Polymer Physics*, Oxford University Press, Oxford, UK, **2003**.

[21] B. Hammouda, *Macromolecular Theory and Simulations* **2012**, *21*, 372-381.

[22] B. Hammouda, in *Advances in Polymer Science, Vol. 106*, Springer, Berlin, Heidelberg, **1993**, pp. 87-133.

[23] A. J. Moreno, F. Lo Verso, A. Sanchez-Sanchez, A. Arbe, J. Colmenero, J. A. Pomposo, *Macromolecules* **2013**, *46*, 9748-9759.

[24] M. Doi, S. F. Edwards, *The Theory of Polymer Dynamics*, Clarendon Press, Oxford, **1986**.

[25] A. M. Stadler, L. Stingaciu, A. Radulescu, O. Holderer, M. Monkenbusch, R. Biehl, D. Richter, *J Am Chem Soc* **2014**, *136*, 6987-6994.

[26] A. J. Moreno, F. Lo Verso, A. Arbe, J. A. Pomposo, J. Colmenero, *The Journal of Physical Chemistry Letters* **2016**, *7*, 838-844.

[27] P. E. Rouse, *The Journal of Chemical Physics* **1953**, *21*, 1272-1280.

[28] D. Richter, M. Monkenbusch, A. Arbe, J. Colmenero, in *Neutron Spin Echo in Polymer Systems*, Springer Berlin Heidelberg, Berlin, Heidelberg, **2005**, pp. 1-221.

[29] B. Ewen, D. Richter, in *Neutron Spin Echo Spectroscopy Viscoelasticity Rheology*, Springer Berlin Heidelberg, Berlin, Heidelberg, **1997**, pp. 1-129.

[30] G. Allegra, F. Ganazzoli, **1989**, *75*, 265-348.

[31] P. G. De Gennes, *Journal de Physique* **1981**, *42*, 735-740.

[32] B. H. Zimm, *The Journal of Chemical Physics* **1956**, *24*, 269-278.

[33] A. Arbe, M. Monkenbusch, J. Stellbrink, D. Richter, B. Farago, K. Almdal, R. Faust, *Macromolecules* **2001**, *34*, 1281-1290.

[34] M. Monkenbusch, J. Allgaier, D. Richter, J. Stellbrink, L. J. Fetters, A. Greiner, *Macromolecules* **2006**, *39*, 9473-9479.

[35] D. Richter, M. Monkenbusch, J. Allgeier, A. Arbe, J. Colmenero, B. Farago, Y. Cheol Bae, R. Faust, *The Journal of Chemical Physics* **1999**, *111*, 6107-6120.

[36] B. S. Khatri, T. C. B. McLeish, *Macromolecules* **2007**, *40*, 6770-6777.

[37] P. Stepanek, in *Dynamic Light Scattering: The Method and Some Applications* (Ed.: W. Brown), Clarendon Press, Oxford, **1993**.

[38] R. Biehl, B. Hoffmann, M. Monkenbusch, P. Falus, S. Preost, R. Merkel, D. Richter, *Phys Rev Lett* **2008**, *101*, 138102.

[39] A. Arbe, J. A. Pomposo, A. J. Moreno, F. LoVerso, M. González-Burgos, I. Asenjo-Sanz, A. Iturrospe, A. Radulescu, O. Ivanova, J. Colmenero, *Polymer* **2016**, *105*, 532-544.

CHAPTER 5

The Novel SCNPs Synthesized: Emerging Properties and Potential Applications

5.1. Introduction

Single-chain polymer nanoparticles are one of the most promising outputs of emerging single-chain technology (scheme 5.1).[1] The folding/collapse of single polymer chains to single-chain polymer nanoparticles (SCNPs) is reminiscent of the folding of proteins to their native, functional state.[2-4] The morphology of SCNPs in solution is expected to affect activity and selectivity, for instance, during catalysis or in sensing applications. As explained previously, two limiting molecular architectures were found, as schematically illustrated in scheme 5.1.

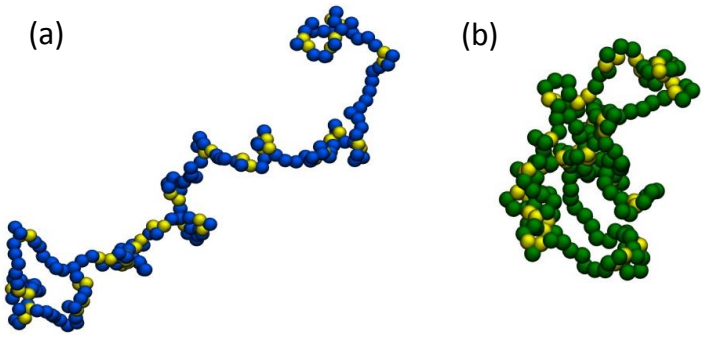

Scheme 5.1: Illustration of: sparse single-chain polymer nanoparticle (a) and globular single-chain polymer nanoparticle (b).

On one hand, synthesis of single-chain polymer nanoparticles in good solvent gives rise, in general, to non-globular sparse nano-objects [scheme 5.1(a)]. Since under such circumstances most of the cross-linking events taking place during single-chain polymer nanoparticle formation are inefficient for global compaction, a "pearl necklace" conformation is actually obtained showing locally compact portions of the chain connected by flexible segments. This particular morphology resembles that observed in intrinsically disordered proteins

(IDPs)[5] and has inspired some recent proof-of-concept applications of single chain polymer nanoparticles.

On the other hand, globular nanoparticles [scheme 5.1(b)] mimicking the typical conformation of enzymes have been synthesized by involving special precursors and techniques, such as a combination of multi-functional reactive groups and relatively long cross-linkers,[6] self-assembly of individual chains of neutral amphiphilic random copolymers[7] and self-assembly of charged amphiphilic random copolymers.[8] Both morphologies are of great interest for the development of potential applications of single-chain polymer nanoparticles.

Remarkably, sparse single-chain polymer nanoparticles show the presence of multiple locally compact, but accessible, sites/cavities/zones, so-called "local pockets" [scheme 5.2(a)], whereas globular single-chain polymer nanoparticles display, on average, a single pocket of larger size [scheme 5.2(b)]. The possibility to anchor, either temporally or permanently, active species like catalyst or drugs onto these local pockets paves the way to some bioinspired applications of single-chain polymer nanoparticles.

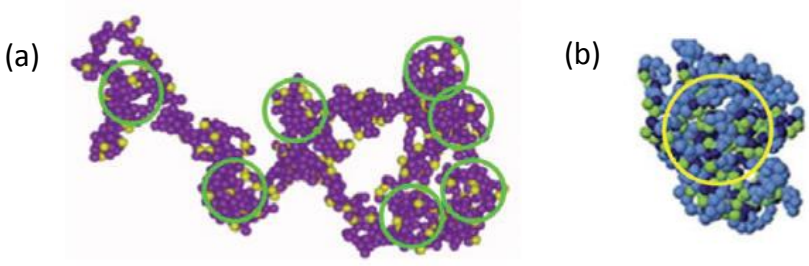

Scheme 5.2: Sparse single chain nanoparticles (a) show the presence of multiple locally compact, but accessible, sites/cavities/zones, so-called "local pockets", whereas globular SCNPs (b) show a single pocket of larger size.

Single-chain polymer nanoparticles are poised to make major contributions to a wide range of fields, from nanomedicine to sensing, catalysis, and other diverse uses (figure 5.1). The field of single-chain polymer nanoparticles is a relatively new one: irreversible single-chain polymer nanoparticles were first described in 2001,[9] whereas reversible ones were first disclosed in 2008.[10] Consequently, the main applications of single-chain polymer nanoparticles reported in the last decades cover mainly proof-of-concept experiments, which however demonstrate the huge possibilities of single-chain polymer nanoparticles for these fields.

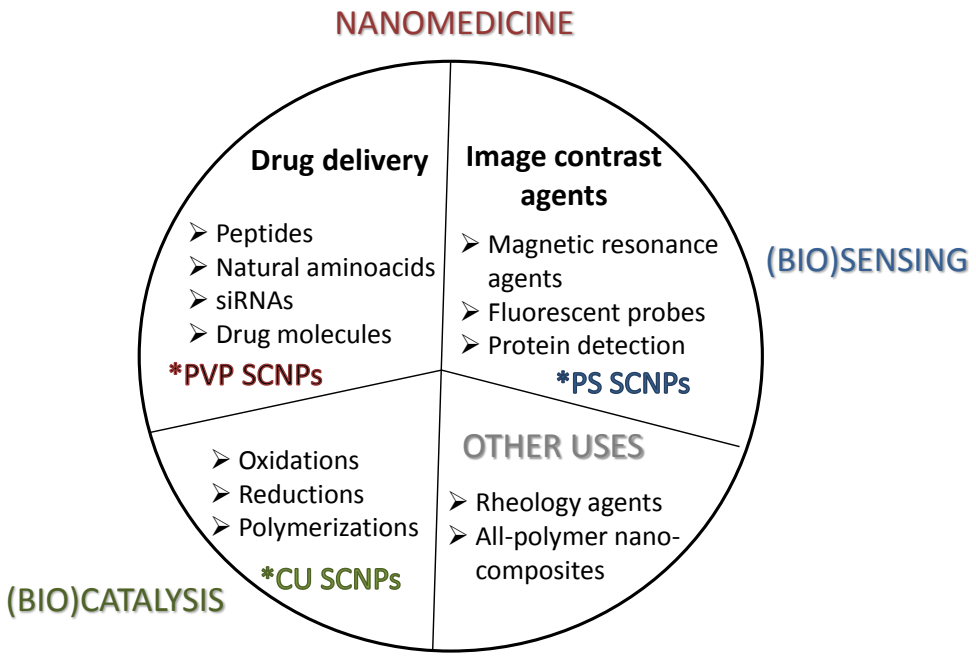

Figure 5.1: Main applications of single-chain polymer nanoparticles, including new applications introduced in this thesis (*).

This chapter describes the novelty of the properties and potential applications of single-chain nanoparticles, as well as new synthesis routes developed in this thesis. Concerning potential applications we have considered SCNPs for catalysis and SCNPs for nanomedicine (drug delivery and fluorescent probes).

Hence, based on a previously reported synthesis, an unexplored pathway for tuning the internal structure of metallo-folded single-chain nanoparticles is described, which paves the way for tuning the catalytic properties of this SCNPs (Cu-SCNPs in figure 5.1). Next, a new microwave-assisted synthesis route leading to PS based SCNPs with an unexpected functionality is explained. As it will be shown, this functionality is used to endow these SCNPs with fluorescent properties (PS SCNPs in figure 5.1). Finally, a highly-efficient synthesis for the preparation of PVP SCNPs able to encapsulate and release drugs is presented (see figure 5.1).

5.2. Internal Structure of Metallo-Folded SCNPs

5.2.1. Introduction

The SCNP folding/unfolding process has been followed mainly by dynamic light scattering (DLS), size exclusion chromatography (SEC), Fourier transform infrared (FTIR), among others. More recently, atomic force microscopy (AFM)-based single-molecule core spectroscopy[11] has been employed to acquire information about the stability of the internal folding structures of supramolecular SCNPs via AFM-induced mechanical unfolding. Also, the effect of solvent quality and temperature on the coil-to-globule transition has been investigated for SCNPs with a chiral internal secondary structure.[12]

However, the tuning of the internal structure of the SCNPs has remained an unsolved issue. Control over the spatial distribution of internal catalytic sites in metallo-folded SCNPs should be beneficial for the rational design of improved catalytic soft nano-objects. Several strategies have been developed to synthesize Ru-,[13] Rh-,[14] Cu-,[15-17] Pd-,[18-19] Ir-/Ni-[20] and Fe-[21] containing SCNPs. To the best of our knowledge, no attempt to modulate the internal structure of metallo-folded SCNPs was carried out previously.

5.2.2. Objective

Our objective is to investigate an unexplored pathway for tuning the internal structure of metallo-folded SCNPs. The method is based on the use of amphiphilic random copolymers and two different synthesis procedures involving selective and nonselective solvents, that we call “protocols”. Protocol I

involves the conventional SCNP synthesis *via* intra-chain metal complexation in good solvent. Protocol II is based on the use of amphiphilic random copolymers and transfer –after SCNP formation *via* intra-chain metal complexation– from selective to good solvent conditions (see scheme 5.3).

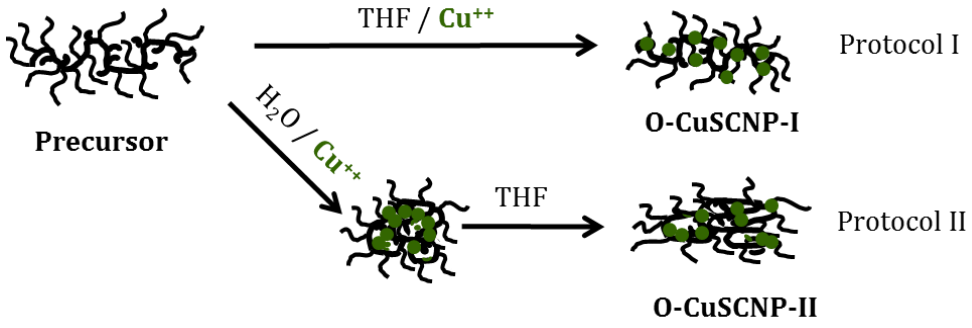

Scheme 5.3: Tuning the internal structure of metallo-folded SCNPs by using amphiphilic random copolymers and two different synthesis procedures involving nonselective (Protocol I) and selective (Protocol II) solvents.

The size, morphology and spatial distribution of catalytic sites in SCNPs derived from protocols I and II have been determined by combining results from size exclusion chromatography (SEC), small-angle X-ray scattering (SAXS) and molecular dynamics (MD) simulations of a bead-spring model.

5.2.3. Results and Discussion

A. Size of SCNPs Synthesized by Protocols I and II

A series of amphiphilic poly(oligo(ethylene glycol) methyl eyher metacrylate-*co*-2-acetoacetoxy ethyl methacrylate), poly(OEGMA-co-AEMA), random copolymers having different AEMA content, high molar mass and low molar mass dispersity were synthesized, by optimizing a previously reported

procedure.[17] The poly(OEGMA-co-AEMA) copolymers (so-called precursors) were folded/collapsed to SCNPs via intra-chain copper(II) complexation at a concentration of 1 mg/ml using two different protocols. Once the Cu complex is formed, no significant Cu-ligand exchange is expected (for more details about the synthesis see 'Standard synthesis routes' in chapter 2).

In protocol I, the synthesis was carried out in good solvent conditions (THF), while in protocol II SCNP formation was performed in water, which is a good solvent for OEGMA, but a bad solvent for AEMA. In this situation, the precursor is expected to form a core-shell structure with AEMA groups in the core.[17] After performing the synthesis in water, further solvent transfer of the resulting single-chain nanoparticles to THF was carried out.

The main characteristics of the four used samples of poly(OEGMA-co-AEMA) copolymer (denoted as O_x, with x = 1-4), the SCNPs synthesized in THF (denoted as O_x-SCNP-I) and the SCNPs synthesized in water and transferred to THF (denoted as O_x-SCNP-II) are summarized in table 5.1 The data have been determined from SEC with triple detection (differential refractive index (DRI), multi-angle laser light scattering (MALLS) and viscosimetric (VI) detectors).

As can be seen in table 5.1, upon increasing the AEMA content in O_x the relative reduction in the average values of the radius of gyration, $\bar{R}_g$, and hydrodynamic radius, $\bar{R}_H$, for both O_x-SCNP-I and O_x-SCNP-II, becomes more apparent. The SCNPs produced by protocol II showed slightly lower values of $\bar{R}_g$ and $\bar{R}_H$, when compared to their counterparts produced by protocol I [see table 5.1 and figure 5.2(a)].

Table 5.1: Characteristics of the amphiphilic random poly(OEGMA-co-AEMA) copolymers investigated in this work (denoted as O_x) and the corresponding metallo-folded SCNPs obtained by protocol I (denoted as O_x-SCNP-I) and protocol II (denoted as O_x-SCNP-II).

Sample	AEMA[a] (mol%)	M_w[b] (kg/mol)	M_w/M_n[b]	$\overline{R}_g$[b] (nm)	$\overline{R}_H$[b] (nm)	$\lvert\Delta\overline{R}_g\rvert$[c] (%)	$\lvert\Delta\overline{R}_H\rvert$[d] (%)
O_1	11	110.1	1.04	12.6	7.9		
O_1-SCNP-I		100.3	1.16	11.1	7.0	12	11
O_1-SCNP-II		94.2	1.12	11.0	7.0	13	11
O_2	20	90.4	1.10	9.5	7.1		
O_2-SCNP-I		103.4	1.09	8.3	6.6	13	7
O_2-SCNP-II		88.1	1.07	8.2	6.3	14	11
O_3	35	175.0	1.08	15.6	9.8		
O_3-SCNP-I		172.2	1.13	11.8	8.1	24	17
O_3-SCNP-II		174.6	1.04	11.3	8	28	18
O_4	40	208.0	1.05	16.4	11		
O_4-SCNP-I		200.3	1.07	13.4	8.4	18	24
O_4-SCNP-II		206.5	1.05	9.1	8.2	45	26

[a)]AEMA content in the copolymer as determined by ^{1}H NMR spectroscopy. [b)]As determined by SEC with triple detection (DRI, MALLS and VI detectors) in THF at 30 ºC. [c)]$|\Delta R_g| = |[R_g(O_x) - R_g(O_x\text{-SCNP})]/R_g(O_x)| \times 100$. [d)]$|\Delta R_H| = |[R_H(O_x) - R_H(O_x\text{-SCNP})]/R_H(O_x)| \times 100$

Therefore, we can conclude that SCNPs synthesized in water from poly(OEGMA-co-AEMA) copolymers (adopting a core-shell structure in water[17]) are significantly swollen when transferred to THF, even those with high AEMA content (see next section).

Similar to previous works involving amphiphilic random copolymers,[12, 22] we found that SCNP formation involving protocol II can be carried out up to 100 mg/ml without any aggregation of the resulting SCNPs [see figure 5.2(b)]. This can be attributed to the core-shell structure adopted by the precursor in water.

The steric stabilizing effect of the oligo(ethylene glycol) methyl ether branches from OEGMA units efficiently isolate the AEMA units, preventing inter-particle coupling events. Interestingly enough, the average hydrodynamic size of O_4-SCNP-II synthesized at 100 mg/ml was found to be slightly lower than that for O_4-SCNP-II synthesized at 10 mg/ml, and in turn lower than that for O_4-SCNP-II nanoparticles prepared at 1 mg/ml [figure 5.2(b)]. We can tentatively attribute this progressive size reduction upon increasing the precursor concentration to steric crowding effects.[23] Under crowding, cross-linking between functional groups that are far apart in the chain takes place, leading to improved global compaction.

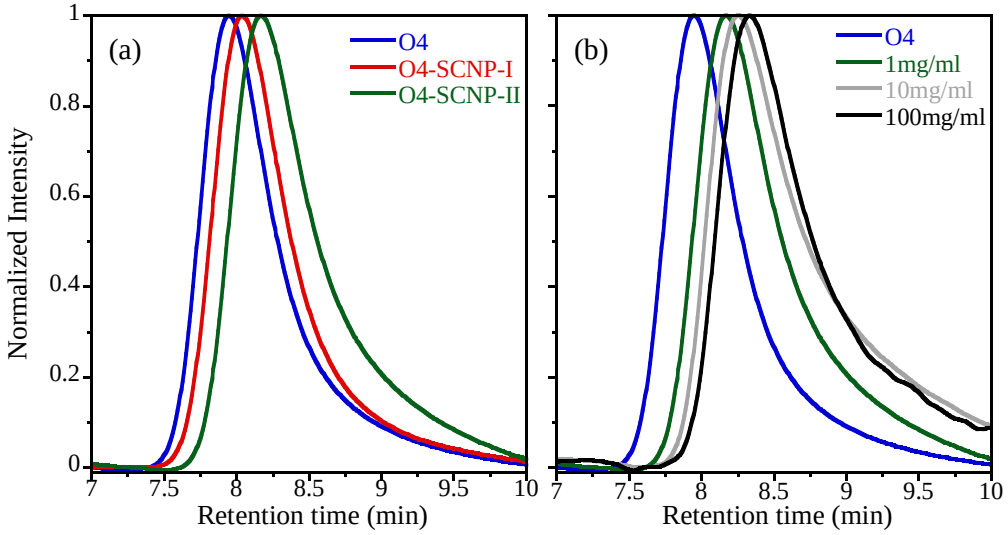

Figure 5.2: (a) Size exclusion chromatography (SEC) traces (MALLS detector) of precursor O_4 (blue curve), metallo-folded SCNPs synthesized from precursor O_4 directly in THF (O_4-SCNP-I, red curve), and SCNPs synthesized from precursor O_4 in water and transferred to THF (O_4-SCNP-II, green curve). (b) SEC traces (MALLS detector) of precursor O_4 (blue curve) and O_4-SCNP-II synthesized in water at: 1 mg/ml (green curve), 10 mg/ml (grey curve) and 100 mg/ml (black curve).

B. Morphology of SCNPs Synthesized by Protocol I and II

Based on previous works, SCNPs synthesized by protocol I are expected to possess relatively sparse morphology in solution. However, two possibilities exist for the SCNPs synthesized by protocol II. If the synthesis leads to tight internal cross-linking, it might be expected that upon transfer from water to THF the SCNP core-shell structure will be weakly altered. If tight cross-linking is not produced, significant swelling of the SCNPs is expected since THF is a good solvent for both OEGMA and AEMA. In that case O-SCNP-II in THF will be sparse nano-objects similar, but presumably not identical, to the SCNPs synthesized directly in THF by protocol I.

We have performed SAXS measurements to determine, unambiguously, the form factor, $P(Q)$, of O_4, O_4-SCNP-I and O_4-SCNP-II, all them in THF. As illustrated in figure 5.3(a), the precursor in THF shows a SAXS form factor corresponding to polymer chains in good solvent. This is demonstrated by the observed scaling behavior in the fractal (intermediate) regime,[24] $P(Q) \sim Q^{-1/\nu}$, showing a value of $\nu = 0.59$ (Flory exponent for a polymer in good solvent[24]). Concerning the SCNPs synthesized by protocol I, they show a value of $\nu = 0.52$ displaying only a modest degree of compaction. According to SAXS, SCNPs synthesized by protocol II do not either display a compact, globular conformation in THF ($\nu = 0.33$ for globules) but, instead, a sparse morphology with a value of $\nu = 0.48$.

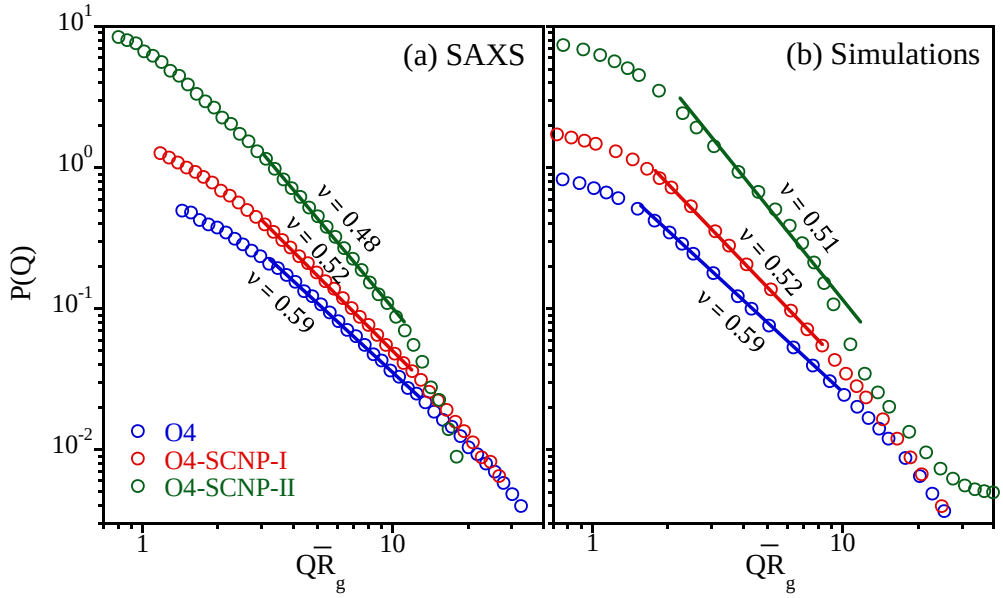

Figure 5.3: (a) Form factor from SAXS of precursor O_4 (blue circles), metallo-folded SCNPs synthesized from O_4 directly in THF (O_4-SCNP-I, protocol I, red circles) and metallo-folded SCNPs synthesized from O_4 in water and transferred to THF (O_4-SCNP-II, protocol II, green circles). (b) Form factor from MD-simulations of the precursor (blue circles) and the SCNPs synthesized trough protocol I (red circles) and II (green circles). Lines are fits to power laws $P(Q)\sim Q^{1/\nu}$. The corresponding values of ν are indicated. In all cases, the data are represented vs. the dimensionless $Q\bar{R}_g$. To facilitate visualization, ordinates have been scaled by arbitrary factors.

The SAXS results were in good agreement with those obtained from MD-simulations in which SCNP synthesis by protocol I and II were simulated [see figure 5.3(b) and chapter 3 for details about the molecular dynamics simulation experiments]. It is worth nothing that, though both protocols I and II produce sparse SCNPs (ν ≈ 0.5), the SCNPs obtained by protocol II are more compact at local scales. This feature is manifested after the fractal regime by the much sharper decay of $P(Q)$ in O-SCNP-II (figure 5.3).

C. Internal Structure of SCNPs Synthesized by Protocol I and II

The good agreement obtained between SAXS and MD-simulations motivates us to have a closer insight on the internal structure of SCNPs synthesized by protocols I and II. This is possible from the MD-simulations. Typical snapshots from MD-simulations of representative O-SCNP-I and O-SCNP-II are given in figure 5.4(a) and figure 5.4(c). The corresponding spatial distribution of the catalytic sites is provided in figure 5.4(b) and figure 5.4(d), respectively.

As can be clearly observed, O-SCNP-I displays a relatively homogeneous spatial distribution of catalytic sites along the nanoparticle. Conversely, O-SCNP-II shows clusters of catalytic sites. This is a consequence of the spatial distribution of the reactive groups in the core of the precursor at the selective solvent. They already form clusters in the precursor and intra-molecular cross-linking creates bonds preferentially between close groups of the same cluster. Due to the permanent character of the bonds, the formed clusters survive in the swollen O-SCNP-II when it is finally transferred to a good solvent.

The clustering can be better appreciated when comparing the radial distribution function $g(r)$ of the catalytic sites for O-SCNP-I and O-SCNP-II [see figure 5.4(e)], $g(r) = \frac{1}{\rho}\langle\sum_{i\neq 0}\delta(r - r_i)\rangle$. The positions r_i used for computing $g(r)$ are not those of the linked beads, but of the centers of the corresponding bonds. In this way, $g(r)$ does not include the trivial peak associated with the bond distance between linked beads.

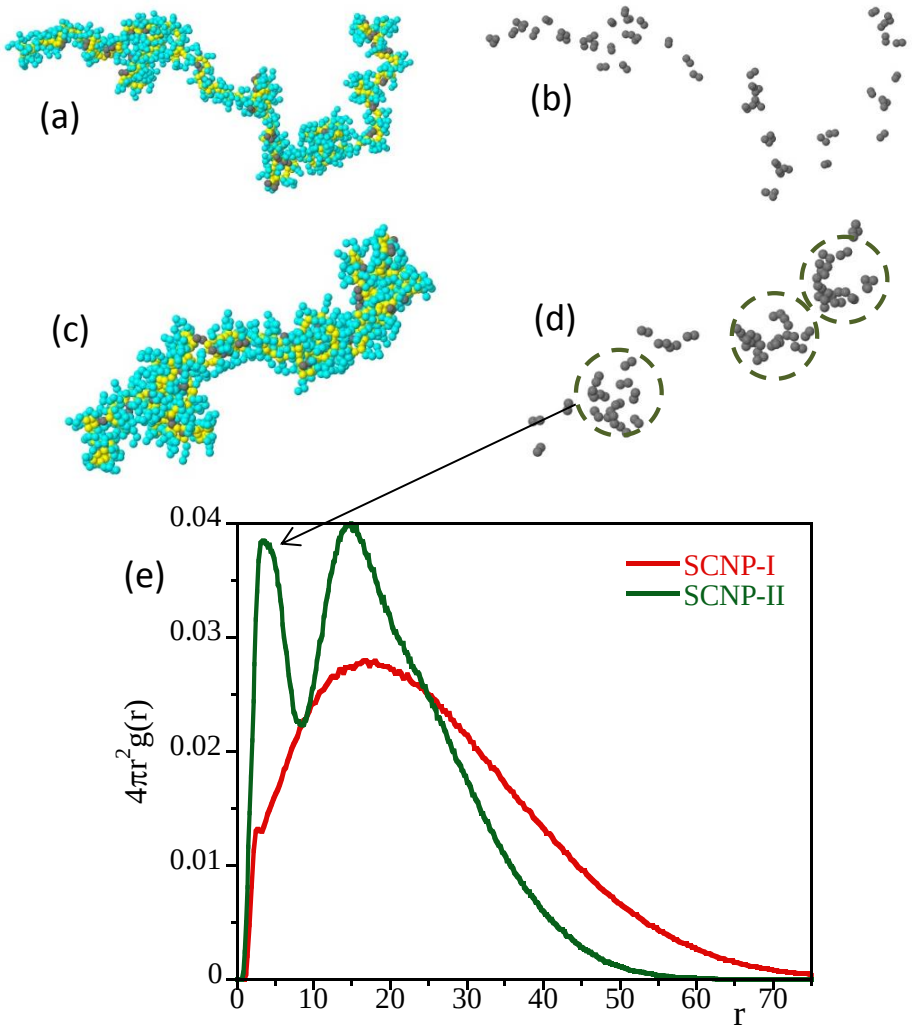

Figure 5.4: (a) Typical snapshot from MD-simulations of a SCNP synthesized directly in a good solvent (protocol I). (b) Same as (a), but only the catalytic sites are displayed. (c) Typical snapshot from MD-simulations of a SCNP synthesized in a selective solvent and then transferred to good solvent (protocol II). (d) Same as (c), but only the catalytic sites are displayed, showing their spatial arrangement into clusters. In panels (a-d), backbone beads are depicted in yellow. Side group beads are depicted in turquoise (unreactive) and grey (reactive). (e) Radial distribution function of the catalytic sites of the SCNPs synthesized by protocol I and II. Distance *r* is given in units of the bead diameter.

In the case of the O-SCNP-I, the relatively homogeneous arrangement of the catalytic sites is confirmed by the unstructured, almost Gaussian shape exhibited by $g(r)$ [red color in figure 5.4(e)]. Rather different features are found in the $g(r)$ of O-SCNP-II [green color in figure 5.4(e)]. A clear maximum is observed at a distance of $r \approx 4\sigma$ (with σ the bead diameter, σ ≈ 5-10 Å, see chapter 3), confirming the existence of clusters of catalytic sites. By integration of $g(r)$ up to the minimum after the peak, we estimate a typical number of 12 catalytic sites (12 bonds) per cluster. The Gaussian behavior is only recovered at large scales. Some structure in $g(r)$ is still observed at $r \approx 15\sigma$ (note the shoulder after the second peak), indicating some degree of correlation between neighboring clusters in O-SCNP-II.

Thus, MD-simulations confirmed that the internal structure of metallo-folded SCNPs synthesized by protocols I and II is rather different.

5.2.4. Conclusion

We have investigated an unexplored pathway for tuning the internal structure of metallo-folded SCNPs, as a first step toward the rational design of improved catalytic soft nano-objects. The method is based on the use of amphiphilic random copolymers and transfer after SCNP formation from selective to good solvent conditions (protocol II) versus conventional SCNP synthesis in good solvent (protocol I).

By combining different results from SEC with triple detection, SAXS and MD-simulations, we have obtained a clear picture of the size, morphology in solution and spatial distribution of catalytic sites (internal structure) of metallo-folded

SCNPs synthesized by the former protocols. A relatively uniform spatial distribution of catalytic sites along the nanoparticle was observed for SCNPs synthesized by the conventional protocol I. Conversely, SCNPs obtained by the protocol II show clusters of catalytic sites. This work paves the way for tuning the catalytic properties of metallo-folded soft nano-objects based on SCNPs.

5.3. PS-based SCNPs by Microwave-Assisted Synthesis

5.3.1. Introduction

Thermal decomposition of organic azides with loss of molecular nitrogen generates highly reactive and poorly discriminating species, i.e. nitrenes, which can participate in a large number of chemical reactions.[25-28] Short-lived nitrenes are quickly stabilized upon intra-molecular rearrangement *via* e.g. Schmidt or Curtius rearrangement, inter-molecular cycloaddition to alkenes or inter-molecular insertion into sp^3 C–H bonds or N–H bonds, among other reactions. Nitrene chemistry –even being known since the 19th century[29]– remains highly attractive for developing new materials with improved characteristics in spite of the complexity of the possible reaction products.[29-31]

Recent advances in nitrene chemistry include new alkene difunctionalization reactions, cascade reactions and heterocycle synthesis based on catalytic nitrene transfers.[32-34] Additionally, cross-linking of azide-containing materials *via* azide decomposition has recently been used for the stabilization of initially soluble organic thin films in high-performance semiconductor devices,[35-36] for nanoscale patterning in nanolithography[37-38] and for synthesis of fluorescent polymer nanoparticles.[39-40] However, precise chemical characterization of the resulting structures was difficult due to a lack of solubility of the resulting cross-linked materials. In spite of the significant studies made in nitrene chemistry, azide decomposition *via* microwave-assisted synthesis has not been investigated in detail.

5.3.2. Objective

The aim of this work is to investigate the microwave-assisted decomposition of azide-containing polystyrene (PS) copolymers at high dilution to promote intra-chain cross-linking towards novel single-chain nanoparticles (scheme 5.4). As control experiments, we have also investigated azide thermal decomposition in the melt of exactly the same precursors.

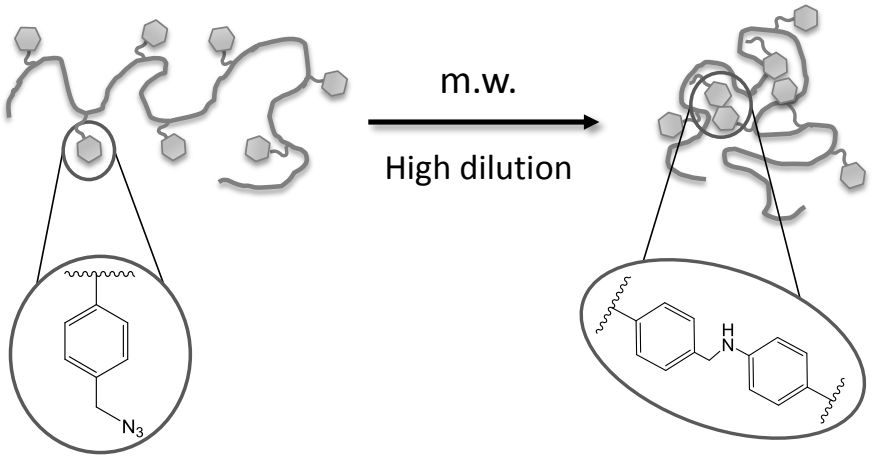

Scheme 5.4: Synthesis of novel single-chain nanoparticles based on microwave-assisted (m.w.) decomposition of azide-containing copolymer precursors at high dilution

The chemical structures resulting upon azide decomposition in the melt state and dissolved at high dilution have been analyzed by means of a combination of characterization techniques including proton (^{1}H) and carbon (^{13}C) nuclear magnetic resonance (NMR) spectroscopy in solution, infrared (IR) spectroscopy, small-angle X-ray scattering (SAXS) and dielectric spectroscopy (DS),[41-42] among other ones.

5.3.3. Results and Discussion

Varying amounts of the azide functionality (9, 16, 21 and 30 mol%) were incorporated into random copolymers of styrene and chloromethyl styrene of similar molecular weight (242 to 316 kg/mol), relatively narrow polydispersity (1.2 to 1.4) and similar size (13 to 14 nm in hydrodynamic radius) through a simple nucleophilic substitution reaction with sodium azide in DMF at room temperature for 24 h.[37] The characteristics of the resulting azide-containing precursors denoted as P9, P16, P21 and P30 are summarized in table 5.2. A sample of neat PS material having no azide functional groups, denoted as P0, was also synthesized as a control for DS measurements (for details about the synthesis see 'New Synthesis Routes' in chapter 2).

Table 5.2: Characteristics of control P0 and precursors P9, P16, P21 and P30.

Code	x[a] (mol%)	M_w[b] (kg/mol)	M_w/M_n[c]	$\overline{R}_H$[d] (nm)	T_g[e] (°C)
P0	0	282.8	1.2	14.5	103
P9	9	259.5	1.3	13.5	100
P16	16	315.7	1.4	13.8	97
P21	21	241.7	1.3	13.6	95
P30	30	274.8	1.3	14.1	63

[a)]Azide content as determined by ^{1}H NMR spectroscopy; [b)]Molecular weight as Determined by SEC with triple detection (DRI, MALLS and VI detector) in THF at 30 °C; [c)]Polydispersity index [d)]Average hydrodynamic radius measured by DLS in DMF at 25 °C; [e)]Glass transition temperature

Initial experiments by thermogravimetric analysis (TGA) revealed that the azide groups decompose in the melt with nitrogen evolution at temperatures above 200 °C [figure 5.5(a)]. As expected, the resulting network materials were found to be insoluble in any solvent as a consequence of inter-chain cross-linking taking place in the melt upon azide decomposition (200 °C, 3 h).

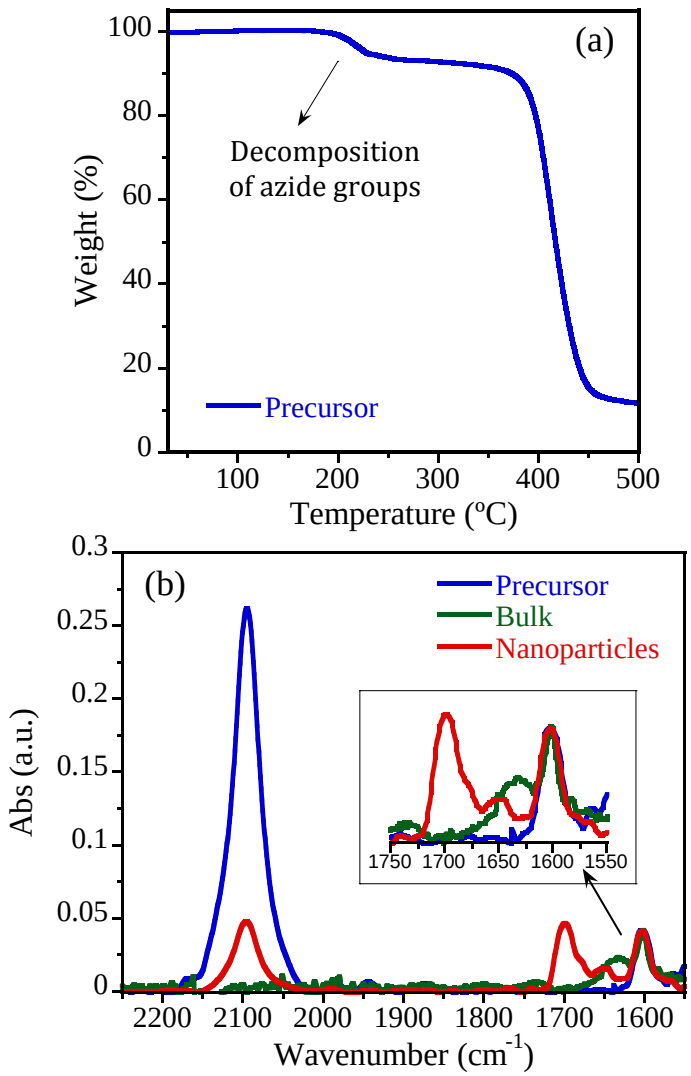

Figure 5.5: (a) Typical TGA curve of P(St-co-AMS) precursor (P21) showing the initial decomposition of azide groups at 200°C. (b) IR spectra of precursor P21, network cross-linked material B21 and intra-chain cross-linked single-chain nanoparticles NP21.

For the azide-containing precursors, the characteristic stretching vibration band of azide groups at 2094 cm^{-1} was observed by IR spectroscopy [blue color in

figure 5.5(b)]. After azide thermal decomposition in the melt state, the analysis by IR spectroscopy of the resulting insoluble sample [green color in figure 5.5(b)] showed the complete disappearance of the azide vibration band and the presence of a new vibration band centered on 1640 cm^{-1}, arising from –NH– groups in the cross-linked segments of the material [scheme 5.5(a)].

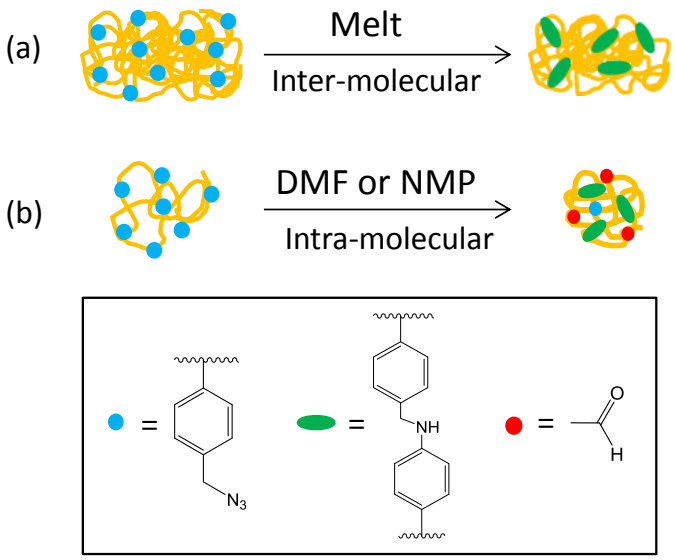

Scheme 5.5: (a) Inter-molecular cross-linking of precursor chains in the melt. (b) Intra-molecular cross-linking of precursor single chains in highly diluted DMF or NMP solution.

In order to avoid inter-molecular cross-linking and obtain individual SCNPs, the microwave-assisted decomposition of the azide-containing polystyrene copolymers dissolved in N,N-dimethylformamide (DMF) or N-methylpyrrolidone (NMP) was carried out at high dilution [scheme 5.5(b)]. Chain compaction,[43-47] which is a signature of nanoparticle formation, was confirmed by size exclusion chromatography (SEC), dynamic light scattering (DLS) and SAXS measurements (figure 5.6).

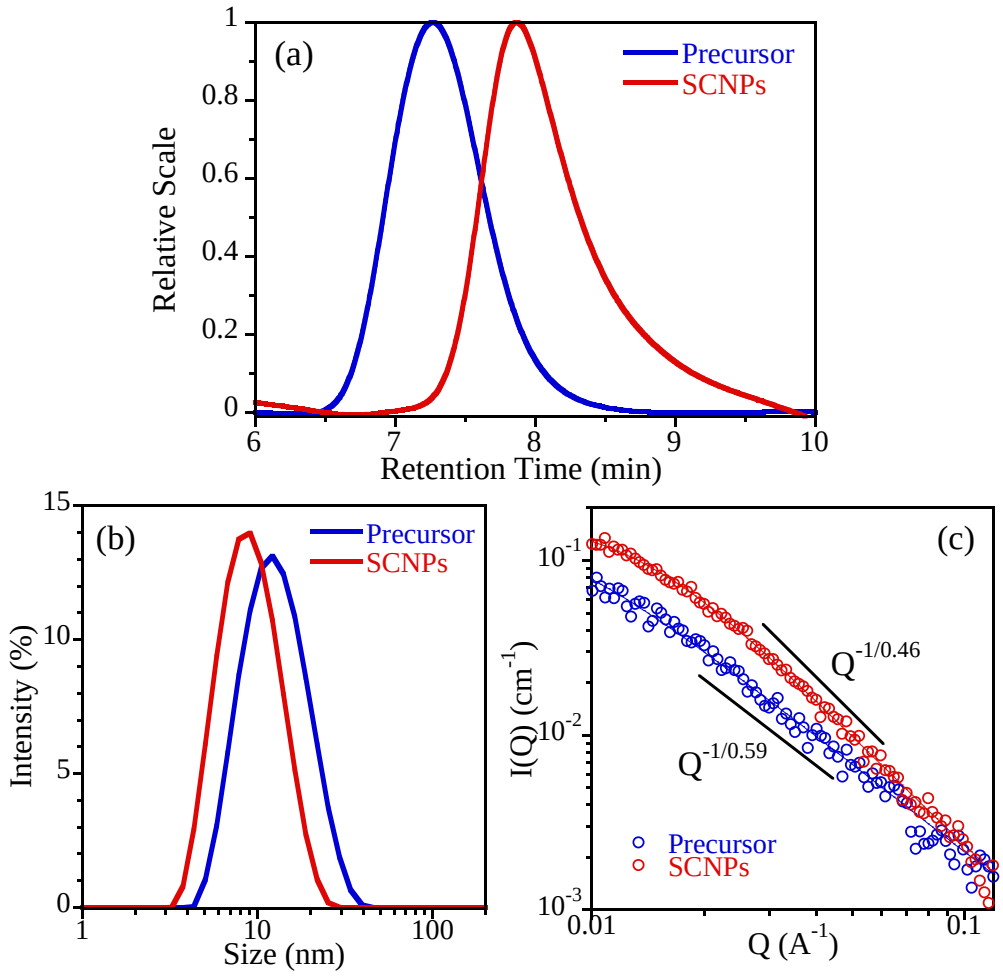

Figure 5.6: Intra-chain cross-linked single-chain nanoparticles (NP21, red color) and its corresponding linear precursor (P21, blue color) showing chain compaction measured by different techniques. (a) SEC traces (MALLS detector), where SCNPs have longer retention time than precursor, thus showing a reduction in hydrodynamic volume; (b) Size distribution by intensity measured by DLS, where SCNPs display smaller hydrodynamic size; (c) SAXS form factors, where SCNPs have smaller values of the scaling exponent (obtained from the intermediate regime as $(Q) \propto Q^{-1/\nu}$) than precursor, which reflects the compaction of the chain upon internal cross-link.

The results shown in figure 5.6 correspond to NP21, but chain compaction was also observed for NP9, NP16 and NP30. As an example, a clear reduction in the average hydrodynamic size ($\bar{R}_H$) was observed for all the single-chain nanoparticles by comparing data from precursors (table 5.2) and SCNPs (table 5.3).

Table 5.3: Characteristics of single-chain nanoparticles NP9, NP16, NP21 and NP30

Code	x[a] (mol%)	y[a] (mol%)	M_w (kg/mol)	M_w/M_n	$\bar{R}_H$ (nm)	T_g (°C)
NP9	0.5	4.3	259.7	1.3	11.4	110
NP16	2.4	6.8	309.8	1.3	11.0	114
NP21	1.1	9.9	241.9	1.3	9.6	123
NP30	4.5	12.8	274.0	1.3	9.7	132

[a)]Residual azide content as determined by ^{1}H NMR spectroscopy; [b)]Aldehyde content as determined by ^{1}H NMR spectroscopy.

For these SCNPs, we also investigated their properties of bulk samples. Intra-chain cross-linking upon azide decomposition gives rise to a significant increase in the glass transition temperature of the bulk of nanoparticles (table 5.3) with respect to that of the corresponding precursor (table 5.2) due to severely hindered segmental chain mobility in the former case.[39, 48-52] When compared to the network cross-linked material (T_g = 60 °C), intra-chain cross-linked nanoparticles show several distinctive features by IR spectroscopy [red color in figure 5.5(b)]: (i) a new intense IR vibration band at about 1700 cm^{-1} which is indicative of the presence of carbonyl groups in the nanoparticles, (ii) a shift to 1650 cm^{-1} of the –NH– vibration band from the cross-linked chemical segments (scheme 5.5) and (iii) incomplete decomposition of the azide functionalities after the microwave treatment (200 °C, 30 min) (figure 5.5 and table 5.3).

^{1}H NMR and ^{13}C NMR spectra in solution confirmed the additional presence of aldehyde groups in the intra-chain cross-linked nanoparticles (figure 5.7). Hence, peaks that can be attributed to aldehydic protons and carbons were observed at 9.8 ppm and 192 ppm, respectively.

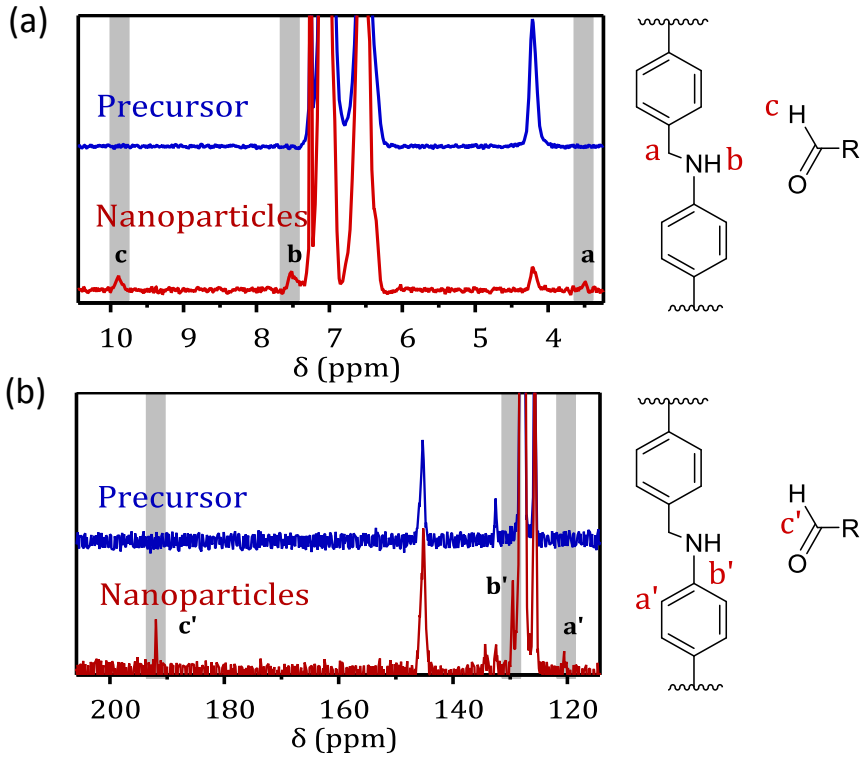

Figure 5.7: (a) ^{1}H NMR and (b) ^{13}C NMR spectra in $CDCl_3$ of precursor P21 and intra-chain cross-linked single-chain nanoparticles NP21.

As illustrated in table 5.3, both the aldehyde content in the SCNPs and the corresponding T_g increase with an increase in azide content in the precursor. No signals from potential enamine products were detected by IR, ^{1}H NMR and ^{13}C NMR spectroscopy. Instead, the blue shift of the –NH– vibration band and the

shoulder in the >C=O band observed in figure 5.5(b) for the SCNPs are suggestive of the involvement of aldehyde/amine hydrogen bonding interactions in the neat material. These directional interactions, in addition to the intra-chain cross-linking, could contribute to the significant increase in glass transition temperature of the single-chain nanoparticles when compared to the precursors.

To further elucidate the precise origin and nature of the aldehyde groups in the intra-chain cross-linked nanoparticles, DS measurements were performed. We hypothesized that signals arising from the products of nitrene chemistry upon azide decomposition, if active, should be easily detected by DS, due to the negligible DS signal of PS at low temperatures.[53-54]

Figure 5.8 illustrates the dielectric spectra corresponding to P0 (reference with 0 mol% of azide groups), azide-containing precursor P21, network cross-linked material B21 and intra-chain cross-linked nanoparticles NP21 and NP9. The spectrum of sample NP9 was normalized by a factor 21/9 showing that the resulting DS signal is approximately proportional to the initial amount of azide groups in the precursor. This is a clear indication that aldehyde groups were generated from a fraction of the total amount of azidomethyl units of the precursor. Consequently, the combined DS, IR and NMR results strongly suggest that the SCNPs were decorated with benzaldehyde pendants.

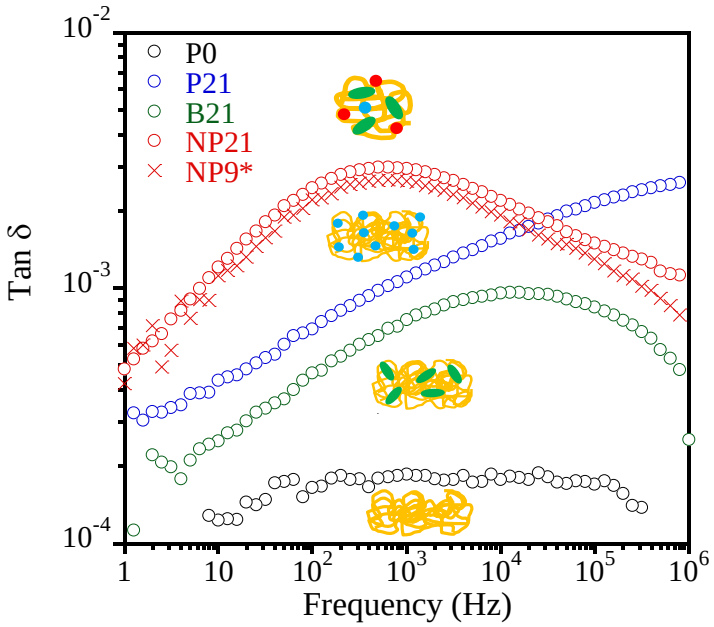

Figure 5.8: Dielectric spectra at T = -93 °C of P0 (as a reference), precursor P21, network cross-linked material B21 and single-chain nanoparticles NP21 and NP9. *Spectrum of NP9 was normalized to that of NP21 by multiplying the loss factor (tan δ) by 21/9.

In fact, the dielectric spectrum of a mixture of P0 (neat PS) and neat benzaldehyde provided compelling evidence of the presence of benzaldehyde pendants in the nanoparticles [figure 5.9(a)]. Hence, the strong dielectric signal of the nanoparticles at low temperature can be attributed to the rotation around the phenyl ring of the benzaldehyde pendant which is known to possess a strong electric dipole moment (μ = 3.14 D).[55]

According to figure 5.8, these benzaldehyde pendants are highly sensitive DS probes when compared to either amine groups of the cross-linked chemical segments or azide pendant moieties of the precursor. Based on the Arrhenius law, a plot of the frequency at the peak maximum (f_{max}) vs. inverse of

temperature ($1/T$) allows one to determine the activation energy (E_a) for the rotation around the phenyl ring of the benzaldehyde pendants in the nanoparticles [figure 5.9(b)]. The value of E_a obtained, 8.1 ± 0.1 kcal mol^{-1}, is similar to that observed for systems with hydrogen bonds of weak strength,[56] i.e., 1–15 kcal mol^{-1} and, hence, consistent with the presence of aldehyde/amine hydrogen bonding interactions in the NP9, NP16, NP21 and NP30 samples. It is worth of mention that benzaldehyde cannot form enamines with secondary amines.

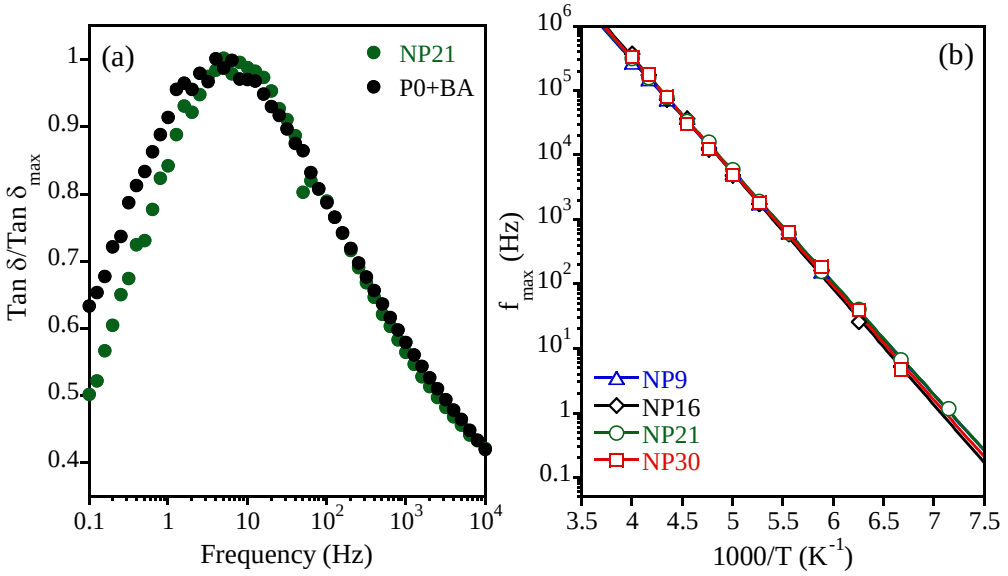

Figure 5.9: (a) Tan δ normalized to its maximum value at T = -123 °C of NP21 (green symbols) and a mixture of P0 and neat benzaldehyde (black symbols). (b) Arrhenius plot giving the activation energy for the rotation around the phenyl ring of the benzaldehyde pendants in nanoparticles NP9, NP16, NP21 and NP30.

Similar results were obtained when the microwave-assisted azide decomposition of precursors P9, P16, P21 and P30 was carried out in NMP

instead of DMF. Figure 5.10(a) shows the IR spectra of NP21 synthesized in DMF (red) and NMP (grey); in both cases the presence of carbonyl groups (intense band at 1700 cm^{-1}) and –NH– groups (1650 cm^{-1}) is observed. Similarly, figure 5.10(b) displays ^{1}H NMR spectra of both samples having the same characteristics peaks, as indicated. Hence, the potential role of DMF as formylation agent[57-60] can be ruled out.

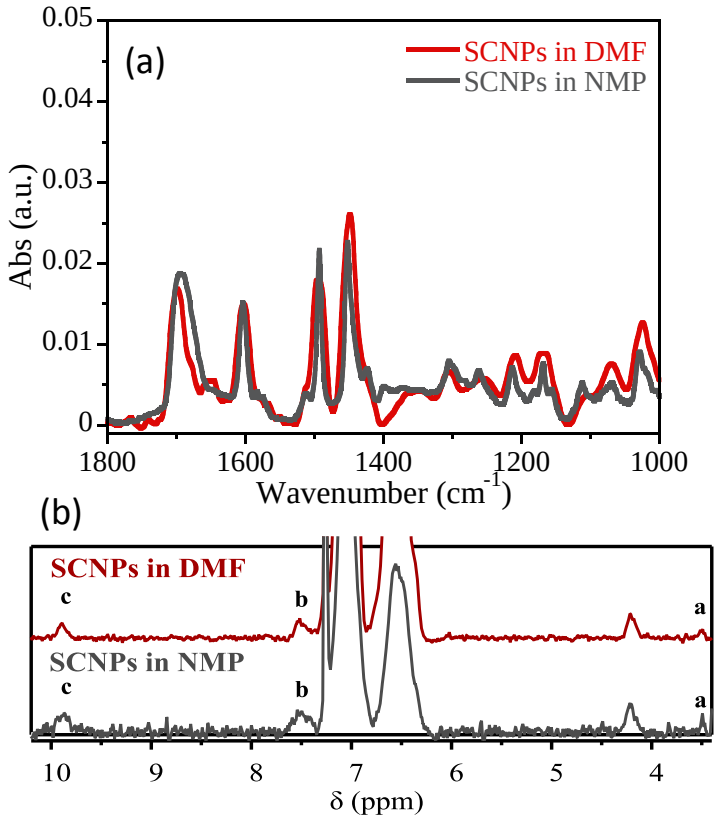

Figure 5.10: Intra-chain cross-linked single chain nanoparticles NP21 synthesized in DMF (red) and NMP (grey). (a) IR spectra of both samples; (b) ^{1}H NMR in $CDCl_3$.

A tentative mechanism of aldehyde formation during azide thermolysis in DMF or NMP is provided in scheme 5.6(a), involving nitrene formation, followed by Schmidt rearrangement and imine hydrolysis during work up in the single-chain nanoparticle isolation step. Such a plausible mechanism is supported by previous observation of azide decomposition under UV light exposure with aldehyde generation[61-62] and control experiments with benzyl azide (synthesis details are described in chapter 2). In these control experiments, no signs of aldehyde groups were detected when benzyl azide was directly analyzed without further purification after microwave irradiation, and only signals coming from –NH– groups were present (blue color in figure 5.11). On the contrary, if benzyl azide was treated with water, the presence of signals from aldehyde groups was clearly observed by ^{1}H NMR (green color in figure 5.11).

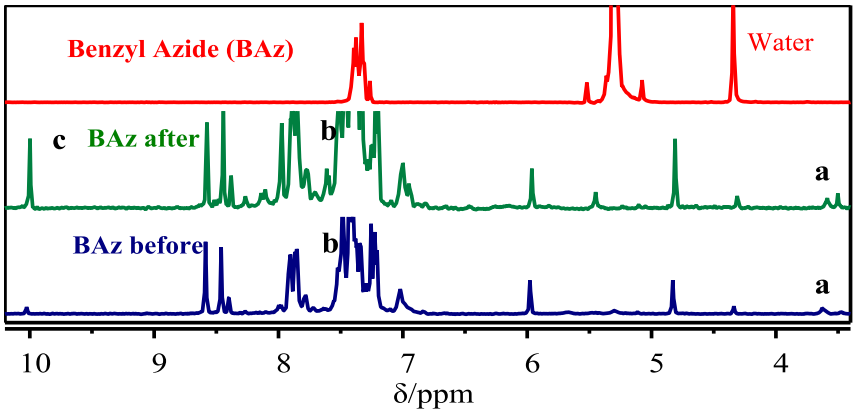

Figure 5.11: ^{1}H NMR spectra in $CDCl_3$ of benzyl azide (red), benzyl azide after m. w. reaction without treatment with water (blue) and benzyl azide after m. w. reaction and treatment with water (green).

In the present system, nitrene insertion into aromatic C–H bonds also takes place leading to intra-chain cross-linking [scheme 5.6(b)].

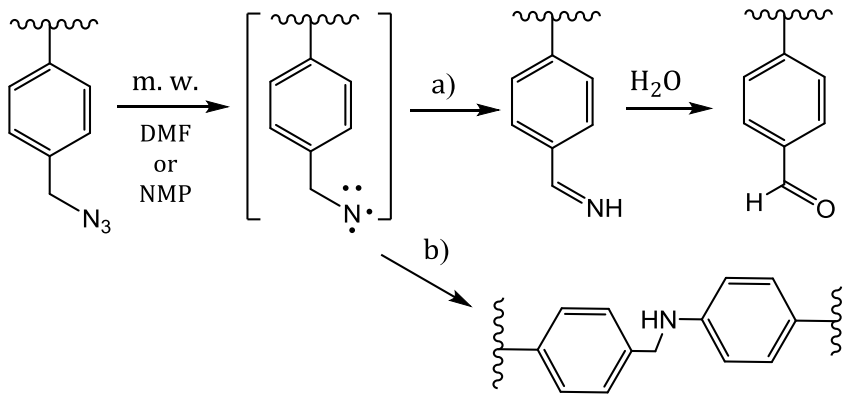

Scheme 5.6: Aldehyde-decorated soft nanoparticles from azides: (a) proposed mechanism of the formylation reaction. (b) Nitrene insertion into C-H bonds leading to intra-chain cross-linking.

As a consequence, aldehyde-decorated ultrafine soft nanoparticles are easily obtained through this new route. To illustrate the versatility of the aldehyde functionality, fluorescent SCNPs were obtained by reaction of the benzaldehyde pendants with dansylhydrazine (figure 5.12).

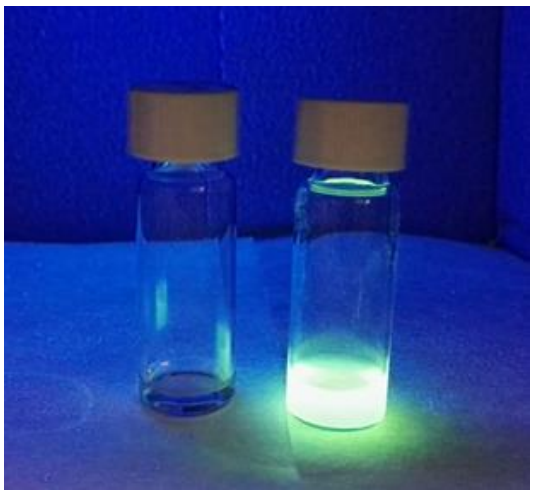

Figure 5.12: Fluorescent SCNPs obtained after functionalization of aldehyde pendants of NP30 with dansylhydrazine.

5.3.4. Conclusion

We have discovered a new and unexpected route towards the straightforward synthesis of aldehyde-decorated ultrafine soft nanoparticles based on microwave-assisted decomposition of azide-containing precursors in DMF or NMP at high dilution. It is worth of mention that the aldehyde functionality is absent upon azide thermal decomposition in the melt of exactly the same precursor. This finding opens new avenues for the rapid and efficient generation of functional ultrafine single-chain nanoparticles with potential use in material science, sensing and biotechnology. Moreover, the facile decoration of other different supports with aldehyde functional groups following this route can be envisioned. It is worth also emphasizing that this is one of the first investigations on a bulk system of SCNPs, and also that a non-conventional technique in this field –dielectric spectroscopy (DS)– has been employed.

5.4. Poly(Vinyl Pyrrolidone) SCNPs *via* Fenton Reaction

5.4.1. Introduction

Hydroxyl radicals, highly reactive species, have been used as initiators for cross-linking reactions. In the presence of polymer macromolecules bearing labile hydrogen atoms they react to produce macroradicals. If favorably positioned, these radicals may undergo recombination leading to a covalent cross-link.[63]

The Fenton reaction, known for more than a century, is a process that relies on the reduction of hydrogen peroxide at the expense of Fe^{2+} ions.[64-66] The hydroxyl radicals generated by Fenton reaction [Eq. (5.1)] are expected to have the same behavior as the hydroxyl radicals produced by high-energy radiation or by photolysis of H_2O_2. Fenton reagents have been used as radical initiator in vinylic polymerization or grafting for more than 50 years.[67-70] These reagents have been also used to initiate cross-linking[71] and prepare hydrogels.[63, 72-74]

$$Fe^{2+} + H_2O_2 \rightarrow Fe^{3+} + OH^- + OH^{\bullet} \qquad (5.1)$$

During the last decade there has been a growing interest in the potential use of soft nanoparticles as carriers for targeting drugs. Unfortunately, most of the current synthesis routes to stable single-chain nanoparticles suffer from different shortcomings, such as the use of extremely high temperatures, requirement of severe anhydrous conditions, or necessity of exotic, noncommercial monomers, which severely limit their potential applications in some promising fields (e.g., nanomedicine).[75] In this sense, the subject of interest in this field is the use of biocompatible, nontoxic and nonantiagenic

polymers, such as poly(vinyl pyrrolidone) (PVP), to produce SCNPs with these useful biological properties. PVP is a valuable water-soluble polymer with a large commercial use in medicine.

5.4.2. Objective

Our objective here is to develop a novel, facile and a higly-efficient method to obtain biocompatible poly(vinyl pyrrolidone) (PVP) based single-chain nanoparticles *via* Fenton reaction. This synthesis process has been achieved by starting from commercially available water-soluble PVP homopolymers and by using reactive oxygen species (ROS) for the intra-chain folding/collapse process of individual polymer chains. As it will be shown, since the resulting PVP SCNPs present potential features to be used in nanomedicine (water-soluble, biocompatible and non-toxic), an experiment to exploit these SCNPs as controlled drug-delivery nanocarriers has been performed.

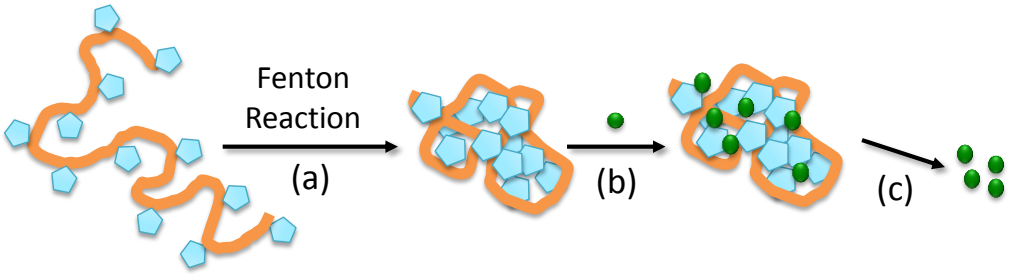

Scheme 5.7: (a) Intra-chain folding/collapse of individual PVP polymer chains to SCNPS *via* Fenton reaction. (b) Drug encapsulation and (c) delivery from PVP SCNPs.

5.4.3. Results and Discussion

Hydroxyl radical is the most reactive radical among the reactive oxygen species (ROS). Its reaction with PVP is expected to generate macroradicals centered in three possible positions, taking into account the labiality of the hydrogen atoms present in its structure (see scheme 5.8). Generally, the rate of hydrogen abstraction is dependent on the dissociation energy of the X-H bond to form the radical. Basic thermodynamic calculations show that C-H bonds α-positioned to a heteroatom or a carbonyl are lower in energy, mainly due to the stabilization of the radical product. From the 5 possible C-H bonds in PVP structure, two of them do not fall into this category and are considered much less reactive.[63]

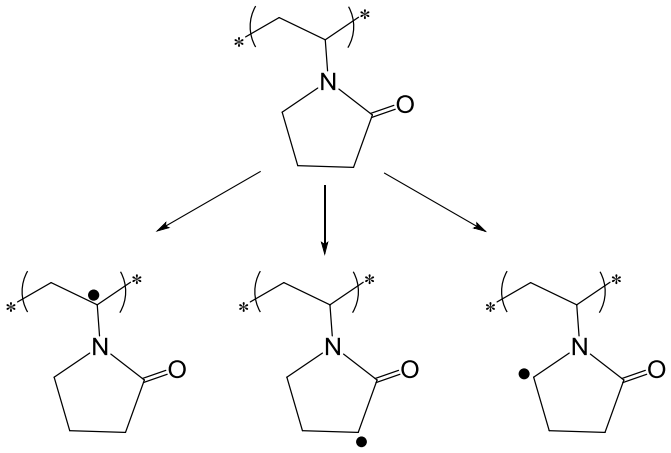

Scheme 5.8: PVP macroradicals formed by Fenton reaction

Within the three possibilities shown in scheme 5.8, the most favorable PVP macroradical obtained by Fenton reaction is the second case. Then, PVP water soluble single-chain nanoparticles will be formed *via* intra-chain coupling of these radicals, as is illustrated in scheme 5.9. Experimentally, the intra-chain

cross-linking of the individual poly(vinyl pyrrolidone) linear chains to single-chain nanoparticles was performed in water, at room temperature in the presence of hydroxyl radicals (generated by Fenton reaction), and at very dilute conditions (0.5 mg/ml) in order to avoid inter-molecular cross-linking processes (all details about the synthesis are described in 'New Synthesis Routes' in chapter 2).

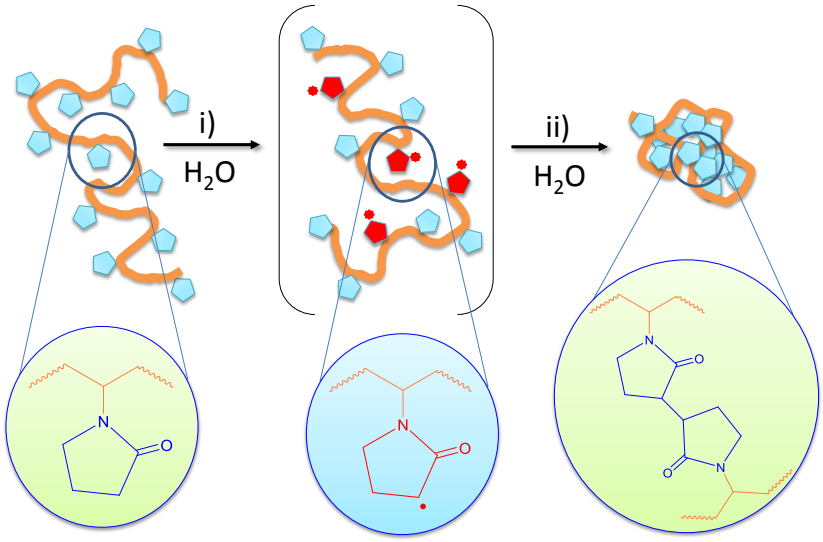

Scheme 5.9: Illustration of the synthesis at high dilution of water-soluble poly(vinyl pyrrolidone) single-chain nanoparticles (PVP SCNPs) via intra-chain coupling (step ii) of radicals generated by Fenton reaction (step i).

Figure 5.13 (upper panels) shows the systematic shift in SEC traces (MALLS detector) towards longer retention time during the synthesis of low molecular weight (M_w = 55 kg/mol) (a) and high molecular weight (M_w = 360 kg/mol) (b) PVP SCNPs. The noticeable shift observed in both cases is a consequence of the progressive reduction in hydrodynamic size and, consequently, in apparent molar mass (M_p^{app}) with reaction time (table 5.4).[76] After 72 h, a significant

increase in retention time, and consequently a reduction in hydrodynamic volume, was achieved so we decided to stop the reaction, and set it as the optimum reaction time.

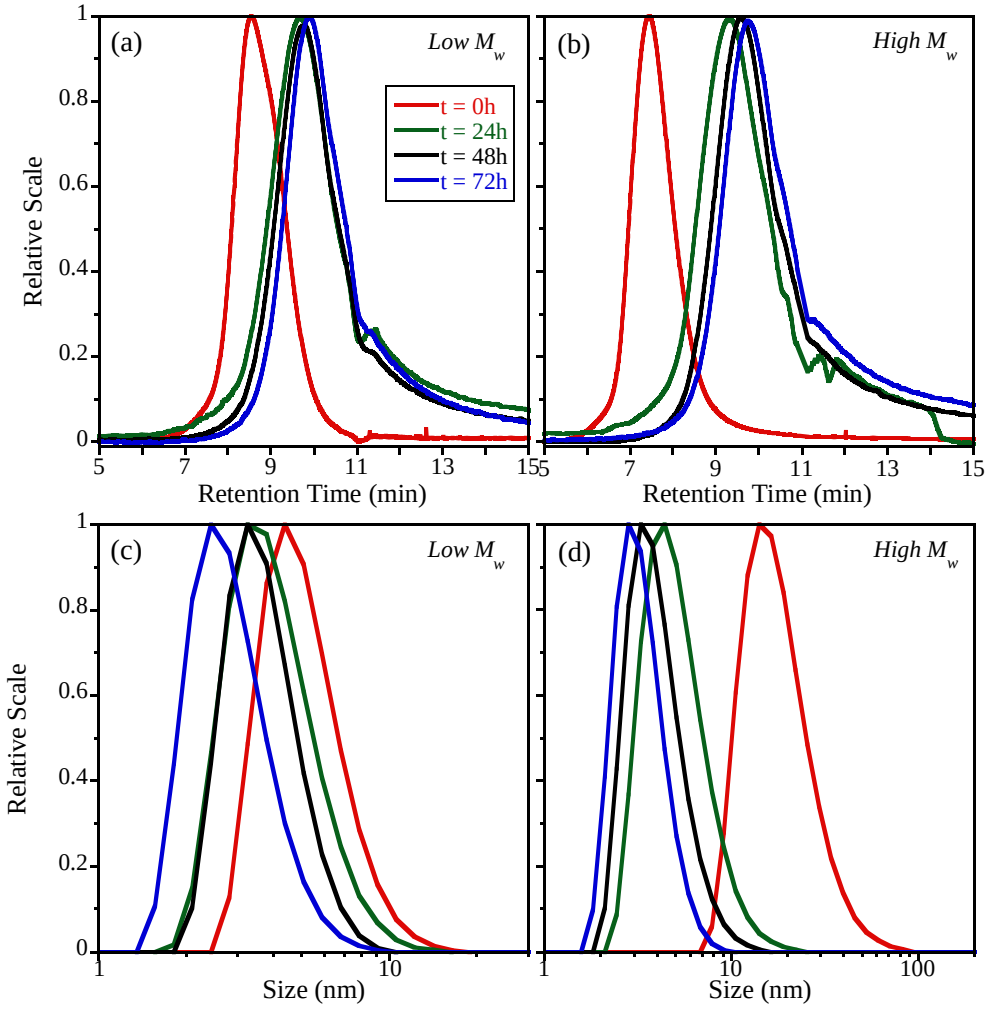

Figure 5.13: *Upper panels*: Evolution of the SEC traces with reaction time [from left to right: 0 h, 24 h, 48 h and 72 h, color code indicated in (a)] for low M_w SCNPs (a) and high M_w SCNPs (b). *Lower panels*: Size distribution evolution with reaction time [color code indicated in (a)] measured by DLS for low M_w SCNPs (c) and high M_w SCNPs (d).

A simple inspection in SEC traces suggested the absence of inter-molecular cross-linking and thus the formation of PVP SCNPs was only happening *via* intra-chain cross-linking of linear polymer chains. The absence of inter-particle aggregation was also confirmed through dynamic light scattering (DLS) measurements, showing a monomodal particle size distribution during the whole synthesis process for both, low molecular weight [figure 5.13(c)] and high molecular weight SCNPs [figure 5.13(d)]. Moreover, from DLS measurements a reduction in hydrodynamic volume was also observed; SCNPs display smaller hydrodynamic radius than the polymer precursor (table 5.4).

Table 5.4: Data of high M_w and low M_w PVP-SCNPs obtained during the synthesis process.

Reaction time	M_p^{app} (kg/mol)[a] High M_w	R_H (nm)[b] High M_w	M_p^{app} (kg/mol)[a] Low M_w	R_H (nm)[b] Low M_w
0 h	360.2	18.9	55.1	5.2
24 h	14.7	5.3	7.6	4.1
48 h	9.1	4.1	6.5	3.8
72 h	6.7	3.3	5.3	2.9

a)Apparent molecular weight as determined by SEC in water; b)Hydrodynamic radius as determined by DLS in water at 25 °C.

It is well known that efficiency of the Fenton reaction depends on relative concentrations on the Fenton reagents, i. e., $[H_2O_2/Fe^{2+}]$ ratio, and pH.[66] PVP SCNPs were successfully obtained when the reaction was carried out in acidic medium (pH = 3.5) and the ratio of $[H_2O_2/Fe^{2+}]$ was 2 (results shown above). However, no SCNPs were obtained when the ratio was increased to 10, probably due to the high amount of PVP macroradicals formed, which would promote inter-molecular cross-linking and hence aggregation. We also performed another reaction in acidic medium where the ratio $[H_2O_2/Fe^{2+}]$ was 1, but no enough

madroradicals were formed to promote intra-chain folding/collapse of PVP polymer chains.

Moreover, to evaluate the pH influence, we carried out a reaction in basic medium (pH = 7.5) with the ratio $[H_2O_2/Fe^{2+}]$ = 2. Dynamic light scattering (DLS) measurements on PVP of high molecular weight showed that after 24 h of reaction in basic medium, polymer chains formed aggregates with a hydrodynamic radius of ~200 nm (figure 5.14).

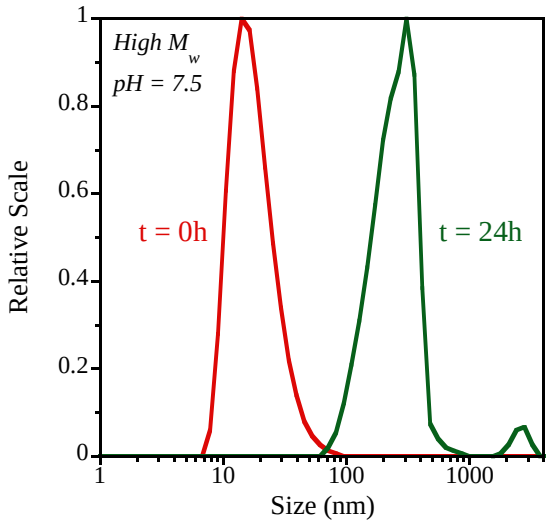

Figure 5.14: Size distribution evolution with reaction time measured by DLS for high M_w PVP at pH = 7.5 and $[H_2O_2]/[Fe^{2+}]$ = 2.

The equation 5.1 above described suggests that the presence of H^+ is favorable for the decomposition of H_2O_2, indicating the necessity of the acid environment to produce hydroxyl radicals in a Fenton system.[64] At higher pH, the oxidation efficiency of Fenton's reagent may decrease due to the transition of iron from a hydrated ferrous ion to a colloidal ferric species, $Fe(OH)_2$. In the latter form, iron

catalytically decomposes the H_2O_2 into oxygen and water, without forming hydroxyl radicals, leading to a heterogeneous dispersion and thus promoting aggregation.

One of the most promising fields of application of single-chain polymer nanoparticles is the design of engineered nano-systems to address diseases and to monitor and to protect human health. Ideally, the resulting nanocarriers should display low toxicity, high biodegradability, appropriate capacity to encapsulate different anti-cancer drugs and tunable control of drug release kinetics. In this sense, we have investigated the drug-delivery properties of PVP SCNPs synthesized by Fenton reaction of cisplatin drug. Cisplatin (CP) is a widely used anticancer agent[77-78] that has been shown to be highly effective in the treatment of testicular, ovarian, breast, bladder, lung and head and neck cancer.

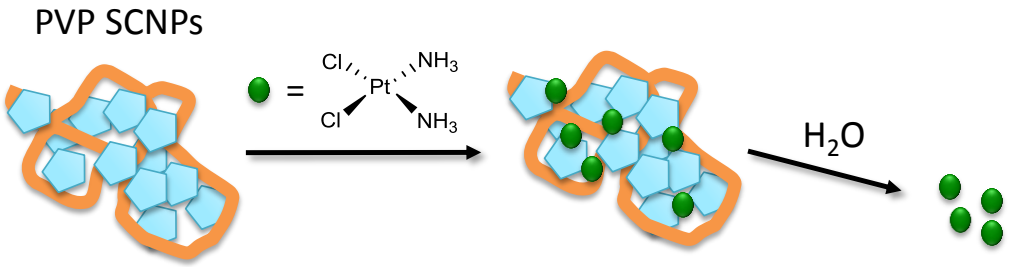

Scheme 5.10: Illustration of the delivery of cisplatin drug from PVP single-chain nanoparticles.

Hence, cisplatin-loaded poly(vinyl pyrrolidone) single-chain nanoparticles were placed in distillated water (scheme 5.10) and a dialysis method was used to investigate their controlled delivery properties (all details about the preparation of cisplatin loaded PVP SCNPs are described in chapter 2). Figure 5.15(a) shows the absorbance increase in in UV-vis spectrum at 265 nm with time due to the

cisplatin release from PVP SCNPs, and figure 5.15(b) illustrates cisplatin release time profile during 96 h deduced from UV-vis measurements.

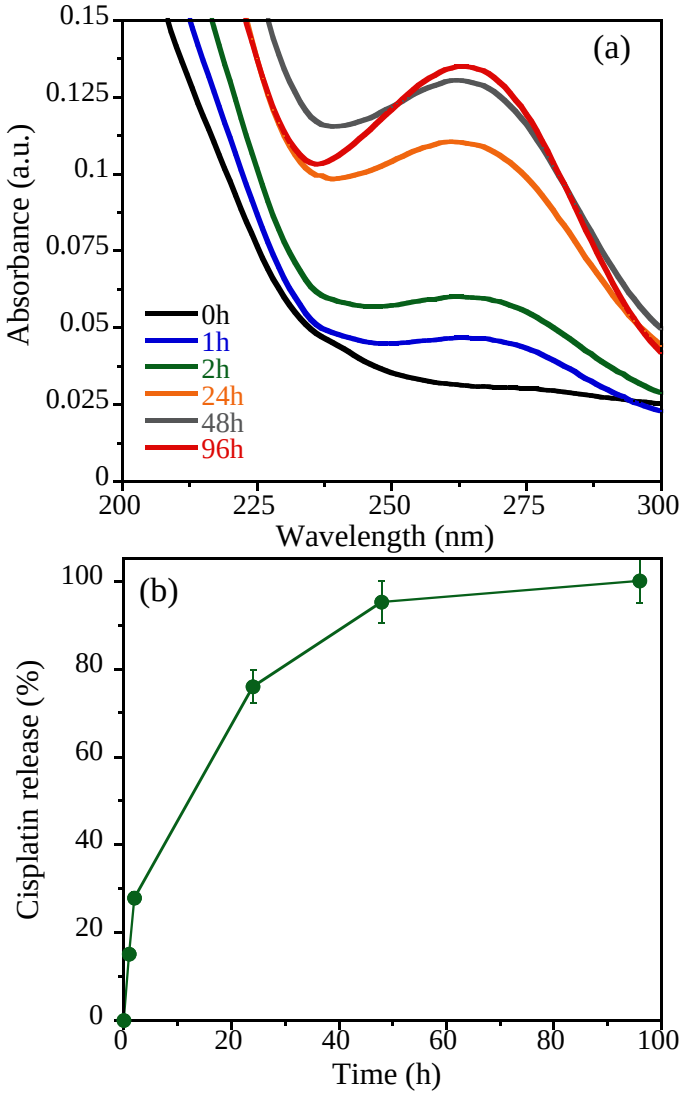

Figure 5.15: (a) Evolution of the UV-vis spectrum at 265 nm with time (0h, 1h, 2h, 24h, 48h an 96h, color code indicated in the figure) due to cisplatin release from PVP SCNPs. (b) Cisplatin delivery curve in % from PVP SCNPs, obtained from UV-vis measurements.

The complete delivery of cisplatin from PVP single-chain nanoparticles was observed to take place in 96 h, but almost the 75% of CP was released in the first 24 h [figure 5.15(b)]. These promising results indicate that PVP based single-chain nanoparticles have a great potential as a biocompatible material with a high efficiency in drug encapsulation and delivery.

5.4.4. Conclusion

In summary, we have developed a new and highly-efficient strategy for the preparation of water-soluble, biodegradable and non-toxic poly(vinyl pyrrolidone) single-chain nanoparticles *via* Fenton reaction. Moreover, we have demonstrated the potential use of PVP single-chain nanoparticles as drug nanocarriers, showing their appropriate capacity to encapsulate and release the drug cisplatin. Thanks to their biocompatibility, these PVP nanocarriers are expected to be applicable in promising fields, such as nanomedicine.

5.5. References

[1] M. Gonzalez-Burgos, A. Latorre-Sanchez, J. A. Pomposo, *Chem. Soc. Rev.* **2015**, *44*, 6122-6142.

[2] J. A. Pomposo, *Polymer International* **2014**, *63*, 589-592.

[3] A. Latorre-Sánchez, J. A. Pomposo, *Polymer International* **2016**, *65*, 855-860.

[4] M. Huo, N. Wang, T. Fang, M. Sun, Y. Wei, J. Yuan, *Polymer* **2015**, *66*, A11-A21.

[5] P. Tompa, *Trends in Biochemical Sciences* **2002**, *27*, 527-533.

[6] I. Perez-Baena, I. Asenjo-Sanz, A. Arbe, A. J. Moreno, F. Lo Verso, J. Colmenero, J. A. Pomposo, *Macromolecules* **2014**, *47*, 8270-8280.

[7] T. Terashima, T. Sugita, K. Fukae, M. Sawamoto, *Macromolecules* **2014**, *47*, 589-600.

[8] C. J. Riddles, W. Zhao, H.-J. Hu, M. Chen, M. R. Van De Mark, *Polymer* **2014**, *55*, 48-57.

[9] D. Mecerreyes, V. Lee, C. J. Hawker, J. L. Hedrick, A. Wursch, W. Volksen, T. Magbitang, E. Huang, R. D. Miller, *Advanced Materials* **2001**, *13*, 204-208.

[10] M. Seo, B. J. Beck, J. M. J. Paulusse, C. J. Hawker, S. Y. Kim, *Macromolecules* **2008**, *41*, 6413-6418.

[11] N. Hosono, A. M. Kushner, J. Chung, A. R. Palmans, Z. Guan, E. W. Meijer, *J Am Chem Soc* **2015**, *137*, 6880-6888.

[12] G. M. ter Huurne, M. A. J. Gillissen, A. R. A. Palmans, I. K. Voets, E. W. Meijer, *Macromolecules* **2015**, *48*, 3949-3956.

[13] T. Terashima, T. Mes, T. F. De Greef, M. A. Gillissen, P. Besenius, A. R. Palmans, E. W. Meijer, *J Am Chem Soc* **2011**, *133*, 4742-4745.

[14] S. Mavila, C. E. Diesendruck, S. Linde, L. Amir, R. Shikler, N. G. Lemcoff, *Angew Chem Int Ed Engl* **2013**, *52*, 5767-5770.

[15] J. Jeong, Y.-J. Lee, B. Kim, B. Kim, K.-S. Jung, H.-j. Paik, *Polym. Chem.* **2015**, *6*, 3392-3397.

[16] A. Sanchez-Sanchez, A. Arbe, J. Colmenero, J. A. Pomposo, *ACS Macro Letters* **2014**, *3*, 439-443.

[17] A. Sanchez-Sanchez, A. Arbe, J. Kohlbrecher, J. Colmenero, J. A. Pomposo, *Macromolecular Rapid Communications* **2015**, *36*, 1592-1597.

[18] J. Willenbacher, O. Altintas, P. W. Roesky, C. Barner-Kowollik, *Macromolecular Rapid Communications* **2014**, *35*, 44-44.

[19] J. Willenbacher, O. Altintas, V. Trouillet, N. Knöfel, M. J. Monteiro, P. W. Roesky, C. Barner-Kowollik, *Polym. Chem.* **2015**, *6*, 4358-4365.

[20] S. Mavila, I. Rozenberg, N. G. Lemcoff, *Chem. Sci.* **2014**, *5*, 4196-4203.

[21] F. Wang, H. Pu, M. Jin, D. Wan, *Macromol Rapid Commun* **2016**, *37*, 330-336.

[22] E. H. H. Wong, G. G. Qiao, *Macromolecules* **2015**, *48*, 1371-1379.

[23] A. J. Moreno, F. Lo Verso, A. Arbe, J. A. Pomposo, J. Colmenero, *J Phys Chem Lett* **2016**, *7*, 838-844.

[24] M. Rubinstein, R. H. Colby, *Polymer Physics*, Oxford University Press, Oxford, UK, **2003**.

[25] B. M. Kriegel, R. G. Bergman, J. Arnold, *J Am Chem Soc* **2016**, *138*, 52-55.

[26] S. P. Heins, W. D. Morris, P. T. Wolczanski, E. B. Lobkovsky, T. R. Cundari, *Angew Chem Int Ed Engl* **2015**, *54*, 14407-14411.

[27] J. Egger, E. M. Carreira, *Nat Prod Rep* **2014**, *31*, 449-455.

[28] C. Wentrup, *Acc Chem Res* **2011**, *44*, 393-404.

[29] F. Tiemann, *Berichte der deutschen chemischen Gesellschaft* **1891**, *24*, 4162-4167.

[30] J. Park, M. Yan, *Acc Chem Res* **2013**, *46*, 181-189.

[31] A. I. Olivos Suarez, V. Lyaskovskyy, J. N. Reek, J. I. van der Vlugt, B. de Bruin, *Angew Chem Int Ed Engl* **2013**, *52*, 12510-12529.

[32] T. A. Ramirez, B. Zhao, Y. Shi, *Chem Soc Rev* **2012**, *41*, 931-942.

[33] G. Dequirez, V. Pons, P. Dauban, *Angew Chem Int Ed Engl* **2012**, *51*, 7384-7395.

[34] F. Collet, C. Lescot, P. Dauban, *Chem Soc Rev* **2011**, *40*, 1926-1936.

[35] R. Q. Png, P. J. Chia, J. C. Tang, B. Liu, S. Sivaramakrishnan, M. Zhou, S. H. Khong, H. S. Chan, J. H. Burroughes, L. L. Chua, R. H. Friend, P. K. Ho, *Nat Mater* **2010**, *9*, 152-158.

[36] H. J. Kim, A. R. Han, C.-H. Cho, H. Kang, H.-H. Cho, M. Y. Lee, J. M. J. Fréchet, J. H. Oh, B. J. Kim, *Chemistry of Materials* **2012**, *24*, 215-221.

[37] J. Bang, J. Bae, P. Löwenhielm, C. Spiessberger, S. A. Given-Beck, T. P. Russell, C. J. Hawker, *Advanced Materials* **2007**, *19*, 4552-4557.

[38] P. Yang, W. Yang, *Chem Rev* **2013**, *113*, 5547-5594.

[39] G. Li, F. Tao, L. Wang, Y. Li, R. Bai, *Polymer* **2014**, *55*, 3696-3702.

[40] X. Jiang, H. Pu, P. Wang, *Polymer* **2011**, *52*, 3597-3602.

[41] V. Raicu, Y. Feldman, *Dielectric Relaxation in Biological Systems: Physical Principles, Methods, and Applications*, Oxford University Press, Oxford, **2015**.

[42] F. Kremer, A. Schönhals, *Broadband Dielectric Spectroscopy*, Springer-Verlag, Berlin, **2003**.

[43] J. A. Pomposo, I. Perez-Baena, F. Lo Verso, A. J. Moreno, A. Arbe, J. Colmenero, *ACS Macro Letters* **2014**, *3*, 767-772.

[44] A. Sanchez-Sanchez, D. A. Fulton, J. A. Pomposo, *Chem Commun (Camb)* **2014**, *50*, 1871-1874.

[45] C. F. Hansell, A. Lu, J. P. Patterson, R. K. O'Reilly, *Nanoscale* **2014**, *6*, 4102-4107.

[46] W. Fan, X. Tong, Q. Yan, S. Fu, Y. Zhao, *Chem Commun (Camb)* **2014**, *50*, 13492-13494.

[47] D. Chao, X. Jia, B. Tuten, C. Wang, E. B. Berda, *Chem Commun (Camb)* **2013**, *49*, 4178-4180.

[48] B. Zhu, J. Ma, Z. Li, J. Hou, X. Cheng, G. Qian, P. Liu, A. Hu, *Journal of Materials Chemistry* **2011**, *21*, 2679.

[49] J. He, L. Tremblay, S. Lacelle, Y. Zhao, *Soft Matter* **2011**, *7*, 2380.

[50] B. Zhu, G. Qian, Y. Xiao, S. Deng, M. Wang, A. Hu, *Journal of Polymer Science Part A: Polymer Chemistry* **2011**, *49*, 5330-5338.

[51] J. Rubio-Cervilla, F. Barroso-Bujans, J. A. Pomposo, *Macromolecules* **2016**, *49*, 90-97.

[52] I. Berkovich, S. Mavila, O. Iliashevsky, S. Kozuch, N. G. Lemcoff, *Chem. Sci.* **2016**, *7*, 1773-1778.

[53] R. Lund, S. Plaza-García, A. Alegría, J. Colmenero, J. Janoski, S. R. Chowdhury, R. P. Quirk, *Macromolecules* **2009**, *42*, 8875-8881.

[54] S. Plaza-García, R. Lund, A. Alegría, J. Colmenero, J. Janoski, R. P. Quirk, *Macromolecules* **2011**, *44*, 7810-7819.

[55] O. Desyatnyk, L. Pszczółkowski, S. Thorwirth, T. M. Krygowski, Z. Kisiel, *Phys. Chem. Chem. Phys.* **2005**, *7*, 1708-1715.

[56] G. R. Desiraju, T. Steiner, *The Weak Hydrogen Bond in Structural Chemistry and Biology*, Oxford University Press, Oxford, **1999**.

[57] S. Ding, N. Jiao, *Angew Chem Int Ed Engl* **2012**, *51*, 9226-9237.

[58] J. Muzart, *Tetrahedron* **2009**, *65*, 8313-8323.

[59] S. Brahma, J. K. Ray, *Tetrahedron* **2008**, *64*, 2883-2896.

[60] A. J. Parker, *Chemical Reviews* **1969**, *69*, 1-32.

[61] G. Abbenante, G. T. Le, D. P. Fairlie, *Chem Commun (Camb)* **2007**, 4501-4503.

[62] A. H. Haines, *Methods for the Oxidation of Organic Compounds*, Academic Press, London, **1988**.

[63] J. A. G. Barros, G. J. M. Fechine, M. R. Alcantara, L. H. Catalani, *Polymer* **2006**, *47*, 8414-8419.

[64] C. Walling, *Accounts of Chemical Research* **2002**, *8*, 125-131.

[65] C. Walling, *Accounts of Chemical Research* **1998**, *31*, 155-157.

[66] E. Neyens, J. Baeyens, *Journal of Hazardous Materials* **2003**, *98*, 33-50.

[67] B. N. Misra, P. S. Chandel, R. Dogra, *Journal of Polymer Science: Polymer Chemistry Edition* **1978**, *16*, 1801-1805.

[68] F. S. Dainton, P. H. Seaman, *Journal of Polymer Science* **1959**, *39*, 279-297.

[69] R. George, C. P. Patel, H. C. Trivedi, D. Mandanwar, *Trends in Carbohydrate Chemistry* **2001**, *7*, 13-19.

[70] L. V., M. Pasteka, F. Kozma, *Cellulose Chemistry and Technology* **1969**, *3*, 139-150.

[71] A. Goessl, N. Tirelli, J. A. Hubbell, *Journal of Biomaterials Science, Polymer Edition* **2004**, *15*, 895-904.

[72] B. Butruk, M. Trzaskowski, T. Ciach, *Mater Sci Eng C Mater Biol Appl* **2012**, *32*, 1601-1609.

[73] Y. Zheng, A. Wang, *Journal of Materials Chemistry* **2012**, *22*, 16552.

[74] L. Sun, S. Zhang, J. Zhang, N. Wang, W. Liu, W. Wang, *Journal of Materials Chemistry B* **2013**, *1*, 3932.

[75] O. Altintas, C. Barner-Kowollik, *Macromol Rapid Commun* **2012**, *33*, 958-971.

[76] J. A. Pomposo, I. Perez-Baena, L. Buruaga, A. Alegría, A. J. Moreno, J. Colmenero, *Macromolecules* **2011**, *44*, 8644-8649.

[77] G. Spenlehauer, M. Veillard, J. P. Benoît, *Journal of Pharmaceutical Sciences* **1986**, *75*, 750-755.

[78] J. D. Rocca, M. E. Werner, S. A. Kramer, R. C. Huxford-Phillips, R. Sukumar, N. D. Cummings, J. L. Vivero-Escoto, A. Z. Wang, W. Lin, *Nanomedicine* **2015**, *11*, 31-38.

CHAPTER 6

Conclusions

6.1. Conclusions

Significant advances have been carried out in recent years in the field of single-chain technology allowing the construction of a variety of single-chain soft nano-objects *via* chain compaction (i.e., chain folding/collapse). One of the most promising outputs of single-chain technology is single-chain polymer nanoparticles. In this thesis we have made progress in this evolving field exploring basic properties of these nano-objects and developing novel synthesis routes towards functional single-chain nanoparticles.

First, we have gained valuable and deeper knowledge about the basic properties of single-chain nanoparticles, in comparison with those of the precursor counterparts. We have performed a complete study about their stability, structure and dynamics in solution combining different techniques. Particularly important has been the application of neutron scattering due to two additional advantages: (i) to match the right length and time scales simultaneously and (ii) to offer the possibility of selectively labeling the components of a complex material. The following outcomes about the basic properties of SCNPs may be particularly highlighted:

- We have found a superior stability against degradation induced by ultrasound irradiation for covalent-bonded SCNPs when compared to their parent linear precursor polymer. We have proposed a new mechanism under sonication involving loop scission events, which explains the excellent stability observed for these nano-objects, instead of the typical chain scission mechanism operative in linear polymers. The increased

stability of SCNPs offers new opportunities for the development of a new generation of mechanically stable ultra-fine soft nanomaterials.

- Regarding the structural investigation, we have applied SAS techniques to determine the macromolecular size and conformation of SCNPs in solution. With these studies we have proved: (i) the collapse with respect to the linear precursor, providing direct microscopic evidence and quantification of the efficiency of the different synthesis routes applied; (ii) the sparse morphology of the usually obtained SCNPs in dilute solutions, rather similar to that exhibited by intrinsically disordered proteins; (iii) the unavoidable aggregation of SCNPs with increasing concentration of the same species, and the recovery of unimolecular solutions upon dilution only for SCNPs obtained by reversible cross-link; (iv) the identification of the overlap concentration of SCNPs as the key magnitude determining the crossover from unperturbed chain conformation in dilute conditions toward a collapse of the macromolecule with increasing crowding.

- As for the dynamics, we have presented the first experimental investigation of the dynamic structure factor of SCNPs in solution. The unique information provided by NSE on the internal macromolecular dynamics has been analyzed in terms of theoretical approximations based on the Zimm model. We have proved that: (i) the internal dynamics for SCNPs in solution is extremely hindered with respect to that of the linear counterparts; (ii) the similarities of SCNPs with the behavior of intrinsically disordered proteins also from a dynamic viewpoint; (iii) the most realistic scenario to describe the experimental observations in the range of concentrations here

investigated considers unperturbed form factor and a Q-dependent diffusion coefficient, reflecting the inter-molecular interactions of the entities in solution.

Furthermore, trying to contribute to the design of nano-objects with improved capabilities, we have presented three novel synthesis routes for the preparation of functional single-chain nanoparticles and we have demonstrate their possible use in potential applications like catalysis or nanomedicine, either by means of proof-of-concept experiments or molecular dynamics simulations. The main results about the novel SCNPs obtained can be summarized as follows:

- We have developed a method for tuning the internal structure of metallo-folded SCNPs by using amphiphilic random copolymers and two different synthesis procedures (protocols). The combination of different results from SEC, SAXS and MD-simulations led us to obtain a clear picture of the size, morphology in solution and spatial distribution of catalytic sites (internal structure). We found a relatively homogeneous spatial distribution of catalytic sites along the SCNPs synthesized by one of the protocols, while SCNPs obtained by the other protocol showed clusters of catalytic sites. These results pave the way for tuning the catalytic properties of metallo-folded soft nano-objects based on SCNPs.

- While investigating the microwave-assisted decomposition of azide-containing polymers at high dilution, we have discovered an unexpected, straightforward route to obtain aldehyde decorated ultrafine single-chain nanoparticles. Fluorescent SCNPs were obtained thanks to the presence of

aldehyde groups distributed along the surface of the nanoparticle. This finding opens new avenues for the rapid and efficient synthesis of functional SCNPs with potential use in material science, sensing and biotechnology.

- We have used Fenton reaction to promote intra-chain homocoupling of poly(vinyl pyrrolidone) (PVP) polymer chains towards water-soluble, biocompatible and non-toxic PVP single-chain nanoparticles. We have performed successful experiments with these SCNPs to exploit their use as controlled drug-delivery nanocarriers, in particular with the drug cisplatin. Thanks to their valuable features, these soft nano-objects are expected to be applicable in promising fields, such as nanomedicine.

Finally, from this thesis we can conclude that an interdisciplinary strategy combining synthesis, proof-of-concept experiments, simulations, and scattering techniques can be considered as the ideal approach for the production of single-chain polymer nanoparticles endowed with useful and smart functions, as well as to disentangle the emerging properties of SCNPs-based materials.

6.2. Publications

This thesis has contributed to the following publications:

- Advances in Single Chain Technology.
  M. Gonzalez-Burgos, A. Latorre-Sanchez and J. A. Pomposo, *Chemical Society Reviews*, 2015, *44*, 6122-6142.

- A Solvent-Based Strategy for Tuning the Internal Structure of Metallo-Folded Single-Chain Nanoparticles.
  S. Basasoro, M. Gonzalez-Burgos, A. J. Moreno, F. Lo Verso, A. Arbe, J. Colmenero and J. A. Pomposo, *Macromolecular Rapid Communications*, 2016, *37*, 1060-1065.

- Structure and Dynamics of Single-Chain Nanoparticles in Solution.
  A. Arbe, J. A. Pomposo, A. J. Moreno, F. Lo Verso, M. Gonzalez-Burgos, I. Asenjo-Sanz, A. Iturrospe, A. Radulescu, O. Ivanova and J. Colmenero, *Polymer*, 2016, *105*, 532-544.

- An Unexpected Route to Aldehyde-decorated Single-Chain Nanoparticles from Azides.
  M. Gonzalez-Burgos, A. Alegría, A. Arbe, J. Colmenero and J. A. Pomposo, *Polymer Chemistry*, 2016, *7*, 6570-6574.

- Excellent Stability in Water of Single-Chain Nanoparticles against Chain Scission by Sonication.
  M. Gonzalez-Burgos, E. Gonzalez and J. A. Pomposo, *Submitted to Macromolecular Rapid Communications* (2017).

- Crowding the Environment of Single-Chain Nanoparticles: Combined Study by SANS and Simulations.
  M. Gonzalez-Burgos, A. Arbe, A. J. Moreno, J. A. Pomposo, A. Radulescu, and J. Colmenero, *Submitted to Macromolecules* (2017).

- Mapping the Extra Solvent Power of Ionic Liquids for Monomers, Polymers and Globular Nanoparticles.
  M. Gonzalez-Burgos and J. A. Pomposo, *Submitted to Langmuir* (2017).

- Folding of Povidone Single Chains *via* Fenton Reaction for Controlled Delivery of Cisplatin.
  M. Gonzalez-Burgos, M. del Corte, I. Asenjo-Sanz, E. Gonzalez and J. A. Pomposo, *in preparation*.

- Photo-Folding of Isolated Polymer Chains.
  M. Gonzalez-Burgos, E. Gonzalez and J. A. Pomposo, *in preparation.*

Acknowledgments

En primer lugar me gustaría mostrar mi agradecimiento al Prof. Juan Colmenero por haberme dado la oportunidad de unirme al grupo de "Polymers and Soft Matter". Mi experiencia en este grupo ha sido muy satisfactoria y productiva. Expreso mi agradecimiento a la *Universidad del País Vasco* (UPV/EHU) por la concesión de la beca PREDOC, y también al *Materials Physics Center* (MPC) por el apoyo financiero concedido durante la realización de esta tesis.

Quisiera agradecer especialmente a los directores de esta tesis Prof. Arantxa Arbe y Prof. José A. Pomposo, por su constante apoyo y dedicación al trabajo realizado durante estos años. Gracias Arantxa por haberme dado la oportunidad de conocer el interesante mundo de los neutrones, un campo totalmente desconocido para mí al inicio de estas tesis, y que ha resultado ser una parte fundamental de este trabajo. Josetxo, gracias por haberme abierto las puertas del laboratorio de síntesis, donde he podido desarrollar la mayor parte de esta tesis y donde he tenido la oportunidad de adquirir una gran experiencia. Gracias por vuestra confianza y cercanía durante estos años.

Por otro lado, me gustaría agradecer al Prof. Angel Alegría por su ayuda y apoyo con las medidas dieléctricas realizadas en este trabajo, así como con las cuestiones relacionadas con el doctorado. Gracias al Dr. Angel Moreno por el trabajo realizado en las simulaciones de dinámica molecular. Agradezco sinceramente a todas las personas del grupo de "Polymers and Soft Matter".

Además, durante estos años de tesis he recibido el apoyo de muchos compañeros y amigos. Es por ello que me gustaría agradecer a todos los que me han ayudado en más de una ocasión. Gracias a mi compañera de despacho Isabel, la que me ha aguantado desde el comienzo de la tesis con su enorme paciencia, la que me ha enseñado todo lo que se de cómo trabajar en el laboratorio, y con la que he compartido muy buenos momentos, tanto en los viajes a Garching o al PSI, como en el día a día. Contigo también he compartido muchas cosas Alex, muchas gracias por todos los momentos vividos y todo tu apoyo durante estos años. Aunque es cierto que el despacho está más tranquilo, ¡te echamos de menos!

También quiero agradecer a Amaia por su trabajo y gran dedicación con las medidas de rayos X, por tu disponibilidad para ayudar en lo que haga falta, siempre dispuesta a echar una mano. Y tampoco me olvido de los viajes que hemos compartido, eskerrik asko igarotako momentu onengatik!

Y por supuesto, no me olvido de agradecer a los "treinteenagers" y al resto de compañeros del grupo: Paula, Dani, Lucía, Natalia, Izaskun, Thomas, Bea, Edurne, Jon, Julen, Jordan, y Maud, gracias por los buenos momentos y por el apoyo recibido cuando lo he necesitado. Gracias a los que ya no siguen en el grupo, pero he tenido la oportunidad de conocer y me han ayudado durante la tesis: Ana Lucía, Ana, Irma, Manuel, Gerardo.

Azkenik, eskerrik handiena nire familiari zor diot, beraiek izan bait dira uneoro nigan konfiatu dutenak, laguntza eta maitasuna ematen didatenak, mila esker benetan! Eta nola ez, nire kuadrilla eta lagun guztiei eskerrik beroena eman nahi diet, beti hor daudelako eta egongo direlako.